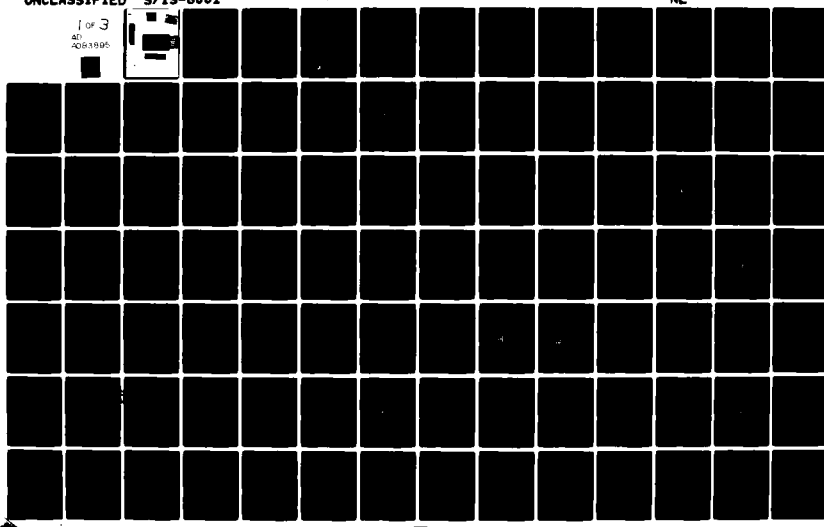


AD-0683 895

YALE UNIV NEW HAVEN CT SYSTEMS AND INFORMATION SCIENCES F/G 20/1
FREQUENCY SPREADING IN UNDERWATER ACOUSTIC SIGNAL TRANSMISSION, (U)
APR 80 H TUNG, F B TUTEUR, J G ZORNIG N00014-77-C-0237
S/IS-8001 NL

UNCLASSIFIED

1 of 3
45
20831995



12

FREQUENCY SPREADING IN
UNDERWATER ACOUSTIC SIGNAL TRANSMISSION

Henti Tung
Franz B. Tuteur
John G. Zornig

Final Report #8001

ONR Contract N00014-77-C-0237

April 1980

This document has been approved
for public release and sale; its
distribution is unlimited.

SECURITY CLASSIFICATION OF THIS PAGE (When Data Entered)

REPORT DOCUMENTATION PAGE			READ INSTRUCTIONS BEFORE COMPLETING FORM
1. REPORT NUMBER S&IS 8001	2. GOVT ACCESSION NO. 14/SIS-111 AD-A083895/9	3. RECIPIENT'S CATALOG NUMBER	
4. TITLE (and Subtitle) Frequency Spreading in Underwater Acoustic Signal Transmission	5. DATE OF REPORT & PERIOD COVERED Final Report, Feb 77-Jun 78, 2-77 to 6-78		
6. AUTHOR(s) Henti Tung Franz B. Tuteur John G. Zornig	7. PERFORMING ORG. REPORT NUMBER 8001		
8. CONTRACT OR GRANT NUMBER(s) N00014-77-C-0237	9. PROGRAM ELEMENT, PROJECT, TASK AREA & WORK UNIT NUMBERS Contract Authority NR 083-322		
10. CONTROLLING OFFICE NAME AND ADDRESS Yale University Dept. of Engineering and Applied Science 2157 Yale Station, New Haven, Connecticut 06520	11. REPORT DATE April 15, 1980		
12. NUMBER OF PAGES 208	13. SECURITY CLASS. (If data security) U		
14. MONITORING AGENCY NAME & ADDRESS (if different from Controlling Office) ONR Resident Representative 715 Broadway New York, New York 10003	15. DECLASSIFICATION/DOWNGRADING SCHEDULE		
16. DISTRIBUTION STATEMENT (of this Report) The content of this report does not necessarily reflect the position or the policy of the Department of the Navy or the Government and no official endorsement should be inferred. The United States Government has at least a royalty-free, non-exclusive and irrevocable license throughout the world for Government purposes to publish, translate, reproduce, deliver, perform, dispose of, and to authorize others so to do, all or any portion of this work.			
17. DISTRIBUTION STATEMENT (of the abstract entered in Block 20, if different from Report) work.			
18. SUPPLEMENTARY NOTES			
19. KEY WORDS (Continue on reverse side if necessary and identify by block number) Underwater Acoustics, Signal Transmission, Scattering, Doppler Shift, Frequency spectra, Asymmetry, Wind-blown Surface, Gaussian Surface, Third-order Moments.			
20. ABSTRACT (Continue on reverse side if necessary and identify by block number) The scattering of acoustic waves from a randomly varying wind-driven water surface is known to introduce both time and frequency spreading of the received signal. The frequency spreading is thought to be related to surface statistics and water wave motion. Therefore, knowledge of this relation leads to the possibility of predicting surface statistics by analysis of the received acoustic signal. One important feature of the frequency spreading function is that the			

DD FORM 1 JAN 73 1473 EDITION OF 1 NOV 68 IS OBSOLETE
S/N 0102-014-6601

SECURITY CLASSIFICATION OF THIS PAGE (When Data Entered)

410315

2 next

162

20.

→ Doppler sidebands are not equal in magnitude on both sides of the carrier. This was first disclosed in some recent papers [1], [2]. In these papers unequal sidebands were predicted if the acoustic source and receiver are not located at the same depths below the water surface and if the direction of the surface wave motion is not perpendicular to the vertical plane containing both the source and the receiver. Experimental results [3] from a model tank operated under various wind conditions have verified the existence of unequal Doppler sidebands under these conditions. However, strong asymmetries in sidebands were also observed under conditions under which the previous theory would have predicted no asymmetries at all. For example, strong asymmetries have been observed in the crosswind direction.

This research is to explain the asymmetries not predicted in previous theory but discovered under laboratory operations, and to predict other asymmetries not yet found in either the experimental or the theoretical phase.

The general approach to the solution of this problem is via the Kirchhoff integral, together with a choice of certain surface wave models. In this way, it is shown that asymmetries can arise not only from unequal depths of source and receiver, but also from small misalignments in the measuring system. Furthermore, it is shown that the usually ignored skew in the surface-slope probability density function also contributes to the observed results.

Accession For	
NTIS	ORALI
DDC TAB	<input checked="" type="checkbox"/>
Unannounced	<input type="checkbox"/>
Justification	
By _____	
Distribution	
Availability	
Dist	Available or special

ABSTRACT
FREQUENCY SPREADING IN
UNDERWATER ACOUSTIC SIGNAL TRANSMISSION

Henti Tung

Yale University

May, 1980

The scattering of acoustic waves from a randomly varying wind-driven water surface is known to introduce both time and frequency spreading of the received signal. The frequency spreading is thought to be related to surface statistics and water wave motion. Therefore, knowledge of this relation leads to the possibility of predicting surface statistics by analysis of the received acoustic signal.

One important feature of the frequency spreading function is that the Doppler sidebands are not equal in magnitude on both sides of the carrier. This was first disclosed in some recent papers [1], [2]. In these papers unequal sidebands were predicted if the acoustic source and receiver are not located at the same depths below the water surface and if the direction of the surface wave motion is not perpendicular to the vertical plane containing both the source and the receiver. Experimental results [3] from a model tank operated under various wind conditions have verified the existence of unequal Doppler sidebands under these conditions. However, strong asymmetries in sidebands were also observed under conditions under which the previous theory would have predicted no asymmetries at all. For

example, strong asymmetries have been observed in the crosswind direction.

This research is to explain the asymmetries not predicted in previous theory but discovered under laboratory operations, and to predict other asymmetries not yet found in either the experimental or the theoretical phase.

The general approach to the solution of this problem is via the Kirchhoff integral, together with a choice of certain surface wave models. In this way, it is shown that asymmetries can arise not only from unequal depths of source and receiver, but also from small misalignments in the measuring system. Furthermore, it is shown that the usually ignored skew in the surface-slope probability density function also contributes to the observed results.

ACKNOWLEDGEMENT

I would like to express my sincere thanks to my advisor Professor F.B. Tuteur, for his support throughout this investigation and for his invaluable comments in the preparation of this dissertation. His patient guidance and constant encouragement made these past years not only educational but also a most delightful experience in my career as a student. To him I am deeply indebted.

I also wish to thank the other members of my dissertation committee: Professor P.M. Schultheiss, for his invaluable discussion and helpful advice concerning this study; Professor R.E. Apfel, for teaching me the fundamentals of acoustics; Professor J.G. Zornig, for his illuminating suggestion and for permission to use his experimental results which have served as important verification to this research.

Thanks are extended to Professor R.C. Barker and Professor R.K. Chang for their constant encouragement; and to Professor J.F. McDonald for his suggestions and interest in this work. Professor T.P. Ma provided much assistance and advice, and this is greatly appreciated. Although it is not possible to thank everyone individually, I am grateful to members of the Department of Engineering and Applied Science for their expertise in various areas which in many ways contributed to this research. In particular, I want to thank Pat Kakalow for the excellent job that she has done in typing this dissertation.

I also wish to thank the U.S. Navy, Office of Naval Research for providing financial support.

I am grateful to my parents and parents-in-law for their great

sacrifice and support which made my studies possible. Finally,
the last and also the deepest thanks go to my wife Peisha, for
her patience, understanding and sympathy which have guided me
through my graduate education.

CONTENTS

	PAGE
Chapter I: FREQUENCY SPREADING	1-1
1.0 Introduction	1-1
1.1 Motivations	1-5
1.2 Historical Background	1-11
Chapter II: MATHEMATICAL PRELIMINARIES	2-1
2.0 Introduction	2-1
2.1 The Kirchhoff integral	2-2
2.2 The Fresnel approximation and other expansion formulae	2-6
2.3 Beam pattern function	2-13
Chapter III: DETERMINISTIC SURFACE	3-1
3.0 Introduction	3-1
3.1 The surface model	3-5
3.2 Downwind	3-7
3.3 Crosswind	3-25
3.4 Summary	3-28
Chapter IV: RANDOM SURFACE	
4.0 Introduction	4-1
4.1 General scattering	4-3
4.2 Random surfaces-small Rayleigh parameter	4-13
4.3 Random surfaces-large Rayleigh parameter	4-29
Chapter V: EXPERIMENTAL DATA COMPARISON AND DISCUSSION	
5.0 Introduction	5-1
5.1 Doppler shift	5-1
5.2 Theoretical analysis of angled paths	5-11
5.3 Bandwidth	5-21

	PAGE
Chapter VI: PHYSICAL ARGUMENTS FOR THE REATION OF ASYMMETRIC SIDEBANDS	
6.0 Introduction	6-1
6.1 Effect of source-receiver geometry	6-1
6.2 Effect of the surface slope distribution	6-6
Chapter VII: SUMMARY AND CONCLUSIONS	7-1
Appendix A: DERIVATION OF HELMHOLTZ INTEGRAL	A-1
Appendix B: SURFACE INTEGRAL TRANSFORMATION	B-1
Appendix C: SPECTRUM COMPUTATION - DETERMINISTIC SURFACE, DOWNWIND	C-1
Appendix D: PROOF OF $X \geq 0$	D-1
Appendix E: SPECTRUM COMPUTATION - DETERMINISTIC SURFACE, CROSSWIND	E-1
Appendix F: REPRESENTATION OF TRANSFER FUNCTION $H(\omega_0, t)$ IN A GENERAL SCATTER GEOMETRY	F-1
Appendix G: SIGN OF THIRD ORDER SLOPE MOMENT	G-1
Appendix H: POWER SPECTRUM-RANDOM SURFACE, SLIGHTLY ROUGH	H-1
Appendix I: POWER SPECTRUM-RANDOM ROUGH SURFACES	I-1
Appendix J: SIGNAL PROCESSING TECHNIQUE	J-1
References	R-1

ILLUSTRATIONS

<u>Figure</u>	<u>Description</u>	<u>Page</u>
1.1	Crosswind source-receiver geometry	1-6
1.2	Wind-driven surface sketch	1-8
1.3	Power spectrum in crosswind scattering geometry	1-9
1.4	The probability distribution of surface slopes	1-16
2.1	Derivation of Helmholtz integral Theorem: region of integration	2-3
2.2	General forward-scatter geometry	2-7
2.3	Illustration of two different reflected rays	2-11
3.1	Waveforms generated from a two harmonic model: $z(t) = h_1 \cos(\omega t + \phi) + h_2 \cos(2\omega t)$	3-3
3.2	General forward-scatter geometry with wind direction	3-4
3.3	Downwind scatter geometry ($r_{00} < r_{10}$)	3-8
3.4	Fresnel zones - symmetrical source-receiver geometry ($r_{00} = r_{10}$)	3-14
3.5	Fresnel zones - asymmetric source-receiver geometry ($r_{00} < r_{10}$)	3-15
3.6	First order side frequency power ratio versus phase angle ϕ	3-19
3.7	First order side frequency power ratio as function of geometry	3-20
3.8	First order side frequency power ratio versus grazing angle ψ_0	3-22
3.9	Crosswind scatter geometry	3-26
4.1	General scatter geometry with wind direction	4-4
4.2	Power spectrum-small and large ϵ_2	4-18
4.3	Doppler sidebands for scattering from slightly rough surfaces, upwind	4-20
4.4	Asymmetric sidebands for different acoustic frequency	4-23

4.5	Asymmetric sidebands for small Rayleigh parameter, $\epsilon_3 = 0$, and $r_{00} > r_{10}$	4-24
4.6	Asymmetric sidebands for small Rayleigh parameter, $\epsilon = 0$, and $r_{00} < r_{10}$	4-25
4.7	Experimentally measured spectrum-crosswind	4-28
4.8	Gaussian spectrum-Downwind	4-34
4.9	Theoretically computed power spectrum (1) - rough surface, upwind	4-35
4.10	Theoretically computed power spectrum (2) - rough surface, upwind	4-36
4.11	Theoretically computed power spectrum (3) - rough surface, upwind	4-37
4.12	Theoretically computed power spectrum (4) - rough surface, upwind	4-38
4.13	Bandwidth coefficient for downwind	4-40
4.14	Bandwidth for different wind direction and grazing angles	4-42
4.15	Theoretically computed power spectrum (1) - rough surface, crosswind	4-43
4.16	Theoretically computed power spectrum (2) - rough surface, crosswind	4-44
4.17	Theoretically computed power spectrum (3) - rough surface, crosswind	4-45
5.1	Power spectrum - upwind, $\psi_0 = 30^\circ$	5-2
5.2	Power spectrum - crosswind, $\psi_0 = 30^\circ$	5-3
5.3	Power spectrum - upwind, $\psi_0 = 17^\circ$	5-4
5.4	Power spectrum - crosswind, $\psi_0 = 17^\circ$	5-5
5.5	Power spectrum - experimentally measured at $\phi_T = 270^\circ$, $\phi_R = 85^\circ$	5-7
5.6	Power spectrum - experimentally measured at $\phi_T = 270^\circ$, $\phi_R = 90^\circ$	5-8
5.7	Power spectrum - experimentally measured at $\phi_T = 270^\circ$, $\phi_R = 95^\circ$	5-9
5.8	Source-receiver geometry for experimental results shown in Figures 5.5-5.7	5-10

5.9	Off-specular source-receiver geometry	5-12
5.10	Frequency displacements for spectra shown in Figures 5.5 to 5.7	5-16
5.11	Shifted power spectrum of Figure 5.1	5-17
5.12	Shifted power spectrum of Figure 5.2	5-18
5.13	Shifted power spectrum of Figure 5.3	5-19
5.14	Shifted power spectrum of Figure 5.4	5-20
6.1	Asymmetric downwind scatter geometry and attenuation factor	6-2
6.2	Asymmetric crosswind scatter geometry and attenuation factor	6-5
6.3	Symmetric downwind scatter geometry and surface slope distribution	6-7
6.4	Symmetric crosswind scatter geometry and surface slope distribution	6-8
B.1	Scatter surface and its projection on X-Y plane	B-2
G.1	Saw-tooth wave	G-2
J.1	Signal representations of acoustic signal transmitted and received underwater	J-2
J.2	Signal spectrum computing block diagram.	J-3

Chapter I. Frequency spreading

1.0 Introduction

When an acoustic signal is scattered from a water surface, the received signal in general depends on the characteristics of the reflecting surface. If the water surface is a moving rough surface, and if the acoustic signal is a pure sinusoid, a substantial amount of frequency spreading around the transmitted frequency can be expected in the received signal [1] - [18]. This frequency spreading behavior is the result of the amplitude and phase modulations of the acoustic signal because of surface roughness. Gulin [36] has described the amplitude and phase modulations of a sinusoidal surface from a physical optics point of view. Parkins [4] generalized the sinusoidal surface case to a time varying ocean situation where he found the scattered acoustic spectrum was related to the surface spectrum. Scharf and Swarts [5] and Eggen [11] have developed a simple model of high frequency scattering which gives a fairly general qualitative description of scattered field spectral characteristics. They found the bandwidth of the frequency spreading function to be a function of surface roughness. Clay and Medwin [7] have looked at the problem in the time domain and derived the temporal correlations of the scattered sound field. McDonald and Tuteur [8] have considered the surface scattering function which contains both time delay and frequency spreading. All of the above papers use the physical optics method (Kirchhoff integral⁺). Harper and Labianca

⁺ See Chapter II, section 1 for detailed descriptions.

[1], [44], and Kuperman [2], [46] have considered the scattering problem from a perturbation point of view. These theoretical treatments of the scattering problem discovered a spectral asymmetry that had previously escaped notice.

There has also been a number of experimental studies of the scattering phenomenon. Typical are sea experiments of Roderick and Cron [16], Brown and Frisk [17], and model tank experiments such as those of Zornig [3] or Gazanhes et al [13], etc. There appears to have been no single theory that explains all the details of the frequency spreading behavior that have been discovered in these experiments. For instance, the perturbation method of Harper and Labianca, and of Kuperman showed that the frequency spreading function may be asymmetric for upwind (or downwind) transmission, but it does not explain the observed asymmetry in the crosswind direction. Furthermore, it applies only in small surface roughness situations. For large surface roughness the physical optics method has generally been used; however, if the usual simplifying approximations are applied, this method gives no spectral asymmetry at all.

In this study, the frequency spreading function, including both the amplitude and bandwidth, is examined. The object of this investigation is to develop a model and a formula from which the general frequency spreading function can be predicted, given the scattering geometry and surface conditions.

The analytical solution to this problem is based on the Kirchhoff integral method. The mathematical results presented are for arbitrary scattering geometry where the locations of source and

receiver are not fixed. These results are specialized for upwind (or downwind) and crosswind geometries, and detailed properties of the function are discussed mainly for these special cases. We will find that the important surface parameters for frequency spreading are the second-order moment of surface waveheight and the second and third-order moments of surface slopes. Although the effect of the surface slopes has frequently been neglected in previous surface scattering studies (e.g. see [4]-[11],[13]), our analysis shows that surface slope statistics may play an important role in determining the shape of the frequency spreading function.

One important aspect of frequency spreading is the sideband asymmetry which was discovered in both theory (perturbation method) and experiment. We will show that similar results can be obtained by use of the Kirchhoff integral method if certain usually neglected higher-order expansion terms of this integral formula are retained.

The organization of this study is as follows: Chapter I describes 1) the frequency spreading function and its general behavior, 2) a brief review of the sideband asymmetries found by the perturbation method, and 3) a historical background review in the areas of underwater acoustical surface scatter. Chapter II contains a review of the Kirchhoff integral and the necessary boundary conditions in order to provide a solution to the surface scattering problem. Chapter III considers a deterministic surface model, from which the solutions to the frequency spreading are obtained. Chapter IV contains a discussion of the scattering of acoustic waves from a random water surface. Both large and small roughness cases are considered. Chapter V gives a

comparison between the theory and the experimental results obtained from a model tank. It is shown that misalignments in source-receiver geometry can cause significant shift in the frequency spreading function. In Chapter VI, the study of frequency spreading behavior of acoustic surface scattering is considered from a physical point of view. Chapter VII offers a summary and conclusions. Appendices A to J provide the necessary mathematical background and computational details for the solutions presented in Chapters II to V.

1.1 Motivations

Consider a monochromatic acoustic wave of frequency ω_0 scattered from a moving rough water surface. The received signal spectrum will generally be spread in frequency around the angular frequency ω_0 . If the surface roughness is small and if the surface deformation is roughly periodic, the spreading consists of a fairly distinct sequence of sideband frequencies. This is the result of phase modulation of the transmitted sinusoid by the moving surface, and the separation between the spectral lines at the receiving point is roughly equal to the surface frequency [5]. If the surface is rough and confused, the sidebands merge together into a more or less continuous spreading of frequencies around the transmitted frequency ω_0 .

In several recent papers [1], [44]-[45], E.Y. Harper and F.M. Labianca showed that if the source and receiver are at different depths, the upper⁺ and lower sidebands may have different spectral amplitudes. A similar result was obtained more recently by Kuperman [2], [46]. The amplitude ratio depends on the direction of the surface wave motion with respect to the source-receiver geometry. Specifically, if the receiver is at a larger depth than the source, and if the wind causes the surface wave to travel away from the source and toward the receiver, then the upper sideband amplitudes are larger.

⁺ The upper (lower) sideband refers to band of frequency higher (lower) than the transmitted frequency ω_0 .

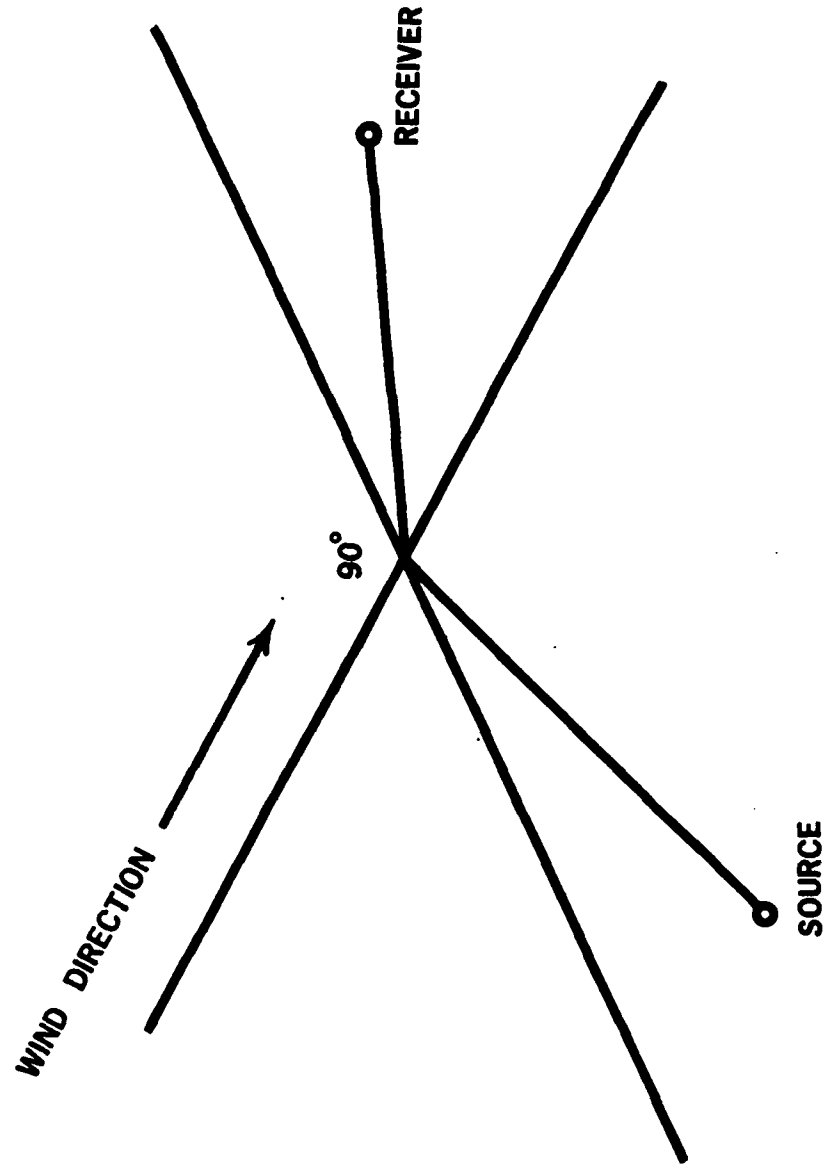


Figure 1.1 Crosswind source-receiver geometry

The existence of sideband asymmetries has been observed in a series of experimental results obtained in a model tank under simulated wind blown surface wave conditions [3], [12]. These measurements showed the predicted asymmetries, but they also showed asymmetry in the frequency spreading function when the source and receiver were at the same depths, and the source-receiver geometry was crosswind. For this arrangement the Harper, Labianca, and Kuperman theory would have predicted symmetrical sideband structures. It is clear, therefore, that there are features of the spreading mechanism that are not yet included in these theories.

The observation of sideband asymmetry in the model tank experiment can be explained heuristically as follows. Consider a crosswind source-receiver configuration in Figure 1.1. Rays reflected from upwind facets have upward doppler shifts, whereas those reflected from downwind facets have downward doppler shifts [21]. In a wind driven water surface the slope distribution at the windward side is different from that at the leeward side [55], [56]. A sketch of a wind blown surface wave is shown in Figure 1.2; note that the surface slopes on the windward side are shallower than those on the leeward side [70]. The area of up-wind slopes capable of reflecting rays from the source to the receiver with upper doppler shifts is larger than the area of the downwind slopes. Hence, one would expect the upper sidebands to be larger than the lower sidebands. This can be seen in the experimental results of J.G. Zornig shown in Figure 1.3. This frequency spectrum was taken in a crosswind condition with the source and receiver at equal depths. The frequency of the

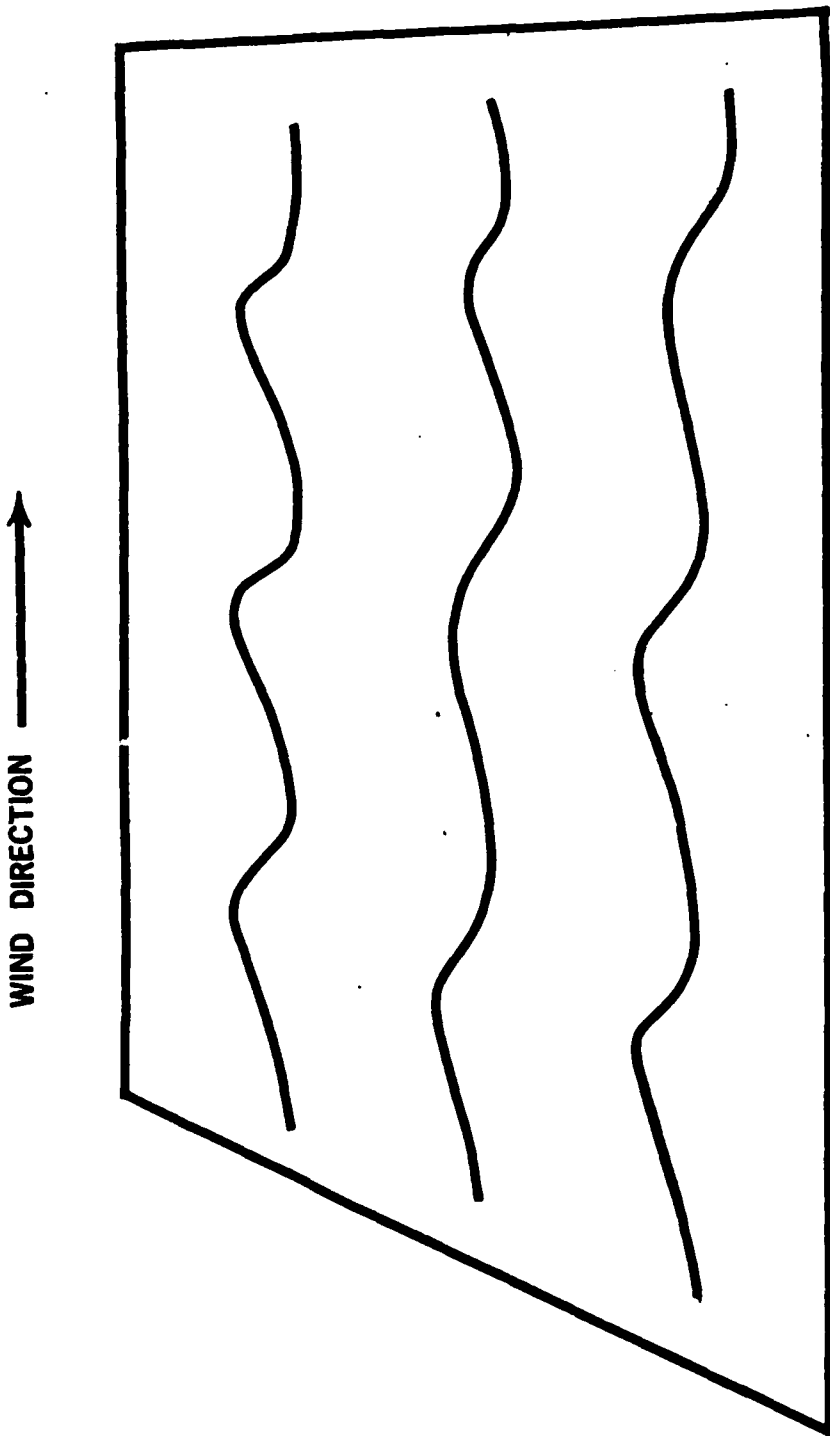


Figure 1.2 Wind-driven surface sketch

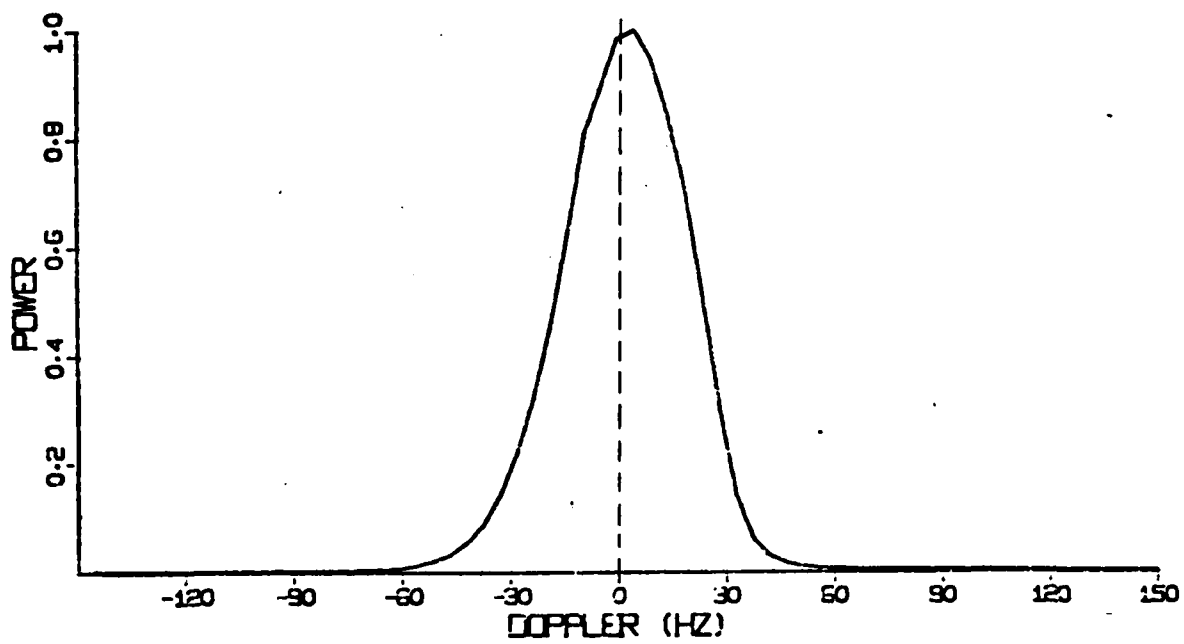


Figure 1.3 Power spectrum in crosswind scattering geometry with grazing angle of 30° and wind speed 8.3m/sec. The acoustic frequency is 256 KHz.

acoustic wave was 256 KHz.⁺ As shown, frequency components higher than the transmitted frequency (i.e. the upper sideband) are larger in amplitude than the corresponding components below the transmitted frequency (i.e. the lower sideband).

We see that in order to investigate this phenomenon analytically, it is necessary that the analysis takes into account the details of surface slopes. Eckart [31], Gulin [36], Parkins [4], McDonald [38], and many other authors generally neglected the slope terms in the Kirchhoff integral by assuming the slope variations to be small. This implies that amplitude and phase modulations on the acoustic signal are due entirely to the up and down motion of the surface. On the other hand, Tolstoy and Clay [69] included slope terms in their version of the Kirchhoff integral. But because of the assumption of a directional source, these slope terms were combined into an average slope term at the surface point from which most of the acoustic energy was reflected. As will be shown in subsequent chapters of this work, all of these approximations eliminate one of the mechanism that causes sideband asymmetry.

⁺ The experimental technique actually involves the transmission of narrow pulses, and the recording of the pulse responses. After Fourier transformation, the response to any desired exciting frequency can, however, be obtained.

1.2 Historical Background

The problem of scatter of acoustic signals from a rough air-water interface has been extensively studied during the last few decades. An excellent survey of the literature to 1958 was compiled by Lysanov [19]. A more recent and more general survey can be found in the excellent paper of Fortuin [20], which covers work up to 1969. The following review leans heavily on Fortuin's paper, but extends it to include the decade 1969 to 1979.

The scattering of sound by a sinusoidal water-air interface was first studied by Lord Rayleigh [21]. This was the first attempt to solve the wave equation in combination with a boundary condition in sound scatter problems. Rayleigh's solution was an intuitive approach which assumed that the scattered sound field from a pressure-release sinusoidal surface could be described by a discrete set of plane waves travelling away from the surface. This simple approach received criticisms [22]-[30] from several authors, such as Uretsky [22], Meecham [28], Heaps [30], who questioned the validity of the boundary conditions assumed by Rayleigh. All of these critics concluded, that "the Rayleigh method is indeed incorrect in the way the boundary conditions are used" [20,p. 1213], however, "for [relatively] smooth surfaces, the method produces results that do not disagree more with experimental data than do other, more rigorous, solutions." Uretsky [22] developed a method which improves upon that of Rayleigh. It is based on a more rigorous mathematical approach with matrix computation and handling techniques

to evaluate the reflection coefficients for the various orders of sound reflection from a sinusoidal surfaces. His method was summarized by Barnard et al. [27] and used to make comparisons with experimental results obtained in a model tank. Satisfactory agreement between theory and experiment was obtained. Both the Rayleigh and Uretsky theories apply to sinusoidal surfaces only.

In 1953, Eckart [31] applied an integral formulation known as the Helmholtz integral [32] to the solution of sound scattering from rough boundaries. He assumed two boundary conditions. One is that the water-air interface is a pressure-release surface; the other is that the first derivatives of the incoming acoustic wave and the scattered fields are equal at the surface. This is a frequently used boundary condition called the Kirchhoff approximation. The use of the Kirchhoff approximation implies that the surface is locally flat, i.e. the radius of the surface curvature is much larger than the acoustic wavelength, and the surface is free of shadowing and multiple reflections. Eckart derived a surface scattering cross-section coefficient in terms of the incident acoustic frequency and surface spatial spectrum. The Kirchhoff integral approach (Helmholtz integral plus Kirchhoff boundary condition) was criticized by Meecham [33] and Mintzer [34] because the limit of the validity of the Kirchhoff boundary condition was not properly considered. It has in fact been said [6] that Eckart "had obtained significant results with minimum mathematical complexity by relying on a highly developed physical insight into the problem". Nonetheless the Kirchhoff integral method has been widely used in studies of surface scatter, and experi-

mental verification of some results [36] seems to indicate that the error introduced by the Kirchhoff approximation may not be too serious. The formulation used by Eckart is equivalent to the Fraunhofer approximation used in optics. An improvement of this approximation is the Fresnel or second-order approximation, first applied to surface-scatter problems by Feinstein [35]. It has also been used by Gulin [36], Melton and Horton [37], Medwin and Clay [7], McDonald and Tuteur [8], etc. The Fresnel corrected Kirchhoff integral is usually applied where the illuminated surface area is large. It has many applications, such as the study of amplitude and phase fluctuations [12], the correlation and power distribution of scattered sound [7], [38], and the studies of frequency spreading and shift in forward and backward scatters [10].

A different approach to the solution of surface scatter problems is the perturbation method introduced by Isakovitch [41] in 1957. Its original application was to solve the normal-mode transformation problem in an irregular waveguide. Bezrodnyi and Fuks [42] used it in the solution to the problem of amplitude and phase fluctuations in a waveguide. Wait [43] analyzed the reflection from two-dimensional periodic sea waves. In 1975, Harper and Labianca [44] used the perturbation method in the study of the spectral behavior of the surface scattered acoustic signal. Their studies show the existence of asymmetrical sidebands in surface scattering. This result was corroborated by the theoretical study of Kuperman [2] using the same method, and by experiment [3]. The perturbation method

is mathematically more rigorous than the Kirchhoff integral method and permits fairly precise bounds to be placed on the validity of the simplifying assumptions [45]. However, its applications are limited to problems with very small roughness.

Both the Fresnel-corrected Kirchhoff integral and the perturbation method require a solution to the wave equation subject to boundary conditions at the water-air interface. If the form of boundary is very complicated, it can be extremely difficult, if not impossible, to reach such a solution. Middleton [47] developed a so-called Quasiphenomenological approach which eliminated the need to simultaneously satisfy the wave equation and boundary conditions. It introduces the surface (boundary) in terms of a group of randomly distributed point scatterers. Each of these point scatterers has its own system function and directivity pattern. This gives the model the ability to handle problems of general scatter geometry with very complex boundary conditions. However, application of this very general theory is severely restricted in practice by the difficulty of relating measured surface parameters to statistical behavior of the scatterers.

The commonly used surface parameters are surface waveheight and surface slopes. In most of the analyses that require descriptions of the water surface boundary, it is assumed, with exceptions e.g. [49], [50], that the water surface height and slopes are stationary Gaussian processes [4]-[5], etc. Experiments performed at sea and in model tanks have shown that this, in fact, is close to the real situation. For example, Kinsman [51] used a capacitance probe held

at the water surface to record the surface displacement. The result of his measurement indicated the surface height distribution was close to Gaussian with zero mean.⁺ This observation was corroborated by Weissman [52] in his ocean waveheight measurement with a two frequency radar interferometer and by Zornig [53] in his height measurement in a model tank. However, Spindel [54] found that the joint distribution of two points on the surface is occasionally far from Gaussian. In particular, he found that the conditional distribution of the surface at one point, given its value at the second point, was occasionally multimodal, especially at high winds. Cox and Munk [55] studied the slope distribution of a wind-driven surface using aerial photograph technique. Their method consisted "in photographing from a plane the sun's glitter pattern on the sea surface, and translating the statistics of the glitter into the statistics of the slope distribution". Figure 1.4 contains the result of the slope measurement by Cox and Munk. The top plot was the slopes measured crosswind and had a symmetrical structure with respect to zero slopes. The bottom plot was the up-down wind slope distribution which showed skewness to the upwind side, i.e. the most probable slope for the sea surface was negative. This distortion probably was due to a wind stress effect, as remarked by Kinsman [51], p. 350]. Schooley [56] made the same sea slope measurement by a similar optic method except the sun was replaced by a flashing gun attached

⁺ The flat surface level is chosen as the reference zero.

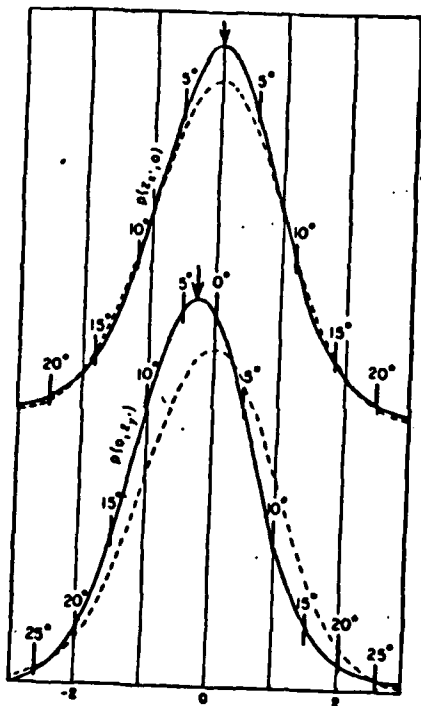


Figure 1.4 The probability distribution of surface slopes. The upper curves are for crosswind; the lower curves are for downwind. The solid curves refer to the observed distribution, the dashed to a Gaussian distribution of equal mean square slope components. The thin vertical lines show the scale for the standardized slope components

$$\frac{1}{\sigma_c} \frac{\partial \zeta}{\partial x} \text{ for crosswind and}$$

$$\frac{1}{\sigma_d} \frac{\partial \zeta}{\partial y} \text{ for downwind.}$$

The wind direction is in the y axis; σ_c and σ_d are the r.m.s. slope in x and y directions respectively. The heavy vertical segments show the surface slope angle for $5^\circ, 10^\circ, \dots, 25^\circ$. In the lower curve, the negative slopes are on the upwind side and the positive slopes are on the downwind side.

(From Cox and Munk, 1954)

to the camera. The same skewness in up-down wind slopes has been observed by Wu [57] and Zornig [58] in model tank experiments.

There are two reasons, as pointed out by Kinsman, why the waveheight and slopes are not strictly Gaussian. One is that the wave motion must satisfy the Bernoulli equation and the free-surface boundary conditions. The other is that waves are limited in height by the wave breaking phenomenon. In summary, it appears that even though the surface distribution is generally not strictly Gaussian, the assumption of a Gaussian distribution is not unreasonable, and it has been widely used.

Another factor to be considered in the development of a scattering theory is shadowing. Shadowing occurs when a part of the surface is screened by some other parts of the surface. In surface scatter terms, this means the illumination of incoming radiation at these parts of the surface is interrupted. Shadowing is more significant when the acoustic source and receiver are very close to the scattering surface. Neglecting this shadowing effect may cause large errors if the theory is based on the assumption of total illumination on the water surface, e.g. the Kirchhoff integral method. Beckman [59] proposed a simple way to treat the shadowing by introducing a shadowing function S which equals unity on the illuminated parts of the surface and equals zero on the screened parts. In other words, the shadowing function S is the probability that this part of surface will get illuminated. He applied this concept of a shadowing function to the study of backscattering from a composite rough surfaces [60]. However, a computer simulated experiment on

shadowing in backscatter by Brockelman and Hagfors [61] showed marked disagreement between their results and those of Beckmann. With a modification to the Beckmann theory that includes the effect of slopes, Wagner [62] developed formulas which consider geometric shadowing. A comparison between his results and those of experiment showed an excellent agreement between theory and experiment [20]. Lynch and Wagner [63], [64] used this geometric shadowing to correct the energy loss in high frequency scatter from random rough surfaces. A simplified method to evaluate Wagner's shadowing function was given by Smith [65]. He omitted the correlation between surface height and slopes but obtained a result which was not very different from the complete solution obtained from Wagner's method. Gardner [66] used Wagner's theory to explain near grazing backscatter through the Kirchhoff integral approach. However, it was pointed out in the experiment by Novarini and Medwin [67] that Wagner's theory of geometric shadowing is inadequate in the sea experiment because of the proven existence of bubbles below the sea surface [68]. In our analysis of the scattering problem, shadowing has been ignored. The analysis therefore is limited to relatively large grazing angles.

Chapter II. Mathematical preliminaries

2.0 Introduction

In this chapter, we introduce some basic mathematical concepts which are of interest in this analysis. These include the derivation of the Kirchhoff integral formula to solve the surface scatter problem, the Fresnel approximation and other expansions, the definition of surface roughness, and the beam pattern function for both source and receiver. Most of the material presented in this chapter can be found elsewhere. For example, Baker and Copson [32] and Eckart [31] give a derivation of Kirchhoff integrals; the Fresnel expansion is a second order approximation and is commonly presented in optics texts [71]; the discussion of the beam pattern function (directivity) for an acoustic source can be found in texts of acoustics, such as Beranek [72].

We shall regard the underwater acoustic surface scattering process as linear and slowly time-varying. This permits us to use a monochromatic signal source.

2.1 The Kirchhoff integral

Consider a function $p(\underline{r}, \omega_0, t)$ which satisfies the wave equation within a volume \bar{V} bounded by a surface S . For our purpose p is regarded as the complex time varying amplitude of the pressure at a location defined by \underline{r} and at the frequency ω_0 and time t . Assume that p and its first-order derivatives are finite and continuous inside the volume \bar{V} . Then, from the Helmholtz theorem (see Appendix A), the value of p at a particular point P inside \bar{V} and at time t is given by

$$p(P, t) = \frac{1}{4\pi} \iint_S \left[\frac{e^{j\frac{\omega_0}{c} r_1}}{r_1} \cdot \frac{\partial p_s}{\partial \underline{n}} - p_s \frac{\partial}{\partial \underline{n}} \left(\frac{e^{j\frac{\omega_0}{c} r_1}}{r_1} \right) \right] \cdot d\underline{s} \quad (2.1.1)$$

where p_s is the pressure amplitude at the surface S , r_1 is the scalar distance from the surface element $d\underline{s}$ to the point P as shown in Figure 2.1, and \underline{n} is the surface normal defined to be positive in the outward direction. The surface pressure p_s and its normal derivative are evaluated at the time $t - \frac{r_1}{c}$, where c is the sound velocity; however, for the time scale of interest in our work this retardation delay can be ignored [74].

In much of our work we are interested in sound transmitted and received by directional hydrophones with directional beam patterns. The effect of such a beam pattern is to give unequal weights to different parts of the surface S , and this effect can be included in equation (2.1.1) by changing the Green's function

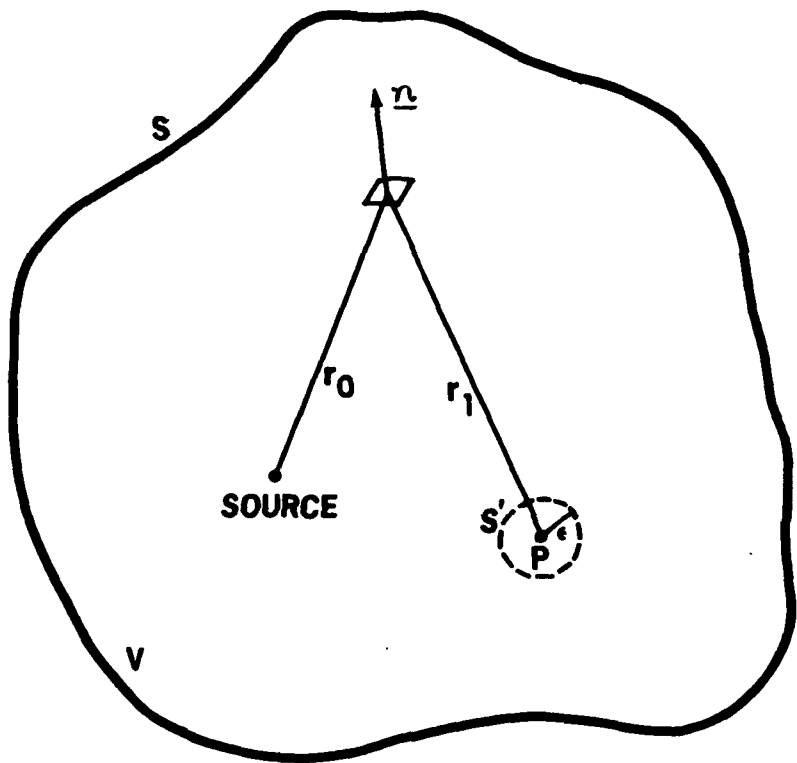


Figure 2.1 Derivation of Helmholtz integral Theorem:
region of integration

$\frac{e^{j\frac{\omega_0}{c}r_1}}{r_1}$ to $B_R \frac{e^{j\frac{\omega_0}{c}r_1}}{r_1}$. This results in

$$p(P, t) = \frac{1}{4\pi} \iint_S [B_R \frac{e^{j\frac{\omega_0}{c}r_1}}{r_1} \cdot \frac{\partial p_s}{\partial \underline{n}} - p_s \frac{\partial}{\partial \underline{n}} (B_R \frac{e^{j\frac{\omega_0}{c}r_1}}{r_1})] \cdot d\underline{s} \quad (2.1.1a)$$

where the beam pattern function B_R is, strictly speaking, evaluated at the retarded time $t - \frac{r_1}{c}$.

We now assume that the water surface is illuminated by a monochromatic acoustic source which has a beam pattern function B_s . The incident acoustic pressure p_i measured on the water surface is then given by

$$p_i = p_0 B_s \frac{e^{j\frac{\omega_0}{c}r_0}}{r_0} \quad (2.1.2)$$

where r_0 is the distance from the source point to the surface element $d\underline{s}$, and p_0 is the amplitude of the acoustic source.

The pressure amplitude p_s appearing in equation (2.1.1) is regarded as the surface reflected pressure. It is related to the incident pressure p_i through a surface boundary condition. For the air-water interface the surface can to a very good approximation be regarded as being a pressure-release surface; hence the boundary condition is

$$p_s + p_i = 0 \quad \text{on } S \quad (2.1.3)$$

Also, the normal derivative $\frac{\partial p_s}{\partial \underline{n}}$ can be related to the normal derivative of the incident pressure by invoking the Kirchhoff boundary

condition:

$$\frac{\partial p_s}{\partial \underline{n}} = \frac{\partial p_i}{\partial \underline{n}} \quad \text{on } S \quad (2.1.4)$$

The Kirchhoff condition implies that the surface is "locally flat", i.e. the radius of the surface curvature is much larger than the acoustic wavelength. It also implies no shadowing or multiple reflections on the surface, i.e. the surface is totally illuminated. As briefly discussed in Chapter I, there are criticisms about the validity of the Kirchhoff condition. A summary of these criticisms can be found in [20], [74]. However, by employing these two boundary conditions and replacing p_i with its equivalent from equation (2.1.2), one can convert the integral in equation (2.1.1a) to the form

$$p(P, t) = \frac{1}{4\pi} \iint_S p_0 \frac{\partial}{\partial \underline{n}} \left\{ B_s B_R \frac{e^{j\frac{\omega_0}{c}(r_0+r_1)}}{r_0 r_1} \right\} \cdot d\underline{s} \quad (2.1.5)$$

If we define the channel transfer function $H(\omega_0, t)$ as the ratio of $p(P, t)$ and p_0 , equation (2.1.5) can be rewritten as

$$H(\omega_0, t) = \frac{1}{4\pi} \iint_S \frac{\partial}{\partial \underline{n}} \left\{ B_s B_R \frac{e^{j\frac{\omega_0}{c}(r_0+r_1)}}{r_0 r_1} \right\} \cdot d\underline{s} \quad (2.1.6)$$

Thus $H(\omega_0, t)$ represents the instantaneous amplitude and phase at the receiver due to a unit amplitude sinusoidal signal with frequency ω_0 at the source.

2.2 The Fresnel approximation and other expansion formulae

A commonly used coordinate system in surface scattering studies is shown in Figure 2.1. The X-Y plane is the plane of the smooth (flat) surface. The positive direction for the Z axis is downward into the water. The origin of coordinates is taken to be at the smooth-surface specular point. The source, receiver and specular point lie in a plane which makes an angle ϕ_R with the -Y axis. Both source and receiver have grazing angles ψ_0 with the flat water surface. The distances from the origin to source and receiver are respectively r_{00} and r_{10} . The locations of source and receiver are described as (X_T, Y_T, Z_T) and (X_R, Y_R, Z_R) , respectively, where

$$\begin{aligned} X_T &= -r_{00} \cos \psi_0 \cos \phi_R & X_R &= r_{10} \cos \psi_0 \cos \phi_R \\ Y_T &= r_{00} \cos \psi_0 \sin \phi_R & Y_R &= -r_{10} \cos \psi_0 \cos \phi_R \\ Z_T &= r_{00} \sin \psi_0 & Z_R &= r_{10} \sin \psi_0 \end{aligned} \quad (2.2.1)$$

We further define $\zeta(x, y, t)$ as the surface displacement at a point (x, y) and time t , with positive ζ being upward. Therefore; the distances from the source and the receiver to an arbitrary point on the surface can be represented by r_0 and r_1 respectively, where

$$r_0 = [(X - X_T)^2 + (Y - Y_T)^2 + (\zeta + Z_T)^2]^{1/2} \quad (2.2.2a)$$

$$r_1 = [(X - X_R)^2 + (Y - Y_R)^2 + (\zeta + Z_R)^2]^{1/2} \quad (2.2.2b)$$

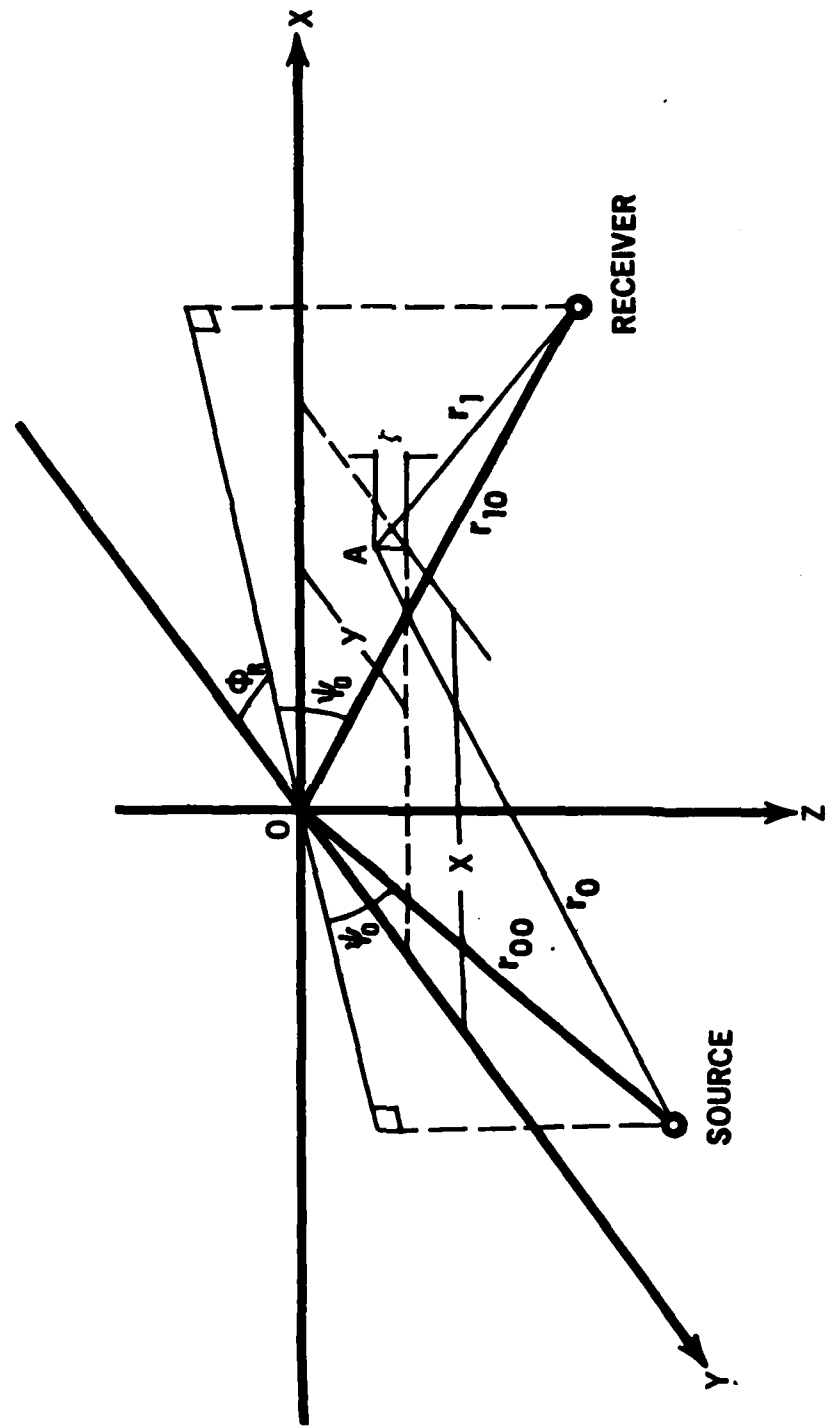


Figure 2.2 General forward-scatter geometry

The integration of equation (2.1.6) cannot be carried out in closed form if we substitute equations (2.2.2a) and (2.2.2b) directly. We therefore first rewrite r_0 and r_1 in the form

$$r_0 = r_{00} \left[1 - \frac{1}{2} \left(2x_T x + 2y_T y - 2z_T \zeta - x^2 - y^2 - \zeta^2 \right) \right]^{\frac{1}{2}} \quad (2.2.3a)$$

$$r_1 = r_{10} \left[1 - \frac{1}{2} \left(2x_R x + 2y_R y - 2z_R \zeta - x^2 - y^2 - \zeta^2 \right) \right]^{\frac{1}{2}} \quad (2.2.3b)$$

If the distances r_{00} and r_{10} are large compared to the dimensions of the insonified area, i.e. $r_{00}, r_{10} \gg X, Y, \zeta$, we can then expand equations (2.2.3a) and (2.2.3b) in a power series by use of the binomial expansion formula

$$(1+a)^n = 1 + na + \frac{n(n-1)}{2!} a^2 + \frac{n(n-1)(n-2)}{3!} a^3 + \dots \quad (2.2.4)$$

for $a^2 < 1$.

We further assume that the surface deformation is small compared with other dimensions, i.e.

$$\zeta(X, Y) \ll X, Y \ll r_{00}, r_{10} \quad (2.2.5)$$

Therefore we retain the first order term in ζ and the X, Y terms up to the second order in the expansion. The result is

$$r_0 \approx r_{00} - \frac{x_T}{r_{00}}x - \frac{y_T}{r_{00}}y + \frac{z_T}{r_{00}}\zeta + \frac{x^2[1-\frac{x_T^2}{r_{00}^2}] + y^2[1-\frac{y_T^2}{r_{00}^2}]}{2r_{00}}. \quad (2.2.6a)$$

$$r_1 \approx r_{10} - \frac{x_R}{r_{10}}x - \frac{y_R}{r_{10}}y + \frac{z_R}{r_{10}}\zeta + \frac{x^2[1-\frac{x_R^2}{r_{10}^2}] + y^2[1-\frac{y_R^2}{r_{10}^2}]}{2r_{10}}. \quad (2.2.6b)$$

Hence, the total transmission distance for any ray path can be approximated by

$$\begin{aligned} r_0 + r_1 &\approx r_{00} + r_{10} - \left(\frac{x_T}{r_{00}} + \frac{x_R}{r_{10}} \right)x - \left(\frac{y_T}{r_{00}} + \frac{y_R}{r_{10}} \right)y + \left(\frac{z_T}{r_{00}} + \frac{z_R}{r_{10}} \right)\zeta \\ &+ \left\{ \frac{x^2[1-\frac{x_T^2}{r_{00}^2}] + y^2[1-\frac{y_T^2}{r_{00}^2}]}{2r_{00}} + \frac{x^2[1-\frac{x_R^2}{r_{10}^2}] + y^2[1-\frac{y_R^2}{r_{10}^2}]}{2r_{10}} \right\} \end{aligned} \quad (2.2.7)$$

Equation (2.2.7) is called the Fresnel approximation.

Eckart [31] retained only the first order expansion terms of $r_0 + r_1$ in his analysis, i.e. he neglected the terms in the brackets of equation (2.2.7). This is called the Fraunhofer approximation. As mentioned in Chapter I, the Fresnel approximation is superior to the Fraunhofer approximation because it includes the second order terms. This permits the Fresnel approximation to be used in problems with large acoustic beam width. In fact, without the second order terms,

equation (2.2.7) can be simplified with the aid of equation (2.2.1) to give

$$r_0 + r_1 \approx r_{00} + r_{10} + 2\zeta \sin \psi_0. \quad (2.2.8)$$

Under these conditions, the path dependence on X and Y is completely eliminated, and the total path fluctuations of $r_0 + r_1$ is proportional only to the surface displacement $\zeta(X, Y, t)$. The total phase fluctuation between rays reflected at surface level $\zeta(X, Y, t)$ and rays reflected from the flat surface plane, i.e. $\zeta = 0$, is

$g_\zeta = \frac{\omega_0}{c} 2 \sin \psi_0 \zeta(X, Y, t)$. Figure 2.3 is a plot of the two reflected rays. If $\zeta(X, Y, t)$ is replaced by its r.m.s. value σ then g_σ , written as g , is called the Rayleigh parameter, and is given by

$$g = \frac{4\pi\sigma \sin \psi_0}{\lambda} \quad (2.2.9)$$

where $\lambda = 2\pi c/\omega_0$ is the acoustic wavelength. The Rayleigh parameter [75] is commonly used as a measure of surface roughness; $g \ll 1$ is a relatively smooth surface while $g \gg 1$ corresponds to a rough surface.

The product term $\frac{1}{r_0 r_1}$ in equation (2.1.6) can be expanded in a similar way. From equations (2.2.3) and (2.2.4), with n being set to $-\frac{1}{2}$, we have

$$\frac{1}{r_0 r_1} \approx \frac{1}{r_{00} r_{10}} \left\{ 1 + \left(\frac{x_T}{r_{00}}^2 + \frac{x_R}{r_{10}}^2 \right) x + \left(\frac{y_T}{r_{00}}^2 + \frac{y_R}{r_{10}}^2 \right) y \right\} \quad (2.2.10)$$

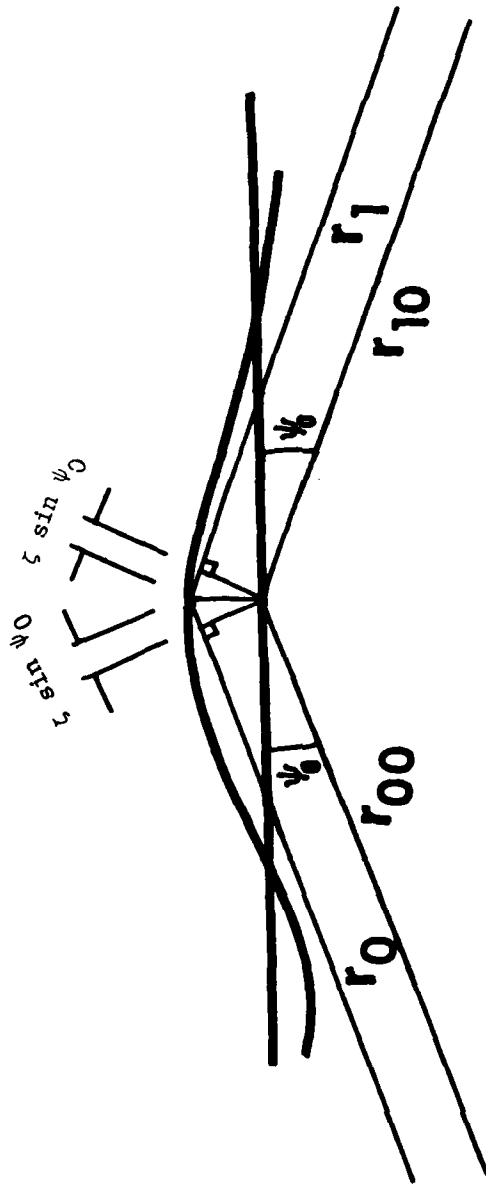


Figure 2.3 Illustration of two different reflected rays

The factor $\frac{1}{r_0 r_1}$ needs to be expanded only to first order in X and Y since it affects only the magnitude of the integrand of equation (2.1.6) whereas the term $r_0 + r_1$ determines the phase. Small changes in $r_0 + r_1$ can produce large changes in phase, but small changes of $\frac{1}{r_0 r_1}$ only cause a relatively small perturbation of the integrand. Also, because of inequality in equation (2.2.5), the dependence of $\frac{1}{r_0 r_1}$ on ζ is negligible.

We find it convenient, furthermore, to treat equation (2.2.10) as the first-order expansion of an exponential function so that another approximation of $\frac{1}{r_0 r_1}$ is

$$\frac{1}{r_0 r_1} \approx \frac{1}{r_{00} r_{10}} \exp \left\{ \left(\frac{x_T}{r_{00}^2} + \frac{x_R}{r_{10}^2} \right) x + \left(\frac{y_T}{r_{00}^2} + \frac{y_R}{r_{10}^2} \right) y \right\} \quad (2.2.11)$$

Substituting equation (2.2.1) into equations (2.2.7) and (2.2.11), $r_0 + r_1$ and $\frac{1}{r_0 r_1}$ can be rewritten in following forms:

$$r_0 + r_1 \approx r_{00} + r_{10} + 2 \zeta \sin \psi_0 + \frac{1}{R} [x^2 (1 - \cos^2 \psi_0 \cos^2 \phi_R) + y^2 (1 - \cos^2 \psi_0 \sin^2 \phi_R)] \quad (2.2.12)$$

$$\frac{1}{r_0 r_1} \approx \frac{1}{r_{00} r_{10}} \exp \left\{ -\left(\frac{1}{r_{00}} - \frac{1}{r_{10}} \right) [x \cos \psi_0 \cos \phi_R - y \cos \psi_0 \sin \phi_R] \right\} \quad (2.2.13)$$

where

$$R = \frac{2r_{00} r_{10}}{r_{00} + r_{10}} \quad (2.2.14)$$

2.3 Beam pattern function

The acoustic source is assumed to be circular-piston pressure transducer of diameter D_T . The beam pattern function for this type of transducer can be written as [72, p. 102]

$$B_T(\theta) = \frac{2J_1\left(\frac{\omega_0 D_T}{2c} \sin \theta\right)}{\frac{\omega_0 D_T}{2c} \sin \theta} \quad (2.3.1)$$

where θ is the angle measured from the center axis of the piston. $J_1(\cdot)$ is a first order Bessel function, having the power series expansion

$$\begin{aligned} J_1(x) &= \frac{x}{2} \sum_{n=0}^{\infty} \frac{\left(\frac{x}{2}\right)^{2n} (-1)^n}{(n+1)! n!} \\ &= \frac{x}{2} \left(1 - \frac{\left(\frac{x}{2}\right)^2}{2} + \frac{\left(\frac{x}{2}\right)^4}{3121} - \dots\right) \\ &= \frac{x}{2} - \frac{x^3}{8} + \frac{x^5}{384} - \dots \end{aligned} \quad (2.3.2)$$

Hence $B_T(\theta)$ can be rewritten as

$$B_T(\theta) = 1 - \frac{\left(\frac{\omega_0 D_T}{2c} \sin \theta\right)^2}{4} + \frac{\left(\frac{\omega_0 D_T}{2c} \sin \theta\right)^4}{192} - \dots \quad (2.3.3)$$

If we assume θ is sufficiently small such that $\sin \theta \approx \theta$, and the beam function can be approximated by the first two terms of equation (2.3.3), then

$$B_T(\theta) \approx 1 - \frac{\omega_0^2 D_T^2 \theta^2}{16c^2} \approx e^{-\frac{\omega_0^2 D_T^2 \theta^2}{16c^2}}. \quad (2.3.4)$$

We assume now that the projection of the beam pattern on the surface can be approximated by a two-dimensional Gaussian function

$$B_T(u, v) = e^{-\frac{1}{L_T^2(\omega_0)} (u^2 + v^2 \sin^2 \psi_T)} \quad (2.3.5)$$

where ψ_T is the grazing angle, and where u and v are transformed coordinates given by

$$u = -X \cos \phi_T - Y \sin \phi_T \quad (2.3.6a)$$

$$v = -X \sin \phi_T + Y \cos \phi_T \quad (2.3.6b)$$

We let the angle θ measured along the u and v directions be θ_u and θ_v respectively. Then for small θ , equation (2.3.5) can be rewritten as

$$B_T(u, v) = e^{-\frac{r_{00}^2}{L_T^2(\omega_0)} (\theta_u^2 + \theta_v^2 \sin^2 \psi_T)} \quad (2.3.7)$$

By comparing equations (2.3.4) and (2.3.7) and assuming a circular beam pattern, we see that

$$\frac{\omega_0^{2D_T^2}}{16c^2} = \frac{r_{00}^2}{L_T^2(\omega_0)} \quad (2.3.8)$$

or

$$L_T(\omega_0) = \frac{4cr_{00}}{\omega_0^{D_T}} = \frac{2c r_{00}}{\pi f_0^{D_T}} \quad (2.3.9)$$

Substituting this into equation (2.3.5), we have

$$B_T(u, v) = \exp \left\{ -\frac{\pi^2 f_0^2}{4c^2} \cdot \frac{D_T^2}{r_{00}^2} (u^2 + v^2 \sin^2 \psi_T) \right\} \quad (2.3.10)$$

By use of equation (2.3.6) the beam pattern function can be expressed in terms of X and Y. Using B_s to indicate the source beam pattern function on the surface, we have

$$B_s(X, Y) = \exp \left\{ -\frac{\pi^2 f_0^2}{4c^2} \cdot \frac{D_T^2}{r_{00}^2} [X^2(1-\cos^2 \psi_T \sin^2 \phi_T) + Y^2(1-\cos^2 \psi_T \cos^2 \phi_T) + XY(\cos^2 \psi_T \sin 2\phi_T)] \right\} \quad (2.3.11)$$

A similar expression is obtained for the receiver beam pattern function

$$B_R(X, Y) = \exp \left\{ -\frac{\pi^2 f_0^2}{4c^2} \cdot \frac{D_R^2}{r_{10}^2} [X^2(1-\cos^2 \psi_R \sin^2 \phi_R) + Y^2(1-\cos^2 \psi_R \cos^2 \phi_R) + XY(\cos^2 \psi_R \sin 2\phi_R)] \right\} \quad (2.3.12)$$

Thus the form of the combined beam pattern response of both source and receiver is

$$B_s B_R = \exp \left\{ -\frac{x^2}{L_{XX}^2(\omega_0)} - \frac{y^2}{L_{YY}^2(\omega_0)} - \frac{2xy}{L_{XY}^2(\omega_0)} \right\} \quad (2.3.13)$$

where

$$L_{XX}^2(\omega_0) = \frac{4c^2}{\pi^2 f_0^2} \left[\frac{r_{00}^2}{D_T^2(1-\cos^2\psi_T \sin^2\phi_T)} + \frac{r_{10}^2}{D_R^2(1-\cos^2\psi_R \sin^2\phi_R)} \right] \quad (2.3.14a)$$

$$L_{YY}^2(\omega_0) = \frac{4c^2}{\pi^2 f_0^2} \left[\frac{r_{00}^2}{D_T^2(1-\cos^2\psi_T \cos^2\phi_T)} + \frac{r_{10}^2}{D_R^2(1-\cos^2\psi_R \cos^2\phi_R)} \right] \quad (2.3.14b)$$

$$L_{XY}^2(\omega_0) = \frac{4c^2}{\pi^2 f_0^2} \left[\frac{r_{00}^2}{D_T^2 \cos^2\psi_T \sin^2\phi_T} + \frac{r_{10}^2}{D_R^2 \cos^2\psi_R \sin^2\phi_R} \right] \quad (2.3.14c)$$

For the simplified situation where the source and the receiver are in a forward specular reflection geometry, i.e. $\psi_T = \psi_R = \psi_0$, and $\phi_T = \phi_R + 180^\circ$, equation (2.3.14) can be simplified as

$$L_{XX}^2(\omega_0) = \frac{L^2(\omega_0)}{1 - \cos^2\psi_0 \sin^2\phi_R} \quad (2.3.15a)$$

$$L_{YY}^2(\omega_0) = \frac{L^2(\omega_0)}{1 - \cos^2\psi_0 \cos^2\phi_R} \quad (2.3.15b)$$

$$L_{XY}^2(\omega_0) = \frac{L^2(\omega_0)}{\cos^2\psi_0 \sin^2 2\phi_R} \quad (2.3.15c)$$

where

$$L^2(\omega_0) = \frac{16c^2}{\omega_0^2} \left(\frac{r_{00}^2}{D_T^2} + \frac{r_{10}^2}{D_R^2} \right) \quad (2.3.16)$$

We now substitute equation (2.2.12), (2.2.13) and (2.3.13) into equation (2.1.6) and convert the integration over S to one over X, Y by using the transformations (see appendix B)

$$ds = \sqrt{1 + \left(\frac{\partial \zeta}{\partial X} \right)^2 + \left(\frac{\partial \zeta}{\partial Y} \right)^2} dX dY \quad (2.3.17)$$

and

$$\frac{\partial}{\partial n} = \frac{1}{\left[1 + \left(\frac{\partial \zeta}{\partial X} \right)^2 + \left(\frac{\partial \zeta}{\partial Y} \right)^2 \right]^{\frac{1}{2}}} \left[\frac{\partial}{\partial \zeta} - \frac{\partial \zeta}{\partial X} \frac{\partial}{\partial X} - \frac{\partial \zeta}{\partial Y} \frac{\partial}{\partial Y} \right] \quad (2.3.18)$$

Then equation (2.1.6) takes the form

$$H(\omega_0, t) = \frac{j\omega_0 \tau_s}{4\pi r_{00} r_{10}} \int_{-\infty}^{\infty} \int_{-\infty}^{\infty} \left[\frac{\partial}{\partial \zeta} - \frac{\partial \zeta}{\partial X} \frac{\partial}{\partial X} - \frac{\partial \zeta}{\partial Y} \frac{\partial}{\partial Y} \right] e^{-AX^2 - BY^2 - CXY - DX - EY + j\frac{\omega_0}{c} F \zeta} dX dY \quad (2.3.19)$$

where

$$A = -j \frac{\omega_0}{cR} (1 - \cos^2 \psi_0 \cos^2 \phi_R) + \frac{1}{L_{XX}^2(\omega_0)} \quad (2.3.20a)$$

$$B = -j \frac{\omega_0}{cR} (1 - \cos^2 \psi_0 \sin^2 \phi_R) + \frac{1}{L_{YY}^2(\omega_0)} \quad (2.3.20b)$$

$$C = -j \frac{2\omega_0}{cR} \cos^2 \psi_0 \sin \phi_R \cos \phi_R + \frac{2}{L_{XY}^2(\omega_0)} \quad (2.3.20c)$$

$$D = \left(\frac{1}{r_{00}} - \frac{1}{r_{10}} \right) \cos \psi_0 \cos \phi_R \quad (2.3.20d)$$

$$E = - \left(\frac{1}{r_{00}} - \frac{1}{r_{10}} \right) \cos \psi_0 \sin \phi_R \quad (2.3.20e)$$

$$F = 2 \sin \psi_0 \quad (2.3.20f)$$

$$\tau_s = \frac{r_{00} + r_{10}}{c} \quad (2.3.21)$$

where $L_{XX}(\omega_0)$, $L_{YY}(\omega_0)$ and $L_{XY}(\omega_0)$ are defined in equations (2.3.14).

Chapter III. Deterministic Surface

3.0 Introduction

The application of the Kirchhoff integral to the general problem of surface scattered acoustic signals was described in the previous chapter. An expression was developed in equation (2.3.10) for a general water surface. Actual ocean surfaces are highly random and complex, but in this chapter we side-step the issue of random surfaces by considering a deterministic one. (Random surfaces are considered in Chapter IV). There is substantial precedent for considering deterministic surface models as a way of approaching a solution for the random surface. For instance, as mentioned in Chapter I, the early work of Rayleigh [21] and the more recent work of Uretsky [22], Murphy and Lord [26], Heaps [30] and Parker [76] used a sinusoidal surface to derive the surface reflection coefficients. Meecham [77] considered the transmission of acoustic wave through a sinusoidal surface by the use of the Kirchhoff integral method. The experimental work of Gulin [36], and of LaCasce and Tamarkin [78] dealing with reflections from pressure-release sinusoidal surfaces shows that much insight is gained by analyzing simple surface models. If the surface scattering process can be regarded as linear (as is always assumed in this work), more complicated surface effects can be obtained by Fourier analysis of the surface and superposition. This was, for instance, done by Beckmann [60] in a study of backscatter from a composite rough surface. He assumed each of the component

waves to be an independent random process, and found that the small structure of the surface (the component waves of small amplitude) played an important role in the determination of backscattered acoustic power.

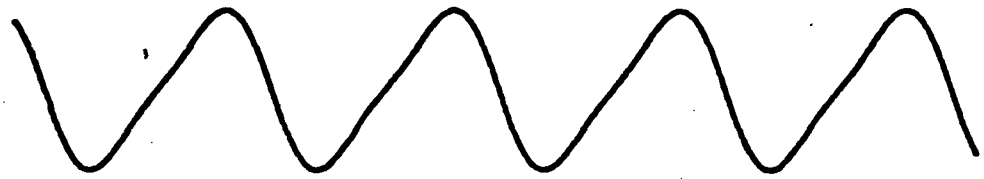
In this chapter, we will demonstrate the effect of small surface structures on the frequency spreading function by considering a wind-blown surface. A commonly observed characteristic of wind-blown surfaces is that the waves are steeper on the downwind side than on the upwind side [70]. A typical wave shape is shown in Figure 1.2. A deterministic model that has the feature of shallower slopes on one side and steeper slopes on the other can be constructed with a sine wave plus its second harmonic; i.e.

$$z(t) = h_1 \cos(\omega t + \phi) + h_2 \cos 2\omega t \quad (3.0.1)$$

Typical waveforms generated from equation (3.0.1) for different values of h_1 , h_2 and ϕ are shown in Figure 3.1. It is seen that by proper choices of amplitudes and phase angles (e.g. $h_1 = 5 h_2$, $\phi=45^\circ$), this two-harmonic surface wave will have a slope distribution similar to that of a wind generated wave.

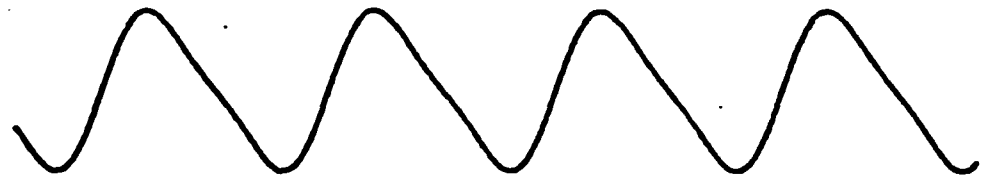
The frequency spreading function of the acoustic signal scattered from this deterministic surface model is discussed for two scatter geometries, crosswind and down(up) wind. Crosswind means that the wind direction is at right angles to a vertical plane containing source and receiver, and down (up) wind indicates that the wind direction is parallel to this plane. Thus in Figure 3.2, $\phi_R = 0^\circ, 90^\circ(270^\circ)$, and 180° correspond respectively to upwind, crosswind and downwind.

(1)



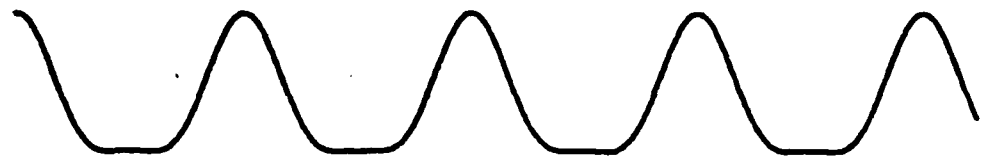
$$h_1 = 5h_2, \phi = 45^\circ$$

(2)



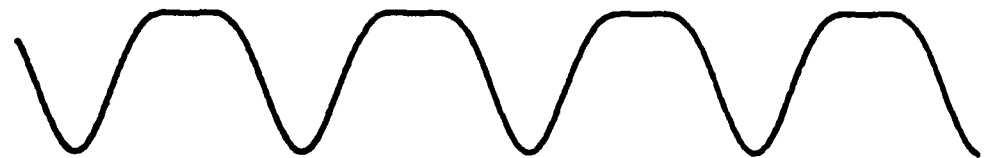
$$h_1 = 5h_2, \phi = 135^\circ$$

(3)



$$h_1 = 3h_2, \phi = 0^\circ$$

(4)



$$h_1 = 3h_2, \phi = 90^\circ$$

Figure 3.1 Waveforms generated from a two harmonic model:

$$z(t) = h_1 \cos(\omega t + \phi) + h_2 \cos 2\omega t$$

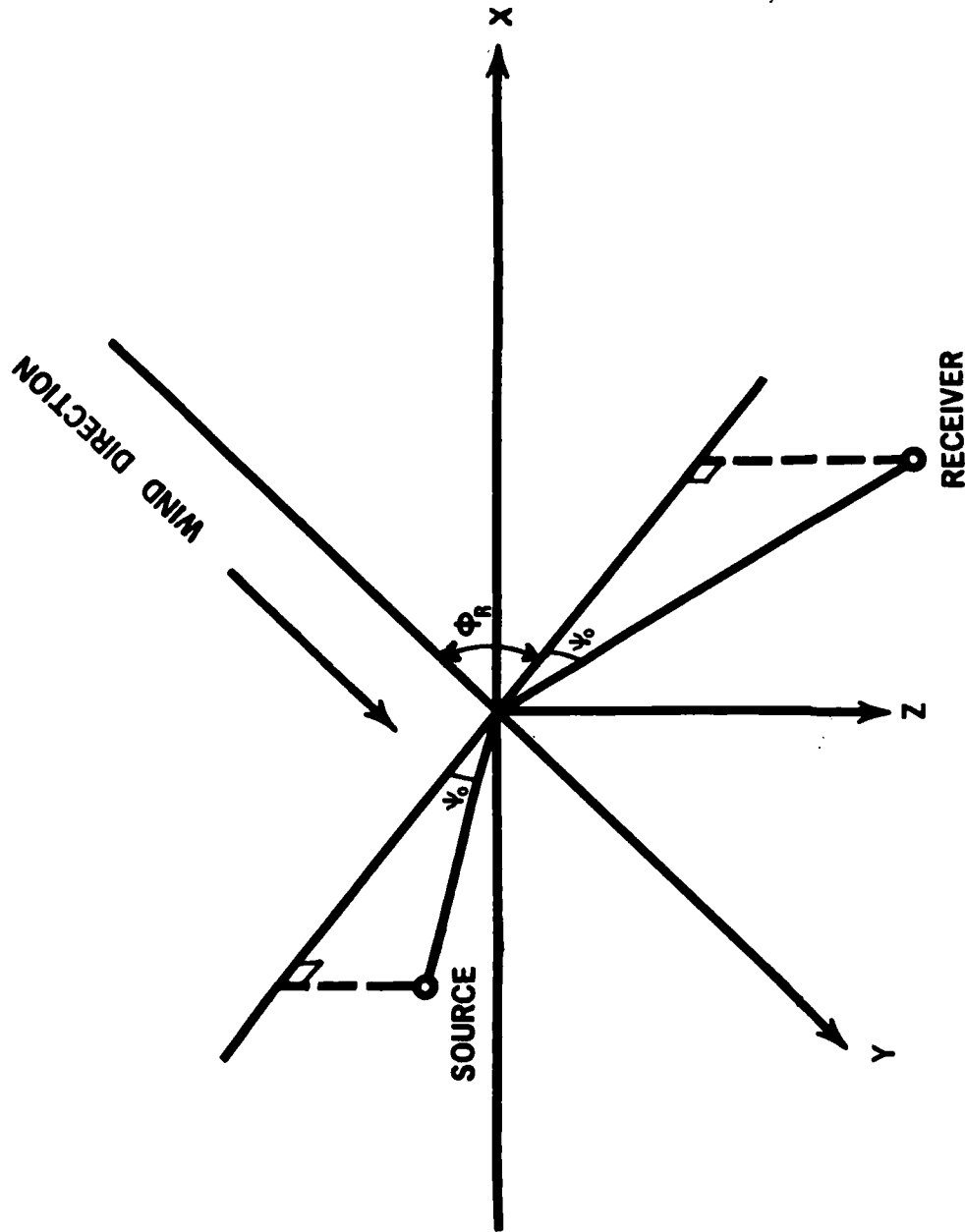


Figure 3.2 General forward-scatter geometry with wind direction

3.1 The surface model

In accordance with our discussion in section 3.0, the surface displacement at an arbitrary point of a wind generated surface is described by a time function as in equation (3.0.1). If we choose our coordinate system such that the wind blows in the positive Y direction and if the surface wave is one-dimensional, the surface wave motion can be expressed in the following form

$$\xi(X, Y, t) = h_1 \cos(\rho Y - \Omega t + \phi) + h_2 \cos(2\rho Y - 2\Omega t) \quad (3.1.1)$$

$$C_p = \frac{\Omega}{\rho} \quad (3.1.2)$$

where ρ is the surface wave number, Ω is the wave frequency, and C_p is the phase velocity.

Observe that the fixed phase angle ϕ in equation (3.1.1) and the constant phase velocity for both harmonics is not consistent with the model usually assumed for gravity waves (e.g. Parkins [4] or Scharf and Swartz [5]). For gravity waves, $\rho_i = \frac{\Omega^2}{g}$, and the phase angle is usually regarded as being uniformly distributed between 0 and 2π . The dispersion relation for gravity waves does not permit persistent slope asymmetries of the kind required in our discussion here. Equation (3.1.1) therefore should be regarded as a rather idealized model for a wind-blown surface.

In order to study the surface scattering behavior from this

model, it is necessary to replace $\zeta(X,y,t)$ of equation (2.3.19) with the expression in equation (3.1.1) and then evaluate the integral. We first consider the downwind case.

3.2 Downwind

Figure 3.3 illustrates a downwind ($\phi_R = 180^\circ$) scatter geometry.

The acoustic source is on the -Y side and the receiver is at the +Y side. As we showed in Chapter II, the distances from an arbitrary surface point to the source and receiver are respectively r_0 and r_1 . These have the forms:

$$r_0 = \sqrt{x^2 + (y+r_{00}\cos\psi_0)^2 + (\zeta+r_{00}\sin\psi_0)^2} \quad (3.2.1)$$

$$r_1 = \sqrt{x^2 + (y-r_{10}\cos\psi_0)^2 + (\zeta+r_{10}\sin\psi_0)^2} \quad (3.2.2)$$

By the use of the Fresnel approximation as described in Chapter II, the total transmission distance $r_0 + r_1$ can be approximated as equation (3.2.3). From equation (2.2.7), we have

$$r_0 + r_1 \approx r_{00} + r_{10} + 2\zeta \sin\psi_0 + \frac{1}{R} [x^2 + y^2 \sin^2\psi_0] \quad (3.2.3)$$

From equation (2.2.11), the approximation of the attenuation factor $(r_0 r_1)^{-1}$ can be put into form:

$$\frac{1}{r_0 r_1} \approx \frac{1}{r_{00} r_{10}} \exp \left\{ - \left(\frac{1}{r_{00}} - \frac{1}{r_{10}} \right) y \cos \psi_0 \right\} \quad (3.2.4)$$

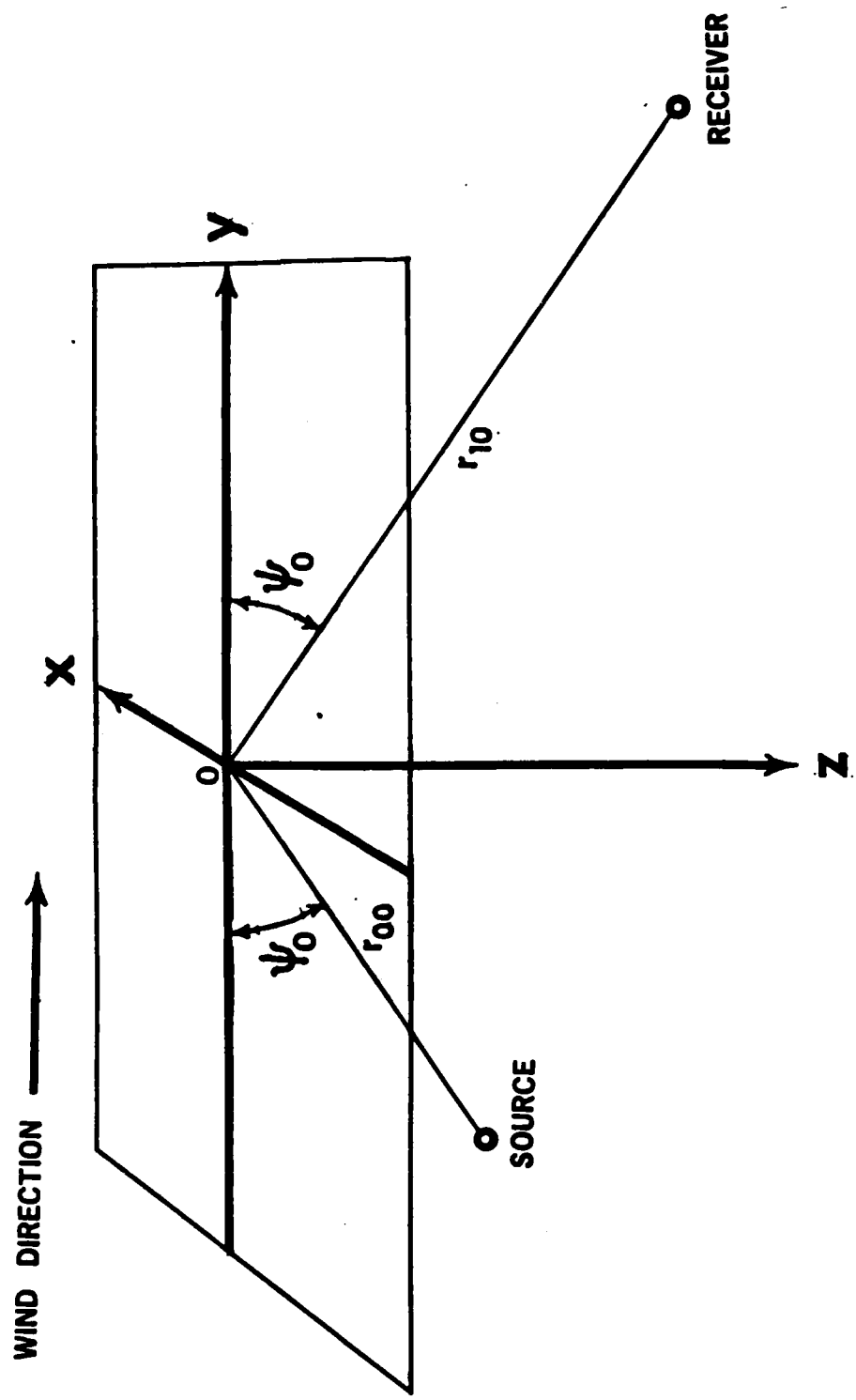


Figure 3.3 Downwind scatter geometry

Both equation (3.2.3) and (3.2.4) are good approximations if the following conditions hold:

$$\zeta(X, Y, t) \ll X, Y \quad (3.2.5a)$$

$$X, Y \ll r_{00}, r_{10} \quad (3.2.5b)$$

In the mathematical preliminaries, we showed that the projection of the combined source-receiver beam response on the X-Y plane can be approximated by a Gaussian function. For a downwind geometry, this combined beam response can be expressed in a simple form as equation (3.2.6) by replacing ϕ_R with 180° in equation (2.3.15)

$$B_s B_R \approx \exp \left\{ -\frac{1}{L^2(\omega_0)} (X^2 + Y^2 \sin^2 \psi_0) \right\} \quad (3.2.6)$$

Thus $L(\omega_0)$ is the acoustic beamwidth measured in the X direction.

In order to compute the power spectrum, we first have to evaluate the transfer function $H(\omega_0, t)$ in equation (2.3.19). After substituting equation (3.2.3, 4, 6) into equation (2.3.19), $H(\omega_0, t)$ can be rewritten as

$$H(\omega_0, t) = \frac{j\omega_0 r_s}{4\pi r_{00} r_{10}} \int_{-\infty}^{\infty} \int_{-\infty}^{\infty} \left[\frac{\partial}{\partial \zeta} - \zeta_X \frac{\partial}{\partial X} - \zeta_Y \frac{\partial}{\partial Y} \right] \cdot \exp \left\{ -\frac{1}{L^2(\omega_0)} (X^2 + Y^2 \sin^2 \psi_0) \right\}$$

$$- \left(\frac{1}{r_{00}} - \frac{1}{r_{10}} \right) Y \cos \psi_0 + j \frac{\omega_0}{c} \left[\frac{X^2 + Y^2 \sin^2 \psi_0}{R} + 2\zeta \sin \psi_0 \right] \} dXdY. \quad (3.2.7)$$

In this section we assume that the surface height $\zeta(X, Y, t)$ is small compared with the incident acoustic wavelength so that $2 \frac{\omega_0}{c} \zeta(X, Y, t) \sin \psi_0 \ll 1$. Thus the phase term can be approximated by its linear expansion, i.e.

$$e^{j2 \frac{\omega_0}{c} \zeta(X, Y, t) \sin \psi_0} \approx 1 + j2 \frac{\omega_0}{c} \zeta(X, Y, t) \sin \psi_0 \quad (3.2.8)$$

Observe that the surface wave motion is assumed to be one-dimensional and is propagating in the Y direction. Therefore, the slope ζ_X is zero. We replace $\zeta(X, Y, t)$ by the expression in equation (3.1.1) and substitute equation (3.2.8) into $H(\omega_0, t)$. The integration of equation (3.2.7) is straightforward but lengthy. Details of the computation are contained in Appendix C. The result of the integration can be put into the form:

$$H(\omega_0, t) = \frac{e^{j\omega_0 \tau_s}}{4r_{00} r_{10} \sqrt{AB}} \left\{ H_0^+ + \sum_{m=1}^6 [H_{m+} e^{-jm\Omega t} + H_{m-} e^{jm\Omega t}] \right\} \quad (3.2.9)$$

Expressions for A, B, H_0 and H_{m+} are also contained in Appendix C.

The expression of the received signal $r(t)$ is the product of $H(\omega_0, t)$ and $e^{-j\omega_0 t}$

$$\begin{aligned} r(t) &= H(\omega_0, t) e^{-j\omega_0 t} \\ &= D_0 e^{-j\omega_0 t} + \sum_{m=1}^6 [D_{m+} e^{-j(\omega_0+m\Omega)t} + D_{m-} e^{-j(\omega_0-m\Omega)t}] \end{aligned} \quad (3.2.10)$$

Equation (3.2.10) indicates that the interaction of an acoustic sinusoidal wave of frequency ω_0 with a moving surface corrugation given by the expression in equation (3.1.1) results in the generation of frequencies $\omega_0 \pm m\Omega$ with m ranging from zero to at least 6. The number 6 arises from the first order expansion of the phase term $\exp[-j2 \frac{\omega_0}{c} \sin \psi_0 \zeta]$. For surfaces of greater roughness, a higher order expansion of the phase term would become necessary, and would result in more frequency components.

From equation (3.2.10) we see that the coefficient D_0 is associated with the transmitted frequency ω_0 and represents the amplitude of the coherent (or specular) surface reflection. If we neglect the beam pattern effect in A and B, i.e. if the beam width $L(\omega_0)$ in equation (C-2) is assumed to be infinity, then D_0 can be written as

$$D_0 = \frac{e^{-j\omega_0(t-\tau_s)}}{r_{00}+r_{10}} \left\{ [1 - \frac{\rho^2 h_1^2}{2} - 2\rho^2 h_2^2] - j \frac{3}{2} \frac{\omega_0}{c} \rho^2 h_1^2 h_2 \sin \psi_0 \cos 2\phi \right\} \cdot \exp \left[j \frac{(r_{10}-r_{00})^2 \cot^2 \psi_0}{2 \frac{\omega_0}{c} r_{00} r_{10} (r_{10}+r_{00})} \right] \quad (3.2.11)$$

The above equation is obtained from equation (C-11). The leading term on the right-hand side of equation (3.2.11) represents the phase change and attenuation due to the transmission distance $r_{00} + r_{10}$ in the specular reflection path. The term in the square brackets, $1 - \frac{\rho^2 h_1^2}{2} - 2\rho^2 h_2^2$, is an additional attenuation of the

smooth surface response due to the surface corrugation. The factors ϕh_1 and ϕh_2 are proportional to the r.m.s. slope of the first and second harmonic of the surface wave. It is reasonable that the larger the corrugation is, i.e. larger ϕh_1 and ϕh_2 , the more the coherent component of the acoustic signal is attenuated. The imaginary term $j \frac{3}{2} \frac{\omega_0}{c} \rho^2 h_1^2 h_2 \sin \psi_0 \cos 2\phi$ is a phase lag which is a function of the phase angle ϕ . It is zero for $\phi = 45^\circ$ and is maximum for $\phi = 0^\circ$. From the surface profile shown in Figure 3.1, we observe that $\phi = 45^\circ$ results in a "zero mean" sawtooth wave from which one would expect no net phase shift. However, for $\phi = 0^\circ$ (or 180°), the surface wave is characterized by a sequence of narrow pulses, and the average height of the reflecting facets can therefore be above or below the smooth-surface reference. The last phase term $\exp \left[j \frac{(r_{10} - r_{00})^2 \cot^2 \psi_0}{2 \frac{\omega_0}{c} r_{00} r_{10} (r_{10} + r_{00})} \right]$ represents the

phase change due to scatter geometry. If the scatter geometry is symmetric, i.e. $r_{00} = r_{10}$, then the argument of this phase term becomes zero. This implies that the coherent reflection is associated with the specular ray-path. When the scatter geometry is asymmetric, i.e. $r_{00} \neq r_{10}$, then there is a net phase shift in addition to the nominal phase change $\omega_0 T_s$. Hence under this condition coherent reflection is no longer associated with the specular ray. This effect can also be explained by considering the Fresnel zones [75]. A symmetric downwind scatter geometry is shown in Figure 3.4. The ellipses on the surface plane represent the Fresnel zones. Figure 3.5 is the similar plot as Figure 3.4 except the scattering geometry is

is asymmetric with $r_{00} < r_{10}$. In Figure 3.4 the specular point is at the center of the first Fresnel zone (the inner-most ellipse) and therefore the specular path is associated with the coherent reflection. In Figure 3.5, the center of the first Fresnel zone is shifted away from the specular point and toward the receiver (toward the source if $r_{00} > r_{10}$). Thus there is a net phase difference between the coherent reflection and specular reflection.

The coefficients of the side-frequencies (the frequency component other than the transmitted frequency) above and below ω_0 are respectively D_{m+} and D_{m-} , $m = 1, 6$. Examination of these coefficients [cf. equation (C-12)] reveals that these coefficients with m ranging from 1 to 4, are in general not complex conjugates of each other. Therefore, the magnitudes of D_{m+} and D_{m-} are not equal for $m = 1$ to 4. We are mainly interested in the power of the first-order side-frequencies⁺, i.e. $|D_{1+}|^2$ and $|D_{1-}|^2$. These can be written in the forms:

$$|D_{1+}(\omega_0, t)|^2 = \left[\bar{X}^2 + Y^2 + \bar{X}Y \sin 2\phi \right] \cdot \left| \exp \left[\frac{(E-j\rho)^2}{2B} \right] \right|^2 \quad (3.2.12)$$

$$|D_{1-}(\omega_0, t)|^2 = \left[\bar{X}^2 + Y^2 - \bar{X}Y \sin 2\phi \right] \cdot \left| \exp \left[\frac{(E+j\rho)^2}{2B} \right] \right|^2 \quad (3.2.13)$$

where

$$\bar{X} = \frac{h_1}{r_{00} + r_{10}} \cdot \frac{\omega_0 \sin \psi_0}{c} \left[1 - \rho^2 \left(\frac{h_1^2}{4} + 2h_2^2 - \frac{c^2}{4\omega_0^2 \sin^2 \psi_0} \right) \right] \quad (3.2.14a)$$

⁺ Because of the first-order expansion of equation (3.2.8), the higher-order side-frequency coefficients are probably not correct in any case.

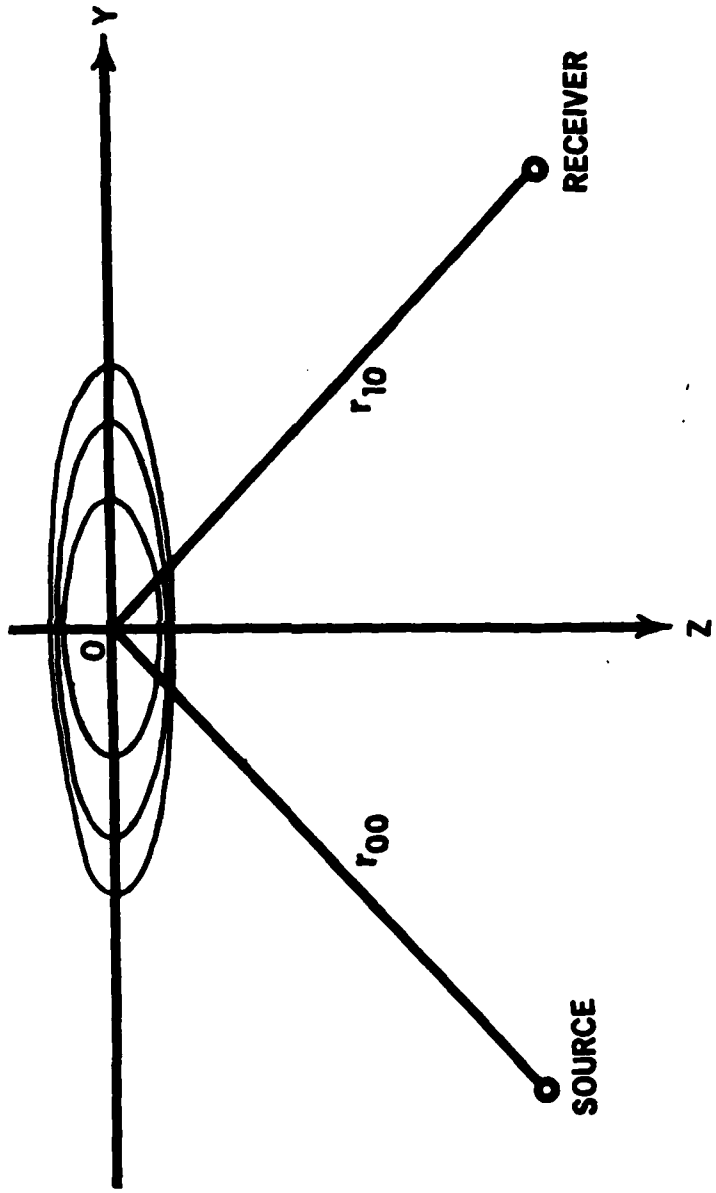


Figure 3.4 Fresnel zones - symmetrical source-receiver geometry

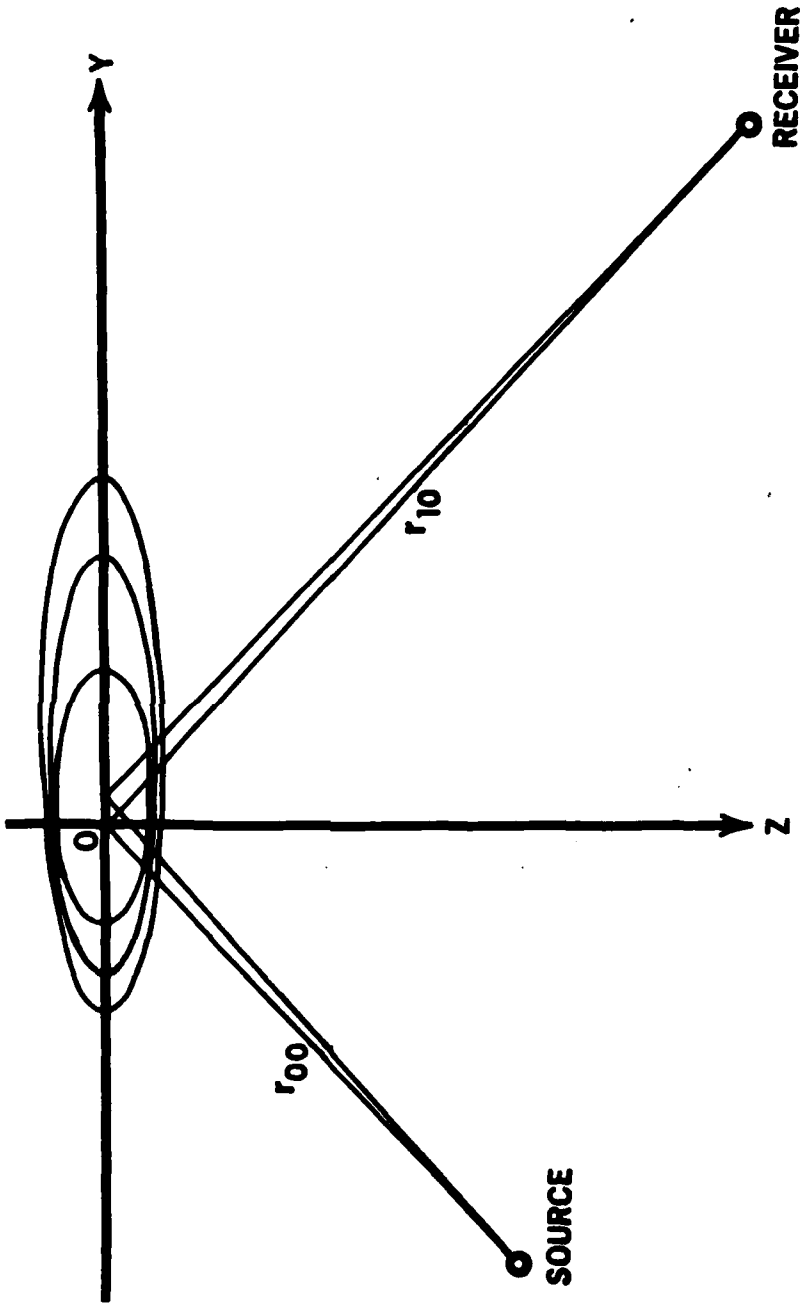


Figure 3.5 Fresnel zones—asymmetric source-receiver geometry ($r_{00} < r_{10}$)

$$Y = \frac{5}{4} \cdot \frac{\rho^2 h_1 h_2}{r_{00} + r_{10}} \quad (3.2.14b)$$

and where from the definition in appendix C, i.e. equation (C-2)

$$B = \left[\frac{1}{L^2(\omega_0)} - j \frac{\omega_0}{cR} \right] \sin^2 \psi_0 \quad (3.2.15a)$$

$$E = \left(\frac{1}{r_{00}} - \frac{1}{r_{10}} \right) \cos \psi_0 \quad (3.2.15b)$$

Notice that $|D_1+(\omega_0, t)|^2$ and $|D_1-(\omega_0, t)|^2$ are in general not equal. They differ because of the sign differences in the bracketed term and in the exponential term. These two sign differences represent two different mechanisms. The sign inside the brackets, associated with the term $\underline{X} Y \sin 2\phi$, is the result of asymmetric water surface slopes (the assumed wind-driven surface model). The second sign difference in the exponential term results from the asymmetric scattering geometry (i.e. $r_{00} \neq r_{10}$).

We consider first the case $r_{00} = r_{10}$. This results in $E = 0$ [cf. equation (3.2.15b)] and leaves only the sign difference in the bracketed term. We observe that the asymmetry (the amplitude difference between $|D_1+(\omega_0, t)|$ and $|D_1-(\omega_0, t)|$) exists when $\phi \neq 0$ (or $\phi = \frac{n\pi}{2}$, $n = \text{integer}$), and is most pronounced when $\phi = 45^\circ$. In Figure 3.1, $\phi = 45^\circ$ represents the most asymmetric saw tooth wave. There is no asymmetry when the amplitude of the second harmonic is zero (i.e. $h_2 = 0$, $Y = 0$). The question as to which one of the two

side-frequencies has the larger power magnitude depends on the sign of \underline{X} ⁺. Generally speaking, the water surface under consideration has no surface slope with magnitude larger than 1. This condition is required by the laws of hydrodynamics for non-breaking surface waves. Hence \underline{X} has a positive magnitude at all times. (see appendix D.)

We can conclude therefore that under the condition $r_{00} = r_{10}$, the upper side-frequency power magnitude $|D_{1+}(\omega_0, t)|^2$ is always larger than the lower side-frequency power magnitude $|D_{1-}(\omega_0, t)|^2$ for $0 < \phi < 90^\circ$. i.e. for wind driven waves.

Observe that the effect considered here is a function of the surface slope asymmetry only and does not depend on source-receiver geometry. Exchanging the positions of source and receiver replaces ψ_0 by $\pi - \psi_0$ (see Figure 3.2), and since ψ_0 enters the expression only through $\sin \psi_0$, replacing ψ_0 by $\pi - \psi_0$ has no effect on the magnitudes of $|D_{1+}(\omega_0, t)|^2$ and $|D_{1-}(\omega_0, t)|^2$. This result can also be justified heuristically by invoking simple reciprocity.

The power ratio between the upper side-frequency and the lower side-frequency can be obtained from equation (3.2.12) and
(3.2.13)

$$\left| \frac{D_{1+}(\omega_0, t)}{D_{1-}(\omega_0, t)} \right|^2 = \frac{\underline{X}^2 + \underline{Y}^2 + 2\underline{XY} \sin 2\phi}{\underline{X}^2 + \underline{Y}^2 - 2\underline{XY} \sin 2\phi} \quad (3.2.16)$$

⁺ The values of ϕ lie between 0° and 90° in order to have the wind driven waves moving in the direction of the steeper wavefront. [70]

A plot of this power ratio as function of ϕ according to equation (3.2.16) is shown in Figure 3.6.

We now focus our attention on the sign difference in the exponential term. To this end, we set $\phi = 0$, i.e. to have a surface wave with symmetric slope distribution. By replacing B and E with the expressions in equation (3.2.15), the exponential term becomes

$$\left| \exp \left[-\frac{(E + j\rho)^2}{2B} \right] \right| = \exp \left[\frac{\frac{1}{L^2(\omega_0)} \left[\frac{\cos^2 \psi_0}{R'^2} - \rho^2 \right] \pm \frac{\omega_0}{cR} \cdot \frac{2\rho \cos \psi_0}{R'}}{2 \sin^2 \psi_0 \left[\frac{1}{L^4(\omega_0)} + \frac{\omega_0^2}{c^2 R'^2} \right]} \right] \quad (3.2.17a)$$

where

$$\frac{1}{R'} = \frac{1}{r_{00}} - \frac{1}{r_{10}} \quad (3.2.17b)$$

The power ratio of the upper and the lower side-frequencies can be written as

$$\left| \frac{D_{1+}(\omega_0, t)}{D_{1-}(\omega_0, t)} \right|^2 = \exp \left[\frac{\frac{\omega_0}{cR} \cdot \frac{\rho \cos \psi_0}{R'}}{2 \sin^2 \psi_0 \left[\frac{1}{L^4(\omega_0)} + \frac{\omega_0^2}{c^2 R'^2} \right]} \right] \quad (3.2.18)$$

Figure 3.7 shows a log-log plot of $|D_{1+}(\omega_0, t)/D_{1-}(\omega_0, t)|^2$ as a function of r_{10}/r_{00} , with grazing angle ψ_0 as a parameter. Observe that the power ratio is unity when $r_{00} = r_{10}$. It is greater than unity when $r_{00} < r_{10}$. Also notice that the power ratio saturates at very large or very small values of r_{10}/r_{00} . The limiting value can be obtained from equation (3.2.18) by letting r_{10}/r_{00} go

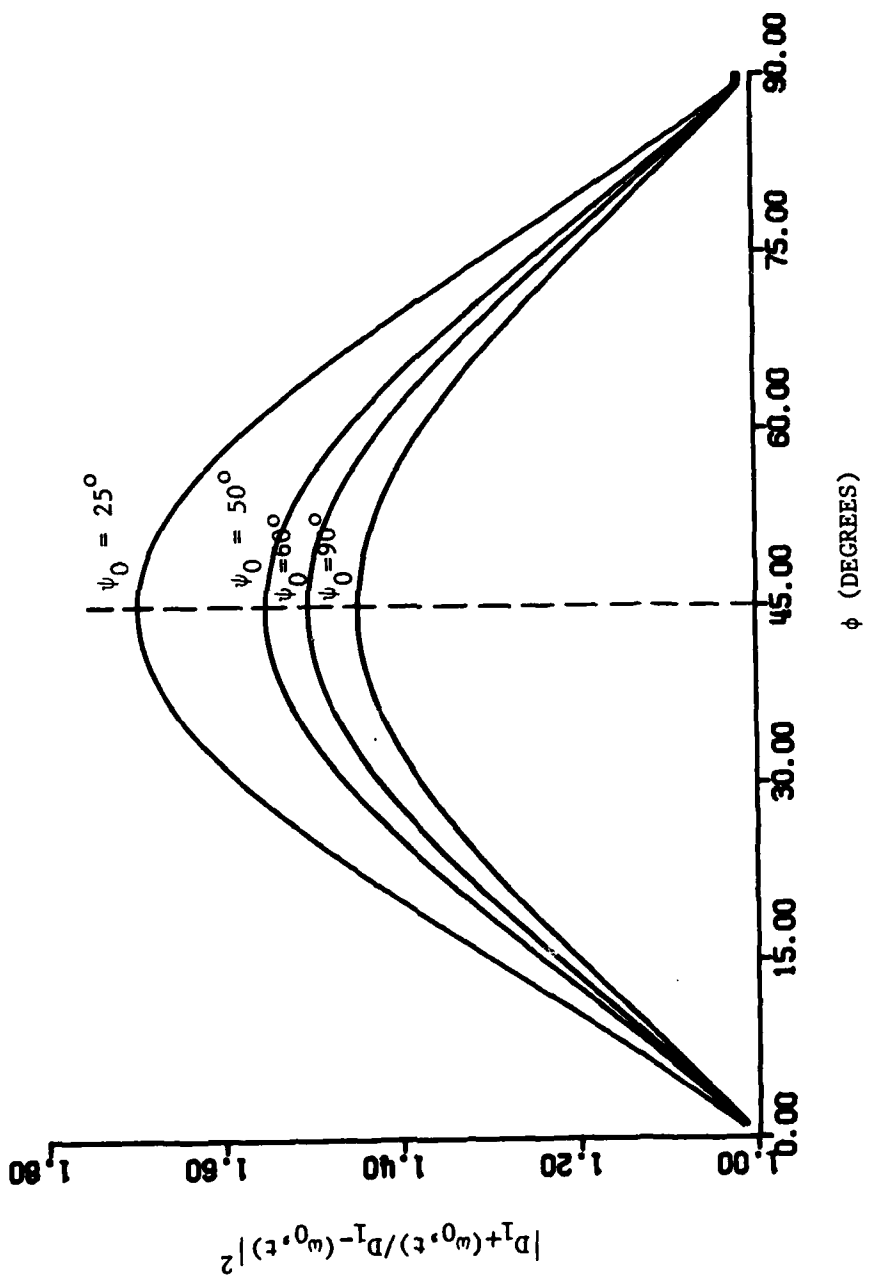


Figure 3.6 First-order side frequency power ratio versus phase angle ϕ

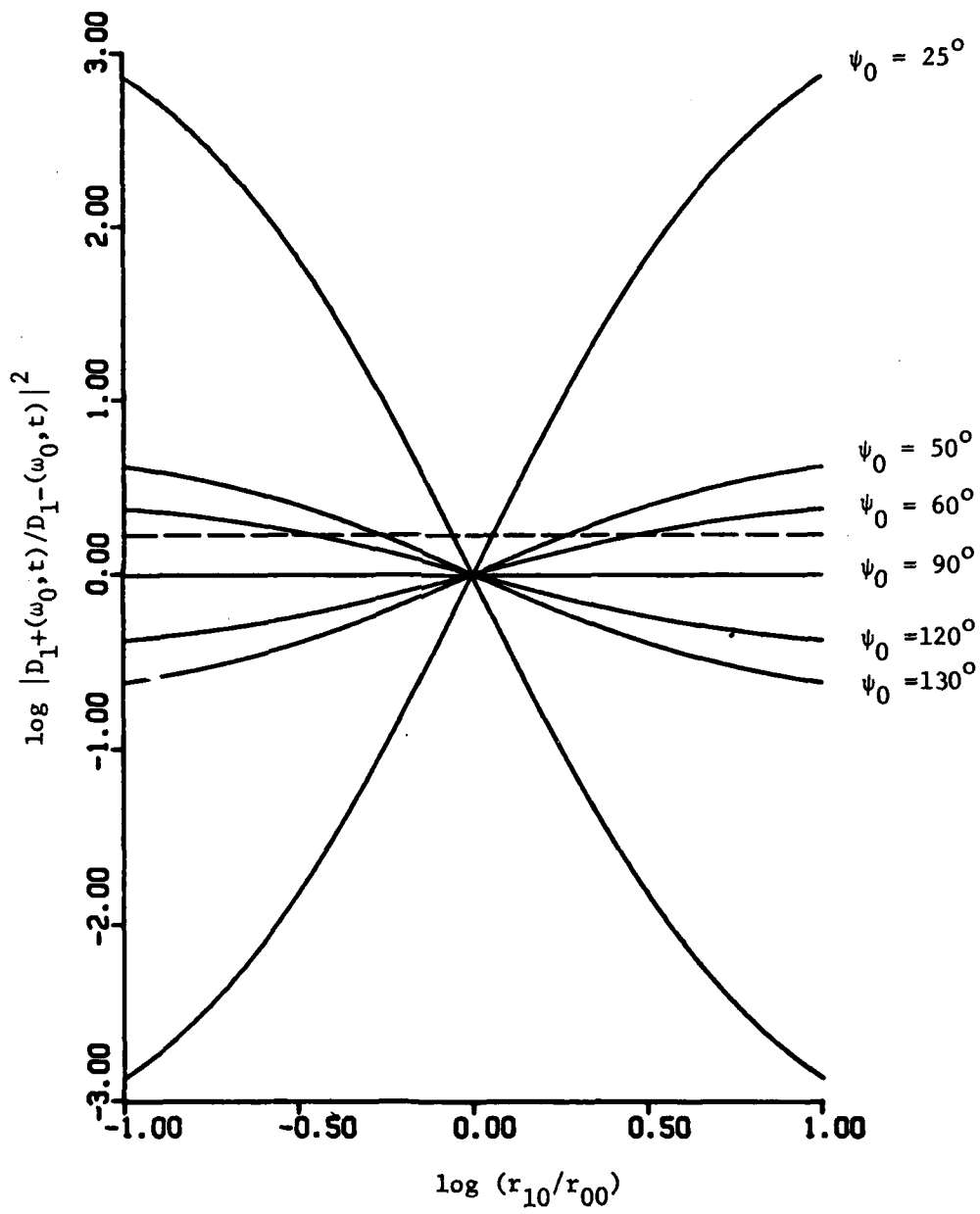


Figure 3.7 First-order side frequency power ratio as function of scattering geometry; dashed curve represents the power ratio maximum in Figure 3.6 for $\phi = 45^\circ$ and $\psi = 25^\circ$

to infinity⁺,

$$\lim_{\frac{r_{10}}{r_{00}} \rightarrow \infty} \left| \frac{D_{1+}(\omega_0, t)}{D_{1-}(\omega_0, t)} \right|^2 = \exp \left[\frac{2\omega_0 c \rho L^4(\omega_0) \cos \psi_0}{\sin^2 \psi_0 [4c^2 r_{00}^2 + \omega_0^2 L^4(\omega_0)]} \right] \quad (3.2.19)$$

where R and R' are approximated by $2r_{00}$ and r_{00} , respectively. As far as the effect of grazing angle ψ_0 is concerned, we see that for $\psi_0 = 90^\circ$ (vertical incidence and reflection) the power ratio is unity, but for very shallow grazing angles this ratio can become very large. Figure 3.8 has a semi-log plot of $\log |D_{1+}(\omega_0, t)/D_{1-}(\omega_0, t)|^2$ versus grazing angle ψ_0 . In fact, in the limit of $\psi_0 = 0^\circ$ or $\psi_0 = 180^\circ$, the power ratio goes to infinity. However, for extremely low grazing angles as well as for extreme values of r_{10}/r_{00} , the assumption of no shadowing is violated, and therefore the results should not be carried out to these limits.

The power ratio in equation (3.2.18) is sensitive to the wind direction, and will change to its reciprocal value when the direction of wind reverses. For example, if we take the scatter geometry in Figure 3.3 with $r_{00} < r_{10}$, then according to equation (3.2.18) the power of the upper side-frequency is larger than that of the lower one. If we reverse the wind direction so that the wind blows along the -y axis, we are effectively replacing the wave number ρ with $-\rho$ in equation (3.2.18). Thus the power ratio is inverted and the lower side-frequency will become the one with a larger power

⁺ The Fresnel approximation breaks down before reaching this limit.

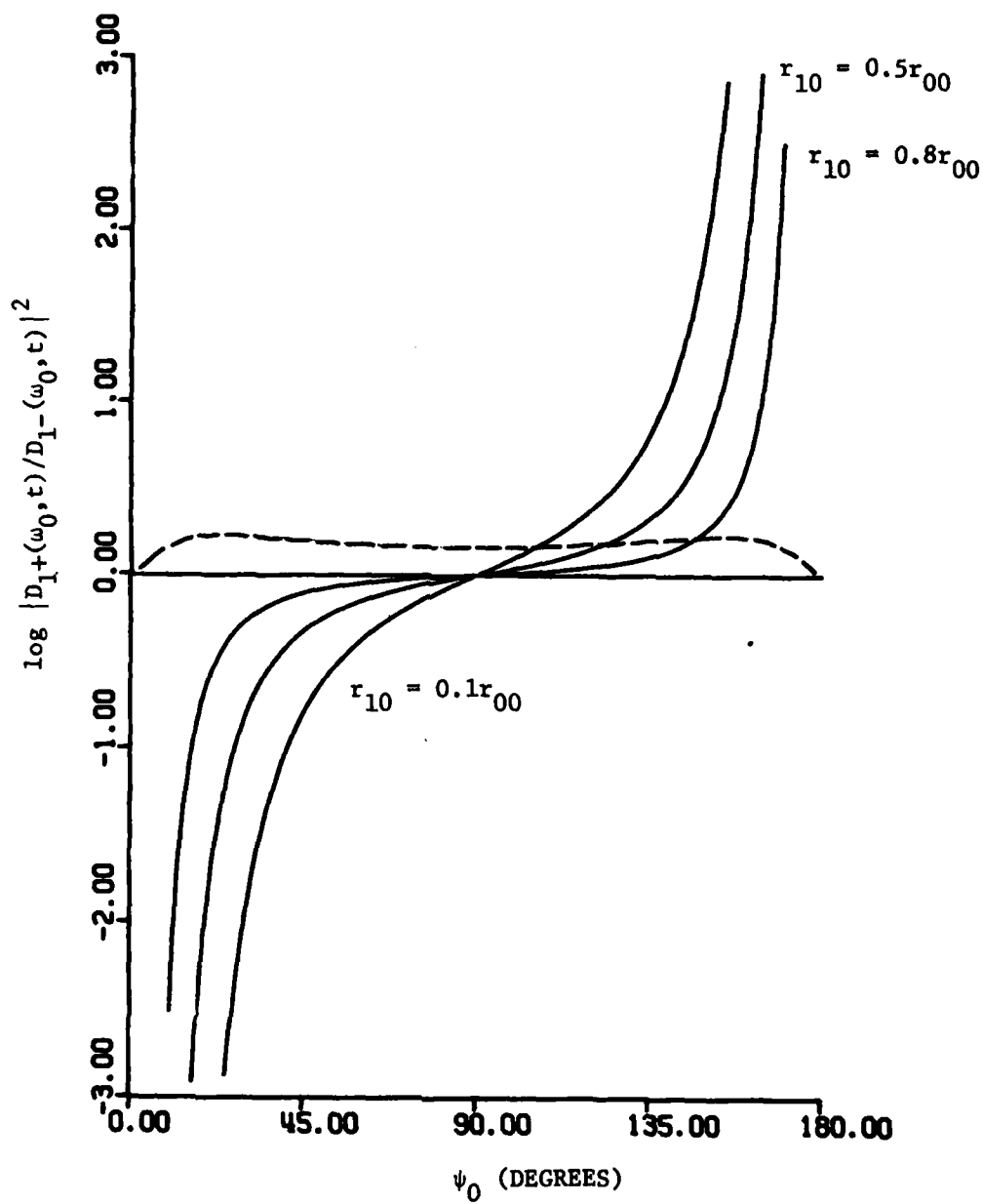


Figure 3.8 First-order side frequency power ratio versus grazing angle ψ_0 ; the dashed curve represents the power ratio due to asymmetric surface slopes for $\phi = 45^\circ$.

(cf. Figure 3.6)

magnitude. This same effect can also be observed from Figure 3.3 and equation (3.2.18) by letting ψ_0 exceed 90° , i.e. the source moves to the +y side and receiver to the -y side, and the wind blows along +y direction.

If the beam width $L(\omega_0)$ of the combined source-receiver beam response becomes very large, i.e. if both source and receiver lose their directivities, and for $r_{00} \ll r_{10}$, equation (3.2.19) can be further simplified to the form:

$$\lim_{\substack{r_{10}/r_{00} \rightarrow \infty \\ L(\omega_0) \rightarrow \infty}} \left| \frac{D_{1+}(\omega_0, t)}{D_{1-}(\omega_0, t)} \right|^2 = \exp \left[\frac{\rho}{\omega_0/c} \cdot \frac{2 \cos \psi_0}{1 - \cos^2 \psi_0} \right] \quad (3.2.20)$$

We see that the argument of the exponential function consists of two parts, one is the ratio of the surface wave number ρ to the acoustic wave number ω_0/c , the other is a function of the grazing angle ψ_0 , a geometric factor. According to equation (3.2.20), the power ratio is large when $\rho c / \omega_0$ is large; and the ratio approaches unity when $\rho c / \omega_0$ closes to zero. A heuristic explanation of this is that for a given acoustic wave number, if $\rho c / \omega_0$ decreases, the surface wavelength must increase. In the limit $\rho c / \omega_0 \rightarrow 0$, the surface wavelength is infinity and the surface wave becomes a plane surface. All reflections become specular, and there is no asymmetry.

The effects of the geometry asymmetry and the surface slope asymmetry on the power ratio are not equal in general. The logarithmic value of the power ratio due to the surface slope effect is plotted

dashed in Figures 3.7 and 3.8. We see that the effect of surface slope is smaller than that of the geometry asymmetry and is significant only when r_{00} and r_{10} are approximately equal or when the grazing angle is close to 90° .

3.3 Crosswind

The discussion for crosswind is very similar to that for downwind. The scattering geometry is shown in Figure 3.9 with the source and receiver located in the x-z plane. The mathematical operations are very similar to those already performed for downwind. Details of the computation are given in appendix E. We find that the received signal can again be expressed as in equation (3.2.10); however, the expressions for the D's are generally different.

The coherent response D_0 has the same form as in the previous section and we need not consider it again.

Expressions for power magnitudes of the first order side-frequencies are

$$|D_{1+}(\omega_0, t)|^2 = \{ \bar{X}^2 + \bar{Y}^2 + \bar{XY} \sin 2\phi \} \cdot \exp \left\{ \frac{E^2 - \rho^2}{2B} \right\} \quad (3.3.1)$$

$$|D_{1-}(\omega_0, t)|^2 = \{ \bar{X}^2 + \bar{Y}^2 - \bar{XY} \sin 2\phi \} \cdot \exp \left\{ \frac{E^2 - \rho^2}{2B} \right\} \quad (3.3.2)$$

where \bar{X} , \bar{Y} , B and E are defined in equations (3.2.14) and (3.2.15).

The sign difference in these two expressions is related to the surface wave slope asymmetry. The sign difference arising from asymmetry in the scatter geometry is no longer present. Therefore, for a symmetric surface, e.g., gravity waves, we would expect symmetric side-frequencies in the crosswind geometry for any r_{00} and r_{10} , (r_{00} and r_{10} are assumed to satisfy the far-field assumptions).

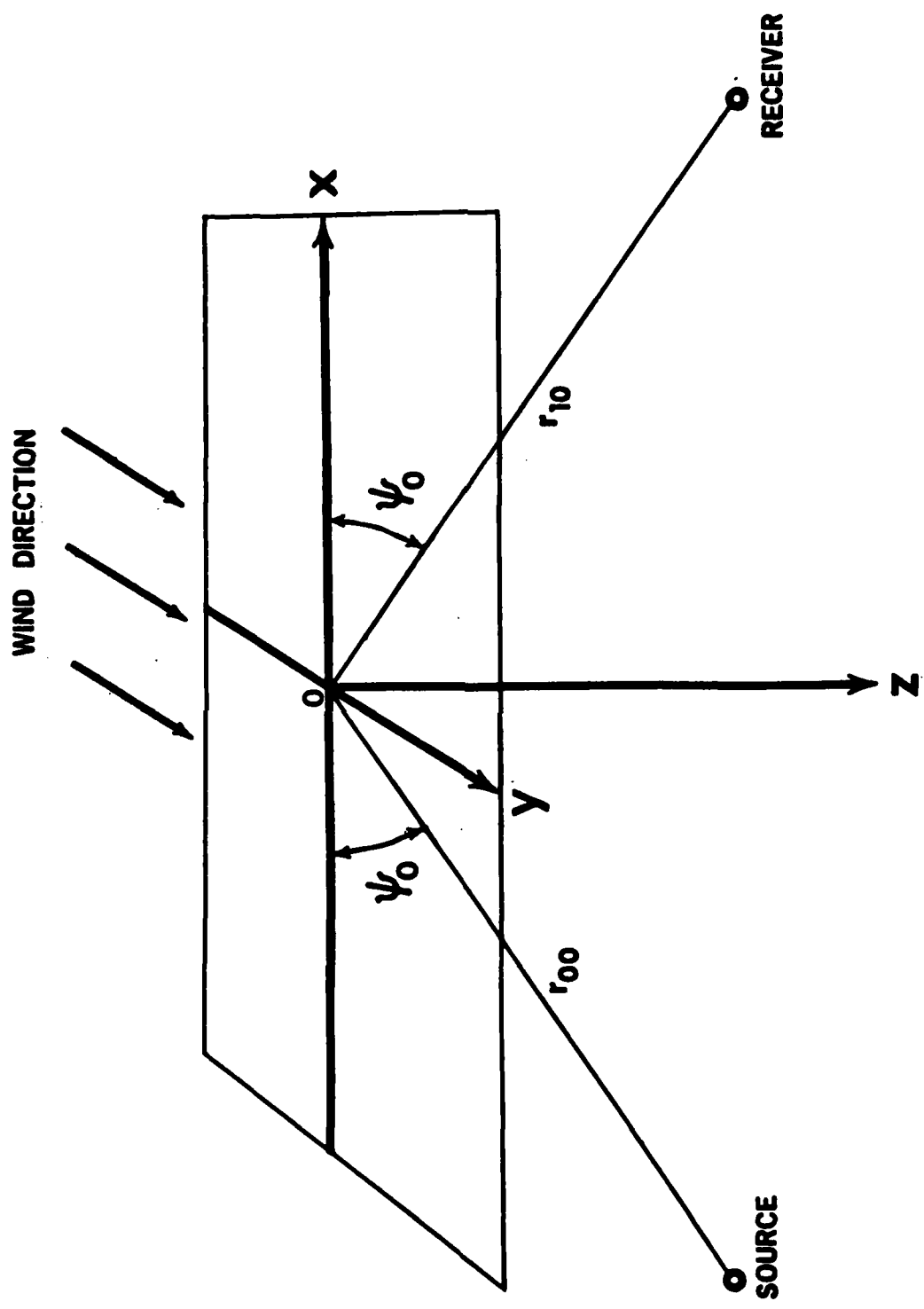


Figure 3.9 Crosswind scatter geometry

The detailed consideration of the sign difference in equations (3.3.1) and (3.3.2) is the same as discussed in the previous section since only the slope effect is presented here, the power magnitude of the upper side-frequency is always larger than that of the lower side-frequency. We see that there is no effect of geometry asymmetry in the crosswind condition; therefore this is a convenient experimental configuration for the observation of surface slope asymmetries [3].

3.4 Summary

In this Chapter we have considered the frequency spreading function for both the downwind and the crosswind conditions using a deterministic model. We have found that the power magnitudes of the upper and the lower side-frequencies produced by this model are generally unequal. There are two different mechanisms that cause inequality. One is the scattering geometric asymmetry, i.e. the source and receiver are at different depths. If the source is located at a smaller depth than the receiver and if the wind blows from the source to the receiver (i.e. surface wave propagates from source to receiver), then the power of the upper side-frequency is larger. This effect is reversed when wind direction (the surface wave direction) is reversed or if the wind direction is unchanged but the source is at the larger depth. This mechanism does not exist in the crosswind condition. The other mechanism is the surface asymmetry caused by asymmetric surface slopes in wind-driven waves. This, taken by itself, always results in a larger power magnitude in the upper side-frequency. The power ratio (asymmetry) caused by asymmetric surface slopes is generally smaller than that caused by the asymmetric scatter geometry as observed in Figures 3.7 and 3.8. Therefore, the overall power difference tends to be mainly a function of the scattering geometry.

Chapter IV Random Surface

4.0 Introduction

In this Chapter we consider a random water surface with a Gaussian surface-height distribution. As already discussed in Chapter I, the Gaussian assumption is frequently used in the analysis of surface scatter even if it is not rigorously correct in all cases. Parkins [4], Scharf and Swarts [5], McDonald and Schultheiss [10] used this assumption to study the frequency spreading in the forward acoustic scattering from random rough surfaces. Schwarze [80] developed the doppler spread of back-scattered acoustic wave from a Gaussian sea surface. Clay and Medwin [7] computed the covariance of signals observed at a pair of receivers with the aid of Gaussian surface. Beckmann [49] has considered the surface scattering by non-Gaussian surfaces. He found that the results in most scattering analyses are not very sensitive to the precise choice of distribution.⁺

The analysis considers a general scattering geometry with arbitrary source and receiver locations. Thus the study includes various oblique and asymmetric scattering situations. In the previous Chapter, we saw that surface slopes played an important role in determining the shape of the frequency spreading function. Hence

⁺ This is probably not true for backscattering. Backscatter may depend heavily on the distribution of high magnitude surface slopes [81]. The high slope distributions offered by different surface distributions are generally quite different from one another.

slope statistics are explicitly included in this analysis. By assuming independence of surface slope and surface height statistics, asymmetry effects in the received signal spectrum that are similar to those obtained for deterministic surfaces can be shown to exist also for random surfaces.

4.1 General scattering geometry

If the water surface is random, the surface scatter process can be regarded as a randomly time-varying linear system having a transfer function $H(\omega_0, t)$. This represents the instantaneous amplitude and phase at the receiver due to a sinusoidal signal of frequency ω_0 from the source. The received signal has the form

$$r(t) = H(\omega_0, t) e^{-j\omega_0 t} \quad (4.1.1)$$

Figure 4.1 shows the scattering geometry. The origin of the coordinate system is chosen to be the aiming point of the acoustic source on the flat surface. In other words, the source has a beam pattern whose center line intercepts the flat surface at the origin. The x, y and z axes are as previously defined. The location of the acoustic source is specified through three polar coordinate parameters, r_{00} , ϕ_T and ψ_T . r_{00} is the distance from source to system origin, ϕ_T is the azimuthal angle of r_{00} projection on the x-y plane, measured positive clockwise from the -y axis, ψ_T is the grazing angle. The receiver location can be described through a similar set of parameters r_{10} , ϕ_R and ψ_R .

The transfer function for this scattering geometry can be derived from the Fresnel-corrected Kirchhoff integral and has the form (see Appendix F)

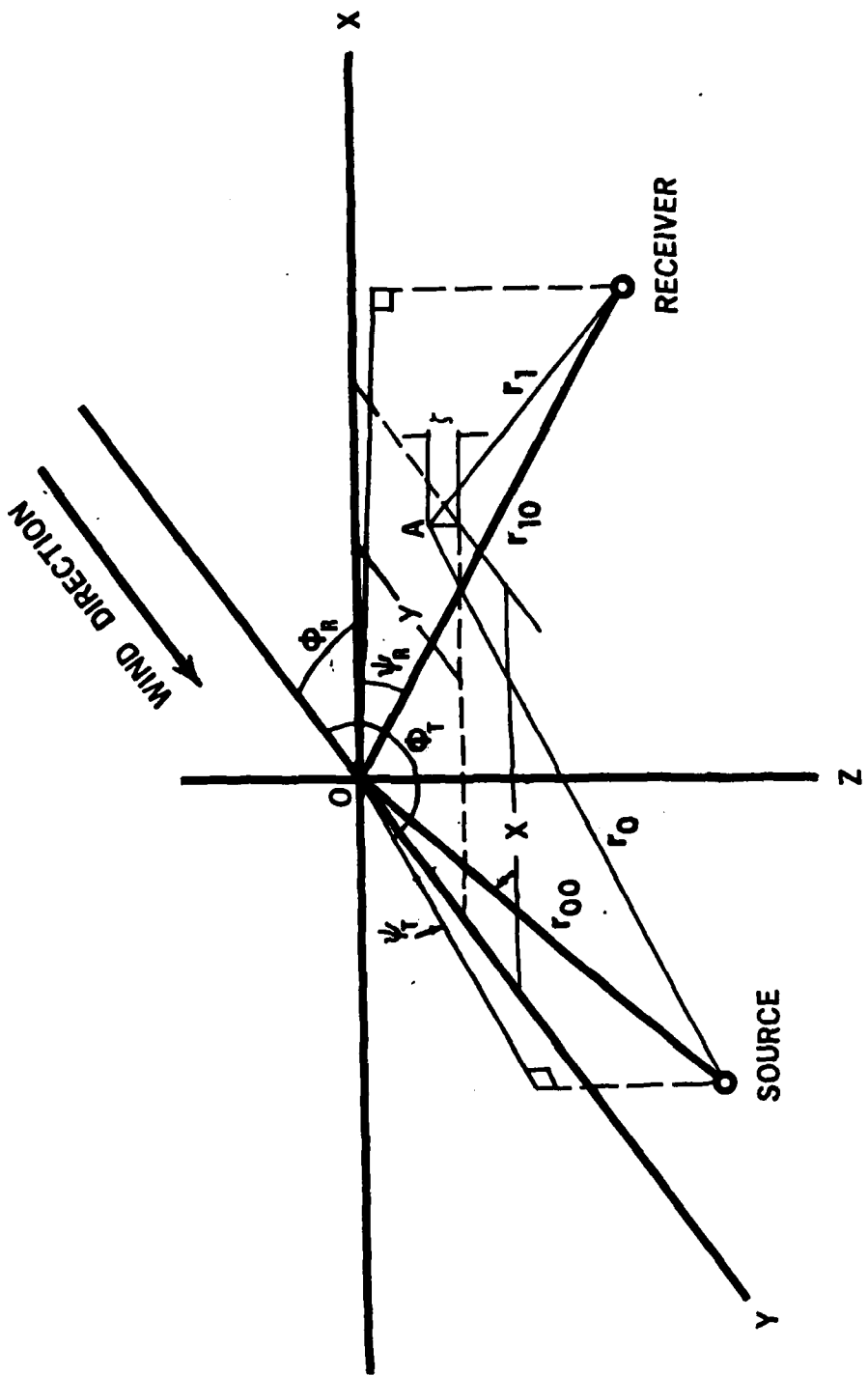


Figure 4.1 General scatter geometry with wind direction

$$H(\omega_0, t) = \frac{e^{j\frac{\omega_0}{c}(r_{00}+r_{10})}}{4\pi r_{00} r_{10}} \int_{-\infty}^{\infty} \int_{-\infty}^{\infty} \left(\frac{\partial}{\partial \zeta} - \zeta_x \frac{\partial}{\partial x} - \zeta_y \frac{\partial}{\partial y} \right) e^{-Ax^2 - By^2 - Cxy - Dx - Ey + j\frac{\omega_0}{c} F \zeta} dx dy$$

(4.1.2)

where A, B, C, D, E and F are specified in Appendix F.

Our interest is in the power spectrum of the received signal due to a sinusoidal input. The power spectrum can be obtained by Fourier transforming the autocorrelation function of the received signal $r(t)$. By the assumption of wide-sense stationarity in the acoustic scatter channel, we can write the autocorrelation function in the form [82]

$$\frac{r(t) r^*(t + \tau)}{r(t) r^*(t + \tau)} = \Phi(\omega_0, \tau) e^{j\omega_0 \tau} \quad (4.1.3)$$

$$\text{where } \Phi(\omega_0, \tau) = \overline{H(\omega_0, t) H^*(\omega_0, t + \tau)} \quad (4.1.4a)$$

is the autocorrelation function of the scatter channel. Substituting the expression of $H(\omega_0, t)$ in equation (4.1.2) into equation (4.1.4a), we get a four-fold integral as follows

$$\Phi(\omega_0, \tau) = \frac{1}{16\pi^2 r_{00}^2 r_{10}^2} \int_{-\infty}^{\infty} \int_{-\infty}^{\infty} \int_{-\infty}^{\infty} \int_{-\infty}^{\infty} \frac{J(\zeta_{x_1}, \zeta_{x_2}; \zeta_{y_1}, \zeta_{y_2}) \cdot Q(\zeta_1, \zeta_2)}{dx_1 dx_2 dy_1 dy_2} \quad (4.1.5)$$

where

$$\begin{aligned}
 & J(\zeta_{x_1}, \zeta_{x_2}; \zeta_{y_1}, \zeta_{y_2}) \\
 = & \{ j \frac{\omega_0}{c} F(1 - \zeta_{x_1}^2 - \zeta_{y_1}^2) + \zeta_{x_1} (2Ax_1 + Cy_1 + D) + \zeta_{y_1} (2By_1 + Cx_1 + E) \} \\
 & \cdot \{ -j \frac{\omega_0}{c} F(1 - \zeta_{x_2}^2 - \zeta_{y_2}^2) + \zeta_{x_2} (2A*x_2 + C*y_2 + D*) + \zeta_{y_2} (2B*y_2 + C*x_2 + E*) \} \\
 & \cdot \exp\{-Ax_1^2 - By_1^2 - Cx_1y_1 - Dx_1 - Ey_1 - A*x_2^2 - B*y_2^2 - C*x_2y_2 - D*x_2 - E*y_2\} \\
 & \quad (4.1.5a)
 \end{aligned}$$

$$Q(\zeta_1, \zeta_2) = \exp\{j \frac{\omega_0}{c} F\zeta_1(x_1, y_1, t) - j \frac{\omega_0}{c} F\zeta_2(x_2, y_2, t + \tau)\} \quad (4.1.5b)$$

We use the subscripts 1 and 2 to indicate variables at time t and $t + \tau$ respectively. Notice that $J(\zeta_{x_1}, \zeta_{x_2}; \zeta_{y_1}, \zeta_{y_2})$ summarizes the channel slope information and $Q(\zeta_1, \zeta_2)$ is a function of surface waveheight. The averaging operation in the integral is over the product of $J(\zeta_{x_1}, \zeta_{x_2}; \zeta_{y_1}, \zeta_{y_2})$ and $Q(\zeta_1, \zeta_2)$. The random variables to be averaged are the surface slopes, $\zeta_{x_1}, \zeta_{x_2}, \zeta_{y_1}, \zeta_{y_2}$, and surface displacements ζ_1 and ζ_2 .

The averaging operation is obviously fairly complicated. In order to simplify this operation we make two assumptions. The first of these is to assume a one-dimensional random surface with randomness only in the wind direction. In this way the cross-wind slope terms and ζ_{x_2} have negligible effect on the final result and can be set to zero. This approximation can be justified by the final result which shows that the effect of all of the slope terms is, in fact,

quite small. We do not wish to eliminate the downwind slope terms since they contribute an asymmetry to the frequency spreading function, whose study is one of the objectives of this analysis. Even though this is a small effect it is important. The crosswind slopes do not contribute such an asymmetry and setting them to zero therefore does not alter the final result in any essential way.

The second assumption concerns the averaging operation itself. It can be performed exactly only if the surface slopes and heights are jointly Gaussian. However, the Gaussian assumption is inconsistent with the directional asymmetry of windblown surfaces that we believe to be partly responsible for the phenomenon being studied here. This follows from the fact that a strictly Gaussian surface can be represented by a two-dimensional "Rice" model [83]; i.e. an expansion in terms of sinusoids with uniformly distributed random phase angles. Such a surface would be statistically isotropic. Hence a more fruitful simplifying assumption for the evaluation of equation (4.1.5) is that the surface heights are approximately Gaussian and that they are uncorrelated from the slopes. A possible basis for the second part of this statement is that the slopes depend largely on small ripples of the surface, when the surface is rough, and that ripples of any slope can occur at any surface level. This may not be quite true for the small-surface-roughness situation. However, if both surface height and slopes have small magnitudes, cross-product terms can be regarded as second-order magnitudes. Hence the assumption of uncorrelated surface heights and slopes results in an approximation that is correct to first order.

With these two assumptions, the integral of equation (4.1.5) can be rewritten as

$$\Phi(\omega_0, \tau) = \frac{1}{16\pi^2 r_{00}^2 r_{10}^2} \int_{-\infty}^{\infty} \int_{-\infty}^{\infty} \int_{-\infty}^{\infty} \int_{-\infty}^{\infty} \frac{J(\zeta_{y_1}, \zeta_{y_2}) \cdot Q(\zeta_1, \zeta_2)}{J(\zeta_{y_1}, \zeta_{y_2}) \cdot Q(\zeta_1, \zeta_2) dx_1 dx_2 dy_1 dy_2} \quad (4.1.6)$$

where

$$\begin{aligned} J(\zeta_{y_1}, \zeta_{y_2}) \\ = \{j \frac{\omega_0}{c} F(1 - \zeta_{y_1}^2) + \zeta_{y_1} (2By_1 + Cx_1 + E)\} \cdot \{-j \frac{\omega_0}{c} F(1 - \zeta_{y_2}^2) + \zeta_{y_2} (2B*y_2 + C*x_2 + E*)\} \\ \cdot \exp\{-Ax_1^2 - By_1^2 - Cx_1y_1 - Dx_1 - Ey_1 - A*x_2^2 - B*y_2^2 - C*x_2y_2 - D*x_2 - E*y_2\} \end{aligned} \quad (4.1.7)$$

The integrand is the product of two averaged terms. One is $J(\zeta_{y_1}, \zeta_{y_2})$, which contains the surface moments up to the fourth order. The other is $\overline{Q(\zeta_1, \zeta_2)}$, which is the characteristic function of the Gaussian distributed variables ζ_1 and ζ_2 . It can be written in the form

$$\overline{Q(\zeta_1, \zeta_2)} = \exp\left\{-\frac{\omega_0^2}{c^2} F^2 \sigma^2 [1 - \Psi(\xi, \eta, \tau)]\right\} \quad (4.1.8)$$

where σ is the r.m.s. surface waveheight and $\Psi(\xi, \eta, \tau)$ is the normalized surface height correlation function, given by

$$\Psi(\xi, \eta, \tau) = \frac{1}{\sigma^2} \overline{\zeta_1(x_1, y_1, t) \zeta_2(x_2, y_2, t+\tau)} \quad (4.1.9)$$

where $\xi = x_2 - x_1$ (4.1.10a)

$\eta = y_2 - y_1$ (4.1.10b)

The surface correlation function is a critical factor in the final result. The expression chosen for it should represent the actual surface with some degree of realism, and at the same time it should be simple enough to permit evaluation of equation (4.1.6). The correlation function of the ocean surface has been measured by a number of researchers, such as Clay and Medwin [7], etc. Model tank measurements have been made by Kingsbury [84], Spindel [54] and Zornig [53], etc. A relatively simple expression that fits these measurements with a fair degree of realism is

$$\Psi(\xi, \eta, \tau) = \exp\left\{-\frac{\xi^2}{\Lambda_x^2} - \frac{\eta^2}{\Lambda_y^2} - \frac{\tau^2}{T_0^2}\right\} \cdot \cos \rho(\eta - C_p \tau) \quad (4.1.11)$$

This represents a surface corrugation moving in the y direction with a velocity C_p . The parameters Λ_x , Λ_y and T_0 are correlation distances in the x, y and t directions, respectively. This expression has been used in scattering studies by Clay and Medwin [7], McDonald and Tuteur [8]. A shortcoming of equation (4.1.11) is that it does not take into account the surface dispersion which is an obvious and easily observed feature of typical water surfaces. Dispersion could be modelled by using a sum of terms of the form given in equation (4.1.11) with different values of ρ and C_p , as in Tuteur, McDonald and Tung [40]. This complication has not been added to our analysis in order to keep the result simple.

In spite of the relative simplicity of equation (4.1.11), the expression that results when it is substituted into equation (4.1.6) is not directly integrable. A standard procedure that permits integration is to use a Taylor series expansion. This can be applied to the characteristic function to give

$$\exp\{-g^2[1-\Psi(\xi, \eta, \tau)]\} = e^{-g^2} \{1+g^2\Psi(\cdot)+\frac{1}{2!}[g^2\Psi(\cdot)]^2+\dots\} \quad (4.1.12)$$

where $g = \frac{\omega_0}{c}$ ω_0 is the Rayleigh parameter which is a measure of effective surface roughness with respect to acoustic frequency.⁺

Since $|\Psi(\xi, \eta, \tau)| \leq 1$, equation (4.1.12) converges rapidly if $g \ll 1$; hence this expansion is appropriate if the surface roughness is small. For very small roughness it is permissible to use only a first-order approximation of equation (4.1.12); for surfaces of larger roughness (larger g) higher order terms can be used as well.

For a very rough surface, i.e. $g \gg 1$, equation (4.1.12) becomes inconvenient to use. In this case we observe that for very large g the expression in equation (4.1.8) has a significantly non-zero value only when $1-\Psi(\xi, \eta, \tau)$ is almost zero. Therefore, if we expand $\Psi(\xi, \eta, \tau)$ in a Taylor series about $\xi = \eta = \tau = 0$, only the first few terms of the series are significant. The linear or the first order term in the series need not be considered since it

⁺ See Chapter II.

corresponds to a non-differentiable surface [10], [85]. Thus the expansion of $\Psi(\xi, \eta, \tau)$ correct to second order is

$$\Psi(\xi, \eta, \tau) \approx 1 - \frac{\xi^2}{\Lambda_x^2} - \frac{\eta^2}{\Lambda_y^2} - \frac{\tau^2}{T_0^2} - \frac{\rho^2}{2} (\eta - C_p \tau)^2 \quad (4.1.13)$$

Using this second order expansion of $\Psi(\xi, \eta, \tau)$ in equation (4.1.8), we get

$$\exp\{-g^2[1 - \Psi(\xi, \eta, \tau)]\} = \exp\left\{-g^2\left[\frac{\xi^2}{\Lambda_x^2} + \frac{\eta^2}{\Lambda_y^2} + \frac{\tau^2}{T_0^2} + \frac{\rho^2}{2}(\eta - C_p \tau)^2\right]\right\} \quad (4.1.14)$$

The other statistical parameters that need to be specified are the slope moments in $\overline{J(\zeta_{y_1}, \zeta_{y_2})}$. The orders of slope moments in $\overline{J(\zeta_{y_1}, \zeta_{y_2})}$ range from 1 to 4. The first order moment is the average surface slope which is zero. The second order moment appears in the form of $\overline{\zeta_{y_1}^2}$, $\overline{\zeta_{y_2}^{*2}}$, and $\overline{\zeta_{y_1} \zeta_{y_2}^*}$. The first two are the mean square slopes. We assume the third term

$\overline{\zeta_{y_1}^2, \zeta_{y_2}^*}$ to be the form

$$\overline{\zeta_{y_1}^2, \zeta_{y_2}^*} = \epsilon_2 \exp\left\{-\frac{\eta^2}{\Lambda_y^2} - \frac{\tau^2}{T_0^2}\right\} \quad (4.1.15)$$

where

$$\epsilon_2 = \overline{\zeta_{y_1}^2} = \overline{\zeta_{y_2}^{*2}} \quad (4.1.16)$$

clearly $\epsilon_2 \geq 0$ for all cases.

The third order slope moment appears in the form

$$\overline{\zeta_{y_1}^2 \zeta_{y_2}^* + \zeta_{y_1} \zeta_{y_2}^{*2}}, \text{ and is assumed to have the form}$$

$$\overline{\zeta_{y_1}^2 \zeta_{y_2}^{*2} + \zeta_{y_1} \zeta_{y_2}^{*2}} = -\varepsilon_3 \exp\left\{-\frac{n^2}{\Lambda_3^2} - \frac{\tau^2}{T_3}\right\} \quad (4.1.17)$$

where

$$\varepsilon_3 = -2 \overline{\zeta_{y_1}^3} = -2 \overline{\zeta_{y_2}^{*3}} \quad (4.1.18)$$

The parameter ε_3 is generally positive, and the appearance of the minus sign in front of ε_3 is explained in Appendix G. Both the second and the third order slope moments are functions of n and τ . We neglect the fourth order moment $\overline{\zeta_{y_1}^2 \zeta_{y_2}^{*2}}$, because it is normally much smaller and it does not contribute any asymmetry to the final result. This follows from equation (4.1.7). The fourth order moment comes from the product of the first terms in the first and the second brackets, which is

$$\overline{[j \frac{\omega_0}{cc} F(1-\zeta_{y_1}^2)][-j \frac{\omega_0}{c} F(1-\zeta_{y_2}^{*2})]} = \left(\frac{\omega_0}{c} F\right)^2 (1-2\varepsilon_2 + \overline{\zeta_{y_1}^2 \zeta_{y_2}^{*2}}) \quad (4.1.19)$$

Notice that the mean square slope term is replaced by its equivalent ε_2 . It will be shown in the final result that $1-2\varepsilon_2$ represents the energy left in the coherent component because of finite surface slopes. $\overline{\zeta_{y_1}^2 \zeta_{y_2}^{*2}}$ represents a higher order correction term to this coherent response only and therefore can be neglected.

4.2 Random Surfaces - Small Rayleigh Parameter

The characteristic function for a Gaussian surface of Rayleigh parameter less than unity was given in equation (4.1.12). For the small Rayleigh parameter case, only the first few terms are important, so that equation (4.1.12) is rewritten as

$$\begin{aligned} \overline{Q(\zeta_1, \zeta_2)} &= \overline{\exp\left\{j \frac{\omega_0}{c} F \zeta_1(t) - j \frac{\omega_0}{c} F \zeta_2(t+\tau)\right\}} \\ &\approx e^{-g^2} \left\{ 1 + g^2 \left[e^{-\frac{\xi^2}{2}} - \frac{\eta^2}{\Lambda_x^2} - \frac{\eta^2}{\Lambda_y^2} - \frac{\tau^2}{T_0^2} \cos \rho(\eta - C_p \tau) \right] \right\} \quad (4.2.1) \end{aligned}$$

Details of the evaluation of the four-fold integral in equation (4.1.6) are presented in Appendix H; this integration is basically straightforward but lengthy. The result can be put into the form:

$$\Phi(\omega_0, \tau) = K_1 [I_0 + I_{1+} + I_{1-}] \quad (4.2.2)$$

where definitions for I_0 , I_{1+} and I_{1-} are given in equation (H-9), and K_1 is a constant coefficient.

The signal spectrum can be computed by substituting equation (4.2.2) into equation (4.1.4) and taking the Fourier transform with respect to the variable τ .

$$\begin{aligned} \Gamma(\omega, \omega_0) &= \int_{-\infty}^{\infty} \overline{r(t)r^*(t+\tau)} e^{-j\omega\tau} d\tau \\ &= K_1 \int_{-\infty}^{\infty} (I_0 + I_{1+} + I_{1-}) e^{-j(\omega - \omega_0)\tau} d\tau \quad (4.2.3) \end{aligned}$$

Details of this computation are also shown in Appendix H. The result of this operation is contained in equation (H-14), repeated here as equation (4.2.4):

$$\Gamma(\omega, \omega_0) = K_1 [Sp_0(\omega, \omega_0) + Sp_{1+}(\omega, \omega_0) + Sp_{1-}(\omega, \omega_0)] \quad (4.2.4)$$

where

$$Sp_0(\omega, \omega_0) = f_{00} \delta(\omega - \omega_0) + \pi^{\frac{1}{2}} \sum_{m=2,3} T_m \epsilon_m f_{m0} \exp\left\{-\frac{T_m^2}{4}(\omega - \omega_0)^2\right\} \quad (4.2.5a)$$

$$Sp_{1\pm}(\omega, \omega_0) = \frac{g^2}{2} \sqrt{\pi} [T_0 f_{0\pm} \exp\left\{-\frac{T_0^2}{4}(\omega - \omega_0 \mp \rho Cp)^2\right\} \\ + \sum_{m=2,3} \frac{T_0 T_m}{(T_0^2 + T_m^2)^{\frac{1}{2}}} \epsilon_m f_{m\pm} \exp\left\{-\frac{T_0^2 T_m^2 (\omega - \omega_0 \mp \rho Cp)^2}{4(T_0^2 + T_m^2)}\right\}] \quad (4.2.5b)$$

The signal spectrum is seen to consist of three parts;

$Sp_0(\omega, \omega_0)$, $Sp_{1+}(\omega, \omega_0)$ and $Sp_{1-}(\omega, \omega_0)$. $Sp_0(\omega, \omega_0)$ represents the coherent response of the scatter channel. $Sp_{1+}(\omega, \omega_0)$ and $Sp_{1-}(\omega, \omega_0)$ are respectively the upper and lower shifted Doppler spectra. The shape of both spectra is approximately Gaussian with center frequencies at $\omega_0 + \rho Cp$ and $\omega_0 - \rho Cp$. The two center frequencies are the transmitted acoustic frequency ω_0 shifted up and down by ρCp , the frequency of the surface wave correlation function.

The width of $Sp_0(\omega, \omega_0)$ is governed by T_2 and T_3 , which are the correlation constants (temporal) of the second and third order

moments of surface slopes. The widths of $S_{p1+}(\omega, \omega_0)$ and $S_{p1-}(\omega, \omega_0)$ are controlled by the combination of T_2 , T_3 and the surface wave-height correlation constant T_0 . If the surface correlation functions are in the form of an undamped sinusoid, then T_0 , T_2 and T_3 are infinite and the signal spectrum consists of three spectral lines at ω_0 , $\omega_0 + pC_p$ and $\omega_0 - pC_p$. This is essentially the same result obtained in the deterministic case. For smaller T_0 , T_2 , and T_3 , the surface wave spectrum is itself a narrow band spectrum and the three spectral lines spread to form three narrow bands.

There would have been more than just one Doppler sideband on each side of the carrier, if we had incorporated more terms of the expansion of the characteristic function in equation (4.2.1). The number of significant sidebands depends on the magnitude of the Rayleigh parameter g .

We consider next the relative magnitudes of the upper and lower sidebands. As in the deterministic case, the results depend on wind direction and we therefore consider the downwind and crosswind geometries separately.

Case I. Downwind geometry

The computational details of the substitution of downwind geometry parameters in the signal spectrum are presented in Appendix H. The result is expressed in equation (H-24) and is repeated in the following equation

$$\Gamma_D(\omega, \omega_0) = \frac{e^{-g^2}}{(r_{00} + r_{10})^2} [S_{D_0}(\omega, \omega_0) + S_{D_{1+}}(\omega, \omega_0) + S_{D_{1-}}(\omega, \omega_0)] \quad (4.2.6)$$

where

$$S_{D_0}(\omega, \omega_0) = (1-2\epsilon_2)\delta(\omega-\omega_0) + (\sqrt{\pi} T_2) \cdot \frac{\rho^2 \sigma^2 \epsilon_2}{g^2} e^{-\frac{T_2^2}{4}(\omega-\omega_0)^2}$$

$$+ (\sqrt{\pi} T_3) \frac{\rho \sigma \epsilon_3}{g} e^{-\frac{T_3^2}{4}(\omega-\omega_0)^2} \quad (4.2.7a)$$

$$S_{D_{1+}}(\omega, \omega_0) = \frac{g^2}{2} (\sqrt{\pi} T_0) e^{-\frac{2\sigma^2 R^2 p^2}{g^2 L^2(\omega_0)}} \pm \frac{4\sigma^2 R^2 dp}{g^2 L^2(\omega_0)}$$

$$\cdot \{(1-2\epsilon_2)e^{-\frac{T_0^2}{4}(\omega-\omega_0+\rho Cp)^2} + \frac{\rho^2 \sigma^2 \epsilon_2}{g^2} e^{-\frac{T_0^2 T_2^2}{4(T_0^2+T_2^2)}(\omega-\omega_0+\rho Cp)^2}$$

$$\pm \frac{\rho \sigma \epsilon_3}{g} e^{-\frac{T_0^2 T_3^2}{4(T_0^2+T_3^2)}(\omega-\omega_0+\rho Cp)^2}\} \quad (4.2.7.b)$$

We observe that the coherent response is an impulse of amplitude $\frac{(1-2\epsilon_2)}{(r_0+r_1)^2} e^{-g^2}$ at frequency ω_0 . If the surface is completely flat, i.e. $\epsilon_2 = \epsilon_3 = g = 0$, the coherent response is the only term in $\Gamma_D(\omega, \omega_0)$ and it has the form $(r_{00} + r_{10})^{-2}$, which is the familiar form of point source response. When the surface is disturbed, ϵ_2 and g are nonzero. The attenuation term e^{-g^2} results from the surface deformation amplitude, while the term

$2\epsilon_2$ represents attenuation caused by the slope terms. To consider the effect of surface waveheight and the effect of slopes separately, we assume the surface to have extremely small deformation, i.e. extremely small g , but have finite surface slopes. In other words, the surface can be modelled as a group of plane facets located on the flat surface. Each facet is random and has its own slope and the correlation of the slopes is described by equations (4.1.15) and (4.1.17). The spectra $S_{D_{1+}}(\omega, \omega_0)$ can be neglected for extremely small g and e^{-g^2} is approximated by 1. The spectrum in equation (4.2.6) can then be rewritten as

$$\Gamma_D(\omega, \omega_0) = \frac{1}{(r_{00} + r_{10})} \left\{ (1 - 2\epsilon_2) \delta(\omega - \omega_0) + (\sqrt{\pi} T_2) \frac{\rho^2 \sigma^2 \epsilon_2}{g^2} e^{-\frac{T_2^2}{4}(\omega - \omega_0)^2} \right. \\ \left. + (\sqrt{\pi} T_3) \frac{\rho \sigma \epsilon_3}{g} e^{-\frac{T_3^2}{4}(\omega - \omega_0)^2} \right\} \quad (4.2.8)$$

It is seen that the energy which is removed from the coherent response is distributed in the frequencies surrounding ω_0 , i.e. the second and the third terms in the brackets in equation (4.2.8). As discussed in the previous section, the bandwidth is determined by T_2 and T_3 , and is not a function of slope moments. Varying the mean square slopes ϵ_2 only changes the absolute magnitude of each spectral component proportionally. Figure 4.2 contains sketches of $\Gamma_D(\omega, \omega_0)$ of equation (4.2.8) for both small and large values of ϵ_2 . Notice that the bandwidth stays the same in both cases.

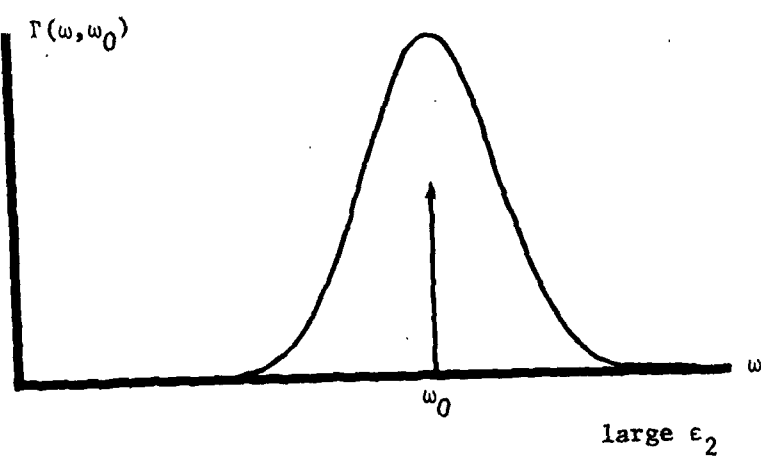
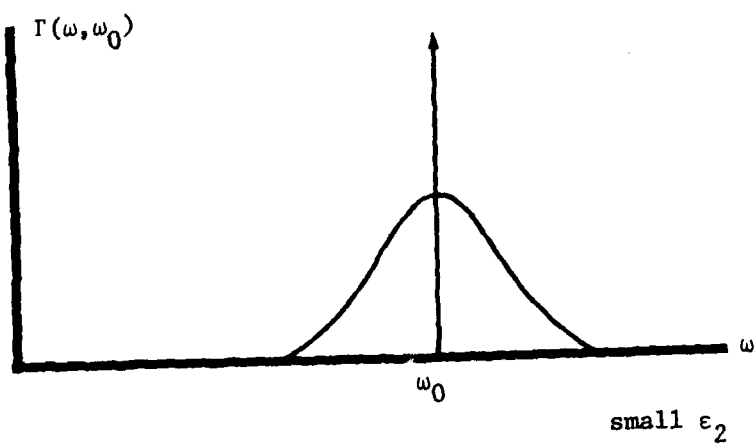


Figure 4.2 Power spectrum - small and large ϵ_2

The effect of somewhat larger surface deformation on the frequency spreading function can be examined by including the two spectra $S_{D_{1+}}(\omega, \omega_0)$ and $S_{D_{1-}}(\omega, \omega_0)$ into our consideration. Each of the spectra is the sum of three Gaussian functions as indicated by equation (4.2.7b). Considering the bandwidths of these three Gaussian functions in more detail, we see that they are respectively $2(\pi T_0)^{-1}$, $2\pi^{-1}(T_0^{-2} + T_2^{-2})^{1/2}$ and $2\pi^{-1}(T_0^{-2} + T_3^{-2})^{1/2}$ Hz. Hence the spread in the first Gaussian is due entirely to the surface waveheight fluctuations, while the spreads in the second and the third Gaussian functions are due to the combined effects of surface fluctuations and surface slopes. The combination is such that the bandwidth is controlled by the process which has the smaller correlation time. To our knowledge, no measurements of slope correlation times have ever been made. To be consistent with the assumption that slopes and heights are independent because the slopes depend largely on small ripples one might argue that $T_2 \approx T_3 \ll T_0$. However, another point of view is to assume $T_2 \approx T_3 \approx T_0$, simply on the basis that all three correlation times result from the same surface wave motion. We have used the second approach in equation (4.2.7b) to compute $S_{D_{1+}}(\omega, \omega_0)$ and $S_{D_{1-}}(\omega, \omega_0)$. All the other parameter values needed for this calculation are taken from data obtained in a model tank.[†] These values are shown in Figure 4.3, which contains a plot of the two spectra. The Rayleigh parameter

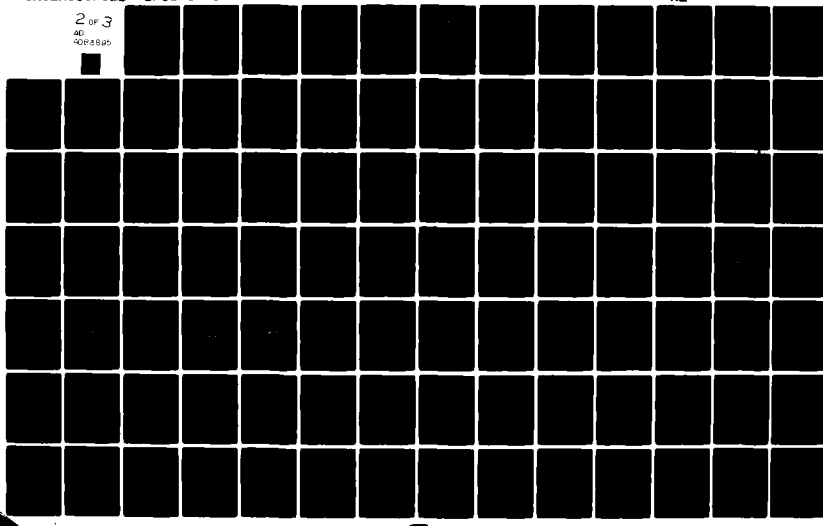
[†] The magnitudes of ϵ_2 and ϵ_3 used in the plot may be larger than the practical value in order to emphasize the asymmetry.

AD-A083 895

YALE UNIV NEW HAVEN CT SYSTEMS AND INFORMATION SCIENCES F/G 20/1
FREQUENCY SPREADING IN UNDERWATER ACOUSTIC SIGNAL TRANSMISSION. (U)
APR 80 H TUNG, F B TUTEUR, J G ZORNIG N00014-77-C-0237
S/IS-8001 NL

UNCLASSIFIED

2 OF 3
40
40-55505



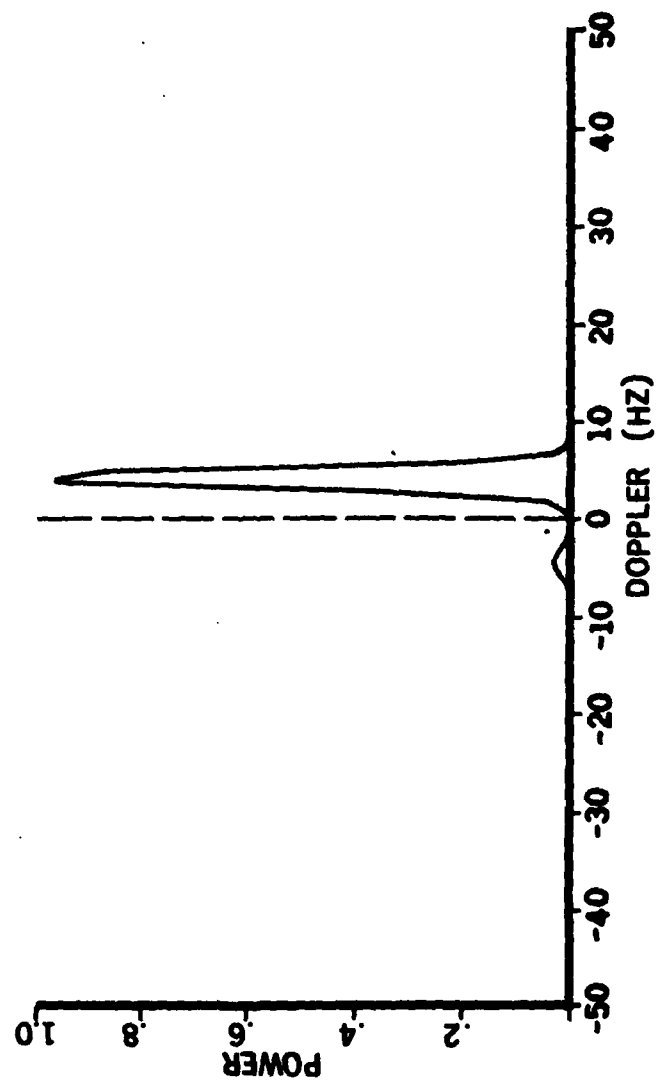


Figure 4.3 Doppler sidebands for scattering from slightly rough surfaces, upwind parameters used are $r_{00} = 50$ cm, $r_{10} = 500$ cm, $\psi_0 = 17^\circ$, $\sigma = 0.05$ cm, $f_0 = 256$ KHz, $C_p = 30$ cm/sec, $T_0 = 0.25$ sec, $\epsilon_3 = 0.2$.

g is 0.3. We observe that the two sideband spectra have completely different amplitudes. The amplitude differences are caused by the two double-signed terms, i.e. $\pm \frac{\rho \sigma \epsilon_3}{g}$ and $\pm \frac{4\sigma^2 R^2 dp}{g^2 L^2(\omega_0)}$. Note that the inequality of the spectral heights does not depend on the correlation times and is therefore unaffected by the assumptions made about the relative values of T_0 , T_2 and T_3 . As in the deterministic case considered in Chapter III, the two double-signed terms can be related to two different mechanisms, i.e. the surface slope asymmetry and the scattering geometry asymmetry. The effect of surface slope asymmetry shows in the term $\frac{\rho \sigma \epsilon_3}{g}$, while the effect of scattering geometric asymmetry is in $\frac{4\sigma^2 R^2 dp}{g^2 L^2(\omega_0)}$.

We first consider only the surface slope asymmetry by setting $d = 0$. From equations (H-13) and (H-22), this implies either

$$r_{00} = r_{10} \quad (4.2.9a)$$

or

$$\psi_0 = 90^\circ \quad (4.2.9b)$$

Since $\epsilon_3 > 0$ for wind-driven surface, we clearly see that the upper sideband $S_{D_{1+}}(\omega, \omega_0)$ is larger than the lower sideband $S_{D_{1-}}(\omega, \omega_0)$. If the direction of surface wave propagation reverses, both C_p and ϵ_3 change sign so that the sideband asymmetry stays the same. The degree of this sideband asymmetry is a function of acoustic frequency. If we increase the acoustic frequency, the Rayleigh parameter g becomes larger, and the term

$\frac{\rho \sigma \epsilon_3}{g}$ becomes smaller. Therefore, we would expect to find less sideband asymmetry for higher ω_0 . This is illustrated in the two sketches of Figure 4.4. The acoustic frequency used to generate the lower sketch is twice the value used in the upper sketch.

We now consider the sideband asymmetry caused by asymmetric scattering geometry. In order to do this, we let $\epsilon_3 = 0$ to eliminate the effect of surface slopes. The form of the exponential term can be rewritten by replacing d with its equivalent expression in equation (H-22). We get

$$\exp\left\{ \pm \frac{4\sigma^2 R^2 d\rho}{g^2 L^2(\omega_0)} \right\} = \exp\left\{ \pm \left[\frac{\rho}{\omega_0/c} \cdot \frac{r_{10}-r_{00}}{r_{10}+r_{00}} \cdot \frac{2 \cos \psi_0}{\sin^2 \psi_0} \right] \right\} \quad (4.2.10)$$

This is similar to equation (3.2.18) for very large $L(\omega_0)$. The upper and the lower sidebands are asymmetric when $r_{00} \neq r_{10}$ and $\psi_0 \neq 90^\circ$. The discussion of the sideband asymmetry is the same as in Chapter III. Figure 4.5 and 4.6 contain sketches of the asymmetric sidebands for $r_{00} > r_{10}$ and $r_{00} < r_{10}$, respectively. The corresponding downwind geometry is shown above each sketch.

Case II. Crosswind

The formulation of the signal spectrum in a crosswind geometry is presented in Appendix H. The resulting spectrum is written as

$$\Gamma(\omega, \omega_0) = \frac{e^{-g^2}}{(r_{00}+r_{10})^2} [S_{c0-}(\omega, \omega_0) + S_{c1+}(\omega, \omega_0) + S_{c1-}(\omega, \omega_0)] \quad (4.2.11)$$

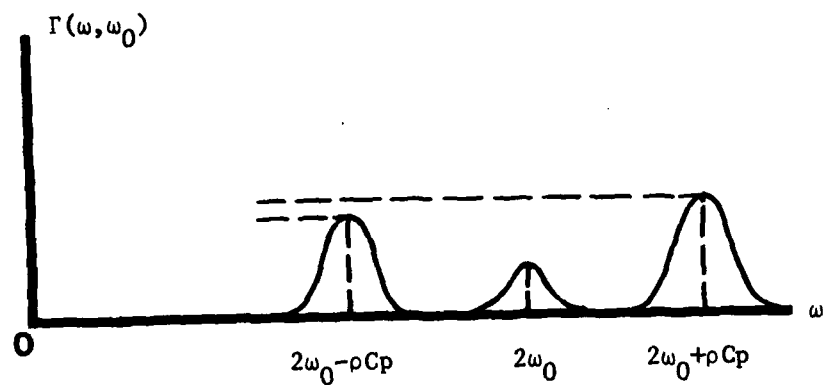
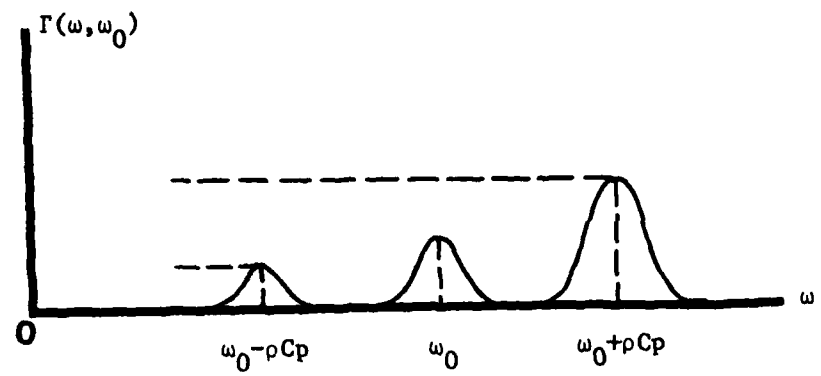


Figure 4.4 Asymmetric sidebands for different acoustic frequency ω_0 and $2\omega_0$

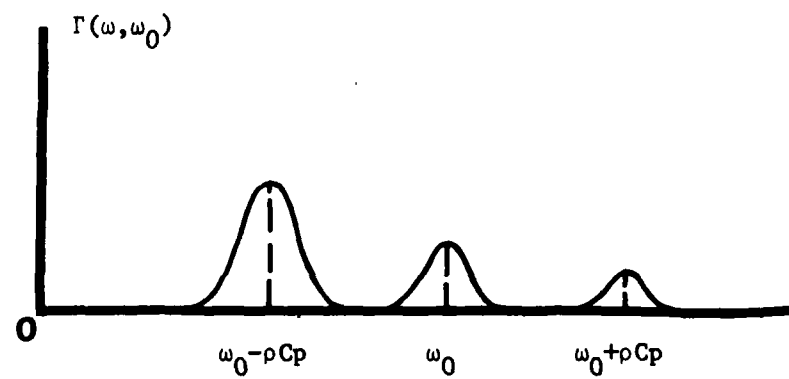
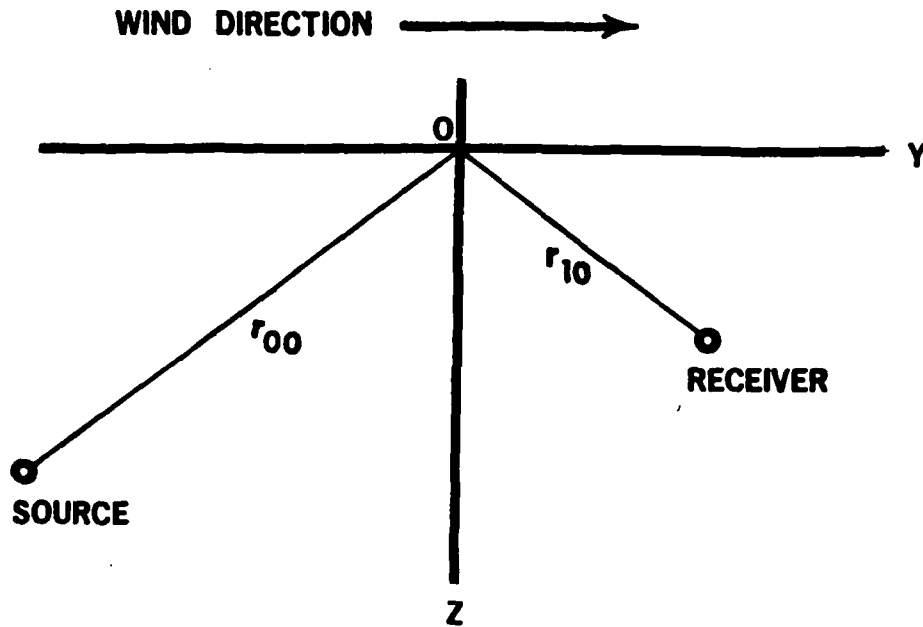


Figure 4.5 Asymmetric sidebands for small Rayleigh parameter,
 $\epsilon_3 = 0$, and $r_{00} > r_{10}$

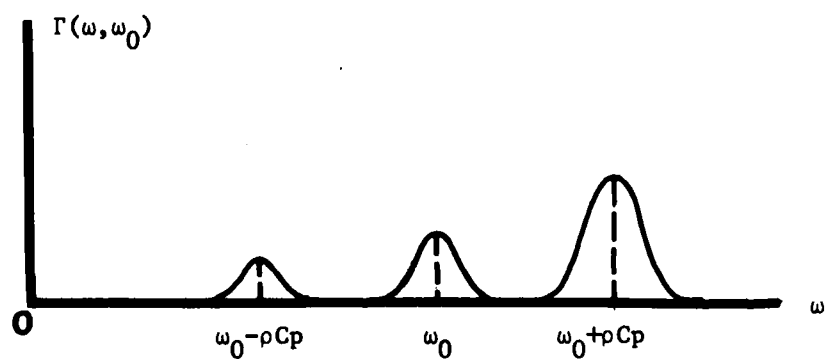
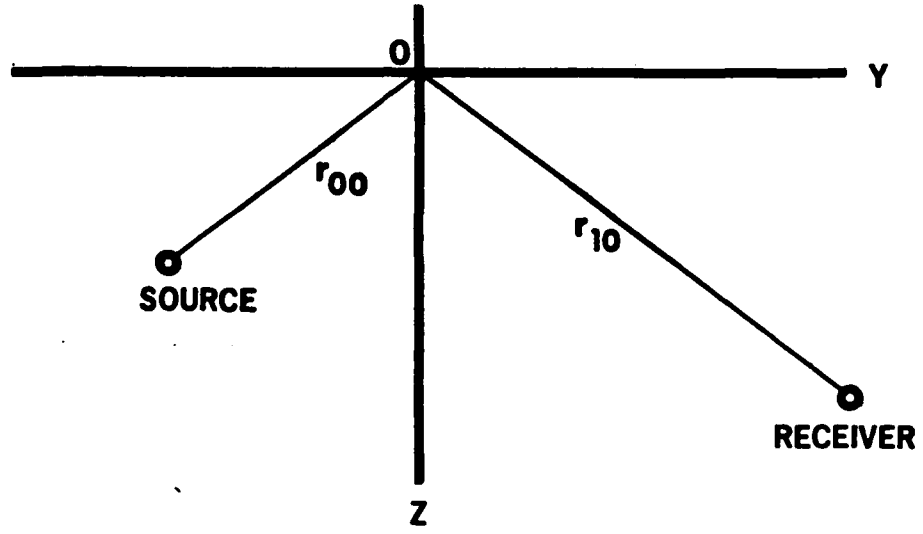


Figure 4.6 Asymmetric sidebands for small Rayleigh parameter,
 $\epsilon_3 = 0$, and $r_{00} < r_{10}$

where

$$S_{c_0}(\omega, \omega_0) = (1-2\epsilon_2)\delta(\omega-\omega_0) + (\sqrt{\pi} T_2) \frac{\rho^2 \sigma^2 \epsilon_2}{g^2} e^{-\frac{T_2^2}{4}(\omega-\omega_0)^2} \\ + (\sqrt{\pi} T_3) \frac{\rho \sigma \epsilon_3}{g} e^{-\frac{T_3^2}{4}(\omega-\omega_0)^2} \quad (4.2.12a)$$

$$S_{c_{1+}}(\omega, \omega_0) = \frac{g^2}{2} (\sqrt{\pi} T_0) e^{-\frac{2\sigma^2 R^2 \rho^2}{g^2 L^2(\omega_0)}} \\ \cdot \{(1-2\epsilon_2)e^{-\frac{T_0^2}{4}(\omega-\omega_0+\rho C_p)^2} + \frac{\rho^2 \sigma^2 \epsilon_2}{g^2} e^{-\frac{T_0^2 T_2^2 (\omega-\omega_0+\rho C_p)^2}{4(T_0^2+T_2^2)}} \\ - \frac{T_0^2 T_3^2 (\omega-\omega_0+\rho C_p)^2}{4(T_0^2+T_3^2)} \\ + \frac{\rho \sigma \epsilon_3}{g} e^{-\frac{T_0^2 T_3^2 (\omega-\omega_0+\rho C_p)^2}{4(T_0^2+T_3^2)}}\} \quad (4.2.12b)$$

We observe that equations (4.2.12) are quite similar to equations (4.2.7) except that the geometry-asymmetry factors, i.e. $\exp\left\{+\frac{4\sigma^2 R^2 \rho}{g^2 L^2(\omega_0)}\right\}$ in equation (4.2.7b), have disappeared. Therefore, the sideband ratio, i.e. $S_{c1+}(\omega, \omega_0)/S_{c1-}(\omega, \omega_0)$, will remain unchanged for all values of r_{00} and r_{10} . The effect of asymmetric slope distribution is, however, still present in

equation (4.2.12). Figure 4.7 shows a crosswind spectrum obtained by Zornig [3] in a model tank experiment.

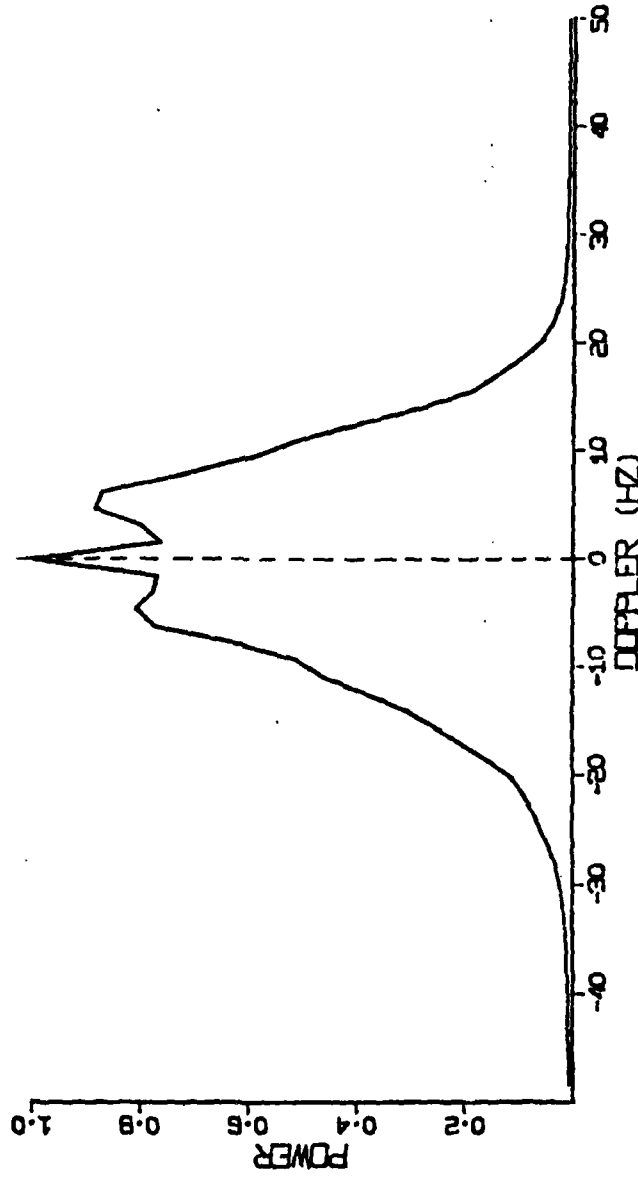


Figure 4.7 Experimentally measured spectrum-crosswind, wind speed at 5.4 m/sec,
 $f_0 = 524$ kHz, $r_{00} = r_{10} = 173$ cm, $\psi_0 = 17^\circ$

4.3 Random surfaces - large Rayleigh parameter

When the surfaces become rougher, i.e. $g = \frac{\omega_0 F \sigma}{c} \gg 1$, either by increasing the r.m.s. surface waveheight σ or by increasing the acoustic frequency ω_0 ; the surface height characteristic function is conveniently approximated by equation (4.1.14) repeated here as equation (4.3.1):

$$\overline{Q(\zeta_1, \zeta_2)} = \exp\left\{-g^2\left[\frac{\xi^2}{\Lambda_x^2} + \frac{\eta^2}{\Lambda_y^2} + \frac{\tau^2}{T_0^2} + \frac{\rho^2}{2} (\eta - C_p \tau)^2\right]\right\} \quad (4.3.1)$$

The received signal spectrum can be computed as in Sec. 4.2, with equation (4.3.1) being used to represent the characteristic function $Q(\zeta_1, \zeta_2)$. Appendix I has the details of this computation. The resulting spectrum is expressed in equation (I-4), repeated here as equation (4.3.2):

$$\begin{aligned} \Gamma(\omega, \omega_0) &= \int_{-\infty}^{\infty} \Phi(\omega_0, \tau) e^{-j(\omega - \omega_0)\tau} d\tau \\ &\approx K_2 \left\{ \left(\frac{\pi}{q_1(0,0)} \right)^{\frac{1}{2}} \cdot f_{10} \cdot \exp\left[-\frac{[\omega - \omega_0 - q_2(0)]^2}{4q_1(0,0)}\right] \right. \\ &+ \left(\frac{\pi}{q_1(\frac{1}{T_2^2}, \frac{1}{\Lambda_2^2})} \right)^{\frac{1}{2}} \cdot \epsilon_2 f_{12} \left(\frac{-j[\omega - \omega_0 - q_2(\frac{1}{T_2^2}, \frac{1}{\Lambda_2^2})]}{2q_1(\frac{1}{T_2^2}, \frac{1}{\Lambda_2^2})} \right) \cdot \exp\left[-\frac{[\omega - \omega_0 - q_2(\frac{1}{T_2^2}, \frac{1}{\Lambda_2^2})]^2}{4q_1(\frac{1}{T_2^2}, \frac{1}{\Lambda_2^2})}\right] \\ &+ \left. \left(\frac{\pi}{q_1(\frac{1}{T_3^2}, \frac{1}{\Lambda_3^2})} \right)^{\frac{1}{2}} \cdot \epsilon_3 f_{13} \left(\frac{-j[\omega - \omega_0 - q_2(\frac{1}{T_3^2}, \frac{1}{\Lambda_3^2})]}{2q_1(\frac{1}{T_3^2}, \frac{1}{\Lambda_3^2})} \right) \cdot \exp\left[-\frac{[\omega - \omega_0 - q_2(\frac{1}{T_3^2}, \frac{1}{\Lambda_3^2})]^2}{4q_1(\frac{1}{T_3^2}, \frac{1}{\Lambda_3^2})}\right] \right\} \end{aligned} \quad (4.3.2)$$

where K_2 , f_{10} , f_{12} , f_{13} , q_1 and q_2 are defined in Appendix I.

Notice that the signal spectrum $\Gamma(\omega, \omega_0)$ is the superposition of three functions. Each of the three functions contains a Gaussian term. The centers of the first, the second, and the third Gaussian are respectively $\omega_0 + q_2(0)$, $\omega_0 + q_2(\frac{1}{\Lambda_2^2})$, and $\omega_0 + q_3(\frac{1}{\Lambda_3^2})$. From equation (I-4b), we get

$$q_2(0) = \frac{\frac{1}{2} \rho^2 g^2 C_{pd}}{\frac{|N|^2}{N+N^*} + \frac{g^2}{\Lambda_y^2} + \frac{\rho^2 g^2}{2}} \quad (4.3.3a)$$

$$q_2(\frac{1}{\Lambda_2^2}) = \frac{\frac{1}{2} \rho^2 g^2 C_{pd}}{\frac{|N|^2}{N+N^*} + \frac{g^2}{\Lambda_y^2} + \frac{\rho^2 g^2}{2} + \frac{1}{\Lambda_2^2}} \quad (4.3.3b)$$

$$q_2(\frac{1}{\Lambda_3^2}) = \frac{\frac{1}{2} \rho^2 g^2 C_{pd}}{\frac{|N|^2}{N+N^*} + \frac{g^2}{\Lambda_y^2} + \frac{\rho^2 g^2}{2} + \frac{1}{\Lambda_3^2}} \quad (4.3.3c)$$

where N is a complex quantity defined in equation (H-4). Equation (4.3.2) is rather unwieldly as it stands and must be simplified considerably to permit easy interpretation. We consider first the equation for $q_2(\cdot)$. From equation (4.3.3) we see that their dependence on Λ_2 and Λ_3 is relatively slight, especially if we make the assumption that Λ_2 , Λ_3 and Λ_y are all of the same order of magnitude (this assumption is based on considerations similar to those used in the

previous section to argue that $T_0 \approx T_2 \approx T_3$). Note that since we are dealing with rough surfaces here, $g^2 \gg 1$, and therefore $g^2/\Lambda_y^2 \gg \frac{1}{\Lambda_2^2}, \frac{1}{\Lambda_3^2}$. Thus we have that

$$q_2\left(\frac{1}{\Lambda_2^2}\right) \approx q_2\left(\frac{1}{\Lambda_3^2}\right) \approx q_2(0) \quad (4.3.4)$$

Furthermore, if the surface slope correlation times T_2 and T_3 are of the same order of magnitude as T_0 , then from equation (I-4a), we have

$$q_1\left(\frac{1}{\Lambda_2^2}, \frac{1}{T_2^2}\right) \approx q_1\left(\frac{1}{T_3^2}, \frac{1}{\Lambda_3^2}\right) \approx q_1(0,0) \quad (4.3.5)$$

By the use of equations (4.3.4) and (4.3.5) the three Gaussian functions in equation (4.3.2) are made to be identical and $\Gamma(\omega, \omega_0)$ can be rewritten as

$$\begin{aligned} \Gamma(\omega, \omega_0) &\approx K_2\left(\frac{\pi}{q_1(0,0)}\right)^{\frac{1}{2}} \cdot \exp\left\{-\frac{[\omega-\omega_0-q_2(0)]^2}{4q_1(0,0)}\right\} \\ &\cdot \{f_{10} + \epsilon_2 f_{12}\left(\frac{-j[\omega-\omega_0-q_2(0)]}{2q_1(0,0)}\right) + \epsilon_3 f_{13}\left(\frac{-j[\omega-\omega_0-q_2(0)]}{2q_1(0,0)}\right)\} \end{aligned} \quad (4.3.6)$$

Except for the terms involving the slope moments ϵ_2 and ϵ_3 , the signal spectrum $\Gamma(\omega, \omega_0)$ is seen to be a Gaussian function with center frequency at $\omega_0 + q_2(0)$ and bandwidth $f_B = 2\pi^{-1}[q_1(0,0)]^{\frac{1}{2}}$. The functions f_{10} , f_{12} , f_{13} , q_1 and q_2 all depend on the scattering geometry, as can be seen in Appendix I. Thus the spectrum $\Gamma(\omega, \omega_0)$

depends on geometry and on slope moments. As in the previous sections we consider in detail only the down (up) wind and crosswind geometries.

Case I. Downwind

Detailed calculations for the downwind case are given in Appendix I, equations (I-5) to (I-9). Equation (I-9) gives the expression for the spectrum, repeated here as equation (4.3.7)

$$\Gamma(\omega, \omega_0) \approx \frac{1}{(r_{00} + r_{10})^2} \cdot \frac{\sqrt{\pi}}{gCp/2} e^{-\frac{[\omega - \omega_0 - q_2(0)]^2}{(2\pi f_B)^2}}$$

$$\{(1-2\epsilon_2) + 2\sigma^2\epsilon_2 [(\frac{1}{\Lambda_y^2} + \frac{\rho^2}{2}) + \frac{1}{g^2\Lambda_2^2}] + \frac{\sigma\epsilon_3}{gCp} [\omega - \omega_0 - q_2(0)]\}$$
(4.3.7)

We see that $\Gamma(\omega, \omega_0)$ is generally not symmetric with respect to ω_0 unless $q_2(0) = 0$ and $\epsilon_3 = 0$. These are the effects of the two mechanisms mentioned previously as we recognize that ϵ_3 represents the slope asymmetry and $q_2(0)$ is the scattering-geometry asymmetry. The expression of $q_2(0)$ can be obtained from equation (4.3.3a) and the expression of d in equation (H-22)

$$q_2(0) = \frac{\frac{1}{2}\rho^2Cp}{\frac{|N|^2}{g^2(N+N^*)} + \frac{1}{\Lambda_y^2} + \frac{\rho^2}{2}} \cdot \frac{\omega_0 L^2(\omega_0) \cos\psi_0}{CR} \cdot (\frac{1}{r_{00}} - \frac{1}{r_{10}})$$
(4.3.8)

We see that $q_2(0)$ is non-zero if $r_{00} \neq r_{10}$ and $\psi_0 \neq 90^\circ$; and $q_2(0)$ is positive (negative) when $r_{00} < r_{10}$ ($r_{00} > r_{10}$). Therefore, considering no slope asymmetry, i.e. $\varepsilon_3 = 0$, we conclude that if the wind blows from source to receiver, and if $r_{00} < r_{10}$ ($r_{00} > r_{10}$), the upper (lower) sideband is larger than the lower (upper) sideband (see Figure 4.8). This conclusion is the same as was reached in the deterministic case and in the slightly rough (random) surface case.

We examine next the sideband asymmetry caused by surface slope asymmetry. As usual, we eliminate the effect of the scattering geometry factor by assuming $r_{00} = r_{10}$. Then equation (4.3.7) becomes

$$\Gamma(\omega, \omega_0) \approx \frac{1}{(r_{00} + r_{10})^2} \cdot \frac{\sqrt{\pi}}{g p C_p / 2} \cdot \exp\left\{-\frac{(\omega - \omega_0)^2}{(2\pi f_B)^2}\right\} \\ \cdot \left\{ (1 - 2\varepsilon_2) + 2\sigma^2 \varepsilon_2 \left[\left(\frac{1}{\Lambda_y^2} + \frac{\rho^2}{2} \right) + \frac{1}{g^2 \Lambda_2^2} \right] + \frac{\sigma \varepsilon_3}{g C_p} (\omega - \omega_0) \right\} \quad (4.3.9)$$

We see that the center of the Gaussian function is at ω_0 . The sideband asymmetry is introduced by the last term in the brackets, viz. $\frac{\sigma \varepsilon_3}{g C_p} (\omega - \omega_0)$, which is positive and therefore increases the upper sideband when $\omega > \omega_0$; and is negative and decreases the lower sideband when $\omega < \omega_0$. Therefore, the upper sideband is always larger than the lower sideband. Figure 4.9 contains a plot of equation (4.3.14) with $f_0 = 256$ KHz, $\psi_0 = 30^\circ$, $r_{00} = r_{10} = 254$ cm. A slight asymmetry can be seen by comparing the corresponding spectral amplitudes on both the upper and lower sidebands. Much greater asymmetry is produced by differences in source and receiver depths. This is illustrated in Figures 4.10 to 4.12, which are plotted for $r_{00}/r_{10} = 0.1, 10, \text{ and } 0.5$ respectively.

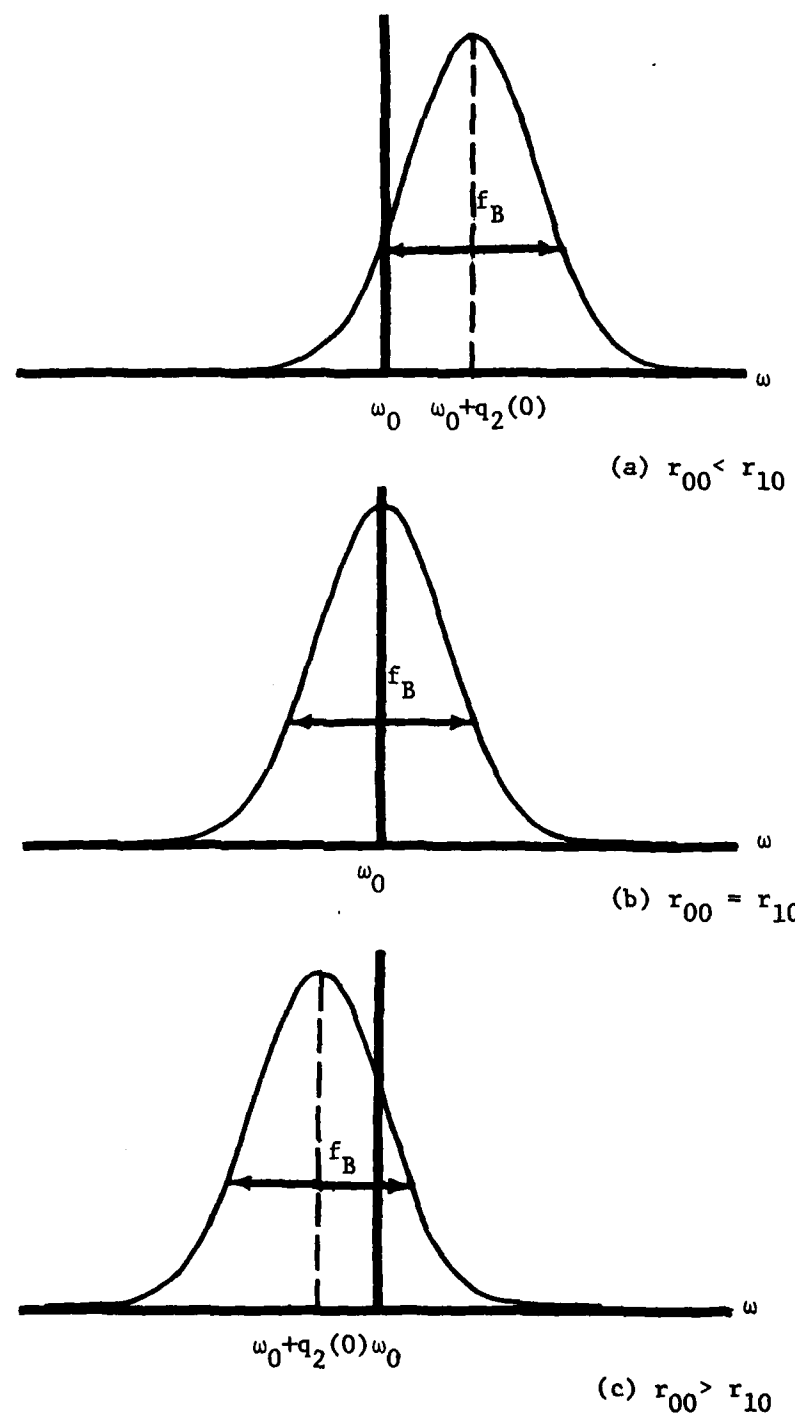


Figure 4.8 Gaussian spectrum-Downwind

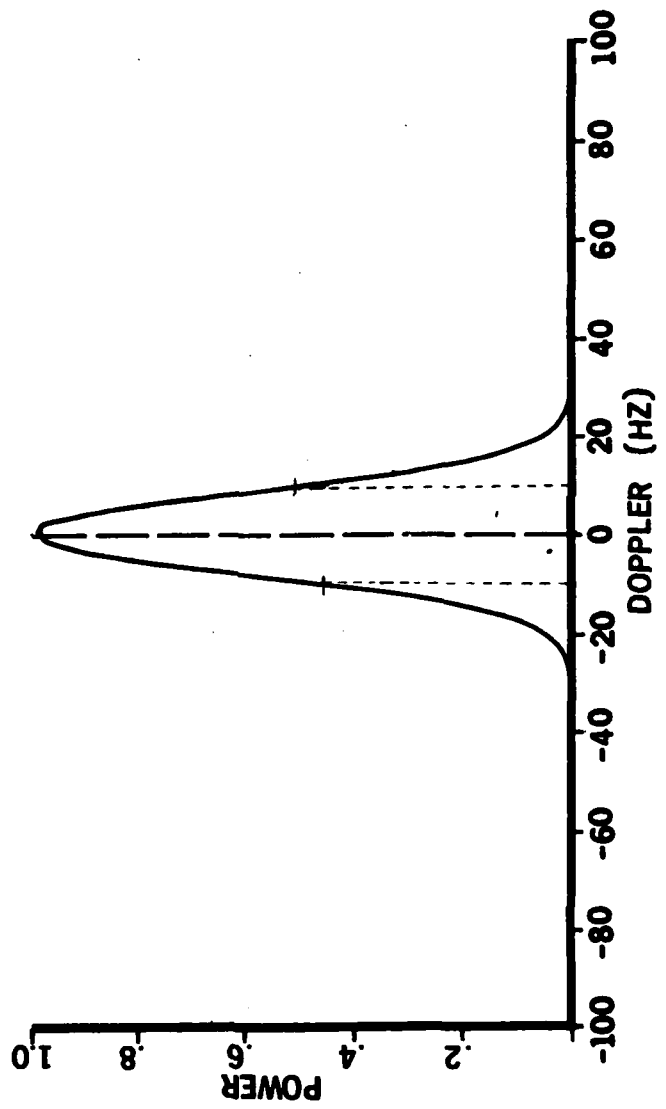


Figure 4.9 Theoretically computed power spectrum (1) - rough surface, upwind.
 Parameters used are $r_{00} = r_{10} = 254$ cm, $\psi_0 = 30^\circ$, $\sigma = 0.2$ cm,
 $f_0 = 256$ KHz, $C_p = 30$ cm/sec, $T_0 = 0.1$ sec, $\epsilon_2 = 0.3$, $\epsilon_3 = 0.2$.

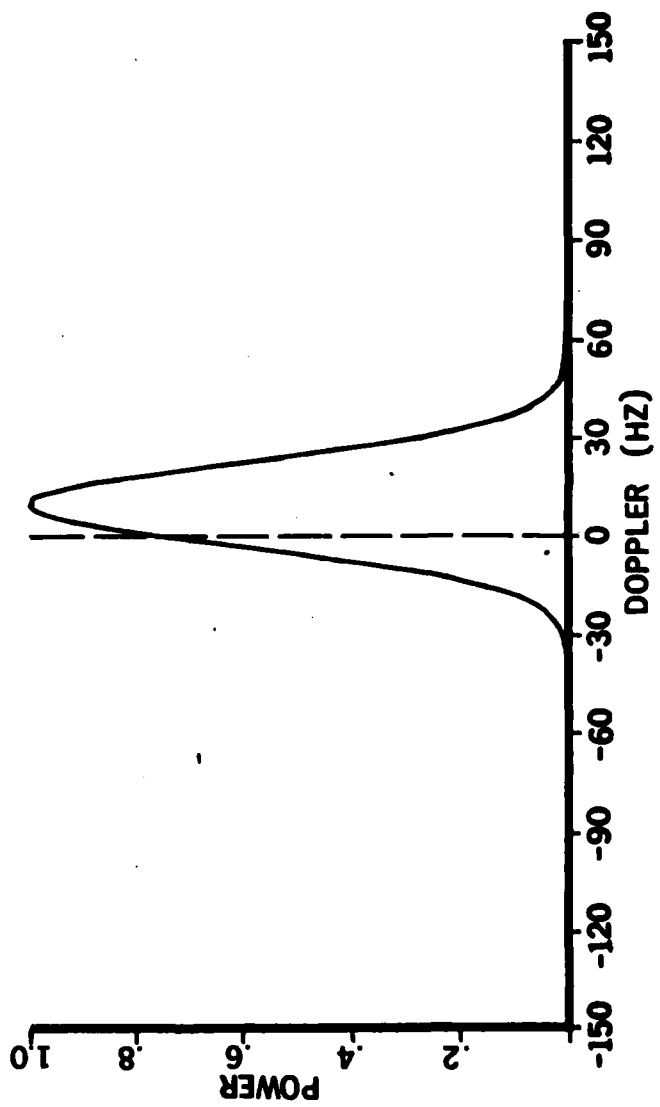


Figure 4.10 Theoretically computed power spectrum (2) - rough surface, upwind.
Parameters used are the same as in Figure 4.9, except that $r_0 = 50$ cm,
 $r_{10} = 500$ cm.

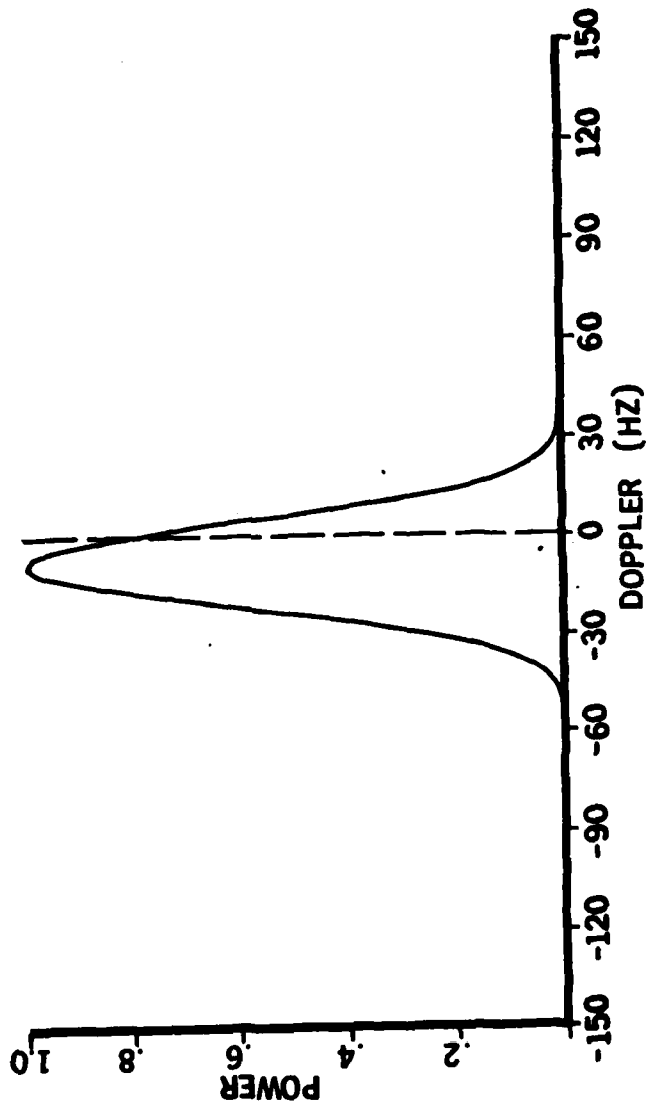


Figure 4.11 Theoretically computed power spectrum (3) - rough surface, upwind.
Parameters used are the same as in Figure 4.9 except that $r_{00} = 500$ cm,
 $r_{10} = 50$ cm.

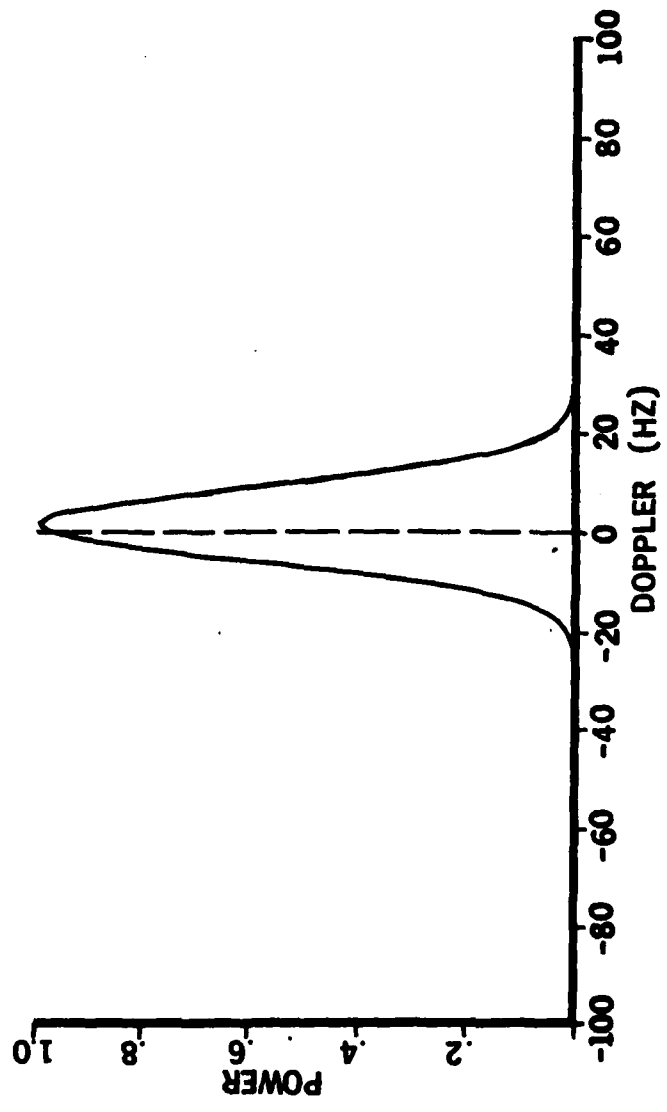


Figure 4.12 Theoretically computed power spectrum (4) - rough surface, upwind.
 Parameters used are the same as in Figure 4.9, except that $r_{00} = 127$ cm,
 $r_{10} = 254$ cm.

Figure 4.12

The amount of frequency spreading is determined by the bandwidth f_B . From equation (I-4a), with $a = b = 0$, we find that this is given by

$$f_B = f_0 \left\{ \frac{4F\sigma}{c} \left[\frac{1}{T_0^2} + \frac{\rho^2 C_p^2}{2} \cdot \frac{\frac{L^2(\omega_0)}{8\sigma^2 R^2} + \frac{1}{\Lambda_y^2}}{\frac{L^2(\omega_0)}{8\sigma^2 R^2} + \frac{1}{\Lambda_y^2} + \frac{\rho^2}{2}} \right]^{\frac{1}{2}} \right\} \quad (4.3.10)$$

where the Rayleigh parameter g has been replaced by $g = \frac{\omega_0 F\sigma}{c} = \frac{(2\pi f_0) F\sigma}{c}$.

We see that the bandwidth f_B is a monotonic function of the acoustic frequency f_0 (in Hz). However, it is not a linear function of f_0 , since the beamwidth $L(\omega_0) \propto \frac{1}{f_0}$ is frequency dependent. For low acoustic frequency, $L(\omega_0)$ is large, and we can assume that $\frac{L^2(\omega_0)}{8\sigma^2 R^2} \gg \frac{1}{\Lambda_y^2} + \frac{\rho^2}{2}$. Hence for small f_0

$$f_B \approx f_0 \left\{ \frac{4F\sigma}{c} \left[\frac{1}{T_0^2} + \frac{\rho^2 C_p^2}{2} \right]^{\frac{1}{2}} \right\} \quad (4.3.11)$$

As the acoustic frequency increases, the beamwidth $L(\omega_0)$ becomes smaller, and at some high frequency, we have $\frac{L^2(\omega_0)}{8\sigma^2 R^2} \ll \frac{1}{\Lambda_y^2}$. Hence, for large f_0 , equation (4.3.10) can be rewritten as

$$f_B \approx f_0 \left\{ \frac{4F\sigma}{c} \left[\frac{1}{T_0^2} + \frac{\rho^2 C_p^2}{2+\rho^2 C_p^2} \right]^{\frac{1}{2}} \right\} \quad (4.3.12)$$

Figure 4.13 contains a plot of f_B/f_0 as function of frequency f_0 according to equation (4.3.10). Notice the asymptotic behavior at both

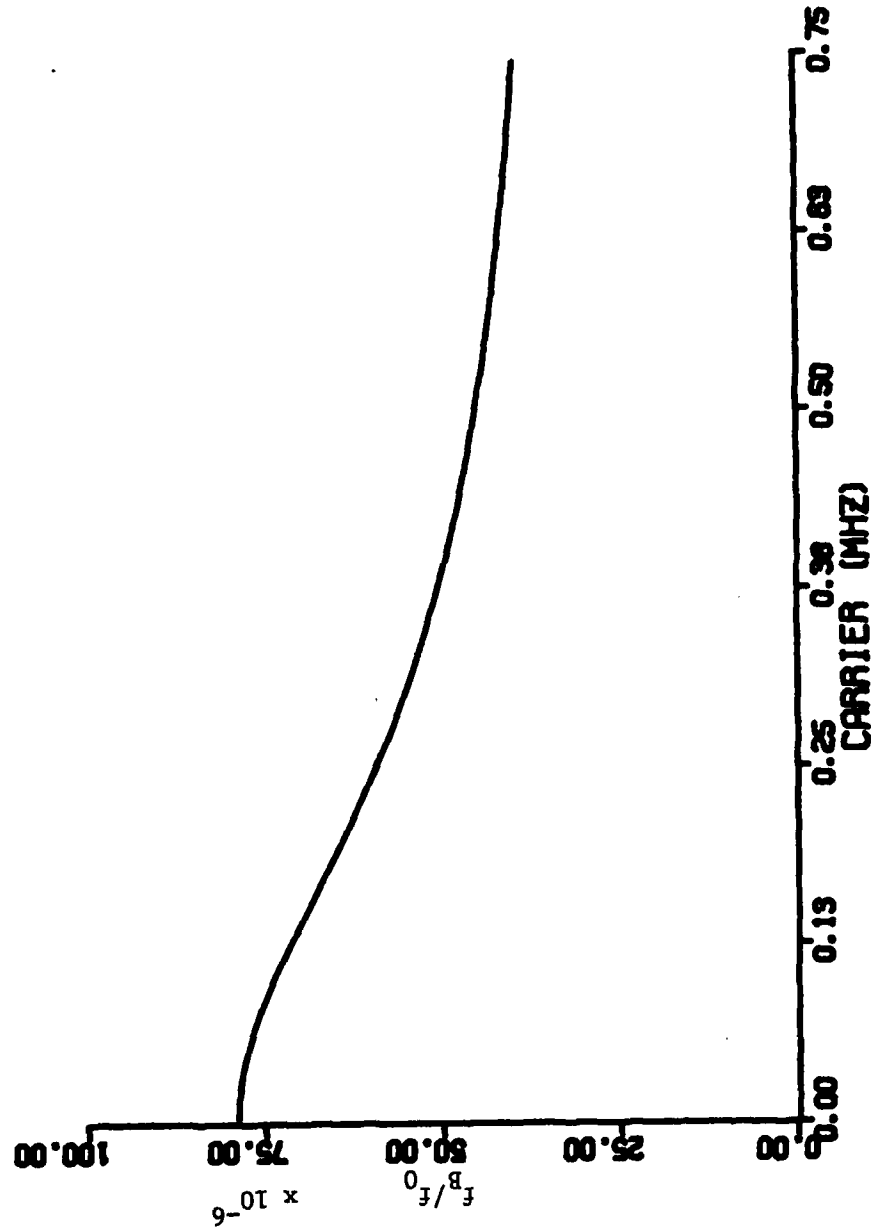


Figure 4.13 Bandwidth coefficient for downwind.

low⁺ and high acoustic frequencies.

Case II. Crosswind

The received signal spectrum for crosswind is derived in Appendix I, equation (I-10), repeated here as equation (4.3.13)

$$\Gamma(\omega, \omega_0) = \frac{1}{(r_{00} + r_{10})^2} \cdot \frac{\sqrt{\pi}}{g\rho C_p/2} \cdot \exp\left\{-\frac{(\omega - \omega_0)^2}{(2\pi f_B)^2}\right\} \\ \cdot \left\{(1-2\epsilon_2) + 2\sigma^2\epsilon_2 \left[\left(\frac{1}{\Lambda_y^2} + \frac{\rho^2}{2} \right) + \frac{1}{g^2\Lambda_2^2} \right] + \frac{\sigma\epsilon_3}{gC_p} (\omega - \omega_0) \right\} \quad (4.3.13)$$

There is only one factor in equation (4.3.16) that can cause sideband asymmetry. It is $\frac{\sigma\epsilon_3}{gC_p} (\omega - \omega_0)$, the surface slope asymmetry. As we discussed in the section dealing with the downwind geometry, this term will make the upper sideband larger than the lower sideband in a wind driven surface. Varying the scattering geometries, i.e. changing r_{00} , r_{10} , has no effect on the sideband asymmetries.

The bandwidth for crosswind is obtained by substituting crosswind parameter values into equation (I-4a). This gives

$$f_B = f_0 \left\{ \frac{4F\sigma}{c} \left[\frac{1}{T_0^2} + \frac{\rho^2 C_p^2}{2} \right] \cdot \frac{\frac{L^2(\omega_0)}{8\sigma^2 R^2 \sin^2 \psi_0} + \frac{1}{\Lambda_y^2}}{\frac{L^2(\omega_0)}{8\sigma^2 R^2 \sin^2 \psi_0} + \frac{1}{\Lambda_y^2} + \frac{\rho^2}{2}} \right\}^{\frac{1}{2}} \quad (4.3.14)$$

⁺ Very low values of f_0 might be inconsistent with the assumption of a very rough surface; i.e. $g \gg 1$. However the inequality leading to equation 4.3.11 depends on beam width, which is partly controlled by transducer size. Hence equation 4.3.11 may hold with $g \gg 1$.

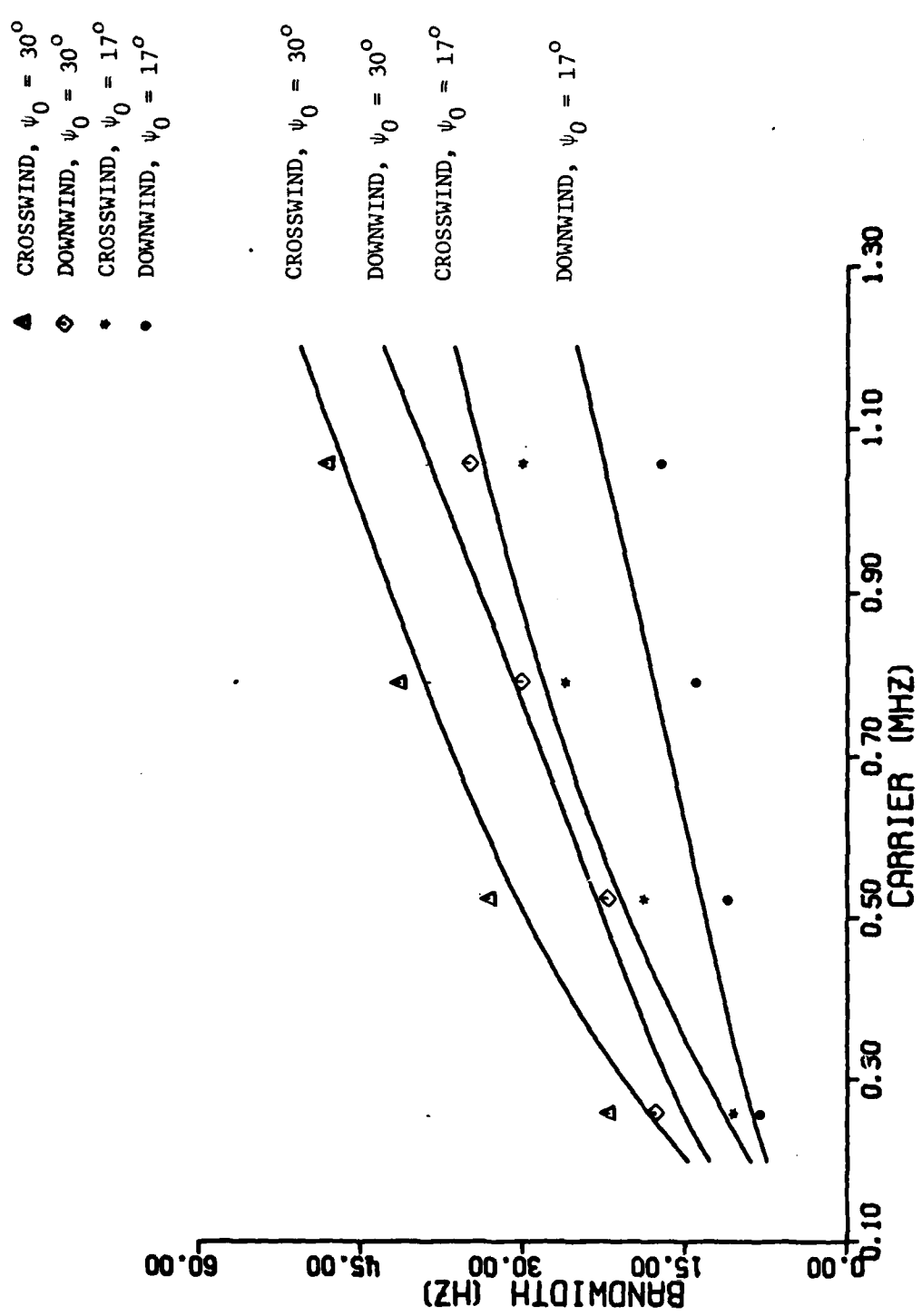


Figure 4.14 Bandwidth for different wind direction and grazing angles
LINE-THEORETICAL, SPECIAL SYMBOLS-EXPERIMENTAL.

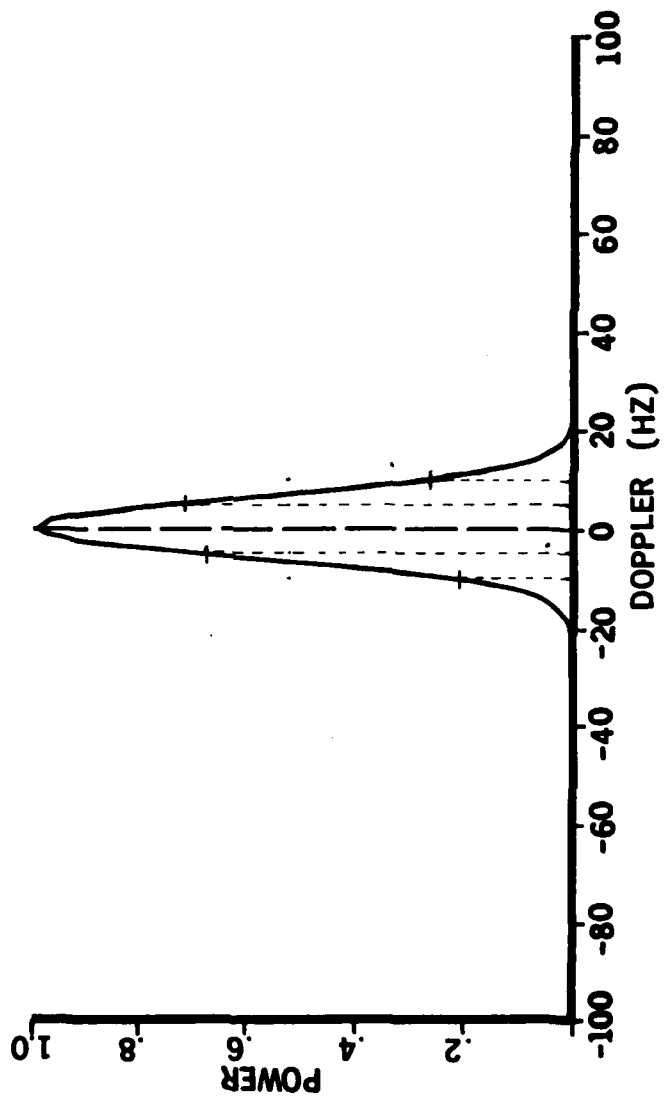


Figure 4.15 Theoretically computed power spectrum (1) - rough surface, crosswind.
Parameters used are the same as in Figure 4.9, except that $\psi_0 = 17^\circ$.

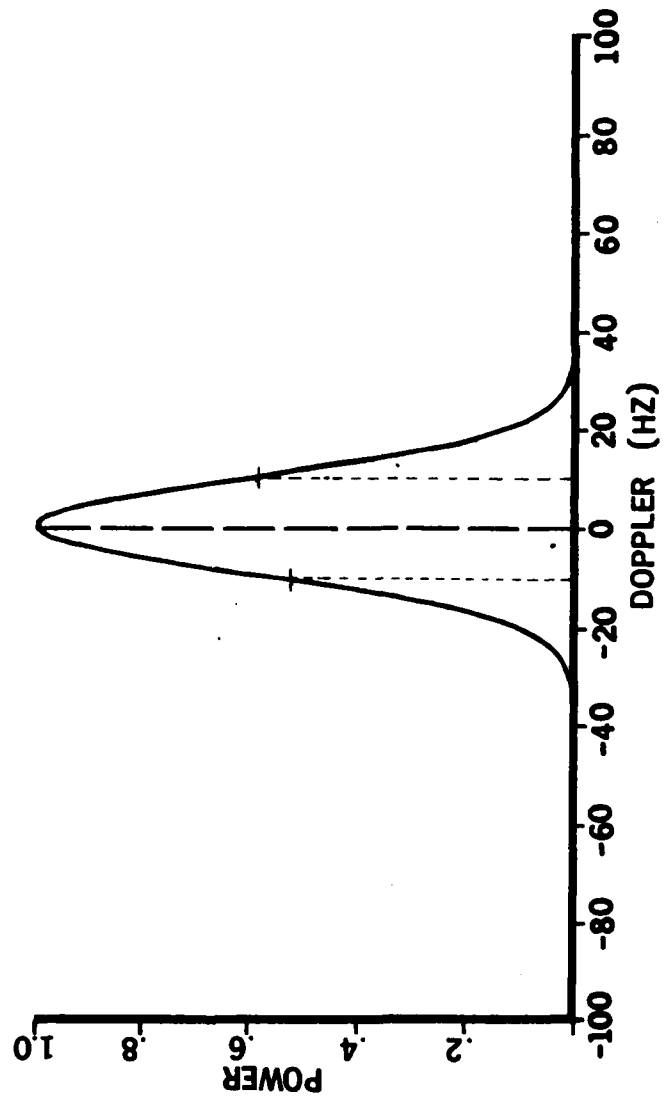


Figure 4.16 Theoretically computed power spectrum (2) - rough surface, crosswind.
Parameters used are the same as in Figure 4.9.

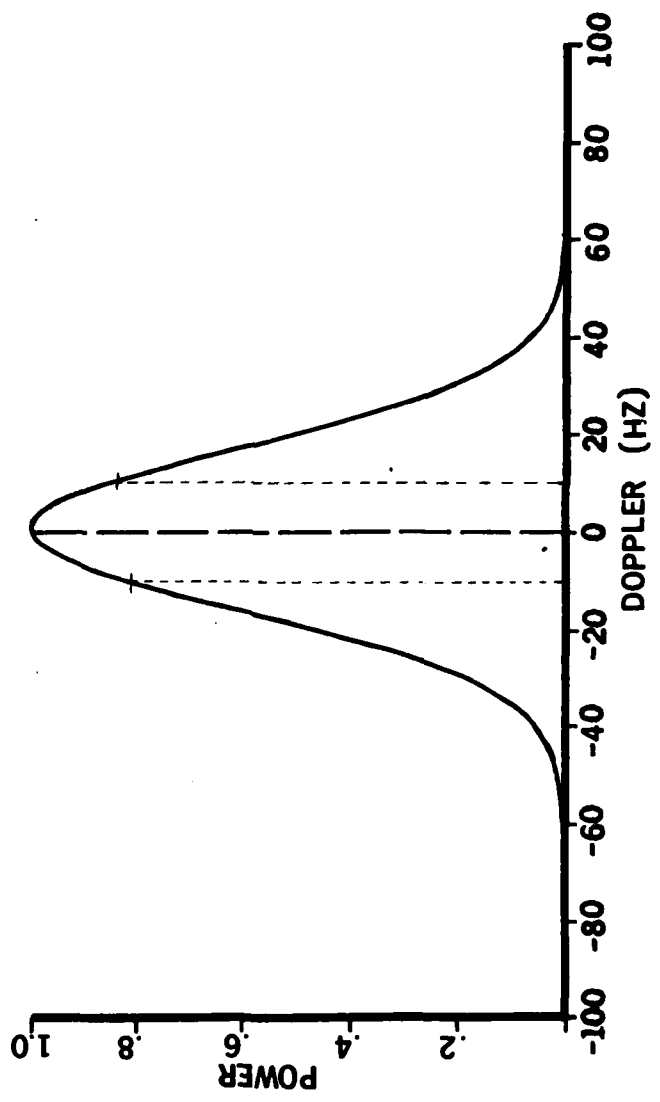


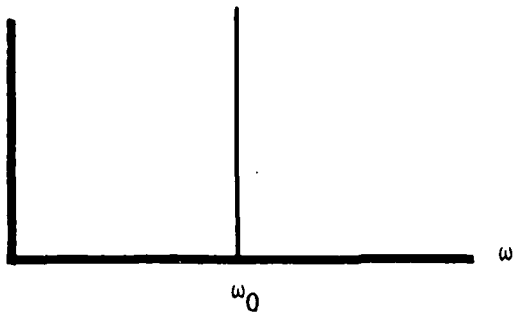
Figure 4.17 Theoretically computed power spectrum (3) - rough surface, crosswind.
Parameters used are the same as in Figure 4.9, except that $f_0 = 524$ kHz.

The main difference between equations (4.3.10) and (4.3.14) is that the term $\frac{L^2(\omega_0)}{8\sigma^2 R^2}$ in equation (4.3.10) is replaced by $\frac{L^2(\omega_0)}{8\sigma^2 R^2 \sin^2 \psi_0}$ in equation (4.3.14). Since $\frac{L^2(\omega_0)}{8\sigma^2 R^2 \sin^2 \psi_0}$ is always larger than $\frac{L^2(\omega_0)}{8\sigma^2 R^2}$, the crosswind bandwidth in equation (4.3.14) is larger than the downwind bandwidth in equation (4.3.10). In other respects the dependence of the bandwidth on f_0 is similar to that already discussed for the downwind case. Figure 4.14 shows plots of bandwidths for both downwind and crosswind at $\psi_0 = 17^\circ$ and 30° . Also shown in this figure are experimental points of bandwidth measurements made in a model tank by J.G. Zornig [3]. The general behavior of the theoretical and experimental results are very similar, and the correspondence between the results for $\psi_0 = 30^\circ$ are well within experimental error. For $\psi_0 = 17^\circ$ there may already be some shadowing, and this might explain the consistently smaller bandwidth observed in the experiment. This issue has not yet been investigated.

In Figures 4.15 to 4.17 are plots of the crosswind signal spectrum according to equation (4.3.13); in Figure 4.15, $f_0 = 256$ KHz and $\psi_0 = 17^\circ$; in Figure 4.16, $f_0 = 256$ KHz, $\psi_0 = 30^\circ$, and in Figure 4.17, $f_0 = 524$ KHz and $\psi_0 = 30^\circ$. Note that the sideband asymmetry becomes less significant with increase in f_0 . Also note that the bandwidth increases both with ψ_0 and with f_0 .

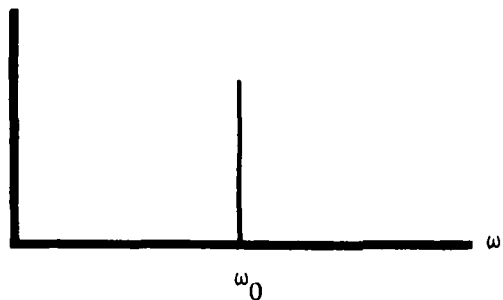
In summary, we have examined the frequency spreading function of the acoustic signal scattered from a random rough surfaces for both the slightly rough case and very rough case. We have found that the amount of frequency spreading (bandwidth) depends on both the surface roughness and surface slopes. The following illustrations summarize the results of section 4.2 and 4.3.

(1)



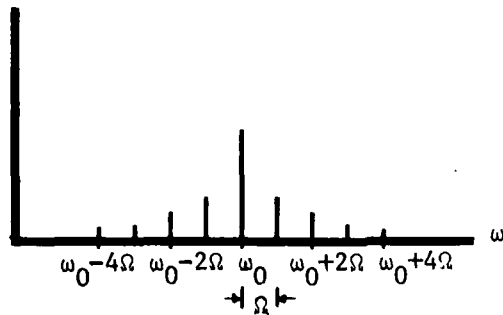
The incident acoustic signal is sinusoidal with frequency ω_0 .

(2)



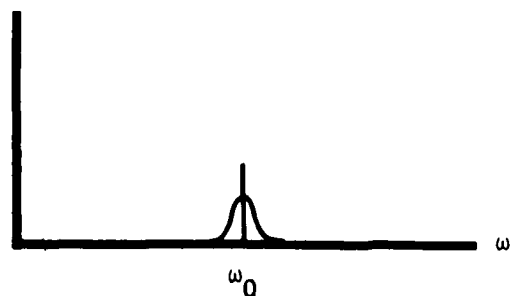
The received signal spectrum reflected from an absolutely flat surface. The spectral amplitude is attenuated.

(3)

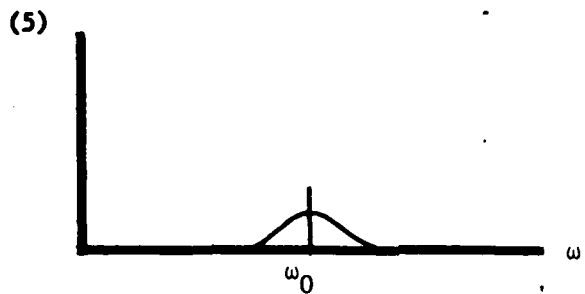


Sinusoidal surface of frequency Ω . The scattered signal spectrum is a sequence of spectral lines of interval Ω .

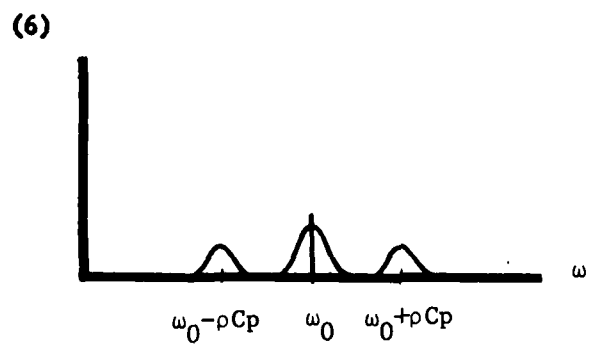
(4)



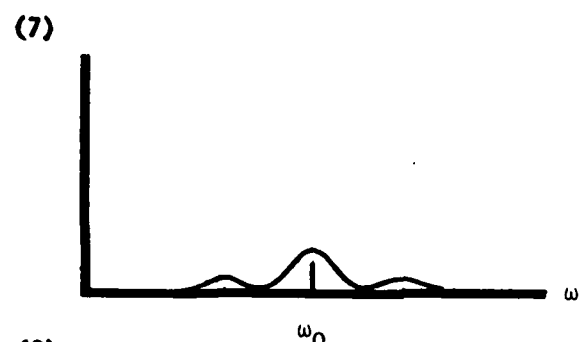
Surface with very small roughness; finite surface slopes with large temporal correlations.



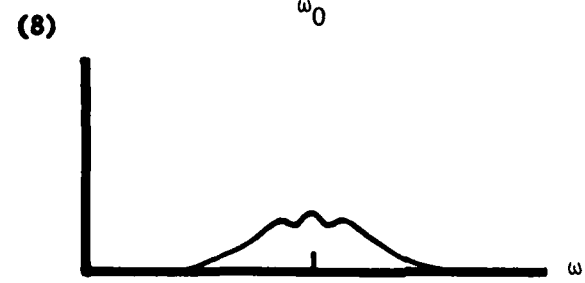
Same as (4), except the slope has smaller temporal correlation (become more uncorrelated).



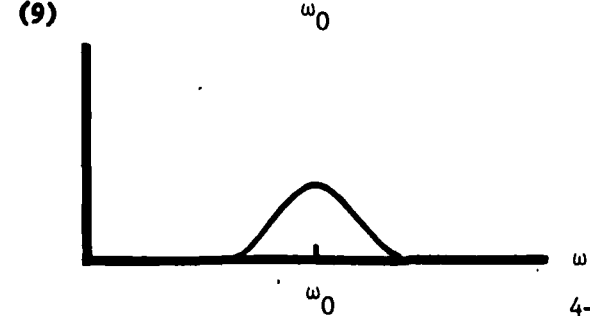
From (4), the surface roughness increases, and the surface wave is a narrow band process with a center frequency of ρC_p .



The surface roughness increases more, and the bandwidth of the surface wave also increases.



A continuation of (7).



For very large surface roughness, the signal spectra merge into one Gaussian.

The amplitudes of the frequency spreading function are in general not symmetric with respect to the transmitted frequency. There are two different mechanisms which are responsible for this amplitude difference. One mechanism is the surface slope asymmetry, i.e. ϵ_3 is positive, which always results in the upper sideband being larger than the lower sideband. This effect does not depend on the wind direction. The other mechanism is the scattering geometry asymmetry caused by unequal depths of source and receiver. This effect is a function of the wind direction and depends on the relative depths of source and receiver. Specifically, if the source is located at a smaller depth and if the wind blows from source to receiver, then the upper sideband is larger than the lower sideband. By either reversing the wind direction or maintaining the wind direction but placing the receiver at a smaller depth than the source, the lower sideband will have a larger amplitude than the upper sideband. Since this mechanism is wind-direction dependent, it has no effect on the sideband amplitude asymmetries in the crosswind condition. The effect of the second mechanism on the sideband asymmetry is in general larger than that of the asymmetric surface slopes. The effect of both mechanisms decreases as the acoustic frequency increases. In other words, the frequency spreading function is more symmetric at higher acoustic frequency than at lower frequency.

The width of the frequency function is controlled by several parameters; it increases with the grazing angle, the surface roughness, and the acoustic frequency. It also depends on the wind direction, the width of the spreading increases as the geometry changes from downwind to crosswind.

Chapter V Experimental Data Comparison and Discussion

5.0 Introduction

A series of surface-scatter experiments has been performed in a model tank by J.G. Zornig [3]. A windblown surface is generated in this tank by a fan blowing air through a wind tunnel suspended above the surface. A detailed description of the experimental equipment and setup can be found in [79]. The experimental technique involves the transmission of narrow pulses that are preemphasized so as to produce an approximately flat received spectrum over the frequency range of 0.2 to 1.2 MHz. The received pulses are acquired by a digital computer and stored on magnetic tape. Data processing to obtain the frequency spreading function can then be performed on the stored data. The data processing techniques are described in detail in Appendix J.

5.1 Doppler Shift

Examples of measured and computed spectra are shown in Figures 5.1 to 5.4. Each figure contains four spectra corresponding to four transmitted frequencies, f_0 : 256 KHz, 524 KHz, 792 KHz, and 1.06 MHz. The zero frequency of all plots is referred to the transmitted frequency. Hence the positive (negative) frequencies correspond to the upper (lower) sideband. Figures 5.1 and 5.3 are for upwind transmission, while Figures 5.2 and 5.4 are for crosswind. The grazing angle in Figures 5.1 and 5.2 is 30° and in Figures 5.3 and 5.4 it is 17° . In all plots the depths of source and receiver are the same. It is clear from these figures that there is a significant discrepancy between theory and experimental results. According to the theory, the asymmetry should decrease with f_0 . This

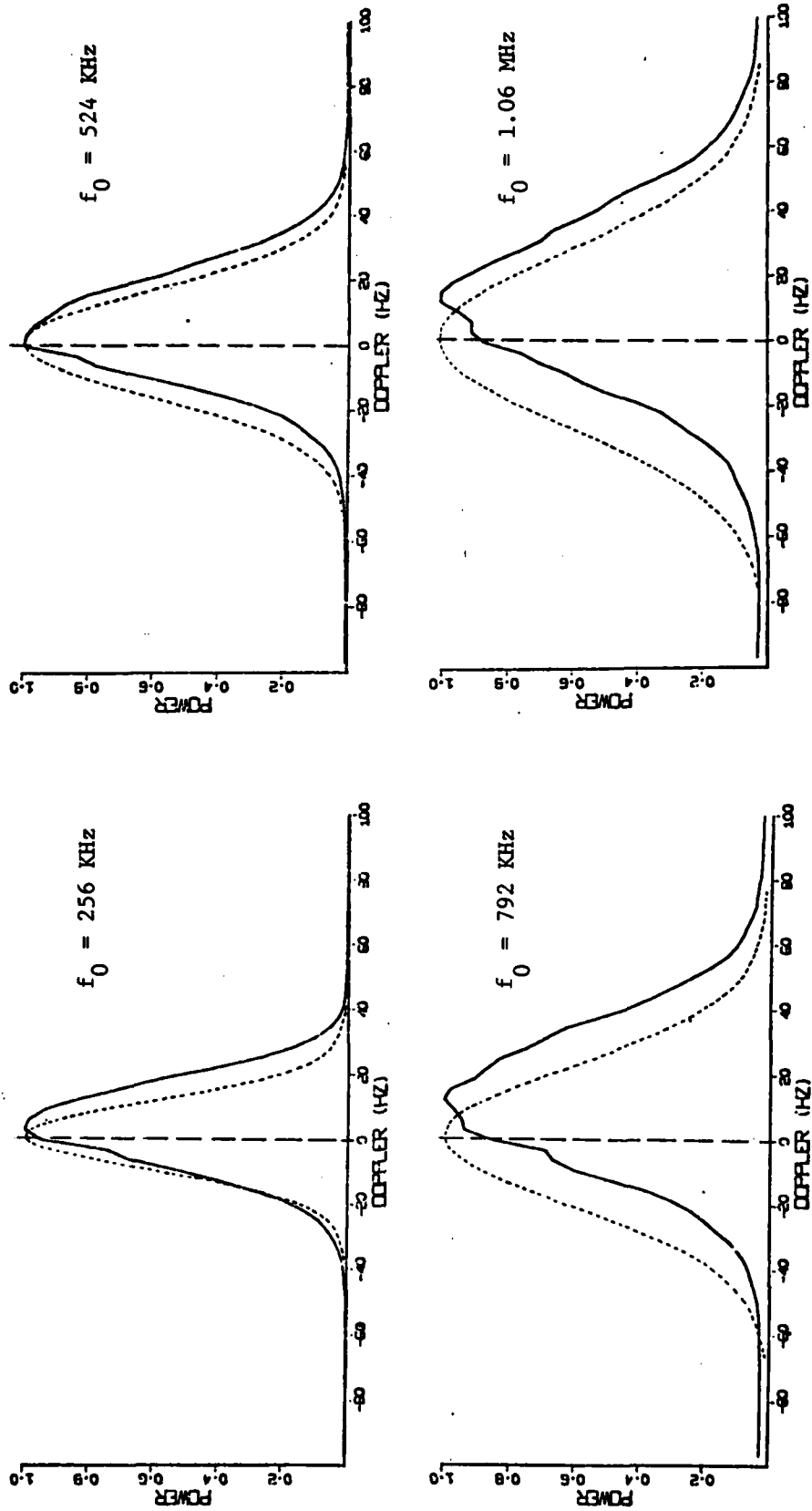


Figure 5.1 Power spectrum - upwind, $\psi_0 = 30^\circ$; Solid curve - experimentally measured spectrum at wind speeds of 8.3 m/sec, $r_{00} = r_{10} = 100$ cm. Dashed curve - theoretically computed spectrum, parameters used, $\sigma_0^2 = 0.2$ cm, $\lambda_y = 7$ cm, $\rho = 0.9$ cm, $C_p = 40$ cm/sec, $T_0 = 0.1$ sec, $\Lambda_2 = 7$ cm.

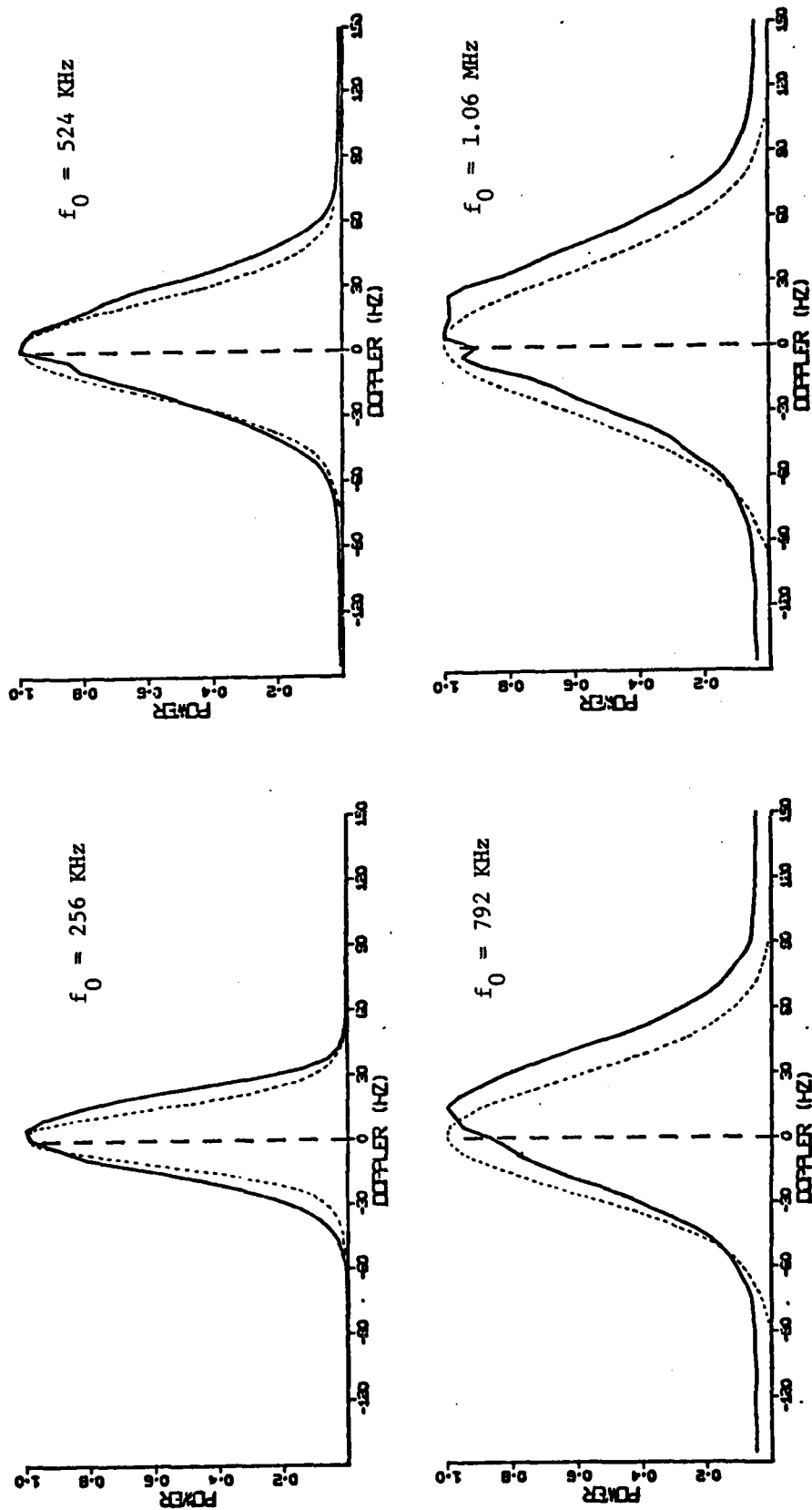


Figure 5.2 Power spectrum - Crosswind, $\psi_0 = 30^\circ$; same as in Figure 5.1.

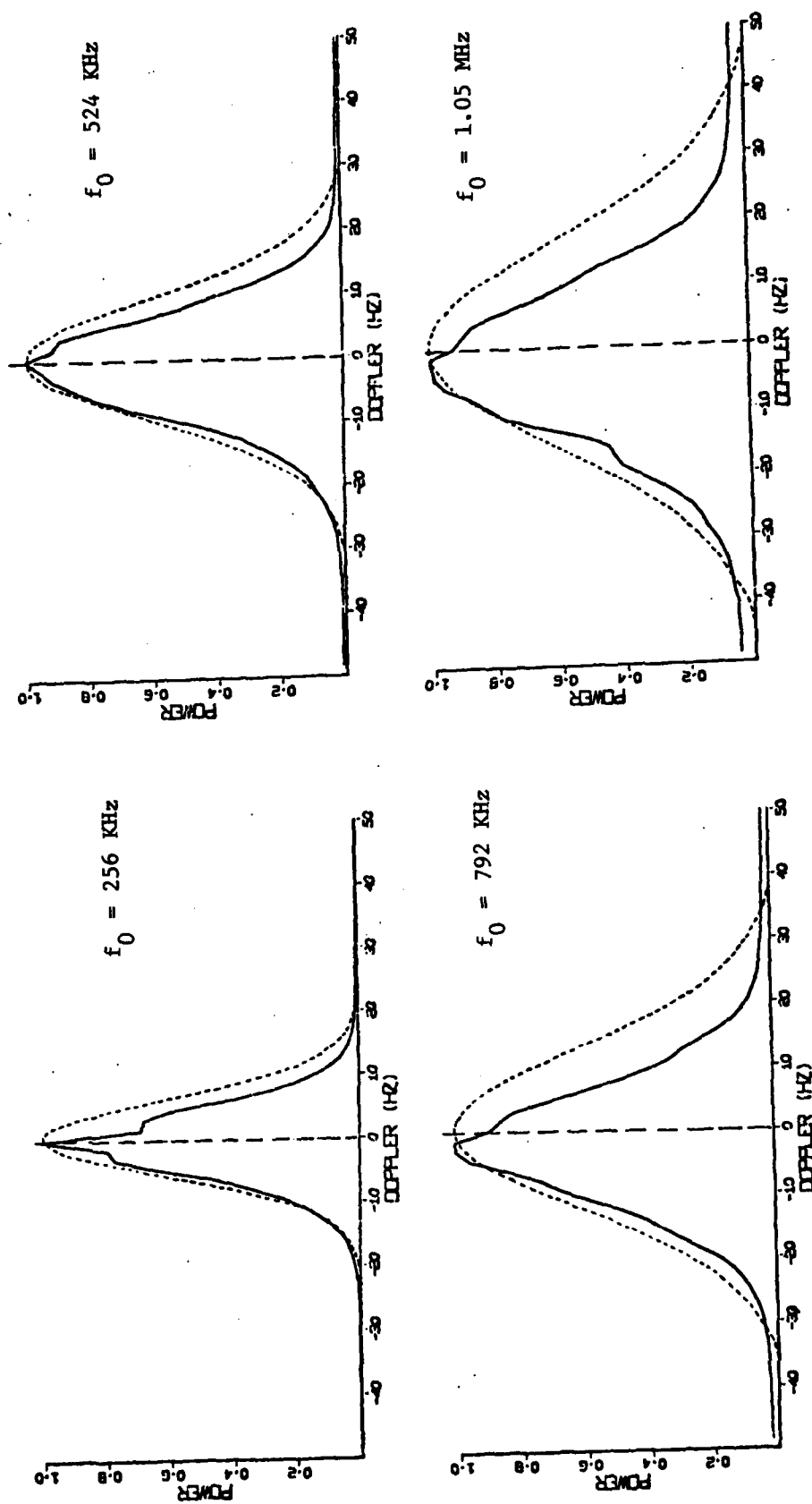


Figure 5.3 Power spectrum - upwind, $\psi_0 = 17^\circ$; same as in Figure 5.1, except
 $r_{00} = r_{10} = 173$ cm.

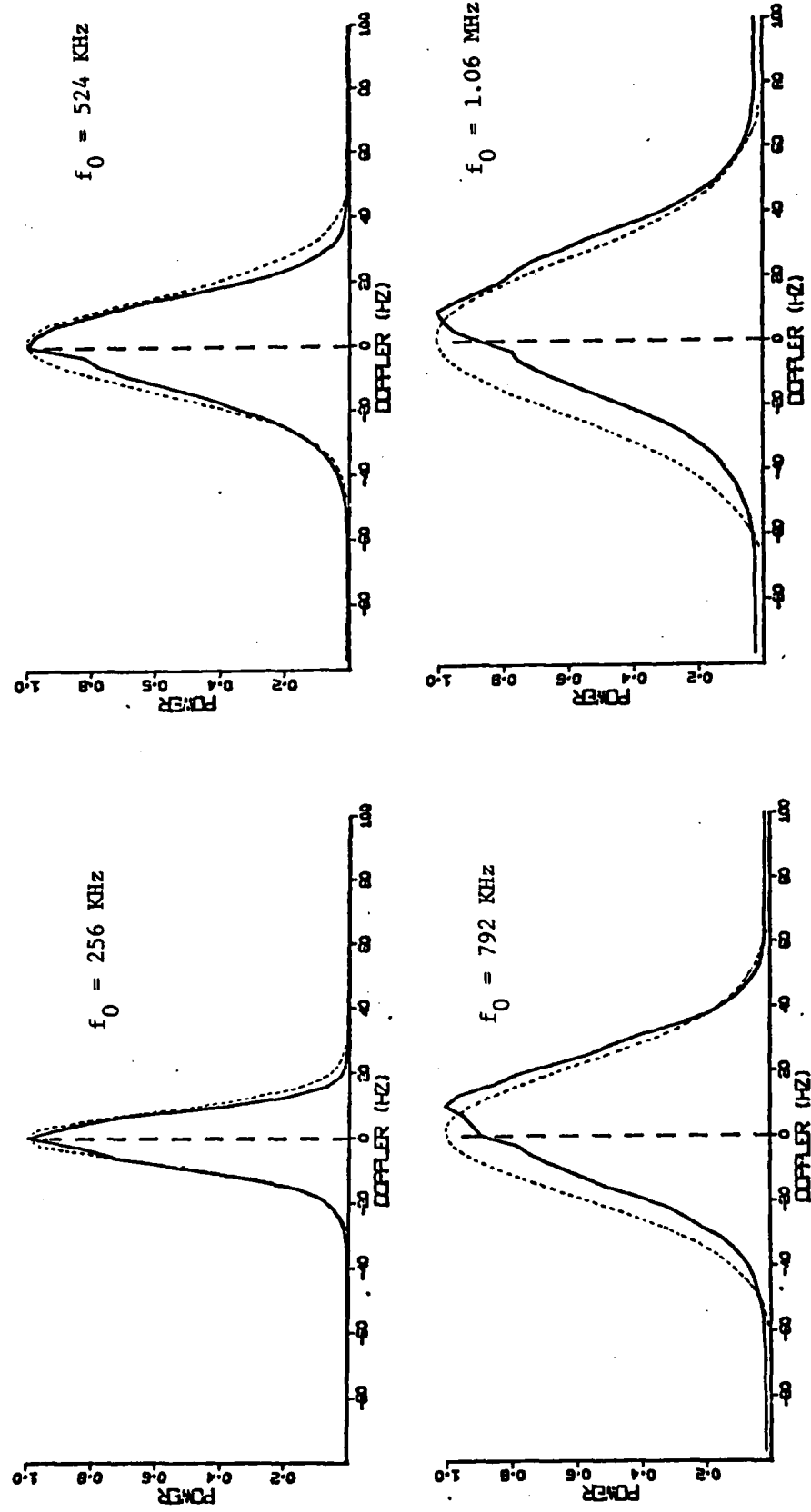


Figure 5.4 Power spectrum - Crosswind, $\psi_0 = 17^\circ$; same as in Figure 5.3.

follows from equations (4.3.7) and (4.3.13). The term that causes asymmetry is the c_3 term, and its coefficient is inversely proportional to acoustic frequency ω_0 . However, the discrepancy between theory and experiment is most significant at high acoustic frequencies. It appears in all of these figures that there is a doppler shift in addition to the theoretically predicted side-band asymmetry.

A possible explanation for this doppler shift can be found in small azimuthal misalignments of the transducers used in the experiment. Even though the transducer mountings were carefully positioned to be exactly opposite each other with respect to the specular point, the possibility remains that small imperfections in the transducers themselves could cause the center lines of their beam patterns to be a few degrees off the boresight direction. Such a divergence is, in fact, indicated in [53].

To test this conjecture several experiments were performed. The results of these experiments are shown in Figures 5.5 to 5.7. Figure 5.6 was obtained from a crosswind geometry with $\phi_T = 270^\circ$ and $\phi_R = 90^\circ$, while Figure 5.5 ($\phi_T = 270^\circ$, $\phi_R = 85^\circ$) and Figure 5.7 ($\phi_T = 270^\circ$, $\phi_R = 95^\circ$) were obtained in a roughly crosswind geometry but with receiver being intentionally misaligned by 5° . The top view of the relative source and receiver positions in these experiments is shown in Figure 5.8. In this figure, the source-receiver pairs for Figures 5.5, 5.6 and 5.7 are respectively (S, R_1) , (S, R_2) and (S, R_3) . Since in Figure 5.6, the source-receiver pair (S, R_2) was supposedly exactly crosswind, we would expect a roughly symmetrical spectrum for high acoustic frequency. However, we find that the most symmetrical spectrum among these figures

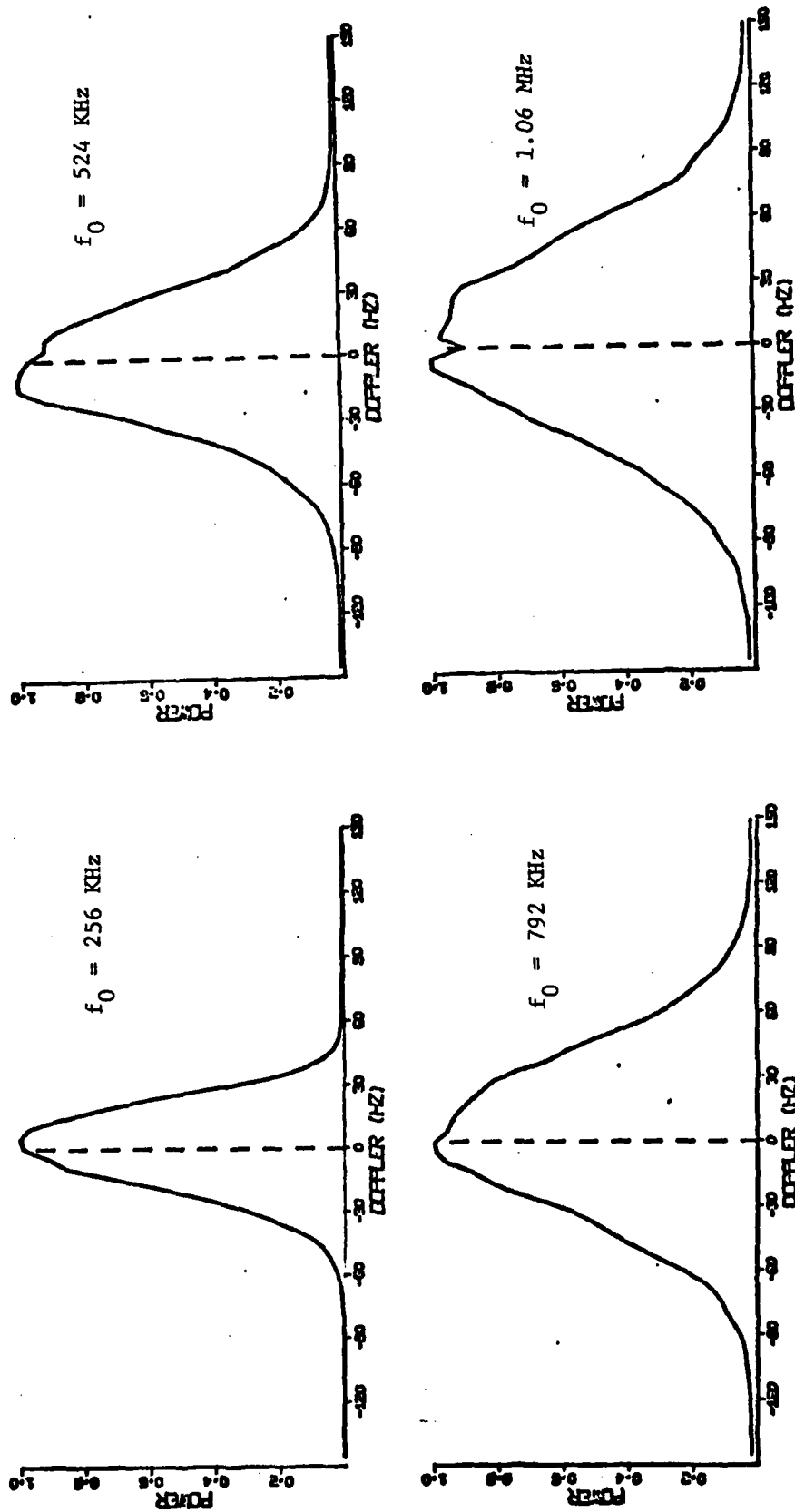


Figure 5.5 Power spectrum - experimentally measured at $\phi_T = 270^\circ$, $\phi_R = 85^\circ$, and $r_{00} = r_{10} = 252 \text{ cm}$.

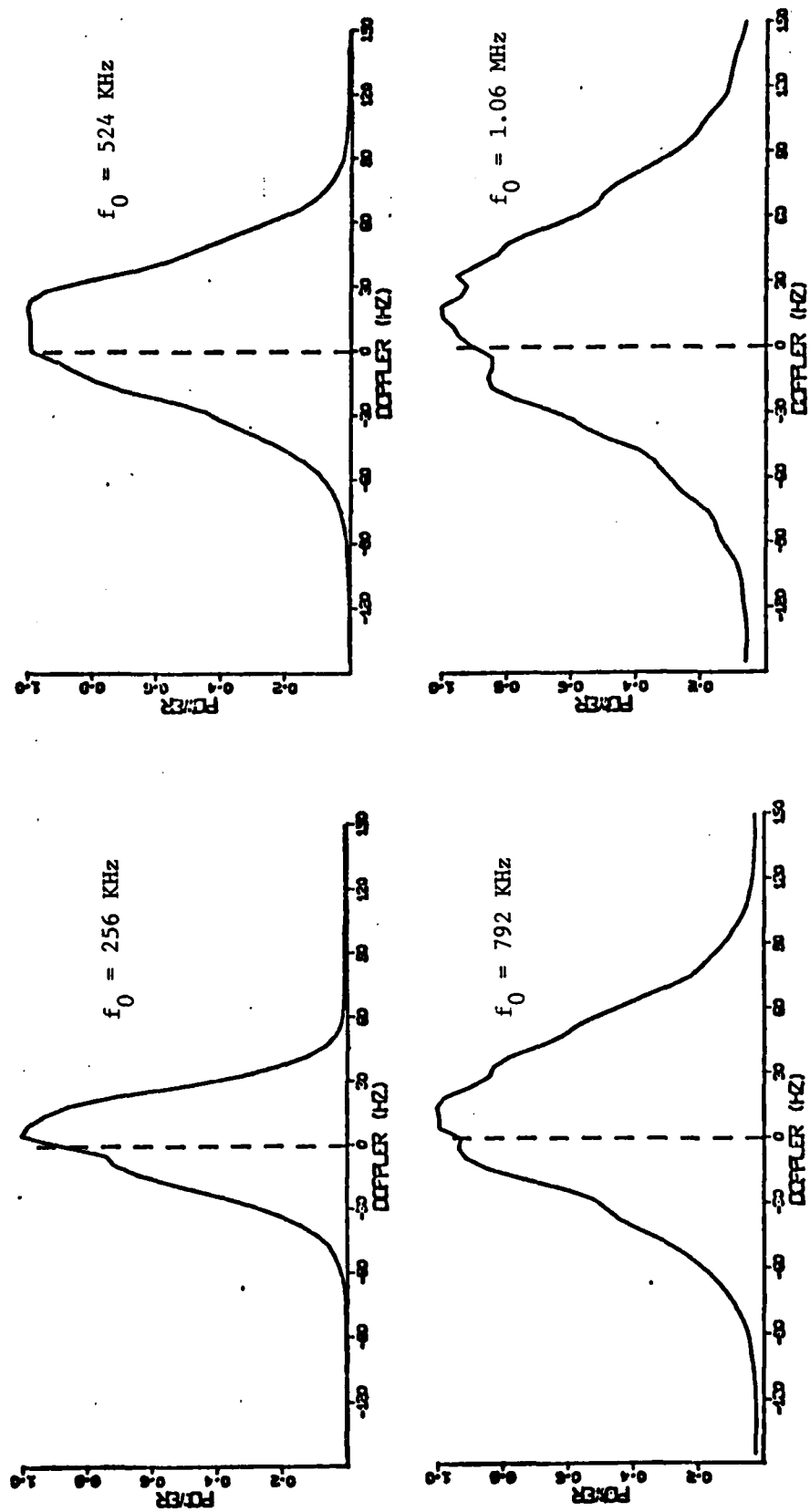


Figure 5.6 Power spectrum - experimentally measured at $\phi_T = 270^\circ$, $\phi_R = 90^\circ$, and $r_{00} = r_{10} = 252 \text{ cm}$.

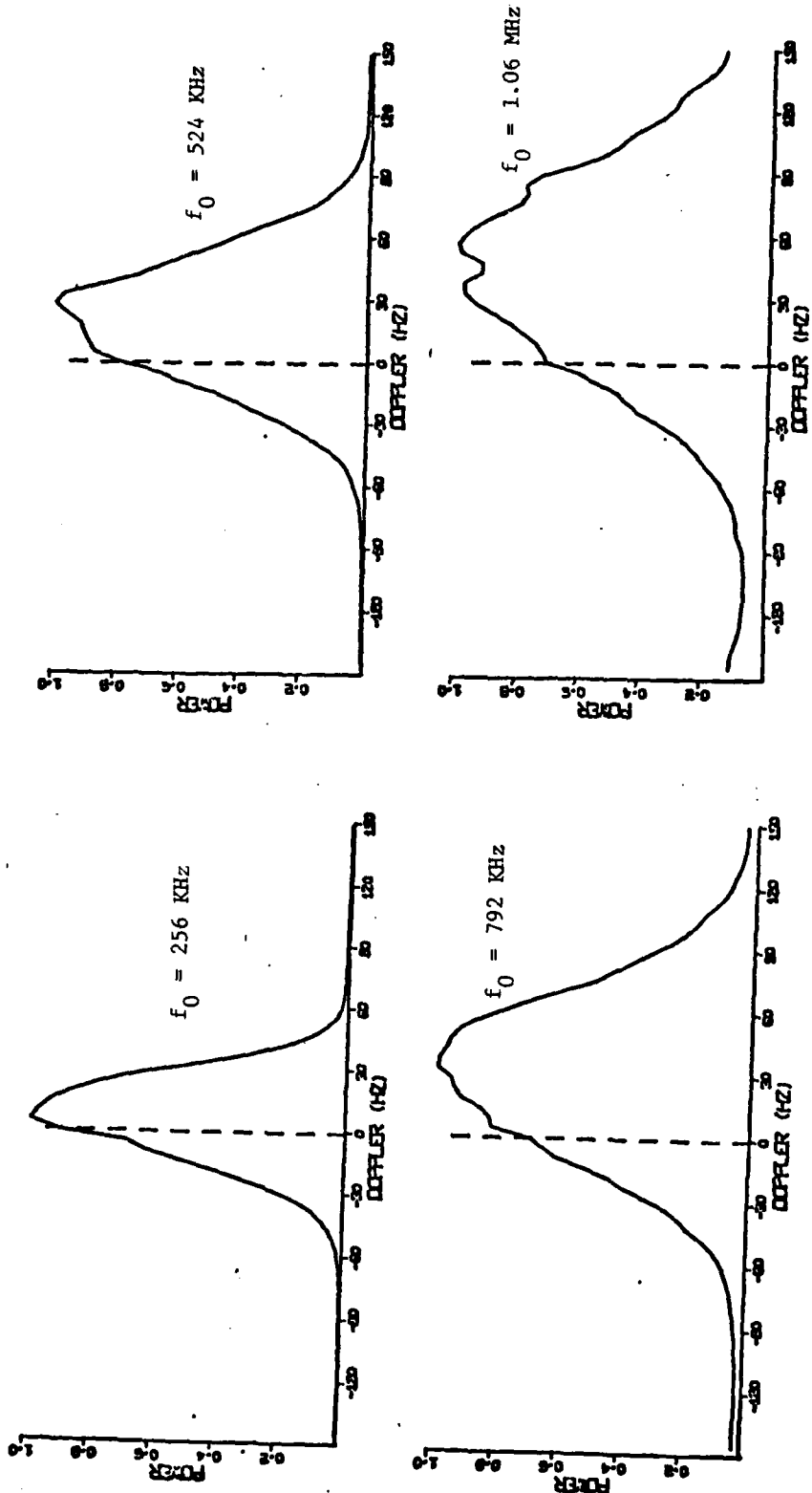


Figure 5.7 Power spectrum - experimentally measured at $\phi_T = 270^\circ$, $\phi_R = 95^\circ$, and $r_{00} = r_{10} = 252 \text{ cm}$.

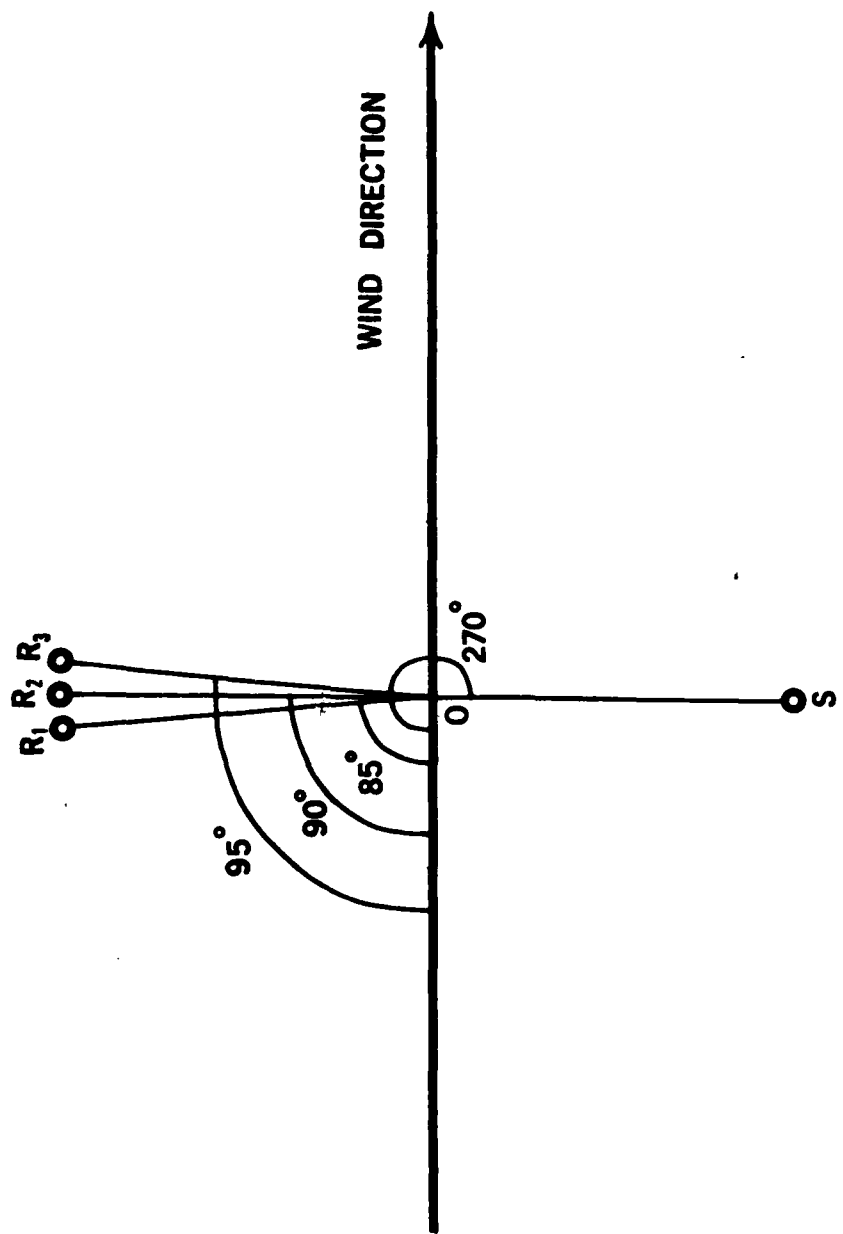


Figure 5.8 Source-receiver geometry for experimental results shown in Fig. 5.5-5.7.

is contained in Figure 5.5, i.e. for the source-receiver pair (S, R_1). In Figure 5.6, we see a fair amount of frequency shift, approximately 12 Hz., in the plot for $f_0 = 1.06$ MHz. There is an even larger frequency shift in Figure 5.7 almost 45 Hz toward the positive side in the plot for $f_0 = 1.06$ MHz.

If we assume that the center lines of the source and receiver beam patterns diverge from their respective bore-sight direction by 2.5° , then it is conceivable that the intentional misalignment in Figure 5.5 could result in a roughly crosswind geometry, with the specular point at $0'$ as shown in Figure 5.9. The other two geometries would then represent angled paths, with both source and receiver pointed slightly upwind. Since both beam patterns would then be larger in the upwind direction than in the downwind direction, we would expect more energy returned with upshifted frequency. The frequency displacement should be larger for the receiver at R_3 than for the one at R_2 . This is exactly what is observed in Figures 5.5 to 5.7

5.2 Theoretical Analysis of Angled Paths

A theoretical treatment of surface scatter over a slightly angled path is easily obtained by modifying the beam pattern function used in the theory. Assume that the center of the beam pattern function on the water surface is off the specular point by a distance Δ_x in the x direction and Δ_y in the y direction. Then the form of the modified beam function can be derived from equation (2.3.13):

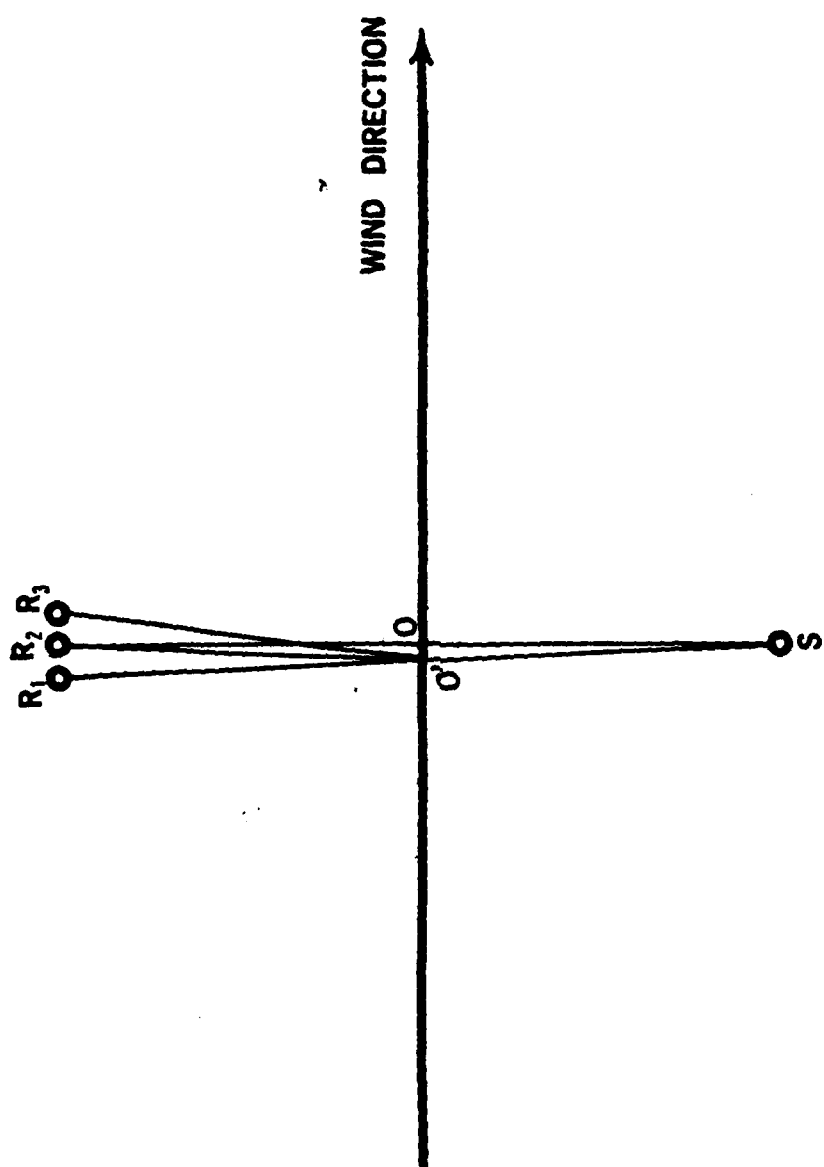


Figure 5.9 Off-specular source-receiver geometry

$$B_S B_R \approx \exp \left\{ - \frac{(x-\Delta_x)^2}{L_{xx}^2(\omega_0)} - \frac{(y-\Delta_y)^2}{L_{yy}^2(\omega_0)} - \frac{2(x-\Delta_x)(y-\Delta_y)}{L_{xy}^2(\omega_0)} \right\} \quad (5.2.1)$$

where $L_{xx}(\omega_0)$, $L_{yy}(\omega_0)$ and $L_{xy}(\omega_0)$ are defined in equation (2.3.14).

Rearranging the terms in the brackets results in

$$B_S B_R \approx \exp \left\{ - \frac{x^2}{L_{xx}^2(\omega_0)} - \frac{y^2}{L_{yy}^2(\omega_0)} - \frac{2xy}{L_{xy}^2(\omega_0)} + \left[\frac{2\Delta_x}{L_{xx}^2(\omega_0)} + \frac{2\Delta_y}{L_{xy}^2(\omega_0)} \right] x \right.$$

$$\left. + \left[\frac{2\Delta_y}{L_{yy}^2(\omega_0)} + \frac{2\Delta_x}{L_{xy}^2(\omega_0)} \right] y - \frac{\Delta_x^2}{L_{xx}^2(\omega_0)} - \frac{\Delta_y^2}{L_{yy}^2(\omega_0)} - \frac{2\Delta_x\Delta_y}{L_{xy}^2(\omega_0)} \right\}$$

(5.2.2)

The first three terms inside the brackets represent the original beam function. The last three terms represent an additional attenuation of the received acoustic power due to the off-specular beam function. They don't have any effect on the sideband asymmetry or the doppler shift and therefore can be neglected. The two remaining terms represent the significant modifications of the theory. Substitution of the new beam pattern function of equation (5.2.2) in equation (F-9) affects mainly the coefficients D and E. If we represent the new values as D_1 and E_1 , then we have

$$D_1 = D - \frac{2\Delta_x}{L_{xx}^2(\omega_0)} - \frac{2\Delta_y}{L_{xy}^2(\omega_0)} \quad (5.2.3)$$

$$E_1 = E - \frac{2\Delta_y}{L_{yy}^2(\omega_0)} - \frac{2\Delta_x}{L_{xy}^2(\omega_0)} \quad (5.2.4)$$

The shift of the center of the Gaussian spectrum was defined as $q_2(0)$ in equation (4.3.3a). The parameter d appearing in this equation is defined in equation (H-13) and is seen to depend on E in equation (H-22). If we use E_1 instead of E in this definition, $q_2(0)$ can be rewritten as follows:

$$q_2(0) = K_3 E_1 = K_3 \left(E - \frac{2\Delta_y}{L_{yy}^2(\omega_0)} - \frac{2\Delta_x}{L_{xy}^2(\omega_0)} \right)$$

$$= K_3 E + 2\pi f_M \quad (5.2.5)$$

where

$$K_3 = \frac{\frac{1}{2} \rho^2 C_p}{\frac{|N|^2}{g^2(N+N^*)} + \frac{1}{\Lambda_y^2} + \frac{\rho^2}{2}} \cdot \begin{vmatrix} B^*-B \\ B^*+B \end{vmatrix} \quad (5.2.6a)$$

$$f_M = -\frac{K_3}{\pi} \left(\frac{\Delta_y}{L_{yy}^2(\omega_0)} + \frac{\Delta_x}{L_{xy}^2(\omega_0)} \right) \quad (5.2.6b)$$

We see that f_M is the additional doppler shift (in Hz) introduced by the misalignment. As we assumed in the previous section, the center of the beam pattern function is at $0'$ as in Figure 5.9. Thus the beam center displacements are $\Delta_x = 0$ and $\Delta_y = -|\underline{00}'|$, where $|\underline{00}'|$ indicates the distance between 0 and $0'$. Hence the frequency displacement $f_M = \frac{K_3}{\pi L_{yy}^2(\omega_0)} |\underline{00}'|$ is a positive quantity, i.e. the Gaussian spectrum is displaced toward positive frequencies. This is what was observed in Figures 5.5 to 5.7. In fact, the frequency displacements shown in all experiments shown in Figures 5.1 to 5.4 can be explained in this way.

The dependence of f_M on the acoustic frequency f_0 can be computed by using equations (2.3.14) and (5.2.6a) in equation (5.2.6b). An expression for B , to be used in equation (5.2.6a) can be found in Appendix F, equation (F-10). When this is done we find that

$$f_M = \frac{\frac{g^2 \rho^2 C_p}{|N|^2} + \frac{g^2}{\Lambda_y^2} + \frac{\rho^2 g^2}{2}}{\frac{|N|^2}{N+N^*}} \cdot \frac{\omega_0}{c} \cdot h(r_{00}, r_{10}, \psi_T, \psi_R, \phi_T, \phi_R) \quad (5.2.7)$$

where $h(r_{00}, r_{10}, \psi_T, \psi_R, \phi_T, \phi_R)$ is a function of geometric parameters only. We show in equation (H-20) that for downwind for crosswind the term $|N|^2/(N+N^*)$ can be approximated by $\frac{\omega_0^2 L^2(\omega_0)}{2c^2 R^2}$ if the beam pattern illuminates several Fresnel zones. Since the beam pattern width is proportional to $1/\omega_0$, $\omega_0^2 L^2(\omega_0)$ is independent of frequency, and therefore $|N|^2/(N+N^*)$ is a constant. On the other hand, g^2 is proportional to ω_0^2 . For frequencies high enough to make $|N|^2/(N+N^*)$ negligible in the denominator of equation (5.2.7), f_M is proportional to ω_0 . Figure 5.10 contains a plot of the measured frequency displacements for the experimental results shown in Figure 5.5 to 5.7. The linear dependence between f_M and f_0 is clearly shown.

Figures 5.11 to 5.14 show the same experimental spectra as those shown in Figures 5.1 to 5.4 and a set of theoretical spectra shifted by values of f_M chosen to provide the best possible match with f_M constrained to be linearly dependent on f_0 . These values are shown in each figure. It is seen that the correspondence between the theoretical and experimental results is very good.

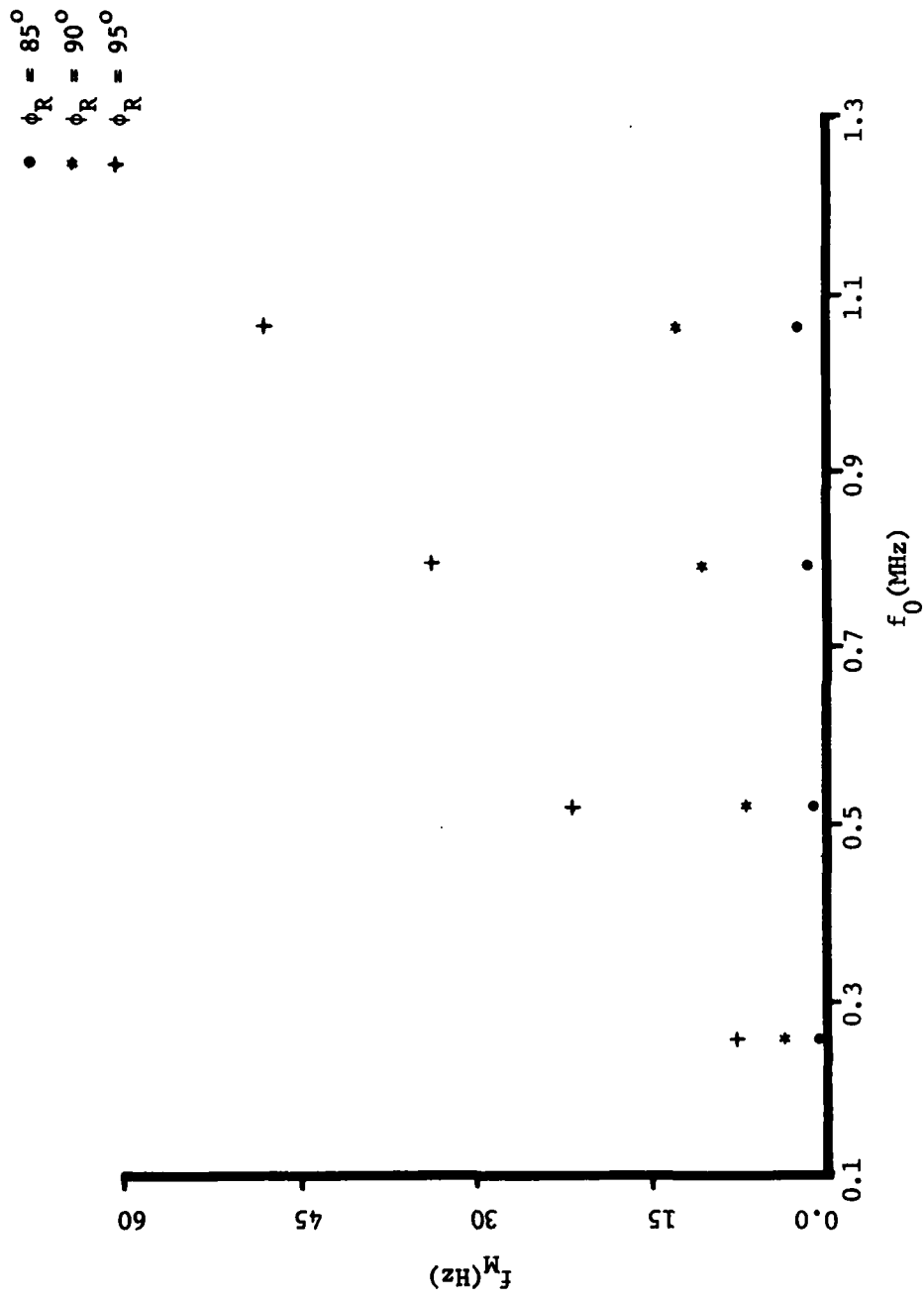


Figure 5.10 Frequency displacements for spectra shown in Figures 5.5 to 5.7.

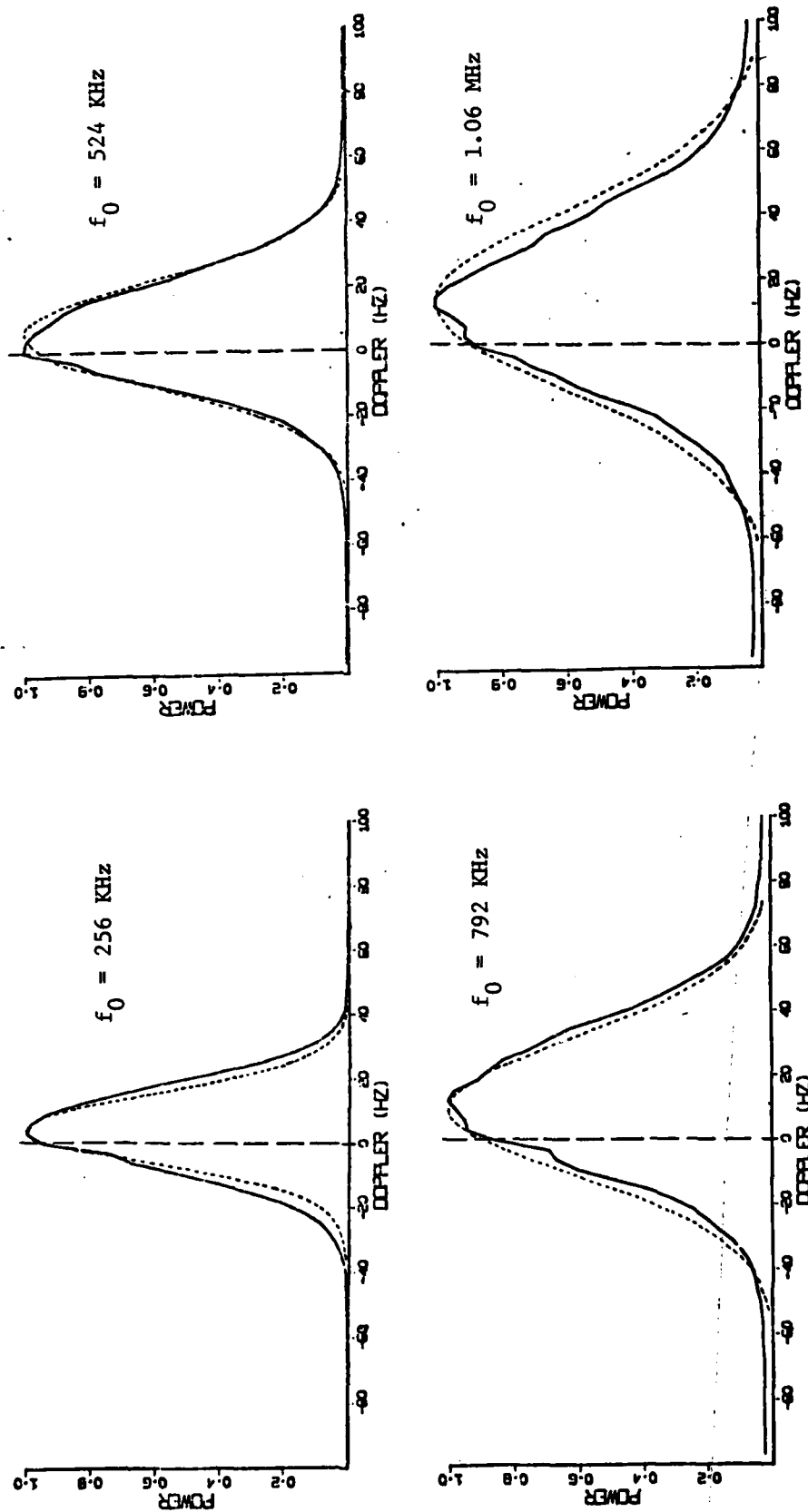


Figure 5.11 Shifted power spectrum of Figure 5.1. The frequency displacements for $f_0 = 256$ kHz, 524 kHz, 792 kHz, and 1.06 MHz are respectively 3 Hz, 6.1 Hz, 9.1 Hz, and 12 Hz.

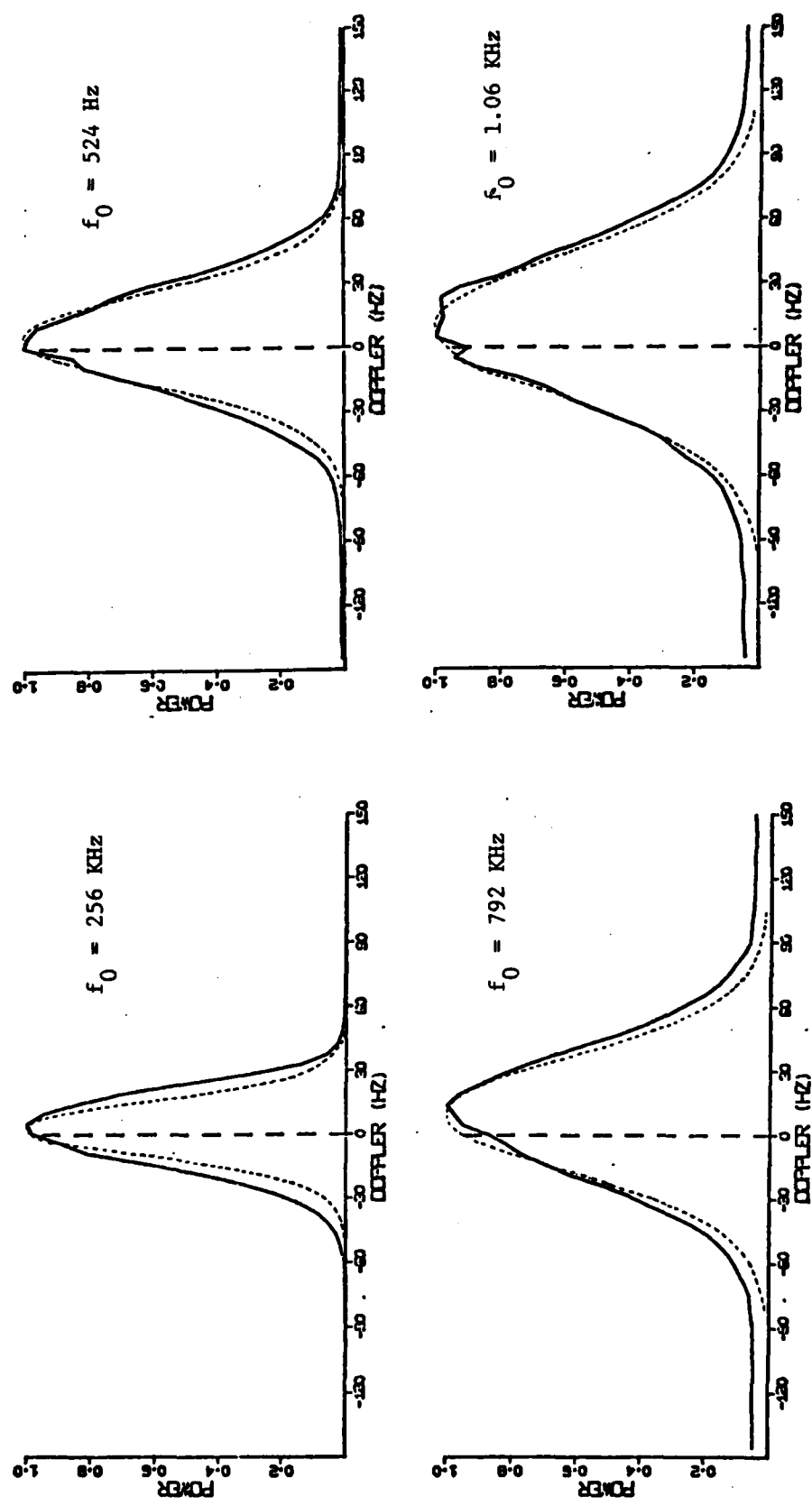


Figure 5.12 Shifted power spectrum of Figure 5.2. The frequency displacements for $f_0 = 256$ kHz, 524 kHz, 792 kHz, and 1.06 MHz are respectively 2 Hz, 4 Hz, 6 Hz, and 8 Hz.

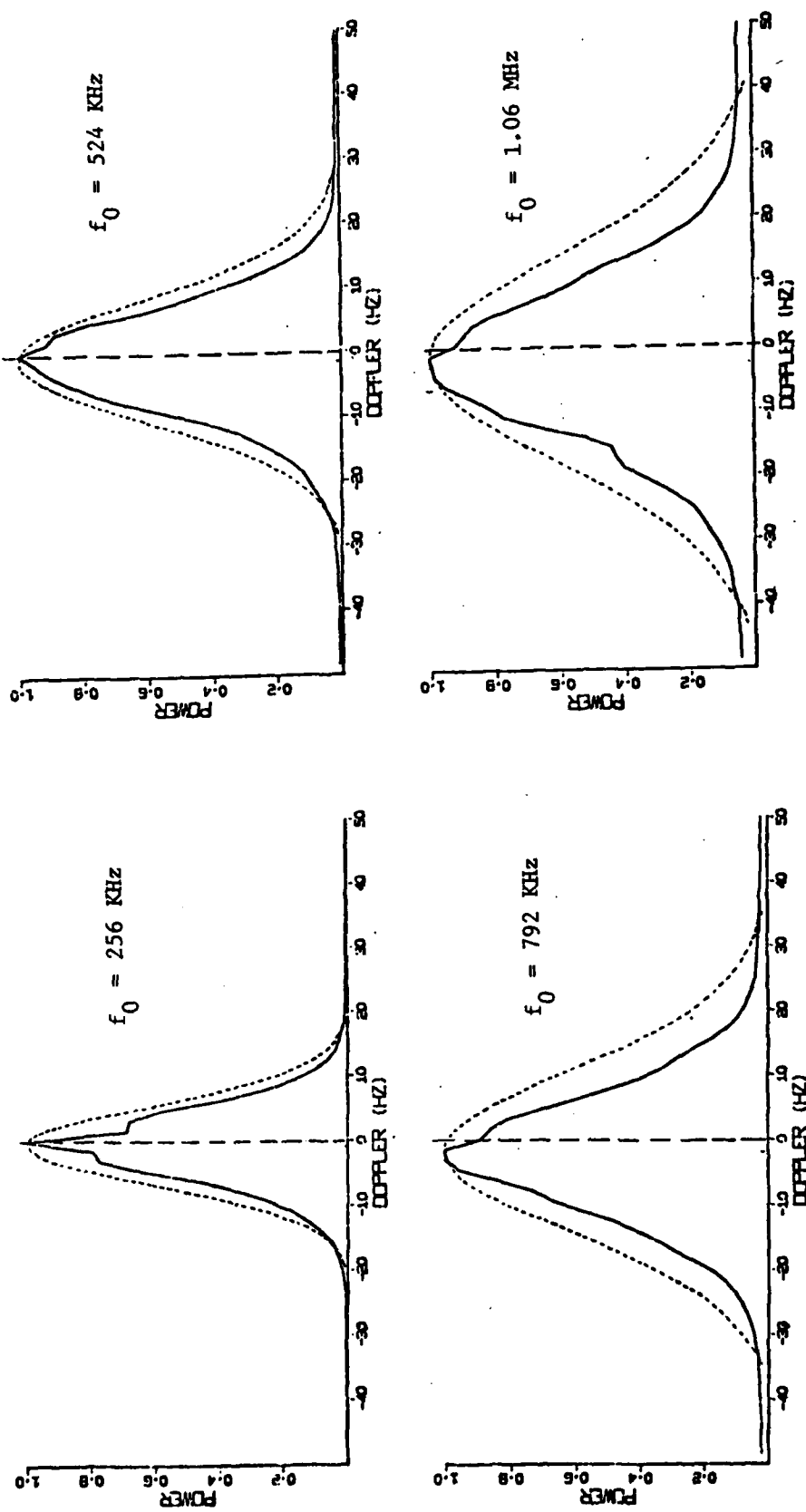


Figure 5.13 Shifted power spectrum of Figure 5.3. The frequency displacements for $f_0 = 256$ kHz, 524 kHz, 792 kHz and 1.06 kHz are respectively -0.7 Hz, -1.43 Hz, -2. Hz, and -2.7 Hz.

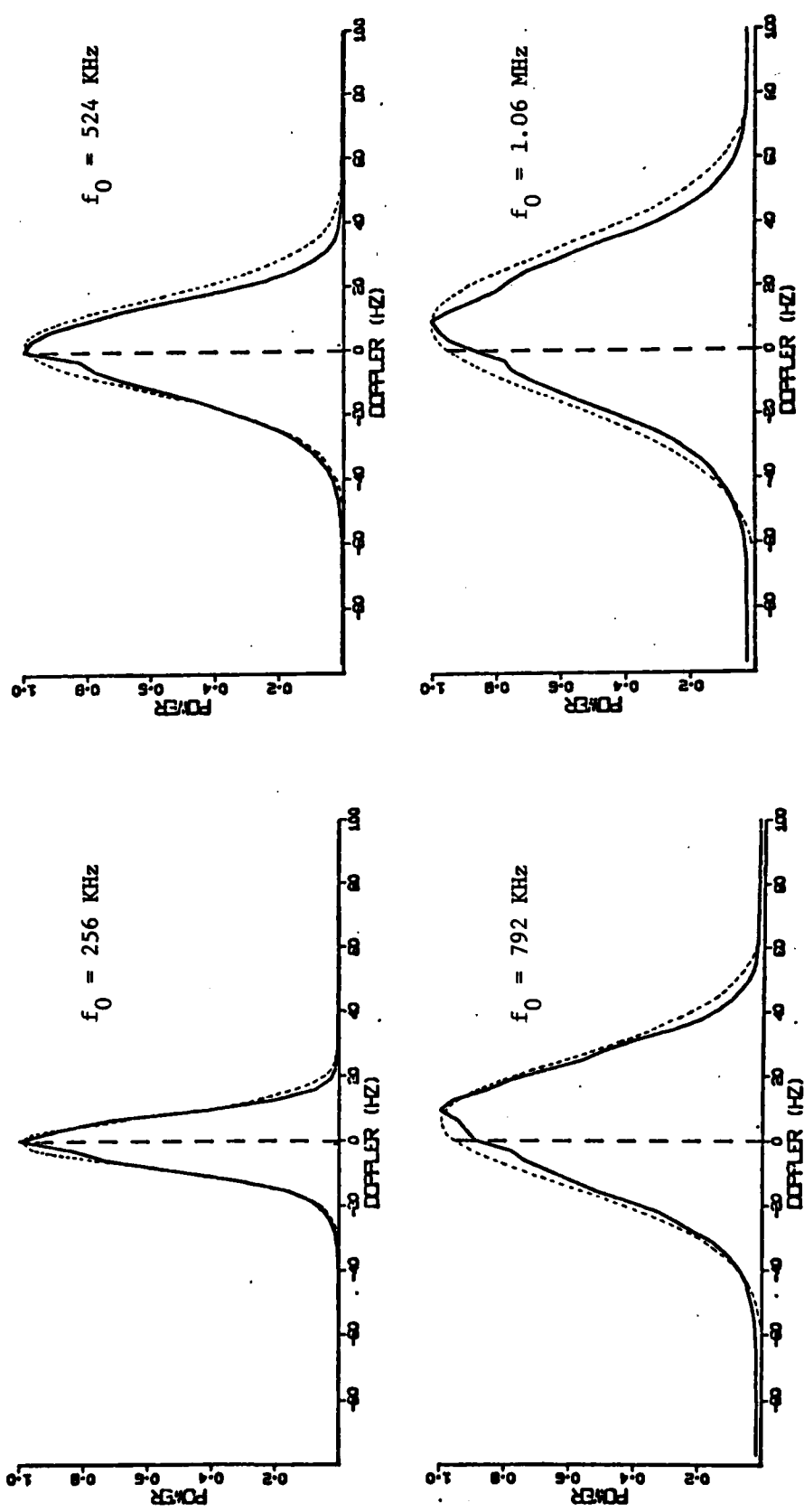


Figure 5.14 Shifted power spectrum of Figure 5.4. The frequency displacements for $f_0 = 256$ kHz, 524 kHz, 792 kHz, and 1.06 MHz are respectively 1.8 Hz, 3.6 Hz, 5.4 Hz, and 7.2 Hz.

5.3 Bandwidth

According to equations (4.3.10) and (4.3.14), the bandwidth should increase with acoustic frequency f_0 , with grazing angle ψ_0 , with surface roughness, and with size of beam pattern. The increase in bandwidth with f_0 appears in all of the figures; the effect of grazing angle increase can be seen in a comparison of Figures 5.11 and 5.13, also in Figures 5.12 and 5.14; the effect of beam pattern increases between Figure 5.12 (small band width) and Figure 5.6 (large beam width) is caused by increasing r_{00} and r_{10} . An additional qualitative check of the theory is in the bandwidth comparison between upwind and crosswind; the theory predicts a larger bandwidth for crosswind and this is corroborated, for instance, in a comparison between Figures 5.11 and 5.12. The qualitative correspondence between theory and experiment is seen to be perfect in these examples. Quantitatively the correspondence between theory and experiment is generally good for not too shallow grazing angles. The less satisfactory bandwidth comparison in Figure 5.13 may be caused by the effect of shadowing as we have already indicated in Chapter IV, Figures 4.14.

In summary, we have shown that the Kirchhoff theory appears to give quite accurate predictions of the frequency spreading function for all surface roughness conditions. We have found that experimental verification of the theory requires very accurate alignment of the transducers, because even small misalignments which might be caused by transducer imperfections can result in significant spectral shifts. However, when all of these factors are taken into account the correspondence between theory and experiment is seen to be very good.

Chapter VI Physical Arguments for the Creation of Asymmetric Sidebands

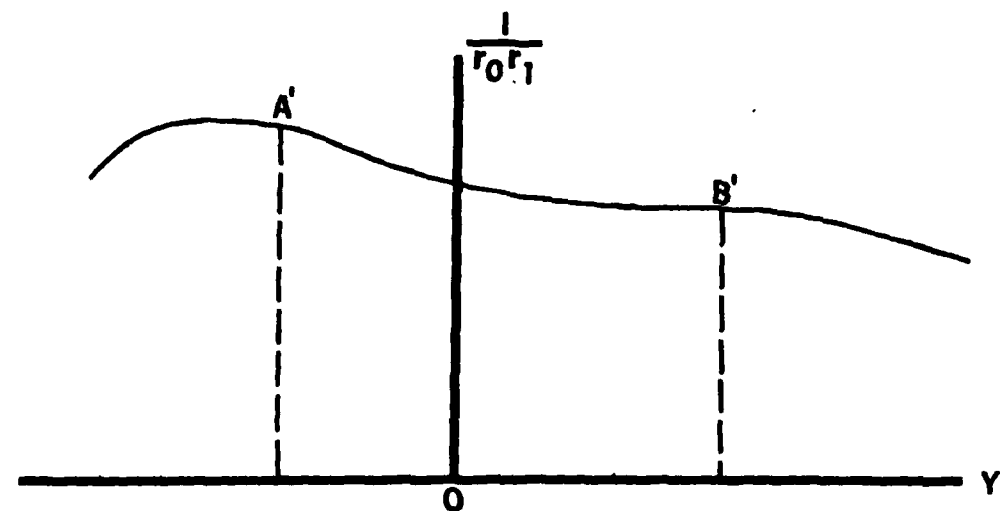
6.0 Introduction

In the previous two chapters we have used the Kirchhoff integral method in a rather formal way to compute the spectral properties of surface-scattered signal. We now consider some physical arguments that provide a more heuristic explanation for some of the results obtained previously. We consider in particular the two mechanisms that have been shown to be responsible for the spectral asymmetry of the scattered signal.

6.1 Effect of Source-Receiver Geometry

Asymmetry of the scattering geometry, i.e. where the source and receiver are at different depths, has been shown to result in a spectral asymmetry if the source and receiver are in an up or downwind configuration. This asymmetry has a simple physical explanation which is illustrated in Figure 6.1, with the source located at a shallower depth than the receiver. The water waves are assumed to move from source to receiver. For this configuration we found earlier that the upper doppler sidebands have a larger amplitude than the lower ones.

Assume that the acoustic wave frequency is high enough so that the reflecting surface can be represented by a tangential plane at that reflecting point. The planes at point A and B in Figure 6.1 represent two of such surface tangential planes, where the reflections from these planes will reach the receiver. Point A represents an arbitrary point on the -Y axis and point B represents the point on the +Y axis. Since



WIND DIRECTION

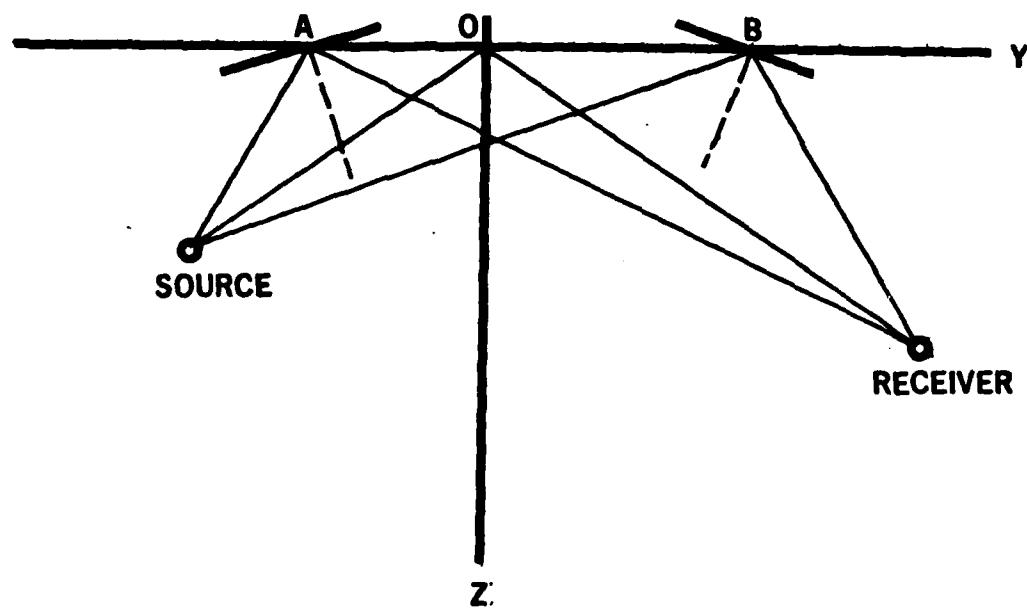
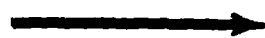


Figure 6.1 Asymmetric downwind scatter geometry and attenuation factor.

the surface wave is moving from source to receiver, the surface plane at point A moves downward and compresses the incoming acoustic wave and therefore produces an up-shifted doppler frequency component in the received signal spectrum. On the other hand, the surface plane at point B moves upward and relaxes the acoustic wave and produces the down doppler shift. If the points A and B are chosen to produce equal doppler shifts, the upper (from point A) and the lower (from point B) doppler sideband amplitudes can be obtained by the intensities of these ray paths. From Huygen's principle, each illuminated surface point becomes the source of new wave front, the attenuation factor for each reflected ray is $(r_0 r_1)^{-1}$. A plot of $(r_0 r_1)^{-1}$ for all the points on the y axis is shown above the scatter geometry in Figure 6.1. For a reflection at the specular point 0, the attenuation factor is $(r_{00} r_{10})^{-1}$. The attenuation factors for points A and B can be found from the corresponding points labelled A' and B' on the $(r_0 r_1)^{-1}$ curve. We see that the magnitude of $(r_0 r_1)^{-1}$ at point A' is larger than that at point B', therefore the upper sideband is larger than the lower sideband. This conclusion is the same as that reached in the earlier chapters.

The same mechanism operates in the Kirchhoff integral which we used to develop the mathematical solutions. The original form of the Kirchhoff integral is given in equation (2.1.6), repeated here for convenience

$$H(\omega_0, t) = \frac{1}{4\pi} \int_S \frac{\partial}{\partial \underline{n}} \{ B_S B_R \frac{e^{j \frac{\omega_0}{c} (r_0 + r_1)}}{r_0 r_1} \} \cdot d\underline{S} \quad (6.1.1)$$

Observe that the attenuation factor is explicitly included. The integral of equation (6.1.1) can be read as the sum of all ray components

reflected from surface S. Each component is a normal derivative of a quantity which has amplitude $(r_0 r_1)^{-1}$ and phase angle $\frac{\omega_0}{c} (r_0 + r_1)$.

If the direction of the surface wave velocity is reversed, the plane at point B will then move downward and compress the acoustic wave. The plane at point A will relax the acoustic wave instead of compressing it. In other words, the role of plane A and B are switched and so are the upper and the lower sidebands. Therefore, the direction of the asymmetry is reversed.

A crosswind geometry is shown in Figure 6.2. On the Y axis, two surface tangential planes, which give the same amount of frequency shift at the receiver, are shown at points A and B. The attenuation factor $(r_0 r_1)^{-1}$ is plotted on top of the scatter geometry. It is observed that A and B are symmetric and the attenuation factors at these two points are identical. In fact, the plot of $(r_0 r_1)^{-1}$ is symmetric with respect to the specular point O. Hence there should be no sideband asymmetries in the crosswind configuration if only the scatter geometry is considered.

As indicated in the previous chapters, the upper and lower sidebands are symmetrical if $r_{00} = r_{10}$ or if the grazing angle is equal to 90° . This result is obvious since $(r_0 r_1)^{-1}$ shows a symmetric distribution under these conditions.

The reason why spectral asymmetry has usually not been observed in scattering computations using the Kirchhoff integral is that the specular-point expansion used by Eckart [31] and by others [36], etc. replaces the factor $(r_0 r_1)^{-1}$ by a constant $(r_{00} r_{10})^{-1}$ for the sake of mathematical convenience. This approximation clearly removes the asymmetry contributed by the geometric factor.

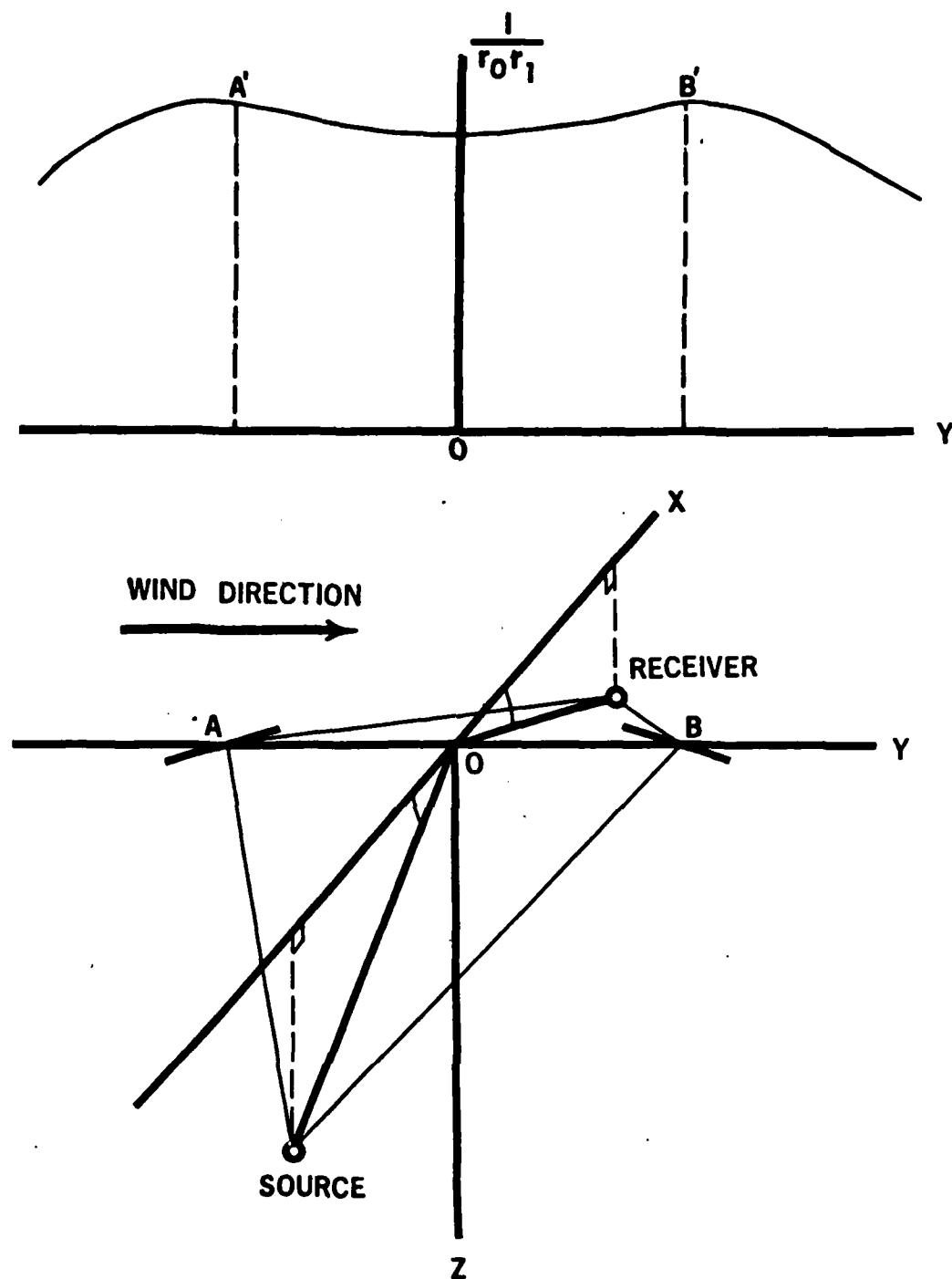


Figure 6.2 Asymmetric crosswind scatter geometry and attenuation factor.

6.2 Effect of the Surface Slope Distribution

In the discussions of Chapters III and IV, we found that slope asymmetry of the surface waves results in asymmetry in the received spectrum. To show only the effect of slopes, we assume a symmetrical scattering geometry by letting $r_{00} = r_{10}$ in an up (down) wind configuration shown in Figure 6.3. The upper plot shows an assumed asymmetric distribution of surface slopes for a wind driven surface. In the lower plot the tangential planes at A and B are indicated as in the previous two figures. The arrow shows the direction of the wind and of the surface wave motion. The slope distributions corresponding to the two surface points A and B are A' and B', respectively. It is seen the slope distribution at point A' is larger than that at point B'. Hence there are more positive slopes and fewer negative slopes on the surface and we would expect more energy in the upper sideband (reflected from positive slopes) than the lower sideband (reflected from the negative slopes).

For the same geometry, if the wind direction is reversed, the slopes at point B will compress the acoustic wave but it also will have a higher slopes distribution. Therefore, reversing wind directions only exchanges the roles of points A and B, and has no effect on the direction of the spectral asymmetry.

The same result can be obtained for the crosswind geometry, which is shown in Figure 6.4. The reflection from surface plane A constitutes the upper sideband and has more energy in this band.

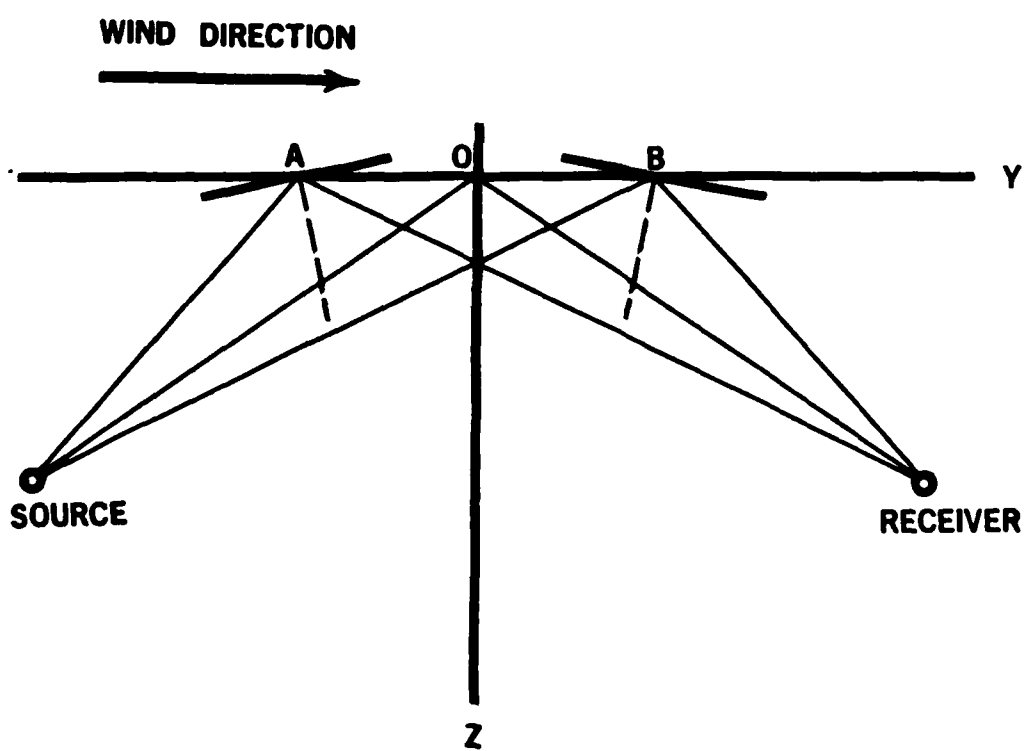
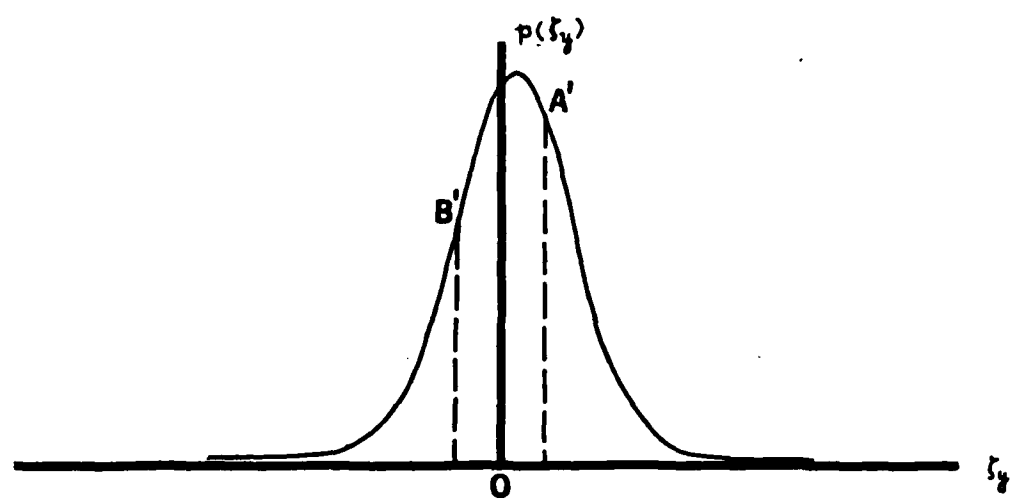


Figure 6.3 Symmetric downwind scatter geometry and surface slope distribution.

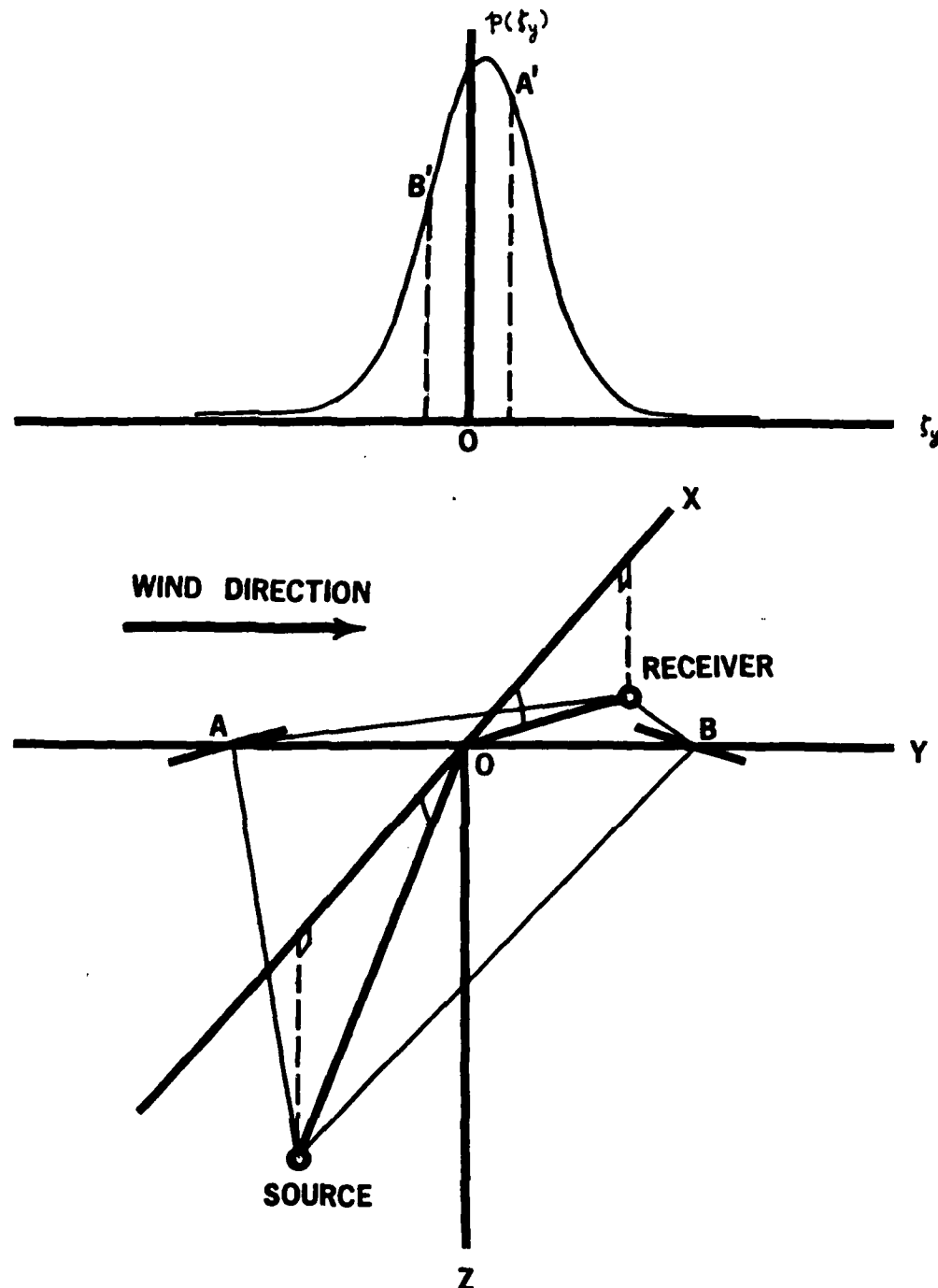


Figure 6.4 Symmetric crosswind scatter geometry and surface slope distribution.

Here again, the reason why the effect of the surface slopes was not observed in earlier analysis of the scattering problem is that in order to simplify the Kirchhoff integral:

$$H(\omega_0, t) = \frac{1}{4\pi} \int_S \frac{\partial}{\partial n} \left\{ \frac{j \frac{\omega_0}{c} (r_0 + r_1)}{e \frac{r_0 r_1}{r_0 + r_1}} \right\} \cdot d\underline{s} \quad (6.2.1)$$

the fact that both $\frac{\partial}{\partial n}$ and $d\underline{s}$ contain slope terms has generally been ignored. Thus, equation (6.2.1) is usually simplified to read

$$H(\omega_0, t) = \frac{1}{4\pi} \int_{-\infty}^{\infty} \int_{-\infty}^{\infty} \frac{\partial}{\partial z} \left\{ \frac{j \frac{\omega_0}{c} (r_0 + r_1)}{e \frac{r_0 r_1}{r_0 + r_1}} \right\} dx dy \quad (6.2.2)$$

rather than the more accurate form

$$H(\omega_0, t) = \frac{1}{4\pi} \int_{-\infty}^{\infty} \int_{-\infty}^{\infty} \left(\frac{\partial}{\partial z} - \frac{\partial z}{\partial x} \frac{\partial}{\partial x} - \frac{\partial z}{\partial y} \frac{\partial}{\partial y} \right) \left(\frac{j \frac{\omega_0}{c} (r_0 + r_1)}{e \frac{r_0 r_1}{r_0 + r_1}} \right) dx dy \quad (6.2.3)$$

When the slope terms are retained, even approximately, we have shown that slope asymmetries result in spectral asymmetries.

Chapter VII Summary and Conclusions

In this study, we have examined the problem of frequency spreading in the acoustic surface scattering from both the mathematical and the physical point of views. The result of this investigation is the establishment of spectral characteristics as a function of three effects; viz., scattering geometry, surface statistics, and acoustic frequency. Expressions are derived based on an arbitrary scattering geometry to allow for general applications.

The analysis considered two different kinds of surface model; a deterministic one and a random one. The deterministic model is treated in Chapter III. A two-harmonic surface wave was used to model a wind-driven surface. The spectral behavior of the acoustic signal scattered from this deterministic surface was derived for small surface waveheight. It was found that the surface scattering process introduced doppler shifted spectral lines into the received signal spectrum. The amount of frequency shift is a function of surface wave frequencies. The amplitudes of the two spectral lines adjacent to the transmitted acoustic frequency are generally unequal. Under crosswind condition, the upper spectral amplitude is always larger than the lower one. In the down (up) wind case, the relative amplitudes depend on wind direction and relative depths of source and receiver. Scattering from a random surface was considered in Chapter IV. The surface height distribution was assumed to be approximately Gaussian, but such as to permit a non-zero third order surface slope moment. It was found that this moment is one of the two mechanisms that control the spectral amplitudes. The other

mechanism is the surface scattering-geometry asymmetry. A detailed discussion of how the two mechanisms control the spectral amplitudes was given for both the slightly rough and the very rough surface situations. In each situation we considered the downwind and cross-wind cases separately. The result obtained from the slightly rough random surfaces was compared against that obtained from the deterministic model. We showed that the latter could be a limit case of the former. All these discussions are for forward specular scattering. In Chapter V, the theoretical and the experimental results are examined, and the amplitude asymmetries due to misaligned source-receiver geometry (off-specular) are discussed. The major mathematical results of Chapter III, IV and V were reviewed from a physical point of view in Chapter VI. A simple surface reflection model was used to explain the analytical results qualitatively.

It was found that the deterministic model, random surface and physical modelling all lead to consistent conclusions about the frequency spreading function. The major results can be summarized as follows:

- (a) The acoustic signal scattered from a sinusoidal surface produces distinct spectral lines as sidebands in the received signal spectrum. The spectral lines are doppler shifted from the source frequency with frequency shifts equal to the surface wave frequency and its harmonics. The number of significant spectrum lines depend on the surface waveheight (the roughness). More spectral lines will result if the surface waveheight increases its value. If the surface wave has more than one frequency, the resulting spectrum will have additional spectral lines with doppler shifts equal to the mixed frequencies. The total energy is

conserved, however, when more spectral lines are formed, the amplitude of each spectral line decreases.

(b) When the acoustic signal is scattered from a random moving surface, the resulting spectrum usually shows frequency spread around the source frequency and frequency spreads around the doppler-shifted surface wave frequencies (i.e. the surface wave still has one or more characteristic frequencies despite the randomness). The width of the spread is usually controlled by the surface waveheight and by the surface slopes correlation constants. The smaller the correlation constants are, i.e. the more the surface height or slopes are uncorrelated, the larger is the frequency spread (bandwidth). For surfaces with very large roughness, the received signal shows a spectrum that has a Gaussian shape. This result can be extended from the small surface roughness situation by widening the doppler shifted spectrum as surface roughness increases, and finally the bandwidth of all sidebands become wide enough so that they merge with the center spectrum to form a single spectrum around the source frequency.

(c) The magnitudes of the sidebands on both sides of the acoustic frequency are in general unequal. Two different mechanisms are responsible for this amplitude difference. One of these is the surface slope asymmetry which always results in the upper sideband being larger than the lower sideband. This effect is independent of wind direction or of the relative depths of source and receiver. The second mechanism is the asymmetry of the scattering geometry; i.e. a difference in the depths of source and receiver. If the ratio between depths of source and receiver exceeds 2 and if the source-receiver configuration is down (or up) wind, the second mechanism becomes dominant in determining the relative sideband amplitudes. Specifically, the conditions are, if the source is at a shallower depth than the receiver is, and if

the wind blows from source to receiver (downwind), then the upper sideband is larger than the lower sideband. By either reversing the wind direction or maintaining the wind direction but placing the source at a larger depth than the receiver, the direction of sideband asymmetry is reversed. Since the second mechanism is a wind-direction dependent effect, it has no effect on the sideband amplitude asymmetries at crosswind.

Good agreement was obtained for random surfaces under a variety of roughness conditions. Some of the differences that were initially found between experimental results and the theory turned out to be the result of small measurement inaccuracies. By modifying the theory to permit consideration of misalignment in hydrophone placement, it was found that very small misalignments could result in fairly substantial doppler shifts. When these misalignments were removed, excellent agreement between experiment and theory was obtained in practically all cases.

The success of the theory in matching experimental results can be regarded as a verification indication of the Kirchhoff integral method for dealing with the forward scattering problem. Although the sideband asymmetries that were one of the major items of interest in this research were not discovered by the Kirchhoff method in its commonly used simplified form, it has been shown that if some often neglected factors were retained, the Kirchhoff method gives experimentally verifiable results. Furthermore, the effect of surface-slope asymmetries and of small hydrophone misalignments had not been

previously predicted. Thus although this method has frequently been criticized, and although it is difficult to justify all the simplifying assumptions on which it rests, it appears to be able to give new and useful results.

APPENDIX A: Derivation of Helmholtz Integral

Consider a monochromatic scalar wave

$$p(x, y, z, t) = p_s(x, y, z)e^{-j\omega t} \quad (A-1)$$

It satisfies the wave equation

$$\left(\nabla^2 + \frac{\omega^2}{c^2}\right)p_s(x, y, z) = 0 \quad (A-2)$$

Let $p(x, y, z)$ be a point within a volume V bounded by a surface S as shown in Figure 2.1. If we assume a function $U(x, y, z)$ which together with its first order derivatives is continuous and finite within and on S , then from Green's theorem

$$\iiint_V (p_s \nabla^2 U - U \nabla^2 p_s) dv = \iint_S (U \frac{\partial p_s}{\partial \underline{n}} - p_s \frac{\partial U}{\partial \underline{n}}) \cdot d\underline{s} \quad (A-3)$$

when \underline{n} is the surface normal defined positive outward. We also assume U to satisfy the wave equation.

$$\left(\nabla^2 + \frac{\omega^2}{c^2}\right)U = 0 \quad (A-4)$$

From equation (A-2) and (A-4), we see that the left side of equation (A-3) is zero for every point of V , therefore we have

$$\iint_S (p_s \frac{\partial U}{\partial \underline{n}} - U \frac{\partial p_s}{\partial \underline{n}}) \cdot d\underline{s} = 0 \quad (A-5)$$

We now assume U to be a function of the form

$$U = \frac{e^{j\frac{\omega}{c} r_1}}{r_1} \quad (A-6)$$

where r_1 is the distance from $p(x,y,z)$ to any other point in V .

We have assumed U to be a continuous function within V , and since $e^{j\frac{\omega_0}{c}r_1}/r_1$ is singular for $r_1 = 0$, we must exclude the point $p(x,y,z)$ from the domain of integration. We surround P by a small sphere of radius ϵ and let the integration be taken throughout the volume between S and S' , where S' is the surface of the small sphere enclosing P . We can rewrite equation (A-5) as

$$\iint_S + \iint_{S'} \left\{ p_s \frac{\partial U}{\partial n} - U \frac{\partial p_s}{\partial n} \right\} \cdot d\underline{s} = 0 \quad (A-7)$$

Hence

$$\iint_S \left\{ U \frac{\partial p_s}{\partial n} - p_s \frac{\partial U}{\partial n} \right\} \cdot d\underline{s} = - \iint_{S'} \left\{ p_s \frac{j}{c} \frac{\omega_0}{r_1} r_1 \left(j \frac{\omega_0}{c} - \frac{1}{r_1} \right) \frac{\partial r_1}{\partial n} - \frac{e}{r_1} \frac{j}{c} r_1 \frac{\partial p_s}{\partial n} \right\} \cdot d\underline{s} \quad (A-8)$$

Notice that the first term and the third term in the kernel of the right-hand side integral are proportional to $\frac{1}{\epsilon}$, where S' is proportional to ϵ^2 , therefore if we let $\epsilon \rightarrow 0$, the first and the third term in the right-hand side integral gives no contribution to the integrated value. However, the integration of the second term yields a value $4\pi p_s$, since $e^{j\frac{\omega_0}{c}\epsilon}$ closes to unity when $\epsilon \rightarrow 0$. Dividing both sides of equation (A-8) by 4π gives equation (2.1.1)

APPENDIX B: Surface Integral Transformation

Consider a surface integral I of the form

$$I = \iint_S \frac{\partial}{\partial n} f(x, y, \zeta(x, y)) \cdot d\underline{s} \quad (B-1)$$

where S represents the surface area over which the integral is to be performed, $d\underline{s}$ is a small surface element whose direction is that of the surface normal; x, y and $\zeta(x, y)$ are the coordinates of an arbitrary point on the surface S in an x, y, z coordinate system as shown in Figure B.1. The location of each point of the surface area S is completely specified by the vector

$$\underline{r}(x, y) = x \hat{x} + y \hat{y} + \zeta(x, y) \hat{z} \quad (B-2)$$

Let S be a smooth surface and assume $\underline{r}'(x, y)$ to have continuous first derivatives along the x and y directions.

$$\frac{\partial \underline{r}}{\partial x} = \hat{x} + \frac{\partial \zeta(x, y)}{\partial x} \hat{z} \quad (B-3)$$

$$\frac{\partial \underline{r}}{\partial y} = \hat{y} + \frac{\partial \zeta(x, y)}{\partial y} \hat{z} \quad (B-4)$$

These two partial derivatives define the slope of the tangential plane of S at the surface point $(x, y, \zeta(x, y))$. Therefore the surface normal \underline{n} at point $(x, y, \zeta(x, y))$ is

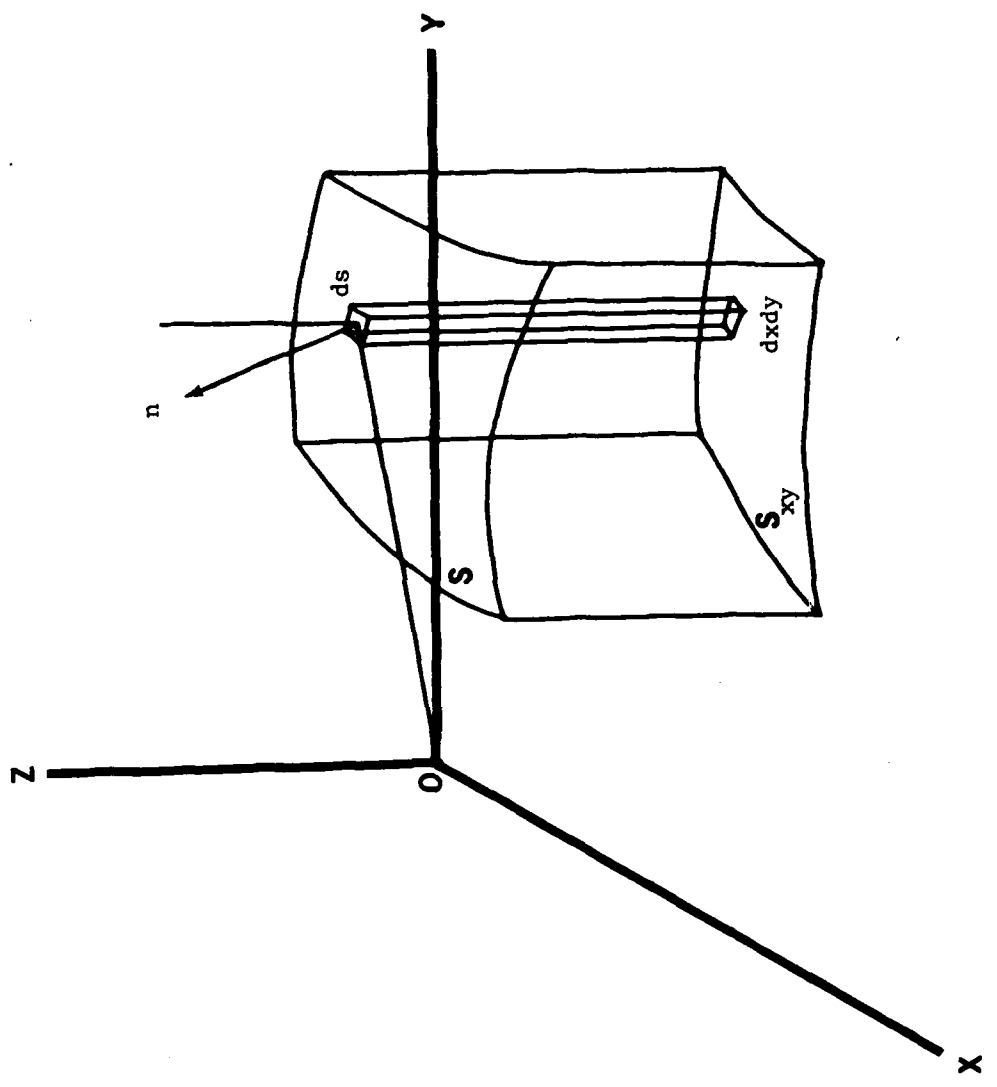


Figure B.1 Scatter surface and its projection on x - y plane.

$$\underline{n} = \frac{\frac{\partial \underline{r}}{\partial x} \times \frac{\partial \underline{r}}{\partial y}}{\left| \frac{\partial \underline{r}}{\partial x} \times \frac{\partial \underline{r}}{\partial y} \right|}$$

$$= \frac{\hat{z} - \frac{\partial \zeta(x,y)}{\partial x} \hat{x} - \frac{\partial \zeta(x,y)}{\partial y} \hat{y}}{\sqrt{1 + \left[\frac{\partial \zeta(x,y)}{\partial x} \right]^2 + \left[\frac{\partial \zeta(x,y)}{\partial y} \right]^2}} \quad (B-5)$$

The angle θ between surface normal \underline{n} and the z axis is the arc cosine of the inner product of \underline{n} and \hat{z} , or

$$\cos \theta = \frac{1}{\sqrt{1 + \left[\frac{\partial \zeta(x,y)}{\partial x} \right]^2 + \left[\frac{\partial \zeta(x,y)}{\partial y} \right]^2}} \quad (B-6)$$

If the surface element is sufficiently small, we can replace $|ds|$ by $dxdy/\cos \theta$; hence

$$ds = \frac{dxdy}{\cos \theta} \underline{n} = \left[\hat{z} - \frac{\partial \zeta(x,y)}{\partial x} \hat{x} - \frac{\partial \zeta(x,y)}{\partial y} \hat{y} \right] dxdy \quad (B-7)$$

The integral in equation (B-1) can now be rewritten as

$$I = \iint_{S_{xy}} \left[\frac{\partial}{\partial x} \hat{x} + \frac{\partial}{\partial y} \hat{y} + \frac{\partial}{\partial z} \hat{z} \right] f(x,y,\zeta(x,y)) \cdot \underline{n} \frac{dxdy}{\cos \theta} \quad (B-8)$$

$$= \iint_{S_{xy}} \left[\frac{\partial}{\partial z} - \frac{\partial \zeta}{\partial x} \frac{\partial}{\partial x} - \frac{\partial \zeta}{\partial y} \frac{\partial}{\partial y} \right] f(x,y,\zeta(x,y)) dxdy \quad (B-9)$$

where S_{xy} represents the projection of S on the $x-y$ plane as shown in Figure B.1. $\frac{\partial}{\partial n}$ has been replaced by its equivalent expression in x,y,z coordinates.

APPENDIX C: Spectrum Computation-Deterministic Surface, Downin

From equation (3.2.7) and $\zeta_x = 0$, $H(\omega_0, t)$ can be rewritten as

$$H(\omega_0, t) = \frac{e^{j\omega_0 \tau_s}}{4\pi r_{00} r_{10}} \int_{-\infty}^{\infty} \int_{-\infty}^{\infty} \left\{ j \frac{\omega_0}{c} F(1 - \zeta_y^2) + \zeta_y (2By + E) \right\} e^{-Ax^2 - By^2 - Ey + j \frac{\omega_0}{c} F \zeta} dx dy \quad (C-1)$$

where

$$A = \frac{1}{L^2(\omega_0)} - j \frac{\omega_0}{CR}$$

$$B = \frac{\sin^2 \psi_0}{L^2(\omega_0)} - j \frac{\omega_0 \sin^2 \psi_0}{CR} = A \sin^2 \psi_0$$

$$E = \left(\frac{1}{r_{00}} - \frac{1}{r_{10}} \right) \cos \psi$$

$$F = 2 \sin \psi \quad (C-2)$$

Since $\zeta(x, y, t)$ is not a function of x , the integral with respect to x in equation (C-1) can be easily performed and $H(\omega_0, t)$ becomes

$$H(\omega_0, t) = \frac{e^{j\omega_0 \tau_s}}{4r_{00}r_{10}\sqrt{\pi A}} \int_{-\infty}^{\infty} \left\{ j \frac{\omega_0}{c} F(1 - \zeta_y^2) + \zeta_y (2By + E) \right\} e^{-By^2 - Ey + j \frac{\omega_0}{c} F \zeta} dy \quad (C-3)$$

By use of the one dimensional surface wave model in equation (3.1.1), $\zeta(x, y, t)$ can be put into the equivalent form

$$\zeta(x, y, t) = \frac{h_1}{2} (e^{j\rho y - j\Omega t + j\phi} + e^{-j\rho y + j\Omega t - j\phi}) \\ + \frac{h_2}{2} (e^{j2\rho y - j2\Omega t} + e^{-j2\rho y + j2\Omega t}) \quad (C-4)$$

The slope along the y direction is obtained by differentiation of equation (C-4), and it becomes

$$\zeta_y(x, y, t) = j \frac{\rho h_1}{2} (e^{j\rho y - j\Omega t + j\phi} - e^{-j\rho y + j\Omega t - j\phi}) \\ + j\rho h_2 (e^{j2\rho y - j2\Omega t} - e^{-j2\rho y + j2\Omega t}) \quad (C-5)$$

and therefore

$$\zeta_y^2 = \frac{\rho^2 h_1^2}{2} + 2\rho^2 h_2^2 + \rho^2 h_1 h_2 [e^{j\rho y - j\Omega t - j\phi} + e^{-j\rho y + j\Omega t + j\phi}] \\ - \frac{\rho^2 h_1^2}{4} [e^{j2\rho y - j2\Omega t + j2\phi} + e^{-j2\rho y + j2\Omega t - j2\phi}] \\ - \rho^2 h_1 h_2 [e^{j3\rho y - j3\Omega t + j\phi} + e^{-j3\rho y + j3\Omega t - j\phi}] \\ - \rho^2 h_2^2 [e^{j4\rho y - j4\Omega t} + e^{-j4\rho y + j4\Omega t}] \quad (C-6)$$

The waveheight of the water surface is assumed to be small compared to the acoustic wavelength. From equation (3.2.8)

$$e^{\frac{j\omega_0}{c} F \zeta} \approx 1 + j \frac{\omega_0}{c} F \frac{h_1}{2} [e^{j\rho y - j\Omega t + j\phi} + e^{-j\rho y + j\Omega t - j\phi}] \\ + j \frac{\omega_0}{c} F \frac{h_2}{2} [e^{j2\rho y - j2\Omega t} + e^{-j2\rho y + j2\Omega t}] \quad (C-7)$$

Substituting equations (C-4) to (C-7) into equation (C-3) results in

$$H(\omega_0, t) = \frac{e^{j\omega_0 t_s}}{4 \sqrt{\pi A} r_{00} r_{10}} \int_{-\infty}^{\infty} H_{COEF} \cdot e^{-By^2 - Ey} dy \quad (C-8)$$

where

$$\begin{aligned}
 H_{COEF} = & \left\{ j \frac{\omega_0}{c} F \left[1 - \frac{\rho^2 h_1^2}{2} - 2\rho^2 h_2^2 \right] \right. \\
 & + e^{-j\Omega t} \left[-j \frac{\omega_0}{c} F \rho^2 h_1 h_2 e^{j\phi y - j\phi} + j \frac{\rho h_1}{2} (2By + E) e^{j\phi y + j\phi} \right] \\
 & + e^{j\Omega t} \left[-j \frac{\omega_0}{c} F \rho^2 h_1 h_2 e^{-j\phi y + j\phi} - j \frac{\rho h_1}{2} (2By + E) e^{-j\phi y - j\phi} \right] \\
 & + e^{-j2\Omega t} \left[j \frac{\omega_0}{c} F \frac{\rho^2 h_1^2}{4} e^{j2\phi y + j2\phi} + j \rho h_2 (2By + E) e^{j2\phi y} \right] \\
 & + e^{j2\Omega t} \left[j \frac{\omega_0}{c} F \frac{\rho^2 h_1^2}{4} e^{-j2\phi y - j2\phi} - j \rho h_2 (2By + E) e^{-j2\phi y} \right] \\
 & + e^{-j3\Omega t} \left[j \frac{\omega_0}{c} F \rho^2 h_1 h_2 e^{j3\phi y + j\phi} \right] \\
 & + e^{j3\Omega t} \left[j \frac{\omega_0}{c} F \rho^2 h_1 h_2 e^{-j3\phi y - j\phi} \right] \\
 & + e^{-j4\Omega t} \left[j \frac{\omega_0}{c} F \rho^2 h_2^2 e^{j4\phi y} \right] \\
 & \left. + e^{j4\Omega t} \left[j \frac{\omega_0}{c} F \rho^2 h_2^2 e^{-j4\phi y} \right] \right\} \\
 & \left\{ 1 + e^{-j\Omega t} \left[j \frac{\omega_0}{c} F \frac{h_1}{2} e^{j\phi y + j\phi} \right] + e^{j\Omega t} \left[j \frac{\omega_0}{c} F \frac{h_1}{2} e^{-j\phi y - j\phi} \right] \right. \\
 & \left. + e^{-j2\Omega t} \left[j \frac{\omega_0}{c} F \frac{h_2}{2} e^{j2\phi y} \right] + e^{j2\Omega t} \left[j \frac{\omega_0}{c} F \frac{h_2}{2} e^{-j2\phi y} \right] \right\} \quad (C-9)
 \end{aligned}$$

or

$$\begin{aligned}
 H_{COEF} = & [j \frac{\omega_0}{c} F (1 - \frac{\rho^2 h_1^2}{2} - 2\rho^2 h_2^2) + \frac{\omega_0^2}{c^2} F^2 \cdot \frac{3\rho^2 h_1^2 h_2}{4} \cos 2\phi] \\
 & + e^{j\rho y - j\Omega t} \left\{ \left(\frac{\omega_0}{c} F \right) [-j\rho^2 h_1 h_2 e^{-j\phi} - \frac{\omega_0}{c} F \frac{h_1}{2} (1 - \frac{\rho^2 h_1^2}{4} - 2\rho^2 h_2^2) e^{j\phi}] \right. \\
 & \quad \left. + \frac{\rho h_1}{2} (2By+E) [je^{j\phi} - \frac{\omega_0}{c} F \cdot \frac{h_2}{2} e^{-j\phi}] \right\} \\
 & + e^{-j\rho y + j\Omega t} \left\{ \left(\frac{\omega_0}{c} F \right) [-j\rho^2 h_1 h_2 e^{j\phi} - \frac{\omega_0}{c} F \frac{h_1}{2} (1 - \frac{\rho^2 h_1^2}{4} - 2\rho^2 h_2^2) e^{-j\phi}] \right. \\
 & \quad \left. + \frac{\rho h_1}{2} (2By+E) [-je^{-j\phi} + \frac{\omega_0}{c} F \frac{h_2}{2} e^{j\phi}] \right\} \\
 & + e^{j2\rho y - j2\Omega t} \left\{ \left(\frac{\omega_0}{c} F \right) [j \frac{\rho^2 h_1^2}{4} e^{j2\phi} - \frac{\omega_0}{c} F \frac{h_2}{2} (1 - \frac{\rho^2 h_1^2}{2} - \rho^2 h_2^2)] \right. \\
 & \quad \left. + (2By+E) [j\rho h_2 - \frac{\omega_0}{c} F \frac{\rho h_1^2}{4} e^{j2\phi}] \right\} \\
 & + e^{-j2\rho y + j2\Omega t} \left\{ \left(\frac{\omega_0}{c} F \right) [j \frac{\rho^2 h_1^2}{4} e^{-j2\phi} - \frac{\omega_0}{c} F \frac{h_2}{2} (1 - \frac{\rho^2 h_1^2}{2} - \rho^2 h_2^2)] \right. \\
 & \quad \left. + (2By+E) [-j\rho h_2 + \frac{\omega_0}{c} F \frac{\rho h_1^2}{4} e^{-j2\phi}] \right\} \\
 & + e^{j3\rho y - j3\Omega t} \left(\frac{\omega_0}{c} F \right) (\rho h_1) [j\rho h_2 e^{j\phi} - \frac{\omega_0}{c} F \frac{\rho h_1^2}{8} e^{j3\phi} - \frac{3h_2}{4} (2By+E) e^{j\phi}] \\
 & + e^{-j3\rho y + j3\Omega t} \left(\frac{\omega_0}{c} F \right) (\rho h_1) [j\rho h_2 e^{-j\phi} - \frac{\omega_0}{c} F \frac{\rho h_1^2}{8} e^{-j3\phi} + \frac{3h_2}{4} (2By+E) e^{-j\phi}] \\
 & + e^{j4\rho y - j4\Omega t} \left(\frac{\omega_0}{c} F \right) (\rho h_2) [j\rho h_2 - \frac{\omega_0}{c} F \frac{5\rho h_1^2}{8} e^{j2\phi} - \frac{h_2}{2} (2By+E)] \\
 & + e^{-j4\rho y + j4\Omega t} \left(\frac{\omega_0}{c} F \right) (\rho h_2) [j\rho h_2 - \frac{\omega_0}{c} F \frac{5\rho h_1^2}{8} e^{-j2\phi} + \frac{h_2}{2} (2By+E)]
 \end{aligned}$$

$$\begin{aligned}
& + e^{j5\rho y - j5\Omega t} \left[- \frac{\omega_0^2}{c^2} F^2 \rho^2 h_1^2 h_2^2 e^{j\phi} \right] \\
& + e^{-j5\rho y + j5\Omega t} \left[- \frac{\omega_0^2}{c^2} F^2 \rho^2 h_1^2 h_2^2 e^{-j\phi} \right] \\
& + e^{j6\rho y - j6\Omega t} \left[- \frac{\omega_0^2}{c^2} F^2 \frac{\rho^2 h_2^3}{2} \right] \\
& + e^{-j6\rho y + j6\Omega t} \left[- \frac{\omega_0^2}{c^2} F^2 \frac{\rho^2 h_2^3}{2} \right]
\end{aligned} \tag{C-10}$$

Since H_{COEF} has the form $c_0 + c_1 y$, the integral in equation (C-8) can be integrated in closed form. The result of this integration is

$$H(\omega_0, t) = \frac{e^{j\omega_0 t}}{4AB r_{00} r_{10}} \cdot \left\{ H + \sum_{m=1}^6 [H_{m+} e^{-jm\Omega t} + H_{m-} e^{jm\Omega t}] \right\} \tag{C-11}$$

where

$$\begin{aligned}
H_0 &= [j \frac{\omega_0}{c} F (1 - \frac{\rho^2 h_1^2}{2} - 2\rho^2 h_2^2) + \frac{\omega_0}{c^2} F^2 \frac{3\rho^2 h_1^2 h_2}{4} \cos 2\phi] e^{\frac{E^2}{4B}} \\
H_{1+} &= \left\{ \left[- \left(\frac{\omega_0}{c} F \right)^2 \frac{h_1}{2} \left(1 - \frac{\rho^2 h_1^2}{4} - 2\rho^2 h_2^2 \right) - \frac{\rho^2 h_1}{2} \right] e^{+j\phi} - j \frac{\omega_0}{c} F \frac{5\rho^2 h_1 h_2}{4} e^{-j\phi} \right\} e^{\frac{(E+j\omega_0)^2}{4B}} \\
H_{2+} &= \left\{ - \left(\frac{\omega_0}{c} F \right)^2 \frac{h_2}{2} \left(1 - \frac{\rho^2 h_1^2}{2} - \rho^2 h_2^2 \right) - 2\rho^2 h_2 - j \frac{\omega_0}{c} F \frac{\rho^2 h_1^2}{4} e^{+j2\phi} \right\} e^{\frac{(E+j2\omega_0)^2}{4B}} \\
H_{3+} &= \left(\frac{\omega_0}{c} F \right) (\rho h_1) \left\{ - \frac{\omega_0}{c} F \frac{\rho h_1^2}{8} e^{+j3\phi} - j \frac{5\rho h_2}{4} e^{+j\phi} \right\} e^{\frac{(E+j3\omega_0)^2}{4B}} \\
H_{4+} &= \left(\frac{\omega_0}{c} F \right) (\rho h_2) \left[- j \rho h_2 - \frac{\omega_0}{c} F \frac{5\rho h_1^2}{8} e^{+j2\phi} \right] e^{\frac{(E+j4\omega_0)^2}{4B}} \\
H_{5+} &= - \left(\frac{\omega_0}{c} F \right)^2 \rho^2 h_1^2 h_2^2 e^{+j\phi} e^{\frac{(E+j5\omega_0)^2}{4B}}
\end{aligned}$$

$$H_{6+} = - \left(\frac{\omega_0}{c} F \right)^2 \frac{\rho^2 h_2^3}{2} e^{\frac{(E + j6\rho)^2}{4B}} . \quad (C-12)$$

APPENDIX D: Proof of $X \geq 0$

The water surface function is

$$\zeta(x, y, t) = h_1 \cos(\rho y - \Omega t + \phi) + h_2 \cos(2\rho y - 2\Omega t) \quad (D-1)$$

which has a slope of the form

$$\zeta_y = \frac{\partial \zeta(x, y, t)}{\partial y} = -\rho h_1 \sin(\rho y - \Omega t + \phi) - 2\rho h_2 \sin(2\rho y - 2\Omega t) \quad (D-2)$$

since the water wave is assumed to be one-dimensional in the y direction, the slope is zero in x direction.

ζ_y^2 is given by

$$\begin{aligned} \zeta_y^2 &= \rho^2 h_1^2 \sin^2(\rho y - \Omega t + \phi) + 4\rho^2 h_2^2 \sin^2(2\rho y - 2\Omega t) \\ &\quad + 4\rho^2 h_1 h_2 \sin(\rho y - \Omega t + \phi) \sin(2\rho y - 2\Omega t) \end{aligned} \quad (D-3)$$

In performing the average over $T = \frac{2\pi}{\Omega}$, the cross-product term vanishes. Hence

$$\overline{\zeta_y^2} = \frac{\rho^2 h_1^2}{2} + 2\rho^2 h_2^2 \quad (D-4)$$

For hydrodynamic reasons, the water surface slope is in general less than unity in absolute magnitude; i.e. slope angles are generally less than 45° . Therefore

$$0 \leq \frac{\rho^2 h_1^2}{2} + 2\rho^2 h_2^2 \leq 1 \quad (D-5)$$

use of this inequality in equation (3.2.14), viz.

$$x = \frac{h_1}{r_{00} + r_{10}} \cdot \frac{\omega_0 \sin \psi_0}{c} \left[1 - \frac{\rho^2 h_1^2}{4} - 2\rho^2 h_2^2 + \frac{\rho^2 c^2}{4\omega_0^2 \sin^2 \psi_0} \right]$$

results in

$$x \geq \frac{h_1}{r_{00} + r_{10}} \cdot \frac{\omega_0 \sin \psi_0}{c} \left[\frac{\rho^2 h_1^2}{4} + \frac{\rho^2 c^2}{4\omega_0^2 \sin^2 \psi_0} \right] \quad (D-6)$$

Since the grazing angle ψ_0 is between 0 and π , $\sin \psi_0 \geq 0$, and therefore $x \geq 0$.

APPENDIX E: Spectrum computation - Deterministic Surface, Crosswind

The distances r_0 and r_1 can be expressed in the following form

$$r_0 = \sqrt{(x - r_{00} \cos \psi_0)^2 + y^2 + (\zeta + r_{00} \sin \psi_0)^2} \quad (E-1)$$

$$r_1 = \sqrt{(x + r_{10} \cos \psi_0)^2 + y^2 + (\zeta + r_{10} \sin \psi_0)^2} \quad (E-2)$$

The Fresnel expansion of equation (E-1) and (E-2) gives, cf. equations (2.2.6)

$$r_0 \approx r_{00} - x \cos \psi_0 + \zeta \sin \psi_0 + \frac{x^2 \sin^2 \psi_0 + y^2}{2r_{00}} \quad (E-3)$$

$$r_1 \approx r_{10} + x \cos \psi_0 + \zeta \sin \psi_0 + \frac{x^2 \sin^2 \psi_0 + y^2}{2r_{10}} \quad (E-4)$$

and the total transmission distance $r_0 + r_1$ is the sum of these two equations

$$r_0 + r_1 \approx r_{00} + r_{10} + 2\zeta \sin \psi_0 + \frac{x^2 \sin^2 \psi_0 + y^2}{R} \quad (E-5)$$

where $R = \frac{2r_{00}r_{10}}{r_{00}+r_{10}}$ was defined in equation (2.2.14).

The attenuation factor $\frac{1}{r_0 r_1}$ can be approximated by (see equation (2.2.11))

$$\frac{1}{r_0 r_1} \approx \frac{1}{r_{00} r_{10}} \exp \left\{ \left(\frac{1}{r_{00}} - \frac{1}{r_{10}} \right) x \cos \psi_0 \right\} \quad (E-6)$$

According to equation (3.2.6), the beam pattern function on the x-y plane can be written as

$$B_S B_R \approx \exp \left\{ -\frac{1}{L^2(\omega_0)} [x^2 \sin^2 \psi_0 + y^2] \right\} \quad (E-7)$$

Substituting equations (E-5) to (E-7) into the Kirchhoff integral formula, one gets

$$H(\omega_0, t) = \frac{j\omega_0 \tau_s}{4\pi r_{00} r_{10}} \int_{-\infty}^{\infty} \int_{-\infty}^{\infty} \left\{ j \frac{\omega_0}{c} F(1 - \zeta_y^2) + 2Ay\zeta_y \right\} e^{-Bx^2 - Ay^2 - Ex + j\frac{\omega_0}{c} F\zeta} dx dy \quad (E-8)$$

where A, B, E and F are defined in Appendix C.

Comparisons of equations (C-1) and (E-8) shows that these two integrals are very similar in form except that in equation (E-8), there is an e^{-Ex} term in place of e^{-Ey} , also $2By + E$ is replaced by $2Ay$. Integrating equation (E-8) with respect to x gives

$$H(\omega_0, t) = \frac{j\omega_0 \tau_s + \frac{E^2}{4B}}{4\sqrt{AB} r_{00} r_{10}} \int_{-\infty}^{\infty} \left\{ j \frac{\omega_0}{c} F(1 - \zeta_y^2) + 2Ay\zeta_y \right\} e^{-Ay^2 + j\frac{\omega_0}{c} F\zeta} dy \quad (E-9)$$

Using the surface wave model of equation (3.1.1), we can evaluate the integral in equation (E-9) in the same way as in Appendix C. The result is

$$H(\omega_0, t) = \frac{j\omega_0 \tau_s + \frac{E^2}{4B}}{4\sqrt{AB} r_{00} r_{10}} \left\{ H_0 + \sum_{m=1}^6 \left[H_{m+} e^{-jm\Omega t} + H_{m-} e^{jm\Omega t} \right] \right\} \quad (E-10)$$

where

$$H_0 = j \frac{\omega_0}{c} F \left(1 - \frac{\rho^2 h_1^2}{2} - 2\rho^2 h_2^2 \right) + \frac{\omega_0^2}{c^2} F^2 \frac{3\rho^2 h_1^2 h_2}{4} \cos^2 \phi$$

$$H_{1+} = \left\{ \left[-\left(\frac{\omega_0}{c} F \right)^2 \frac{h_1}{2} \left(1 - \frac{\rho^2 h_1^2}{4} - 2\rho^2 h_2^2 \right) - \frac{\rho^2 h_1}{2} \right] e^{\pm j\phi} - j \frac{\omega_0 F}{c} \frac{5\rho^2 h_1 h_2}{4} e^{\mp j\phi} \right\} - \frac{\rho^2}{4A}$$

$$H_{2+} = \left\{ -\left(\frac{\omega_0}{c} F \right)^2 \frac{h_2}{2} \left(1 - \frac{\rho^2 h_1^2}{2} - \rho^2 h_2^2 \right) - 2\rho^2 h_2 - j \frac{\omega_0 F}{c} \frac{\rho^2 h_1^2}{4} e^{+j2\phi} \right\} e^{-\frac{(2\rho)^2}{4A}}$$

$$H_{3+} = \left(\frac{\omega_0}{c} F \right) (\rho h_1) \left\{ -\frac{\omega_0 F}{c} \frac{\rho h_1^2}{8} e^{+j3\phi} - j \frac{5}{4} \rho h_2 e^{+j\phi} \right\} e^{-\frac{(3\rho)^2}{4A}}$$

$$H_{4+} = \left(\frac{\omega_0}{c} F \right) (\rho h_2) \left\{ -j\rho h_2 - \frac{\omega_0 F}{c} \frac{5\rho h_1^2}{8} e^{+j2\phi} \right\} e^{-\frac{(4\rho)^2}{4A}}$$

$$H_{5+} = -\left(\frac{\omega_0}{c} F \right)^2 \rho^2 h_1^2 h_2^2 e^{\pm j\phi} - \frac{(5\rho)^2}{4A}$$

$$H_{6+} = -\left(\frac{\omega_0 F}{c} \right)^2 \frac{\rho^2 h_2^3}{2} e^{-\frac{(6\rho)^2}{4A}} \quad (E-11)$$

APPENDIX F: Representation of Transfer Function $H(\omega_0, t)$ in a
General Scatter Geometry

The form of the channel transfer function is

$$H(\omega_0, t) = \frac{1}{4\pi} \int_{-\infty}^{\infty} \int_{-\infty}^{\infty} \left\{ \frac{\partial}{\partial \zeta} - \zeta_x \frac{\partial}{\partial x} - \zeta_y \frac{\partial}{\partial y} \right\} \left\{ B_s B_R \frac{e^{j\frac{\omega_0}{c}(r_0+r_1)}}{r_0 r_1} \right\} dx dy \quad (F-1)$$

where r_0 and r_1 can be expressed as

$$r_0 = \sqrt{(x-r_{00}\cos\psi_T\sin\phi_T)^2 + (y+r_{00}\cos\psi_T\cos\phi_T)^2 + (\zeta+r_{00}\sin\psi_T)^2} \quad (F-2)$$

$$r_1 = \sqrt{(x-r_{10}\cos\psi_R\sin\phi_R)^2 + (y+r_{10}\cos\psi_R\cos\phi_R)^2 + (\zeta+r_{10}\sin\psi_R)^2} \quad (F-3)$$

As in Chapter II, the Fresnel expansion of r_0 and r_1 have the forms

$$\begin{aligned} r_0 &\approx r_{00} - x \cos\psi_T \sin\phi_T + y \cos\psi_T \cos\phi_T + \zeta \sin\psi_T + x^2 \left(\frac{1 - \cos^2\psi_T \sin^2\phi_T}{2r_{00}} \right) \\ &\quad + y^2 \left(\frac{1 - \cos^2\psi_T \cos^2\phi_T}{2r_{00}} \right) + xy \left(\frac{\cos^2\psi_T \sin 2\phi_T}{2r_{00}} \right) \end{aligned} \quad (F-4)$$

$$\begin{aligned} r_1 &\approx r_{10} - x \cos\psi_R \sin\phi_R + y \cos\psi_R \cos\phi_R + \zeta \sin\psi_R + x^2 \left(\frac{1 - \cos^2\psi_R \sin^2\phi_R}{2r_{10}} \right) \\ &\quad + y^2 \left(\frac{1 - \cos^2\psi_R \cos^2\phi_R}{2r_{10}} \right) + xy \left(\frac{\cos^2\psi_R \sin 2\phi_R}{2r_{10}} \right) \end{aligned} \quad (F-5)$$

Therefore $r_0 + r_1$ can be obtained from the sum of these two equations

$$\begin{aligned}
r_0 + r_1 &\approx r_{00} + r_{10} - x \left[\cos\psi_T \sin\phi_T + \cos\psi_R \sin\phi_R \right] \\
&+ y \left(\cos\psi_T \cos\phi_T + \cos\psi_R \cos\phi_R \right) \\
&+ z \left(\sin\psi_T + \sin\psi_R \right) \\
&+ x^2 \left(\frac{1-\cos^2\psi_T \sin^2\phi_T}{2r_{00}} + \frac{1-\cos^2\psi_R \sin^2\phi_R}{2r_{10}} \right) \\
&+ y^2 \left(\frac{1-\cos^2\psi_T \cos^2\phi_T}{2r_{00}} + \frac{1-\cos^2\psi_R \cos^2\phi_R}{2r_{10}} \right) \\
&+ xy \left(\frac{\cos^2\psi_T \sin^2\phi_T}{2r_{00}} + \frac{\cos^2\psi_R \sin^2\phi_R}{2r_{10}} \right)
\end{aligned} \tag{F-6}$$

The attenuation factor $\frac{1}{r_0 r_1}$ is approximated as (see Chapter II)

$$\frac{1}{r_0 r_1} \approx \frac{1}{r_{00} r_{10}} \exp \left\{ x \left(\frac{\cos\psi_T \sin\phi_T}{r_{00}} + \frac{\cos\psi_R \sin\phi_R}{r_{10}} \right) - y \left(\frac{\cos\psi_T \cos\phi_T}{r_{00}} + \frac{\cos\psi_R \cos\phi_R}{r_{10}} \right) \right\} \tag{F-7}$$

The beam pattern function on the x-y plane can be computed as in Chapter II, equation (2.3.13)

$$B_S B_R \approx \exp \left\{ - \frac{x^2}{L_{xx}^2(\omega_0)} - \frac{y^2}{L_{yy}^2(\omega_0)} - \frac{2xy}{L_{xy}^2(\omega_0)} \right\} \tag{F-8}$$

where $L_{xx}(\omega_0)$, $L_{yy}(\omega_0)$ and $L_{xy}(\omega_0)$ are defined as in equation (2.3.14).

If we express $B_S B_R \frac{e^{j \frac{\omega_0}{c}(r_0+r_1)}}{r_0 r_1}$ in the general form

$$B_S B_R \frac{e^{j \frac{\omega_0}{c} (r_0 + r_1)}}{r_0 r_1} \approx \frac{e^{j \omega_0 \tau_s}}{r_{00} r_{10}} \exp\left\{-Ax^2 - By^2 - Cxy - Dx - Ey + j \frac{\omega_0}{c} F\right\}$$
(F-9)

Then A, B, C, D, E and F are defined by

$$\begin{aligned}
 A &= -j \frac{\omega_0}{c} \left(\frac{1 - \cos^2 \psi_T \sin^2 \phi_T}{2r_{00}} + \frac{1 - \cos^2 \psi_R \sin^2 \phi_R}{2r_{10}} \right) + \frac{1}{L_{xx}^2(\omega_0)} \\
 B &= -j \frac{\omega_0}{c} \left(\frac{1 - \cos^2 \psi_T \cos^2 \phi_T}{2r_{00}} + \frac{1 - \cos^2 \psi_R \cos^2 \phi_R}{2r_{10}} \right) + \frac{1}{L_{yy}^2(\omega_0)} \\
 C &= -j \frac{\omega_0}{c} \left(\frac{\cos^2 \psi_T \sin 2\phi_T}{2r_{00}} + \frac{\cos^2 \psi_R \sin 2\phi_R}{2r_{10}} \right) + \frac{1}{L_{xy}^2(\omega_0)} \\
 D &= j \frac{\omega_0}{c} (\cos \psi_T \sin \phi_T + \cos \psi_R \sin \phi_R) - \left(\frac{\cos \psi_T \sin \phi_T}{r_{00}} + \frac{\cos \psi_R \sin \phi_R}{r_{10}} \right) \\
 E &= -j \frac{\omega_0}{c} (\cos \psi_T \cos \phi_T + \cos \psi_R \cos \phi_R) + \left(\frac{\cos \psi_T \cos \phi_T}{r_{00}} + \frac{\cos \psi_R \cos \phi_R}{r_{10}} \right) \\
 F &= \sin \psi_T + \sin \phi_R
 \end{aligned}$$
(F-10)

APPENDIX G: Sign of Third-Order Slope Moment

In general, the surface slope on the windward side is shallower than that on the leeward side. To demonstrate that the third-order slope moment is always negative, we consider an idealized surface profile as shown in Figure G.1.

The wind direction is from left to right. The slope on the windward side is $|\frac{\underline{BD}}{\underline{AD}}|$ and on the leeward side it is $-|\frac{\underline{BD}}{\underline{CD}}|$. The underline represents the distance between the two points. By hypothesis

$$\left| \frac{\underline{BD}}{\underline{AD}} \right| < \left| \frac{\underline{BD}}{\underline{CD}} \right| \quad (G-1)$$

so that

$$|\frac{\underline{AD}}{\underline{CD}}| > |\frac{\underline{CD}}{\underline{AD}}| \quad (G-2)$$

The third order moment ϵ_3 is defined as the average of the cube of the surface slope. The idealized surface wave is periodic, therefore ϵ_3 can be calculated as

$$\begin{aligned} \epsilon_3 &= \frac{1}{|\underline{AC}|} \left(\left| \frac{\underline{BD}}{\underline{AD}} \right|^3 \cdot |\frac{\underline{AD}}{\underline{CD}}| - \left| \frac{\underline{BD}}{\underline{CD}} \right|^3 \cdot |\frac{\underline{CD}}{\underline{AD}}| \right) \\ &= \left| \frac{\underline{BD}}{\underline{AC}} \right|^3 \cdot \left(\left| \frac{1}{\underline{AD}} \right|^2 - \left| \frac{1}{\underline{CD}} \right|^2 \right) < 0 \end{aligned} \quad (G-3)$$

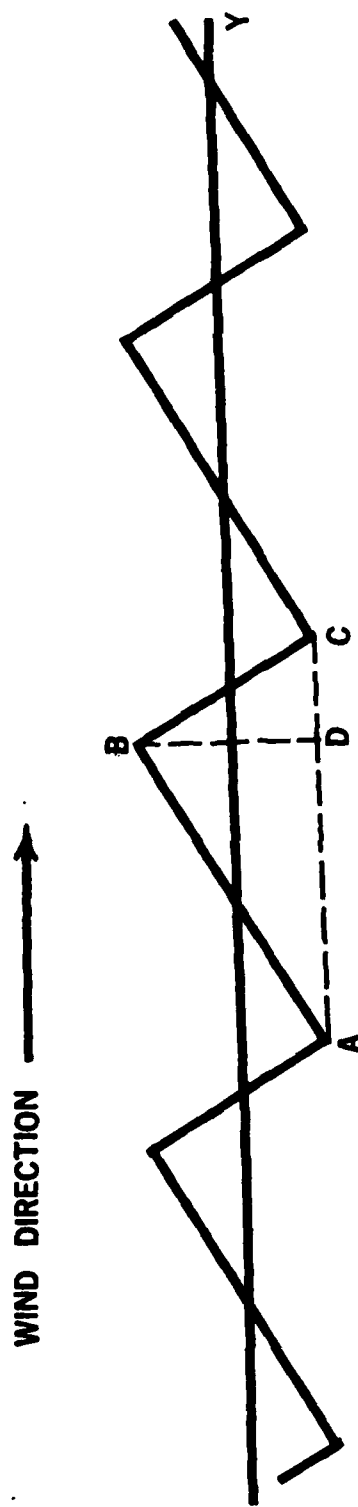


Figure G.1 Saw-tooth wave

APPENDIX H: Power Spectrum-Random Surface, Slightly Rough

We first rewrite $\overline{J(\zeta_{y_1}, \zeta_{y_2})}$ in equation (4.1.7) by computing the average of the product of two brackets.

$$\begin{aligned} \overline{J(\zeta_{y_1}, \zeta_{y_2})} &= \left\{ \frac{\omega_0^2}{c^2} F^2 (1-2\varepsilon_2) + j \frac{\omega_0}{c} F \overline{\zeta_{y_1} \zeta_{y_2}^*}^2 (2By_1 + Cx_1 + E) \right. \\ &\quad - j \frac{\omega_0}{c} F \overline{\zeta_{y_1}^* \zeta_{y_2}} (2B^* y_2 + C^* x_2 + E^*) \\ &\quad \left. + \overline{\zeta_{y_1} \zeta_{y_2}^*} (2By_1 + Cx_1 + E)(2B^* y_2 + C^* x_2 + E^*) \right\} \\ &\cdot \exp\{-Ax_1^2 - By_1^2 - Cx_1 y_1 - Dx_1 - Ey_1 - A^* x_2^2 - B^* y_2^2 - C^* x_2 y_2 - D^* x_2 - E^* y_2\} \end{aligned} \quad (H-1)$$

Make a change of variable $x_2 = x_1 + \xi$, the integration over x_1 and ξ in equation (4.1.6) is easily performed.

$$\begin{aligned} \Phi(\omega_0, \tau) &\approx \frac{1}{16\pi r_{00}^2 r_{10}^2 |A|} \int_{-\infty}^{\infty} \int_{-\infty}^{\infty} \left\{ \frac{\omega_0^2}{c^2} F^2 (1-2\varepsilon_2) + j \frac{\omega_0}{c} F \overline{\zeta_{y_1} \zeta_{y_2}^*}^2 \left[2By_1 - \frac{C(Cy_1 + D)}{2A} + E \right] \right. \\ &\quad - j \frac{\omega_0}{c} F \overline{\zeta_{y_1}^* \zeta_{y_2}} \left[2B^* y_2 - \frac{C^*(Cy_2 + D^*)}{2A^*} + E^* \right] \\ &\quad \left. + \overline{\zeta_{y_1} \zeta_{y_2}^*} \left[2By_1 - \frac{C(Cy_1 + D)}{2A} + E \right] \cdot \left[2B^* y_2 - \frac{C^*(Cy_2 + D^*)}{2A^*} + E^* \right] \right\} \\ &\quad \cdot Q(\zeta_1, \zeta_2) \cdot \exp\{-By_1^2 - Ey_1^2 - B^* y_2^2 - E^* y_2^2 + \frac{(Cy_1 + D)^2}{4A} + \frac{(Cy_2 + D^*)^2}{4A^*}\} dy_1 dy_2 \end{aligned} \quad (H-2)$$

We make another change of variable

$$y_2 = y_1 + \eta \quad (H-3)$$

and define

$$N = B - \frac{C^2}{4A} \quad (H-4)$$

$$M = E - \frac{CD}{2A} \quad (H-5)$$

Then

$$\begin{aligned} & \Phi(\omega_0, \tau) \\ &= \frac{e^{\frac{D^2}{4A} + \frac{D^*2}{4A*}}}{16\pi r_{00}^2 r_{10}^2 |A|} \int_{-\infty}^{\infty} \int_{-\infty}^{\infty} \left\{ \frac{\omega_0^2}{c^2} F^2 (1-2\epsilon_2) + j \frac{\omega_0}{c} F \overline{\zeta_{y_1} \zeta_{y_2}}^* {}^2 [2Ny_1 + M] \right. \\ & \quad - j \frac{\omega_0}{c} F \overline{\zeta_{y_1} {}^2 \zeta_{y_2}}^* [2N^* y_1 + 2N^* \eta + M^*] \\ & \quad \left. + \overline{\zeta_{y_1} \zeta_{y_2}}^* [4|N|^2 (y_1^2 + ny_1) + 2NM^* y_1 + 2N^* M(y_1 + \eta) + |M|^2] \right. \\ & \quad \left. \overline{Q(\zeta_1, \zeta_2)} \cdot e^{-\frac{(N+N^*)y_1^2 - [M+M^*+2N^*\eta]y_1 - N^*\eta^2 - M^*\eta}{dy_1 d\eta}} dy_1 d\eta \right\} \end{aligned} \quad (H-6)$$

Performing the integration over y_1 results in

$$\begin{aligned}
& \Phi(\omega_0, \tau) \\
&= \frac{e^{\frac{D^2}{4A} + \frac{D^*^2}{4A*} + \frac{(M+M^*)^2}{4(N+N^*)}}}{16\sqrt{\pi} r_{00}^2 r_{10}^2 |A|^{N+N^*}} \int_{-\infty}^{\infty} \left\{ \frac{\omega_0}{c^2} F^2 (1-2\varepsilon_2) \right. \\
&\quad - j \frac{\omega_0}{c} F \left(\overline{\zeta_{y_1} \zeta_{y_2}^*}^2 + \overline{\zeta_{y_1}^2 \zeta_{y_2}^*} \right) \left[\frac{2|N|^2 n - N^* M + NM^*}{N+N^*} \right] \\
&\quad + \frac{\overline{\zeta_{y_1} \zeta_{y_2}^*}}{(N+N^*)^2} \left[-4|N|^4 n^2 + 4|N|^2 (N^* M - NM^*) n - (N^* M - NM^*)^2 \right. \\
&\quad \left. \left. + 2|N|^2 (N+N^*) \right] \right\} \\
&\quad \cdot \overline{Q(\zeta_1, \zeta_2)} e^{-\frac{|N|^2}{N+N^*} n^2 + \frac{N^* M - NM^*}{N+N^*} n} dn
\end{aligned} \tag{H-7}$$

If we now substitute equations (4.1.17) and (4.2.1) into equation

(H-7), $\Phi(\omega_0, \tau)$ can be written as

$$\Phi(\omega_0, \tau) = K_1 [I_0 + I_{1+} + I_{1-}] \tag{H-8}$$

where

$$K_1 = \frac{\exp\left\{\frac{D^2}{4A} + \frac{D^*^2}{4A*} + \frac{(M+M^*)^2}{4(N+N^*)} - g^2\right\}}{16 \pi^{\frac{1}{2}} r_{00}^2 r_{10}^2 |A| (N+N^*)^{\frac{1}{2}}} \tag{H-8a}$$

$$\begin{aligned}
I_0 = & \int_{-\infty}^{\infty} \left\{ \frac{\omega_0^2}{c^2} F^2 (1-2\epsilon_2) e^{-\frac{|N|^2}{N+N^*} n^2 + \frac{N^* M-NM^*}{N+N^*} n} \right. \\
& + \frac{\epsilon_2}{(N+N^*)^2} [-4|N|^4 n^2 + 4|N|^2 (N^* M-NM^*) n - (N^* M-NM^*)^2 + 2|N|^2 (N+N^*)] \\
& \left. e^{-[\frac{|N|^2}{N+N^*} + \frac{1}{\Lambda_2^2}]n^2 + \frac{N^* M-NM^*}{N+N^*} n - \frac{\tau^2}{T_2^2}} \right\} d\eta \\
& + j \frac{\omega_0}{c} F \epsilon_3 \left[\frac{2|N|^2 n - N^* M + NM^*}{N+N^*} \right] e^{-[\frac{|N|^2}{N+N^*} + \frac{1}{\Lambda_3^2}]n^2 + \frac{N^* M-NM^*}{N+N^*} n - \frac{\tau^2}{T_3^2}} \} d\eta
\end{aligned}$$

(H-9a)

$$\begin{aligned}
I_{1+} = & \frac{g^2}{2} \int_{-\infty}^{\infty} \left\{ \frac{\omega_0^2}{c^2} F^2 (1-2\epsilon_2) e^{-[\frac{|N|^2}{N+N^*} + \frac{1}{\Lambda_y^2}]n^2 + [\frac{N^* M-NM^*}{N+N^*} \mp j\rho]n - \frac{\tau^2}{T_0^2} \mp j\rho C_p \tau} \right. \\
& + \frac{\epsilon_2}{(N+N^*)^2} [-4|N|^4 n^2 + 4|N|^2 (N^* M-NM^*)^2 n - (N^* M-NM^*)^2 + 2|N|^2 (N+N^*)] \\
& \left. e^{-[\frac{|N|^2}{N+N^*} + \frac{1}{\Lambda_y^2} + \frac{1}{\Lambda_2^2}]n^2 + [\frac{N^* M-NM^*}{N+N^*} \mp j\rho]n - [\frac{1}{T_0^2} + \frac{1}{T_2^2}] \tau^2 \pm j\rho C_p \tau} \right\} d\tau \\
& + j \frac{\omega_0}{c} F \epsilon_3 \left[\frac{2|N|^2 n - N^* M + NM^*}{N+N^*} \right] \\
& \left. e^{-[\frac{|N|^2}{N+N^*} + \frac{1}{\Lambda_y^2} + \frac{1}{\Lambda_3^2}]n^2 + [\frac{N^* M-NM^*}{N+N^*} \mp j\rho]n - [\frac{1}{T_0^2} + \frac{1}{T_3^2}] \tau^2 \pm j\rho C_p \tau} \right\} d\tau
\end{aligned}$$

(H-9b)

The remaining integration over η are straightforward, but involve a lot of algebra. The results are

$$I_0 = f_0 \left(\frac{|N|^2}{N+N^*}, \frac{N^* M - NM^*}{N+N^*} \right) + \epsilon_2 f_2 \left(\frac{|N|^2}{N+N^*} + \frac{1}{\Lambda_2^2}, \frac{N^* M - NM^*}{N+N^*} \right) e^{-\frac{\tau^2}{T_2^2}} \\ + \epsilon_3 f_3 \left(\frac{|N|^2}{N+N^*} + \frac{1}{\Lambda_2^2}, \frac{N^* M - NM^*}{N+N^*} \right) e^{-\frac{\tau^2}{T_3^2}} \quad (H-10a)$$

$$I_{1+} = \frac{g^2}{2} \left\{ f_0 \left(\frac{|N|^2}{N+N^*} + \frac{1}{\Lambda_y^2}, \frac{N^* M - NM^*}{N+N^*} + j\rho \right) e^{-\frac{\tau^2}{T_0^2}} \pm j\rho C_p \tau \right. \\ + \epsilon_2 f_2 \left(\frac{|N|^2}{N+N^*} + \frac{1}{\Lambda_y^2} + \frac{1}{\Lambda_2^2}, \frac{N^* M - NM^*}{N+N^*} + j\rho \right) e^{-\left[\frac{1}{T_0^2} + \frac{1}{T_2^2} \right] \tau^2 + j\rho C_p \tau} \\ + \epsilon_3 f_3 \left(\frac{|N|^2}{N+N^*} + \frac{1}{\Lambda_y^2} + \frac{1}{\Lambda_3^2}, \frac{N^* M - NM^*}{N+N^*} + j\rho \right) e^{-\left[\frac{1}{T_0^2} + \frac{1}{T_3^2} \right] \tau^2 + j\rho C_p \tau} \left. \right\} \quad (H-10b)$$

with

$$f_0(a, b) = \frac{\omega_0^2}{c^2} F^2 (1 - 2\epsilon_2) \cdot \frac{\pi^{\frac{1}{2}}}{a^{\frac{1}{2}}} e^{\frac{b^2}{4a}} \quad (H-11a)$$

$$f_2(a, b) = \frac{1}{(N+N^*)^2} \left\{ -4|N|^4 \left[\left(\frac{b}{2a}\right)^2 + \frac{1}{2a} \right] + 4|N|^2 (N^* M - NM^*) \frac{b}{2a} - (N^* M - NM^*)^2 \right. \\ \left. + 2|N|^2 (N+N^*) \right\} \frac{\pi^{\frac{1}{2}}}{a^{\frac{1}{2}}} e^{\frac{b^2}{4a}} \quad (H-11b)$$

$$f_3(a, b) = j \frac{\omega_0}{c} Q F \left[\frac{|N|^2}{N+N^*} \cdot \frac{b}{a} - \frac{N^* M - NM^*}{N+N^*} \right] - \frac{\pi^{\frac{1}{2}}}{a^{\frac{1}{2}}} e^{-\frac{b^2}{4a}} \quad (H-11c)$$

The final signal spectrum is

$$\begin{aligned} \Gamma(\omega, \omega_0) &= \int_{-\infty}^{\infty} \Phi(\omega_0, \tau) e^{j\omega_0\tau - j\omega\tau} d\tau \\ &= \frac{e^{\frac{D^2}{4A} + \frac{D^*^2}{4A^*} + \frac{(M+M^*)^2}{4(N+N^*)} - g^2}}{16 \pi^{\frac{1}{2}} r_{00}^2 r_{10}^2 |A| (N+N^*)^{\frac{1}{2}}} \cdot \\ &\quad \int_{-\infty}^{\infty} \left\{ [f_{00} + \epsilon_2 f_{20} e^{-\frac{\tau^2}{T_2^2}} + \epsilon_3 f_{30} e^{-\frac{\tau^2}{T_3^2}}] \right. \\ &\quad \left. - \frac{\tau^2}{T_0^2} e^{-\frac{\tau^2}{T_0^2} + j\beta C_p \tau} - \frac{\tau^2}{T_2^2} e^{-\frac{\tau^2}{T_2^2} - j\beta C_p \tau} - \frac{\tau^2}{T_3^2} e^{-\frac{\tau^2}{T_3^2} - j\beta C_p \tau} \right. \\ &\quad \left. + \frac{g^2}{2} e^{-\frac{\tau^2}{T_0^2} - j\beta C_p \tau} + \epsilon_2 f_{2+} e^{-\frac{\tau^2}{T_2^2}} + \epsilon_3 f_{3+} e^{-\frac{\tau^2}{T_3^2}} \right. \\ &\quad \left. + \frac{g^2}{2} e^{-\frac{\tau^2}{T_0^2} - j\beta C_p \tau} + \epsilon_2 f_{2-} e^{-\frac{\tau^2}{T_2^2}} + \epsilon_3 f_{3-} e^{-\frac{\tau^2}{T_3^2}} \right\} \\ &\quad \cdot e^{-j(\omega - \omega_0)\tau} d\tau \end{aligned} \quad (H-12)$$

Again, we have defined new symbols to simplify the expression, they are

$$f_{00} = f_0 \left(\frac{|N|^2}{N+N^*}, jd \right)$$

$$f_{20} = f_2 \left(\frac{|N|^2}{N+N^*} + \frac{1}{\Lambda_2^2}, jd \right)$$

$$f_{30} = f_3 \left(\frac{|N|^2}{N+N^*} + \frac{1}{\Lambda_3^2}, jd \right)$$

$$f_{0\pm} = f_0 \left(\frac{|N|^2}{N+N^*} + \frac{1}{\Lambda_y^2}, jd \mp jp \right)$$

$$f_{2\pm} = f_2 \left(\frac{|N|^2}{N+N^*} + \frac{1}{\Lambda_y^2} + \frac{1}{\Lambda_2^2}, jd \mp jp \right)$$

$$f_{3\pm} = f_3 \left(\frac{|N|^2}{N+N^*} + \frac{1}{\Lambda_y^2} + \frac{1}{\Lambda_3^2}, jd \mp jp \right)$$

$$d = \frac{\frac{N^* M - NM^*}{N+N^*}}{j(N+N^*)} \quad (H-13)$$

Hence $\Gamma(\omega, \omega_0)$ can finally be expressed as a three-part spectrum

$$\Gamma(\omega, \omega_0) = K_1 [S_{P0}(\omega, \omega_0) + S_{P1+}(\omega, \omega_0) + S_{P1-}(\omega, \omega_0)] \quad (H-14)$$

$$S_{P0}(\omega, \omega_0) = f_{00} \delta(\omega - \omega_0) + \sqrt{\pi} T_2 \epsilon_2 f_{20} e^{-\frac{T_2^2 (\omega - \omega_0)^2}{4}} + \sqrt{\pi} T_3 \epsilon_3 f_{30} e^{-\frac{T_3^2 (\omega - \omega_0)^2}{4}}$$

(H-15a)

$$S_{P1\pm}(\omega, \omega_0) = \left\{ \frac{g^2}{2} \sqrt{\pi} T_0 f_{0\pm} e^{-\frac{T_0^2 (\omega - \omega_0 \mp \rho C_p)^2}{4}} \right. \\ + \frac{\sqrt{\pi} T_0 T_2}{(T_0^2 + T_2^2)^{\frac{1}{2}}} \epsilon_2 f_{2\pm} e^{\frac{T_0^2 T_2^2 (\omega - \omega_0 \mp \rho C_p)^2}{4(T_0^2 + T_2^2)}} \\ + \frac{\sqrt{\pi} T_0 T_3}{(T_0^2 + T_3^2)^{\frac{1}{2}}} \epsilon_3 f_{3\pm} e^{-\frac{T_0^2 T_3^2 (\omega - \omega_0 \mp \rho C_p)^2}{4(T_0^2 + T_3^2)}} \left. \right\}$$

(H-15b)

Case I. Down-Wind Geometry

$$\phi_T = 0^\circ$$

(H-16)

$$\phi_R = 180^\circ$$

and the grazing angles of transmitter and receiver are the same

$$\psi_T = \psi_R = \psi_0$$

(H-17)

From equation (F-13)

$$A = -j \frac{\omega_0}{CR} + \frac{1}{L^2(\omega_0)}$$

$$B = -j \frac{\omega_0}{CR} \sin^2 \psi_0 + \frac{\sin^2 \psi_0}{L^2(\omega_0)}$$

$$C = 0$$

$$D = 0$$

$$E = \cos \psi_0 \left(\frac{1}{r_{00}} - \frac{1}{r_{10}} \right)$$

$$F = 2 \sin \psi_0 \quad (H-18)$$

And from equation (H-4) and (H-5)

$$N = \frac{4AB - C^2}{4A} = B \quad (H-19a)$$

$$M = E - \frac{CD}{2A} = E \quad (H-19b)$$

$$\frac{|N|^2}{N+N^*} = \frac{|B|^2}{B+B^*} = \frac{\omega_0^2 L^2(\omega_0)}{2c^2 R^2} \sin^2 \psi_0 + \frac{\sin^2 \psi_0}{2L^2(\omega_0)} \quad (H-19c)$$

If the beamwidth $L(\omega_0)$ is larger than the dimension of the second Fresnel zone, then from [75]

$$\frac{\omega_0^2 L^4(\omega_0)}{c^2 R^2} \geq (2\pi)^2 \quad (H-19d)$$

Thus

$$\frac{\omega_0^2 L^2(\omega_0)}{c^2 R^2} \geq \frac{(2\pi)^2}{L^2(\omega_0)} > \frac{1}{L^2(\omega_0)} \quad (H-19e)$$

Hence equation (H-19c) can be approximated as

$$\frac{|N|^2}{N+N^*} \approx \frac{\omega_0^2 L^2(\omega_0)}{2c^2 R^2} \sin^2 \psi_0 \quad (H-20)$$

Note that $M = E$ is real, therefore from equation (H-13)

$$d = \frac{N^* M - NM^*}{j(N+N^*)} = \frac{E(B^* - B)}{j(B+B^*)} \quad (H-21)$$

or

$$d = \frac{\omega_0^2 L(\omega_0)}{cR} \left(\frac{1}{r_{00}} - \frac{1}{r_{10}} \right) \cos \psi_0 \quad (H-22)$$

Then from equations (H-11) and (H-13)

$$\begin{aligned} f_{00} &= f_0 \left(\frac{|N|^2}{N+N^*}, \frac{N^* M - NM^*}{N+N^*} \right) \\ &= \frac{\omega_0^2}{c^2} F^2 (1-2\epsilon_2) \cdot \frac{\sqrt{2\pi} cR}{\omega_0^2 L(\omega_0) \sin \psi_0} e^{-\frac{L^2(\omega_0) \cot^2 \psi_0}{2R^2}} \end{aligned} \quad (H-23a)$$

$$f_{20} = \rho^2 \frac{\sqrt{2\pi} cR}{\omega_0^2 L(\omega_0) \sin \psi_0} \exp \left\{ -\frac{L^2(\omega_0) \cot^2 \psi_0}{2R^2} \right\} \quad (H-23b)$$

$$f_{30} = \frac{\omega_0}{c} F \rho \frac{\sqrt{2\pi} cR}{\omega_0^2 L(\omega_0) \sin \psi_0} \exp \left\{ -\frac{L^2(\omega_0) \cot^2 \psi_0}{2R^2} \right\} \quad (H-23c)$$

$$f_{0\pm} = \frac{\omega_0^2}{c^2} F^2 (1-2\epsilon_2) \cdot \frac{\sqrt{2\pi} cR}{\omega_0^2 L(\omega_0) \sin \psi_0} \exp \left\{ -\frac{c^2 R^2 (d \mp \rho)^2}{2\omega_0^2 L^2(\omega_0) \sin^2 \psi_0} \right\} \quad (H-23d)$$

$$f_{2\pm} = \rho^2 \frac{\sqrt{2\pi} cR}{\omega_0^2 L(\omega_0) \sin \psi_0} \exp \left\{ -\frac{c^2 R^2 (d \mp \rho)^2}{2\omega_0^2 L^2(\omega_0) \sin^2 \psi_0} \right\} \quad (H-23e)$$

$$f_{3\pm} = \pm \frac{\omega_0}{c} F \rho \frac{\sqrt{2\pi} cR}{\omega_0^2 L(\omega_0) \sin \psi_0} \exp \left\{ -\frac{c^2 R^2 (d \mp \rho)^2}{2\omega_0^2 L^2(\omega_0) \sin^2 \psi_0} \right\} \quad (H-23f)$$

AD-A083 895

YALE UNIV NEW HAVEN CT SYSTEMS AND INFORMATION SCIENCES F/6 20/1
FREQUENCY SPREADING IN UNDERWATER ACOUSTIC SIGNAL TRANSMISSION. (U)
APR 80 H TUNG, F B TUTEUR, J G ZORNIG N00014-77-C-0237
UNCLASSIFIED S/IS-8001 NL

3 of 3
AC/DR/ab

END
DATE 11-10-80
10-10-80
DTIC

Hence

$$\Gamma(\omega, \omega_0) = \frac{e^{-g^2}}{(r_{00} + r_{10})^2} [S_{D0}(\omega, \omega_0) + S_{D1+}(\omega, \omega_0) + S_{D1-}(\omega, \omega_0)] \quad (H-24)$$

$$S_{D0}(\omega, \omega_0) = (1-2\epsilon_2)\delta(\omega - \omega_0) + \frac{\rho^2 \sigma^2 \epsilon_2^2}{g^2} \sqrt{\pi} T_2 e^{-\frac{T_2^2}{4} (\omega - \omega_0)^2} \\ + \frac{\rho \sigma \epsilon_3}{g} \sqrt{\pi} T_3 e^{-\frac{T_3^2}{4} (\omega - \omega_0)^2} \quad (H-24a)$$

$$S_{D1+}(\omega, \omega_0) = \frac{g^2}{2} (\sqrt{\pi} T_0) e^{-\frac{2\sigma^2 R^2 \rho^2}{g^2 L^2(\omega_0)} \pm \frac{2\rho}{\omega_0/c} \cdot \left(\frac{r_{10} - r_{00}}{r_{10} + r_{00}} \right) \frac{\cos \psi_0}{\sin^2 \psi_0}} \quad (H-24b)$$

$$\left\{ (1-2\epsilon_2) + \frac{\rho^2 \sigma^2 \epsilon_2^2}{g^2} \pm \frac{\rho \sigma \epsilon_3}{g} \right\} e^{-\frac{T_0^2}{4} (\omega - \omega_0 \mp \rho c p)^2}$$

Case II Cross-Wind

$$\phi_T = 90^\circ \quad (H-25)$$

$$\phi_R = 270^\circ$$

All the assumptions and variables are identical to those of Case I, except we now have

$$D = -[\frac{1}{r_{00}} - \frac{1}{r_{10}}] \cos \psi_0 \quad (H-26)$$

$$E = 0$$

Subsequently, in equation (H-13)

$$d = 0$$

(H-27)

The signal spectrum can be written as

$$\Gamma(\omega, \omega_0) = \frac{e^{-g^2 + \frac{2c^2 \cos^2 \psi_0}{\omega_0^2 L^2(\omega_0)} \left(\frac{r_{10} - r_{00}}{r_{10} + r_{00}} \right)^2}}{(r_{00} + r_{10})^2} [S_{C0}(\omega, \omega_0) + S_{C1+}(\omega, \omega_0) + S_{C1-}(\omega, \omega_0)]$$

(H-28)

$$S_{C0}(\omega, \omega_0) = (1-2\varepsilon_2)\delta(\omega-\omega_0) \\ + \frac{\rho^2 \sigma^2 \varepsilon_2}{g^2} \sqrt{\pi} T_2 e^{-\frac{T_2^2}{4}(\omega-\omega_0)^2} + \frac{\rho \sigma \varepsilon_3}{g} \sqrt{\pi} T_3 e^{-\frac{T_3^2}{4}(\omega-\omega_0)^2}$$

(H-28a)

$$S_{C1\pm}(\omega, \omega_0) = \frac{g^2}{2} (\sqrt{\pi} T_0) e^{-\frac{g^2 L^2(\omega_0)}{2\sigma^2 R_p^2}} \\ \left\{ (1-2\varepsilon_2) + \frac{\rho^2 \sigma^2 \varepsilon_2}{g^2} \pm \frac{\rho \sigma \varepsilon_3}{g} \right\} e^{-\frac{T_0^2}{4} (\omega-\omega_0 \mp \rho C_p)^2}$$

(H-28b)

APPENDIX I: Power Spectrum-Random Rough Surfaces

The integration over x_1 , x_2 and y_1 are the same as in Appendix H. The result is equation (H-7)

$$\begin{aligned}
 & \Phi(\omega_0, \tau) \\
 &= K_2 \int_{-\infty}^{\infty} \left\{ \frac{\omega_0}{c} F^2(1-2\varepsilon_2) \right. \\
 &+ \frac{\zeta_{y_1} \zeta_{y_2}^*}{(N+N^*)^2} [-4|N|^4 n^2 + 4|N|^2 (N^* M - NM^*) n - (NM - NM^*)^2 + 2|N|^2 (N+N^*)] \\
 &- j \frac{\omega_0}{c} \overline{F(\zeta_{y_1} \zeta_{y_2}^*)^2} + \overline{\zeta_{y_1}^2 \zeta_{y_2}^*} \left[\frac{2|N|^2 n - N^* M + NM^*}{N+N^*} \right] \} \\
 &- \frac{|N|^2}{n^2} - \frac{N^* M - NM^*}{N+N^*} n \\
 &\cdot Q(\zeta_1, \zeta_2) e^{-\frac{N+N^*}{2}} d\eta \quad (I-1)
 \end{aligned}$$

where

$$K_2 = \frac{\exp \left\{ \frac{D^2}{4A} + \frac{D^{*2}}{4A^*} + \frac{(M+M^*)^2}{4(N+N^*)} \right\}}{16 \pi^{\frac{1}{2}} r_{00}^2 r_{10}^2 |A| \left(N+N^* \right)^{\frac{1}{2}}} \quad (I-1a)$$

where the corresponding definitions are contained in Appendix H.

Replacing $\overline{Q(\zeta_1, \zeta_2)}$ and the slope moments with the expressions in equations (4.3.1), (4.1.16) and (4.1.17), we would have

$$\Phi(\omega_0, \tau) = K_2 \left\{ I_{00} + I_{22} + I_{33} \right\} \quad (I-2)$$

Where

$$I_{00} = \int_{-\infty}^{\infty} \frac{\omega_0^2}{c^2} F^2 (1 - 2\varepsilon_2) e^{-[\frac{|N|^2}{N+N^*} + g^2(\frac{1}{\Lambda_y^2} + \frac{\rho^2}{2})]\eta^2 + [\frac{N^* M - NM^*}{N+N^*} + g^2 \rho^2 C_p \tau] \eta} \\ \cdot e^{-g^2(\frac{1}{T_0^2} + \frac{\rho^2 C_p^2}{2}) \tau^2} d\eta \quad (I-2a)$$

$$I_{22} = \int_{-\infty}^{\infty} \frac{\varepsilon_2}{(N+N^*)^2} [-4|N|^4 \eta^2 + 4|N|^2 (N^* M - NM^*) \eta - (N^* M - NM^*)^2 + 2|N|^2 (N+N^*)] \\ \cdot e^{-[\frac{|N|^2}{N+N^*} + g^2(\frac{1}{\Lambda_y^2} + \frac{\rho^2}{2}) + \frac{1}{\Lambda_2^2}] \eta^2 + [\frac{N^* M - NM^*}{N+N^*} + g^2 \rho^2 C_p \tau] \eta} \\ \cdot e^{-[g^2(\frac{1}{T_0^2} + \frac{\rho^2 C_p^2}{2}) + \frac{1}{T_2^2}] \tau^2} d\eta \quad (I-2b)$$

$$I_{33} = \int_{-\infty}^{\infty} j \frac{\omega_0}{c} F \varepsilon_3 [\frac{2|N|^2 \eta - N^* M + NM^*}{N+N^*}] e^{-[\frac{|N|^2}{N+N^*} + g^2(\frac{1}{\Lambda_y^2} + \frac{\rho^2}{2}) + \frac{1}{\Lambda_3^2}] \eta^2} \\ \cdot e^{[\frac{N^* M - NM^*}{N+N^*} + g^2 \rho^2 C_p \tau] \eta - [g^2(\frac{1}{T_0^2} + \frac{\rho^2 C_p^2}{2}) + \frac{1}{T_3^2}] \tau^2} d\eta \quad (I-2c)$$

Carrying out the integration over η and applying equation (H-11), we can express $\Phi(\omega_0, \tau)$ as

$$\begin{aligned} \Phi(\omega_0, \tau) = K_2 \left\{ f_{10} e^{-\left[\frac{g^2}{T_0^2} + \frac{\rho^2 g^2 C_p^2}{N_0} \left(\frac{|N|^2}{N+N^*} + \frac{g^2}{\Lambda_y^2} \right)\right] \tau^2 + \frac{j g^2 \rho^2 C_p d \tau}{2 N_0}} \right. \\ - \left[\frac{g^2}{T_0^2} + \frac{1}{T_2^2} + \frac{\rho^2 g^2 C_p^2}{N_0} \left(\frac{|N|^2}{N+N^*} + \frac{g^2}{\Lambda_y^2} + \frac{1}{\Lambda_2^2} \right) \right] \tau^2 + \frac{j g^2 \rho^2 C_p d \tau}{2[N_0 + \frac{1}{\Lambda_2^2}]} \\ + \epsilon_2 f_{12}(\tau) e^{-\left[\frac{g^2}{T_0^2} + \frac{1}{T_3^2} + \frac{\rho^2 g^2 C_p^2}{N_0} \left(\frac{|N|^2}{N+N^*} + \frac{g^2}{\Lambda_y^2} + \frac{1}{\Lambda_3^2} \right)\right] \tau^2 + \frac{j g^2 \rho^2 C_p d \tau}{2[N_0 + \frac{1}{\Lambda_3^2}]}} \\ \left. + \epsilon_3 f_{13}(\tau) e^{-\left[\frac{g^2}{T_0^2} + \frac{1}{T_3^2} + \frac{\rho^2 g^2 C_p^2}{N_0} \left(\frac{|N|^2}{N+N^*} + \frac{g^2}{\Lambda_y^2} + \frac{1}{\Lambda_3^2} \right)\right] \tau^2 + \frac{j g^2 \rho^2 C_p d \tau}{2[N_0 + \frac{1}{\Lambda_3^2}]} } \right\} \end{aligned}$$

(I-3)

where d has the same definition as in equation (H-13) and

$$f_{10} = f_0(N_0, jd) \quad (I-3a)$$

$$f_{12}(\tau) = f_2(N_0 + \frac{1}{\Lambda_2^2}, jd + g^2 \rho^2 C_p \tau) \quad (I-3b)$$

$$f_{13}(\tau) = f_3(N_0 + \frac{1}{\Lambda_3^2}, jd + g^2 \rho^2 C_p \tau) \quad (I-3c)$$

$$N_0 = \frac{|N|^2}{N+N^*} + g^2 \left(\frac{1}{\Lambda_y^2} + \frac{\rho^2}{2} \right) \quad (I-3d)$$

The signal spectrum is

$$\begin{aligned}
 \Gamma(\omega, \omega_0) &= \int_{-\infty}^{\infty} \phi(\omega_0, \tau) e^{-j(\omega-\omega_0)\tau} d\tau \\
 &= K_2 \left\{ f_{10} \frac{\pi^{\frac{1}{2}}}{\sqrt{q_1(0,0)}} e^{-\frac{[\omega-\omega_0-q_2(0)]^2}{4q_1(0,0)}} \right. \\
 &\quad \left. - \frac{[\omega-\omega_0-q_2(\frac{1}{\Lambda_2^2})]^2}{4q_1(\frac{1}{T_2^2}, \frac{1}{\Lambda_2^2})} \right. \\
 &\quad \left. + \epsilon_2 f_{12} \left(\frac{-j[\omega-\omega_0-q_2(\frac{1}{\Lambda_2^2})]}{2q_1(\frac{1}{T_2^2}, \frac{1}{\Lambda_2^2})} \right) \frac{\pi^{\frac{1}{2}}}{\sqrt{q_1(\frac{1}{T_2^2}, \frac{1}{\Lambda_2^2})}} e^{-\frac{[\omega-\omega_0-q_2(\frac{1}{\Lambda_2^2})]^2}{4q_1(\frac{1}{T_2^2}, \frac{1}{\Lambda_2^2})}} \right. \\
 &\quad \left. - \frac{[\omega-\omega_0-q_2(\frac{1}{\Lambda_3^2})]^2}{4q_1(\frac{1}{T_3^2}, \frac{1}{\Lambda_3^2})} \right. \\
 &\quad \left. + \epsilon_3 f_{13} \left(\frac{-j[\omega-\omega_0-q_2(\frac{1}{\Lambda_3^2})]}{2q_1(\frac{1}{T_3^2}, \frac{1}{\Lambda_3^2})} \right) \frac{\pi^{\frac{1}{2}}}{\sqrt{q_1(\frac{1}{T_3^2}, \frac{1}{\Lambda_3^2})}} e^{-\frac{[\omega-\omega_0-q_2(\frac{1}{\Lambda_3^2})]^2}{4q_1(\frac{1}{T_3^2}, \frac{1}{\Lambda_3^2})}} \right\} \\
 &\quad (I-4)
 \end{aligned}$$

where

$$q_1(a, b) = \frac{g^2}{T_0^2} + a + \frac{\frac{\rho^2 g^2}{2} \left(\frac{|N|^2}{N+N^*} + \frac{g^2}{\Lambda_y^2} + b \right)}{\frac{|N|^2}{N+N^*} + \frac{g^2}{\Lambda_y^2} + \frac{\rho^2 g^2}{2} + b} c_p^2$$

(I-4a)

$$q_2(a) = \frac{\frac{1}{2} \rho^2 g^2 C_{pd}}{\frac{|N|^2}{N+N^*} + \frac{g^2}{\Lambda_y^2} + \frac{\rho^2 g^2}{2} + a} \quad (I-4b)$$

Case I. Downwind

The conditions in equations (H-16~20) are still valid. Let's consider a large beam situation where

$$\frac{|N|^2}{N+N^*} \approx \frac{\omega_0^2 L^2(\omega_0)}{2c^2 R^2} \sin^2 \psi_0 > > \frac{1}{\Lambda_y^2}, \frac{1}{\Lambda_2^2}, \frac{1}{\Lambda_3^2} \quad (I-5)$$

From equation (I-3)

$$N_0 \approx \frac{|N|^2}{N+N^*} \quad (I-5a)$$

$$f_{10} = \frac{\omega_0^2}{c^2} F^2 (1-2\epsilon_2) \cdot \frac{\sqrt{2\pi} cR}{\omega_0^2 L(\omega_0) \sin \psi_0} e^{-\frac{d^2}{4N_0}} \quad (I-5b)$$

$$f_{12} \approx 2 [g^2 (\frac{1}{\Lambda_y^2} + \frac{\rho^2}{2}) + \frac{1}{\Lambda_2^2}] \frac{\sqrt{2\pi} cR}{\omega_0^2 L(\omega_0) \sin \psi_0} e^{-\frac{d^2}{4N_0}} \quad (I-5c)$$

$$f_{13} \sim j \frac{\omega_0}{c} F g^2 \rho^2 C_p \cdot \frac{-j[\omega - \omega_0 - q_2(\frac{1}{\Lambda_3^2})]}{2[\frac{g^2}{T_0^2} + \frac{1}{\Lambda_3^2} + \frac{g^2 \rho^2 C_p^2}{2}]} \cdot \frac{\sqrt{2\pi} cR}{\omega_0^2 L(\omega_0) \sin \psi_0} e^{-\frac{d^2}{4N_0}}$$

$$\approx \frac{\omega_0 F}{c} \cdot \frac{\omega - \omega_0 - q_2(\frac{1}{\Lambda_3^2})}{C_p} \cdot \frac{\sqrt{2\pi} cR}{\omega_0^2 L(\omega_0) \sin \psi_0} e^{-\frac{d^2}{4N_0}} \quad (I-5d)$$

Assuming T_0, T_2, T_3 are of the same order, and since
 $g > > 1$ then

$$\frac{g^2}{T_0^2} > > \frac{1}{T_2^2}, \frac{1}{T_3^2} \quad (I-6)$$

also if

$$\rho CpT_0 \approx 2\pi$$

then

$$\rho Cp \approx \frac{2\pi}{T_0} > > \frac{1}{T_0} \quad (I-7)$$

Therefore from equation (I-4)

$$q_1(0,0) \approx q_1\left(\frac{1}{T_2^2}, \frac{1}{\Lambda_2^2}\right) \approx q_1\left(\frac{1}{T_3^2}, \frac{1}{\Lambda_3^2}\right) \approx \frac{g^2 \rho^2 C_p^2}{2} \quad (I-8)$$

Finally, equation (I-4) can be simplified as

$$\begin{aligned} \Gamma(\omega, \omega_0) &= \frac{[\omega - \omega_0 - q_2(0)]^2}{(2\pi f_B)^2} \\ &\approx \frac{1}{(\tau_{00} + \tau_{10})^2} \cdot \frac{\pi^{\frac{1}{2}}}{g\rho C_p / 2} e^{-\frac{[\omega - \omega_0 - q_2(0)]^2}{(2\pi f_B)^2}} \\ &\quad \left\{ (1 - 2\epsilon_2) + 2\sigma^2 \epsilon_2 \left[\left(\frac{1}{\Lambda_y^2} + \frac{\rho^2}{2} \right) + \frac{1}{g^2 \Lambda_2^2} \right] + \frac{\sigma \epsilon_3}{g C_p} [\omega - \omega_0 - q_2(0)] \right\} \quad (I-9) \end{aligned}$$

where

$$f_B = \frac{g}{\pi} \left\{ \frac{1}{T_0^2} + \frac{\rho^2 C_p^2}{2} \cdot \frac{\frac{|N|^2}{N+N^*} + \frac{g^2}{\Lambda_y^2}}{\frac{|N|^2}{N+N^*} + \frac{g^2}{\Lambda_y^2} + \frac{\rho^2 g^2}{2}} \right\}^{1/2} \quad (I-9a)$$

Case II. Crosswind

Combining equations (H-25~27) and the conditions in the downwind geometry, the signal spectrum of cross-wind geometry is

$$\Gamma(\omega, \omega_0) = \frac{1}{(r_{00} + r_{10})^2} \cdot \frac{\pi^{\frac{1}{2}}}{g\sigma Cp/2} \cdot e^{-\frac{2c^2 \cos^2 \psi_0}{\omega_0^2 L^2(\omega_0)} \left(\frac{r_{10} - r_{00}}{r_{10} + r_{00}} \right)^2 - \frac{(\omega - \omega_0)^2}{(2\pi f_B)^2}}$$

$$\left\{ (1 - 2\epsilon_2) + 2\sigma^2 \epsilon_2 \left[\left(\frac{1}{\Lambda_y^2} + \frac{\rho^2}{2} \right) + \frac{1}{g^2 \Lambda_2^2} \right] + \frac{\sigma \epsilon_3}{gCp} (\omega - \omega_0) \right\}$$
(I-10)

APPENDIX J: Signal Processing Technique

The acoustic source signal is shown on the left side of Figure J.1. It consists of a series of narrow pulses, with a time interval of 10 msec between pulses. The transmitted signal is wideband with bandwidth ranging from 0.2 MHz to 1.2 MHz.

The signal received at the receiver is also in pulse form corresponding to each pulse sent at the source. The received signal $h(\tau, t)$ is sampled and recorded. Each received pulse is sampled at a sampling interval of 350 nsec, 256 samples per pulse. The beginning time of each received pulse is recorded in t_m , with m ranging from 1 to 64. A data file consists of $64 \times 256 = 16,384$ samples.

The signal spectrum computational technique is shown in Figure J.2. Each data file is first passed through a 256 point FFT for each t_m . For 350 ns sampling time, this gives a frequency range from 0 Hz to 1.42 MHz with a frequency resolution of 11.16 KHz. One of the 256 FFT outputs corresponding to the desired acoustic frequency ω_0 is selected for each t_m . The 64 values of $H(\omega_0, t)$ in each file are passed through a 64 point FFT, the output of which is the raw signal spectrum for that file. This has a frequency resolution of 1.5 Hz. The final spectrum $\Gamma(\omega, \omega_0)$ is an average of the outputs of N of such files.

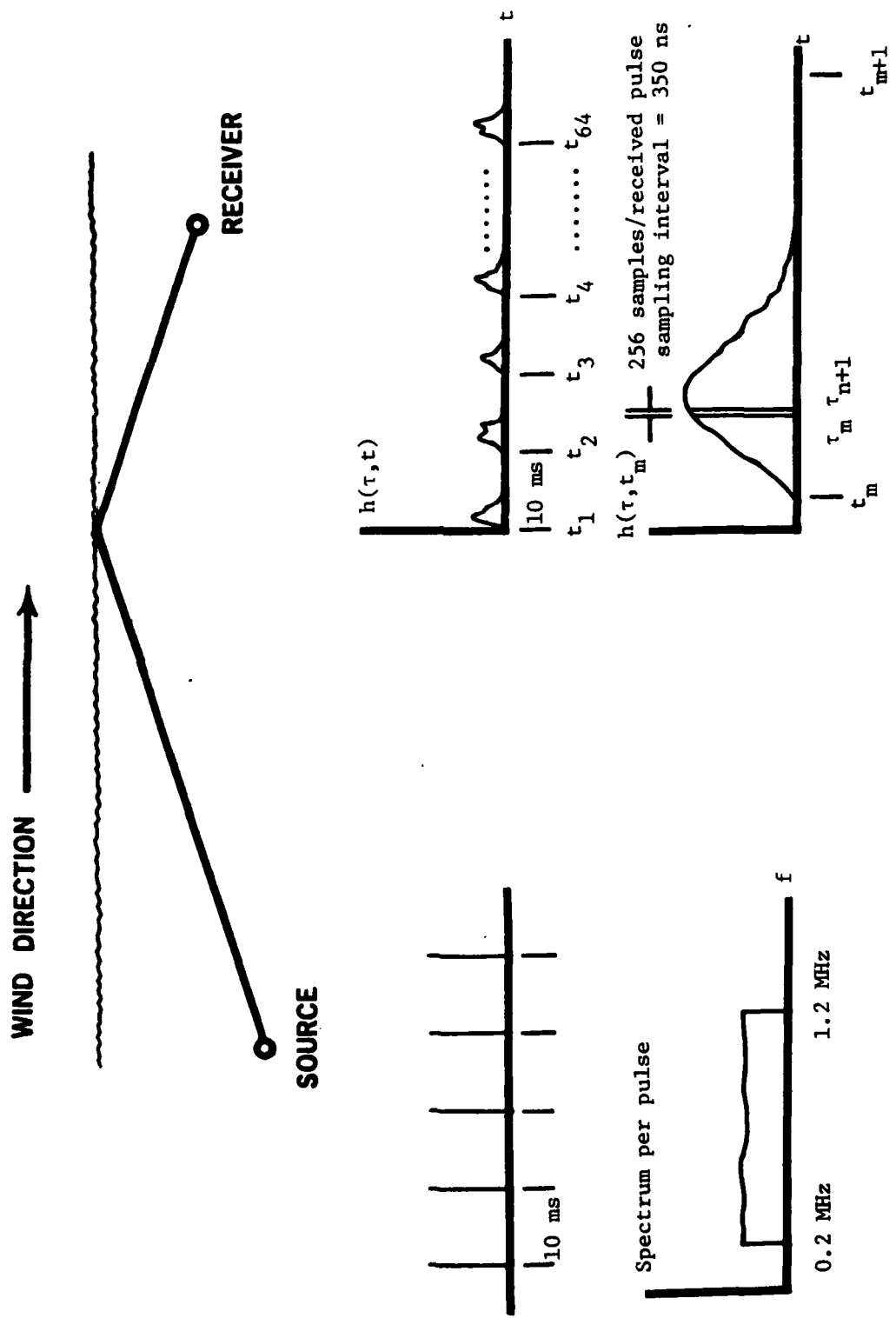


Figure J.1 Signal representation of acoustic signal transmitted and received underwater.

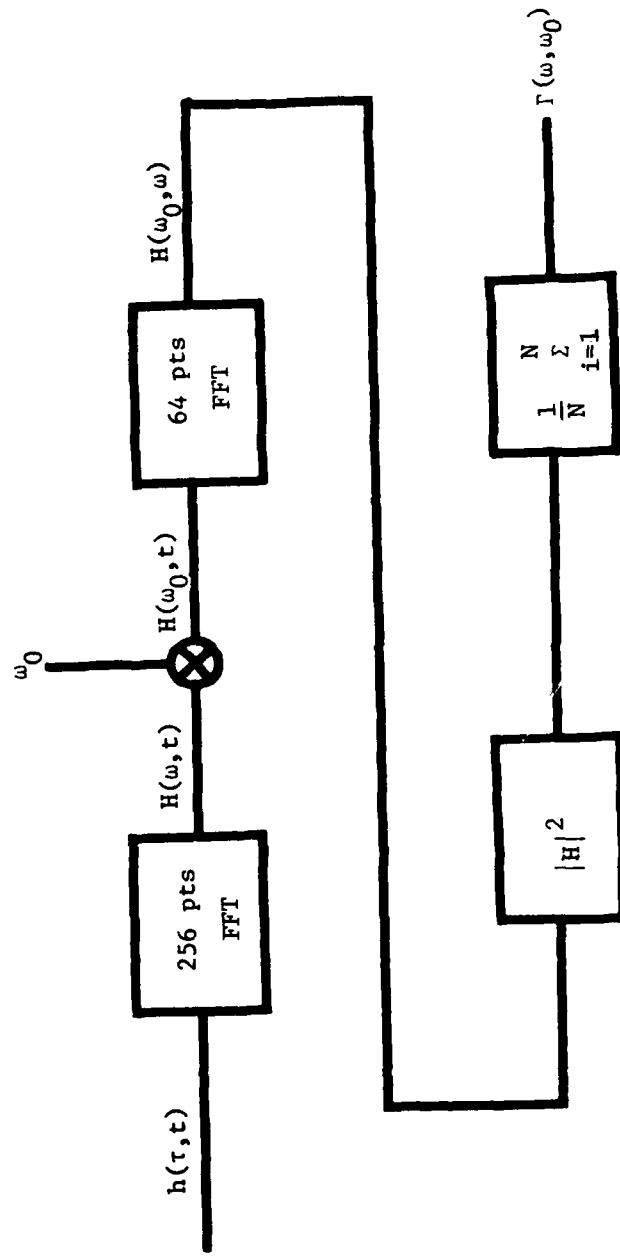


Figure J.2 Signal spectrum computing block diagram

REFERENCES

- [1] F.M. Labianca, and E.Y. Harper, "Sideband Structure of Sound from a Harmonic Point Source Scattered by a Rough Surface Moving over an Upward-refracting Ocean", *J. Acoust. Soc. Am.* Vol. 61, No. 2, 378-389, 1977.
- [2] W.A. Kuperman, "On Scattering from a Moving Rough Surface Without a Kirchhoff or a Farfield Approximation", *J. Acoust. Soc. Am.*, Vol. 64, No. 4, 1113-1116, 1978.
- [3] J.G. Zornig, "Frequency Spreading in Forward Surface Scattering", Tech. Report #7710, Dept. Engineering and Applied Science, Yale University, New Haven, Ct., December 1977.
- [4] B.E. Parkins, "Scattering from the Time-Varying Surface of the Ocean", *J. Acoust. Soc. Am.*, Vol. 42, 1262-1267, 1967.
- [5] L. Scharf and R. Swarts, "Acoustic Scattering from a Stochastic Sea Surface", *J. Acoust. Soc. Am.*, Vol. 55, 247-253, 1974.
- [6] C.W. Horton and T.G. Muir, "Theoretical Studies on the Scattering of Acoustical Waves from a Rough Surface", *J. Acoust. Soc. Am.*, Vol. 41, 627-634, 1967.
- [7] C.S. Clay and H. Medwin, "Dependence of Spatial and Temporal Correlation of Forward-Scattered Underwater Sound on the Surface Statistics. I. Theory", *J. Acoust. Soc. Am.* Vol. 47, 1412-1418, 1970.
- [8] J.F. McDonald and F.B. Tuteur, "Moment Characterization of a Doubly Spread Surface Scatter Channel at High Rayleigh Parameters", *IEEE Proc.*, Vol. 62, No. 11, 1606-1608, Nov. 1974.
- [9] I.M. Fuks, "Spectral Width of Signals Scattered by a Disturbed Sea Surface", *Sov. Phys. Acoust.*, Vol. 20, 276-281, 1974.
- [10] J.F. McDonald and P.M. Schultheiss, "Asymptotic Frequency Spread in Surface-Scatter Channels at Large Rayleigh Numbers", *J. Acoust. Soc. Am.*, Vol. 57, No. 1, 160-164, 1975.
- [11] R.L. Swarts and C.J. Eggen, "Simplified Model of the Spectral Characteristics of High-Frequency Surface Scatter", *J. Acoust. Soc. Am.*, Vol. 59, No. 4, 846-851, April 1976.
- [12] F.B. Tuteur, J.G. Zornig and H. Tung, "Scattering of Underwater Acoustic Signals from a Rough, Moving Surface", Final Report under Contract No. N00014-75-C-0298, S&IS Report No. 7705, June 1977.
- [13] C. Gazanhes, J. Leandre and J.P. Lefebvre, "Spectral Structure of an Ultrasound Wave Scattered by a Random Surface: Application to the Scattering of Sound from the Sea Surface", *J. Acoust. Soc. Am.*, Vol. 63, No. 5, 1347-1352, 1978.

- [14] C.S. Clay and H. Medwin, "High-Frequency Acoustical Reverberation from a Rough-Sea Surface", J. Acoust. Soc. Am., Vol. 36, 2131-2134, 1964.
- [15] D. Middleton, "Doppler Effects for Randomly Moving Scatterers and Platforms", J. Acoust. Soc. Am., Vol. 61, 1231-1250, 1977.
- [16] W.I. Roderick and B.F. Cron, "Frequency Spectra of Forward-Scattered Sound from the Ocean Surface", J. Acoust. Soc. Am., Vol. 48, No. 3, Pt. 2, 759-766, Sept. 1970.
- [17] M.V. Brown and G.V. Frisk, "Frequency Smearing of Sound Forward-Scattered from the Ocean Surface", J. Acoust. Soc. Am., Vol. 55, 744-749, 1974.
- [18] J.A. Shooter and S.K. Mitchell, "Observations of Acoustic Sidebands in CW Tones Received at Long Ranges", J. Acoust. Soc. Am., Vol. 60, 829-832, 1976.
- [19] I.P. Lysanov, "Theory of the Scattering of Waves at Periodically Uneven Surfaces", Sov. Phys. Acoust., Vol. 4, No. 1, 1-10, 1958.
- [20] L. Fortuin, "Survey of Literature on Reflection and Scattering of Sound Waves at the Sea Surface", J. Acoust. Soc. Am., Vol. 47, No. 5, Pt. 2, 1970.
- [21] Lord Rayleigh, The Theory of Sound, (Dover, New York, 1945).
- [22] J.L. Uretsky, "Reflection of a Plane Sound Wave from a Sinusoidal Surface", J. Acoust. Soc. Am., Vol. 35, 1293-1294 (L), 1963.
- [23] H.W. Marsh, "In Defense of Rayleigh's Scattering from Corrugated Surfaces", J. Acoust. Soc. Am., Vol. 35, 1835 (L), 1963.
- [24] R.F. Millar, "On the Rayleigh Assumption in Scattering by a Periodic Surface", Proc. Cambridge Phil. Soc., Vol. 65, 773-791, 1969.
- [25] J.G. Parker, "Reflection of Plane Sound Waves from an Irregular Surface", J. Acoust. Soc. Am., Vol. 28, 672-680, 1956.
- [26] S.R. Murphy and G.E. Lord, "Scattering from a Sinusoidal Surface--A Direct Comparison of the Results of Marsh and Uretsky", J. Acoust. Soc. Am., Vol. 36, 1598-1599 (L), 1964.
- [27] G.R. Barnard et al., "Underwater-Sound Reflection from a Pressure-Release Sinusoidal Surface", J. Acoust. Soc. Am., Vol. 39, 1162-1169, 1966.
- [28] W.C. Meecham, "Variational Method for the Calculation of the Distribution of Energy Reflected from a Periodic Surface. I.", J. Appl. Phys., Vol. 27, No. 4, 361-367, 1956.

- [29] W.C. Meecham, "Fourier Transform Method for the Treatment of the Problem of the Reflection of Radiation from Irregular Surfaces", J. Acoust. Soc. Am., Vol. 28, No. 4, 370-377, 1956.
- [30] H.S. Heaps, "Reflection of Plane Waves of Sound from a Sinusoidal Surface", J. Appl. Phys., Vol. 28, 815-818, 1957.
- [31] C. Eckart, "The Scattering of Sound from the Sea Surface", J. Acoust. Soc. Am., Vol. 25, 566-570, 1953.
- [32] B.B. Baker and E.T. Copson, The Mathematical Theory of Huygen's Principle, (Oxford University Press, New York 1950), Second Edition, Chapter 2.
- [33] W.C. Meecham "On the Use of the Kirchhoff Approximation for the Solution of Reflection Problems", J. Rational Mech. Anal., Vol. 5, 323-333, 1956.
- [34] D. Mintzer, "Discussion of the Paper by C. Eckart on Sea Surface Scattering", J. Acoust. Soc. Am., Vol. 25, 1015 (L), 1953.
- [35] J. Feinstein, "Some Stochastic Problems in Wave Propagation. I", Trans. IRE AP-2, 23-30, 1954.
- [36] E.P. Gulin, "Amplitude and Phase Fluctuations of a Sound Wave Reflected from a Sinusoidal Surface", Sov. Phys.--Acoust., Vol. 8, 223-227, 1963.
- [37] D.R. Melton and Sr. C.W. Horton, "Importance of the Fresnel Corrections in Scattering from a Rough Surface" I. Phase and Amplitude Fluctuations", J. Acoust. Soc. Am., Vol. 47, 290-298, 1970.
- [38] J.F. McDonald, "Fresnel-Corrected Second-Order Interfrequency Correlations for a Surface-Scatter Channel", IEEE Trans. Commu., Vol. COM-22, No. 2, 138-145, 1974.
- [39] R.L. Swarts and L.L. Scharf, "Note on Acoustic Scattering from Random-Amplitude/Random-Phase Sinusoidal Sea Surfaces", J. Acoust. Soc. Am., Vol. 56, No. 2, 686-687, 1974.
- [40] F.B. Tuteur, J.F. McDonald and H. Tung, "Second-Order Statistical Moments of a Surface Scatter Channel with Multiple Wave Direction and Dispersion," IEEE Trans. Commu., Vol. COM-24, No. 8, 820-831, 1976.
- [41] M.A. Isakovitch, "Scattering of Acoustic Waves at Small Inhomogeneities in a Waveduct", Sov. Phys.-Acoust., Vol. 3, 35, 1957.
- [42] V.G. Bezrodnyi and I.M. Fuks, "Amplitude and Phase Fluctuations of the Field in a Waveguide Having a Rough Wall", Sov. Phys.-Acoust., Vol. 17, No. 4, 444-449, 1972.

- [43] J.R. Wait, "Perturbation Analysis for Reflection from Two-Dimensional Periodical Sea Waves", *Radio Sci.*, Vol. 6, 387-391, 1971.
- [44] E.Y. Harper and F.M. Labianca, "Perturbation Theory for Scattering from a Point Source by a Moving Rough Surface in the Presence of Refraction", *J. Acoust. Soc. Am.* Vol. 57, No. 5, 1044-1051, 1975.
- [45] F.M. Labianca and E.Y. Harper, "Connection Between Various Small-waveheight Solutions of the Problem of Scattering from the Ocean Surface", *J. Acoust. Soc. Am.*, Vol. 62, 1144-1157, 1977.
- [46] W.A. Kuperman, "Coherent Component of Specular Reflection and Transmission at a Randomly Rough Two-fluid Interface", *J. Acoust. Soc. Am.*, Vol. 58, 365-370, 1975.
- [47] D. Middleton, "A Statistical Theory of Reverberation and Similar First-Order Scattered Fields-Part I: Waveforms and the General Process," *Trans. IEEE Information Theory*, Vol. 13, 372-392, 1967.
- [48] W.J. Jobst, "An Application of Poisson Process Models to Multipath Sound Propagation of Sinusoidal Signals", *J. Acoust. Soc. Am.*, Vol. 57, No. 6, Pt. 2, 1409-1412, June 1975.
- [49] P. Beckmann, "Scattering by Non-Gaussian Surfaces", *Trans. IEEE Antennas Propaga.*, Vol. AP-21, No. 2, 169-175, 1973.
- [50] J.F. McDonald and R.C. Spindel, "Implications of Fresnel Correlations in a Non-Gaussian Surface Scatter Channel", *J. Acoust. Soc. Am.*, Vol. 50, No. 3, Part 1, 746-757, 1971.
- [51] B. Kinsman, Wind Waves, Their Generation and Propagation on the Ocean Surface, (Prentice-Hall, Englewood Cliffs, N.J., 1965)
- [52] D.E. Weissman, "Two Frequency Radar Interferometry Applied to the Measurement of Ocean Wave Height", *Trans. IEEE Antennas Propaga.*, Vol. AP-21, 649-656, 1973.
- [53] J.G. Zornig, "Measurement of the Statistics of a Surface Scatter Channel", Ph.D. Dissertation, Dept. of Engineering and Applied Science, Yale University, New Haven, Ct., 1974.
- [54] R.C. Spindel, "An Experimental Investigation of a Statistically Distributed Scattering Surface and Acoustic Scattering", Ph.D. Dissertation, Dept. of Engineering and Applied Science, Yale University, New Haven, Ct., 1971.
- [55] C. Cox, and W. Munk, "Measurement of the Roughness of the Sea Surface from Photographs of the Sun's Glitter", *J. Opt. Soc. Am.*, Vol. 44, 838-850, 1954.

- [56] A.H. Schooley, "A Simple Optical Method for Measuring the Statistical Distribution of Water Surface Slopes", *J. Opt. Soc. Am.*, Vol. 44, 37-40, 1954.
- [57] J. Wu, "Directional Slope and Curvature Distributions of Wind Waves", *J. Fluid Mech.*, Vol. 79, Pt. 3, 463-480, 1977.
- [58] J.G. Zornig and J. Snyder, unpublished results.
- [59] P. Beckmann, "Shadowing of Random Rough Surfaces", *Trans. IEEE Antennas Propaga.*, AP-13, 384-388, 1965.
- [60] P. Beckmann, "Scattering by Composite Rough Surfaces", *IEEE Proc.*, 1012-1015, 1965.
- [61] R.A. Brockelman and T. Hagfors, "Note on The Effect of Shadowing on The Backscattering of Waves from Random Rough Surface", *IEEE Trans. Antennas Propag.*, AP-14, 621-629, 1966.
- [62] R.J. Wagner, "Shadowing of Randomly Rough Surfaces", *J. Acoust. Soc. Am.*, Vol. 41, 138-147, 1967.
- [63] P.J. Lynch and R.J. Wagner, "Energy Conservation for Rough-Surface Scattering", *J. Acoust. Soc. Am.*, Vol. 47, 816-821, 1970.
- [64] P.J. Lynch, "Curvature Corrections to Rough-Surface Scattering at High Frequencies", *J. Acoust. Soc. Am.*, Vol. 47, No. 3, Part 2, 804-815, 1970.
- [65] B.G. Smith, "Geometrical Shadowing of a Random Rough Surface", *Trans. IEEE Antennas Propaga.*, AP-15, 668-671, 1967.
- [66] R.R. Gardner, "Acoustic Backscattering from a Rough Surface at Extremely Low Grazing Angles", *J. Acoust. Soc. Am.*, Vol. 53, 848-857, 1973.
- [67] J.C. Novarini, and H. Medwin, "Diffraction, Reflection and Interference during Near-grazing and Near-normal Ocean Surface Backscattering", *J. Acoust. Soc. Am.*, Vol. 64, No. 1, 260-268, July 1978.
- [68] V.P. Glotov and Y.P. Lysanov, "Relative Contribution of Surface Air Bubbles and Waves to the Formation of Sea Reverberation" Sov. Phys. --Acoust., Vol. 14, 311-314, 1969.
- [69] I. Tolstoy and C.S. Clay, Ocean Acoustics, (McGraw-Hill, New York, 1966).
- [70] A.H. Schooley, "Simple Tools for Measuring Wind Fields above Wind-Generated Water Waves", *J. Geophys. Res.*, Vol. 68, No. 19, 5497-5504, 1963.

- [71] M. Born and E. Wolf, Principles of Optics (Pergamon, New York, 1970). Chap. 8, pp. 448-452.
- [72] L.L. Beranek, Acoustics, (McGraw-Hill, New York, 1954).
- [73] R.J. Urick, Principles of Underwater Sound for Engineers, (McGraw-Hill, New York, 1967).
- [74] J.F. McDonald, "Passive Detection and Tracking Using Surface Scattered Signals", Ph.D. Dissertation, Dept. of Engineering and Applied Science, Yale University, New Haven, Conn. 1970.
- [75] P. Beckmann and A. Spizzichino, The Scattering of Electromagnetic Waves from Rough Surfaces, (MacMillan, New York, 1963).
- [76] J.G. Parker. "Reflection of Plane Sound Waves from a Sinusoidal Surface", J. Acoust. Soc. Am., Vol. 29, 377-380, 1957.
- [77] W.C. Meecham, "Point Source Transmission Through a Sinusoidal Ocean Surface", J. Acoust. Soc. Am., Vol. 64, No. 5, 1478-1481, 1978.
- [78] E.O. LaCasce and P. Tamarkin, "Underwater Sound Reflection from a Corrugated Surface", J. Appl. Phys., Vol. 27, 138-148, 1956.
- [79] J.G. Zornig and J.F. McDonald, "Direct Measurement of Surface-Scatter Channel Coherence by Impulse Probing", J. Acoust. Soc. Am., Vol. 55, 1205-1211, 1974.
- [80] H. Schwarze, "Model for the Frequency Spread of Backscattered Underwater Sound Based on The Facet Model of The Rough Sea Surface," J. Acoust. Soc. Am., Vol. 64, No. 2, 605-613, Aug. 1978.
- [81] P.M. Schultheiss, J. Snyder, H. Tung and J.G. Zornig, "Acoustic Scattering from a Wind Driven Surface", Final Report under Contract N00014-75-C-1014, Dept. of Engineering and Applied Science, Yale University, June 1976.
- [82] W.B. Davenport and W.L. Root, An Introduction to the Theory of Random Signals and Noise, (McGraw-Hill, New York, 1958).
- [83] S.O. Rice, "The Mathematical Analysis of Random Noise", Bell Sys. Tech. J. 23(1944), 282-332, 24(1945), 46-156.
- [84] F.J. Kingsbury, "An Experimental Model Study of Underwater Acoustic Scattering from a Wind-driven Surface", Ph.D. Dissertation, Dept. of Engineering and Applied Science, Yale University, New Haven, Conn. 1970.

- [85] A.K. Fung and R.K. Moore, "The Correlation Function in Kirchoff's Method of Solution of Scattering of Waves from Statistically Rough Surfaces", J. Geophys. Res., Vol. 71, No. 12, 2939-2943, 1966.